



The
University
Of
Sheffield.

Design and Development of Novel Nanocarriers for Targeted Drug Delivery

By

Mhd Anas Tomeh

A thesis submitted in partial fulfilment of the requirements for the
degree of Doctor of Philosophy

2021

The University of Sheffield

Faculty of Engineering

Department of Chemical and Biological Engineering

Acknowledgement

I would like to thank my supervisors, Dr Xiubo Zhao and Dr Stephen Brown for offering me the chance to do this multi-disciplinary project and guide me through my PhD journey.

Also, my tremendous gratitude to Dr Jordan MacInnes for his patience and helpful guidance and kind supervision in essential parts of this project.

Special thanks to my friend Dr Roja Hadianamrei for her kind training, advice, and contribution to my papers.

Thanks to Miss Lucie N' Koy, Mr Chris Hill, Dr Christian Wong and Dr Wenxing Song for their technical support.

And finally, thanks to my wonderful family especially my father Kamal who believed in me and stood by me all the way.

Abstract

In this thesis, several nanoformulations have been prepared using different combinations of biomaterials including silk fibroin, sodium alginate, lipids, and amphiphilic cationic peptides as drug delivery systems. The physiochemical properties of these formulations were characterized and their efficiency as drug delivery systems was evaluated *in vitro* including 2D and 3D cell culture. ASC-J9 has been selected as a hydrophobic small molecule anticancer model drug that requires nanocarriers to modify its kinetics, prolong its circulation time and improve its activity. The designed nanocarriers successfully encapsulated ASC-J9, modify its release and enhanced cellular uptake. In the first experimental chapter, the particle elasticity theory was investigated by preparing stiffness-tunable nanoformulation. This novel formulation allows for manipulating the stiffness of the nanocarriers by changing the combination of the two biopolymers within the core of the carrier and without adding any synthetic or immunogenic materials.

One of the main limitations in large scale production of nanomaterials is batch to batch variation and lack of controllability during processing. To address these limitations a newly designed microfluidic mixer was introduced (swirl mixer) and its performance was assessed in comparison to conventional microfluidic designs. In the last experimental chapter, magnetic silk nanoparticles were manufactured and functionalised with G(IKK)₃-NH₂ amphiphilic cationic anticancer peptide. These functionalised nanoparticles not only improve the delivery of ASC-J9 but also demonstrated an augmented anticancer activity. Overall, the data presented in this thesis contributes to the field of nanomedicine and introduces new preparation techniques for the pharmaceutical industry and potential nanoformulations for cancer therapy.

Publications

➤ Published papers based on chapter 1

[1] **M.A. Tomeh**, R. Hadianamrei, X. Zhao, A review of curcumin and its derivatives as anticancer agents, *International journal of molecular sciences*, 20 (2019) 1033.

[2] **M.A. Tomeh**, R. Hadianamrei, X. Zhao, Silk Fibroin as a Functional Biomaterial for Drug and Gene Delivery, *Pharmaceutics*, 11 (2019).

[3] **M.A. Tomeh**, X. Zhao, Recent Advances in Microfluidics for the Preparation of Drug and Gene Delivery Systems, *Molecular Pharmaceutics*, 17 (2020) 4421-4434.

➤ Published paper based on chapter 3

[1] **M.A. Tomeh**, R. Hadianamrei, W. Sun, D. Xu, S. Brown, X. Zhao, Stiffness-tuneable nanocarriers for controlled delivery of ASC-J9 into colorectal cancer cells. *Journal of Colloid and Interface Science*, J.C.I.S. 2021.03.086

➤ Paper draft based on chapter 5

G3- Functionalised magnetic silk nanoparticles produced by the swirl mixer for enhanced anticancer activity (under review).

Conference abstracts

- The impact of organic solvents on processing protein-based formulation.
11th World Meeting on Pharmaceutics, Biopharmaceutics and Pharmaceutical Technology, Granada, Spain (2018).
- Stiffness tunable nanocarrier for drug delivery.
10th APS International PharmSci Conference, Greenwich, UK (2019).

Table of Contents

| | |
|---|----|
| Chapter 1 | 12 |
| 1.1 Introduction | 12 |
| 1.1.1 Nanocarriers for targeted drug delivery..... | 12 |
| 1.1.2 Barriers to clinical application of current nanocarriers | 14 |
| 1.1.3 Strategies and developments in nanocarrier design..... | 15 |
| 1.1.4 Mechanisms of nanocarrier targeting | 17 |
| 1.2 Curcumin and its Derivatives as Anticancer Agents | 20 |
| 1.2.1 Structural activity of curcumin and its derivatives | 21 |
| 1.2.2 Different types of curcumin delivery systems used in cancer therapy | 23 |
| 1.3 Silk Fibroin as a Functional Biomaterial for Drug and Gene Delivery | 30 |
| 1.3.1 Physicochemical Properties of Silk Fibroin | 32 |
| 1.3.2 SF-Based Drug Delivery Systems..... | 34 |
| 1.3.3 Applications of Silk Fibroin for Drug and Gene Delivery..... | 39 |
| 1.3.4 Modification of SF for Enhanced Delivery | 43 |
| 1.4 Microfluidics for preparation of drug and gene delivery systems | 46 |
| 1.4.1 Principles of mixing under controlled conditions | 47 |
| 1.4.2 Microfluidic techniques control the properties of the DDSs | 51 |
| 1.4.3 Industrial application | 53 |
| 1.5 Research motivation | 56 |
| 1.6 Thesis outline | 57 |
| 2 Chapter 2: Materials and Methods | 58 |
| 2.1 Materials | 58 |
| 2.2 Methods | 58 |
| 2.2.2 Preparation of SF nanoparticles and SF-magnetic nanoparticles by microfluidic platform..... | 60 |
| 2.2.3 Characterization | 66 |
| 2.3 Techniques and instrumental principles | 71 |
| 2.3.1 Dynamic light scattering (DLS) | 71 |
| 2.3.2 Nanoparticle tracking analysis (NTA) | 72 |
| 2.3.3 Transmission electron microscopy (TEM)..... | 74 |
| 2.3.4 Atomic force microscopy (AFM) | 75 |
| 2.3.5 Fourier transform infrared (FTIR) spectroscopy..... | 78 |
| 2.3.6 High content fluorescent imaging microscope..... | 79 |

| | | |
|----------|--|------------|
| 3 | Chapter 3: Stiffness-tuneable nanocarriers for controlled delivery of ASC-J9 into colorectal cancer cells | 81 |
| 3.1 | Introduction | 81 |
| 3.2 | Results & Discussion | 84 |
| 3.2.1 | Physical characterization of the ASC-J9 nanocarriers | 85 |
| 3.2.2 | ASC-J9 encapsulation and release | 90 |
| 3.2.3 | <i>In vitro</i> cellular uptake study | 93 |
| 3.2.4 | Uptake in 3D tumour spheroids | 95 |
| 3.3 | Conclusion | 99 |
| 4 | Chapter 4: Swirl mixer for the production of silk fibroin nanoparticles | 100 |
| 4.1 | Introduction | 100 |
| 4.2 | Result and discussion | 103 |
| 4.3 | Conclusion | 114 |
| 5 | Chapter 5: G3-Functionalised magnetic silk nanoparticles produced by the swirl mixer for enhanced anticancer activity | 115 |
| 5.1 | Introduction | 116 |
| 5.2 | Results and discussion | 119 |
| 5.2.1 | Characterization and surface analysis of MSNP and (G3)-MSNP | 119 |
| 5.2.2 | Cellular uptake and cytotoxicity study | 128 |
| 5.2.3 | Tumor-spheroid penetration study | 135 |
| 5.3 | Conclusion | 137 |
| 6 | Chapter 6: Conclusion and the future perspective | 138 |
| 6.1 | Conclusion | 138 |
| 6.2 | Future work | 141 |
| 7 | References | 145 |

Table of Figures

| | |
|---|----|
| Figure 1.1. Timeline development of the main nanoparticles design strategies for drug and gene delivery in the past two decades. | 16 |
| Figure 1.2. Tumor targeting of nanocarriers by the enhanced permeability and retention (EPR) effect. Differences between normal (A) and tumour (B) vessels are depicted | 17 |
| Figure 1.3. Schematic representation of nanocarriers with a modified surface using polymers, ligands, or antibodies for cellular targeting. The nanocarriers core can also be modified to load different APIs, control drug release, and target tumour tissues. (1) Encapsulating the hydrophobic drug in the carrier's core or the polymeric or lipid outer layer. (2) Incorporating magnetic particles within the nanocarrier core. (3) Entrapping one or more polymers to modify the physiochemical properties of the carrier. (4) Capturing DNA/ RNA within the carrier core using cationic polymers. | 20 |
| Figure 1.4. (A) Chemical structure of curcumin. (B) The main pharmacophore's structure activity relationship (SAR) of curcumin and potential substitution positions. | 23 |
| Figure 1.5. Examples of current nanoparticle design strategies for improving targeting. | 25 |
| Figure 1.6. (A) Fabrication of magnetic silk particles (MSP) for curcumin delivery. (B) AFM images of MSP before and after curcumin loading. (C) Representative microscopic images of MDA-MB-231 cells incubated with free curcumin and curcumin loaded MSP showing a significant improvement of curcumin cellular uptake. | 28 |
| Figure 1.7. A diverse set of physical assemblies and chemical methods for preparing a variety of silk fibroin (SF) formats for pharmaceutical and biomedical applications | 31 |
| Figure 1.8. Total epirubicin (EPI) release profile from SF nanofilm depending on the ratio of the added glycerol and the solvent treatment. | 41 |
| Figure 1.9. (A) Possible routes toward chemical modification of amino acids of silk proteins. Reprinted from [185]. (B) The new properties obtained by SF when functionalised or modified in different positions. | 44 |
| Figure 1.10. A) Schematic representation of solute concentration trend during the nanoprecipitation and nanoparticle formation steps. B) The staged assembly process of block copolymers to form nanoparticles and the effect of rapid mixing on the properties of the produced nanoparticles. | 49 |
| Figure 1.11. Examples of microfluidic fabrication of DDSs. | 54 |
| Figure 2. 1. A) Formation of multilamellar lipo-gel vesicles (MLVs) by hydration of the thin lipid layer using a rotary evaporator. B) Extrusion of MLVs using Avanti Mini Extruder. | 59 |

| | |
|---|----|
| Figure 2. 2. Angled view of the swirl mixer pattern from the two sides of the PEEK chip. A) One mixing element. B) Two mixing elements. C) Four mixing elements. D) The complete swirl mixer setup connected Chemyx syringe pump..... | 61 |
| Figure 2. 3. Magnetic nanoparticles collected using Neodymium magnet (20 x10 mm)..... | 62 |
| Figure 2. 4. Schematic representation of the testing process of magnetic silk nanoparticles (MSNP) under magnetic field..... | 70 |
| Figure 2. 5. A) Schematic representation of the dynamic light scattering (DLS) instrument. Reprinted from [322]. B) Schematic representation of the layers surrounding the surface of negatively charged particles during Zeta potential measurement. | 72 |
| Figure 2. 6. A) Nanosight for nanoparticle tracking analysis (NTA). B) Schematic representation of the NTA instrument configuration. C) Nanoparticle Tracking Analysis software (NTA 3.1) using the scattered light in the recorded video for measuring the size distribution and determining the standard deviation SD. | 73 |
| Figure 2. 7. A) Transmission electron microscopy (TEM), FEI Tecnai BioTWIN G2 sprint (USA) (the University of Sheffield). B) Schematic representation of the working principle of TEM..... | 75 |
| Figure 2. 8. A) Atomic Force Microscopy (AFM) Dimension FastScan with ScanAsyst, Bruker (University of Sheffield). B) SCANASYST-AIR in PeakForce and Tapping Mode operating software. C) Schematic representation of AFM basic principles (left), real micro-cantilever and components (right) | 76 |
| Figure 2. 9. AFM data analysis software (NanoScope 1.5) for measuring the size, shape and morphology of the scanned sample. | 77 |
| Figure 2. 10. Schematic representation of the principle of a Michelson interferometer. Reprinted from [336] with permission from Taylor & Francis. | 79 |
| Figure 2. 11. A) ImageXpress [®] Micro System. B) MetaXpress [®] software 5.3.01 using custom module tool to design an algorithm that can find nucleus of HCT 116 cells and determine cellular population. C) MetaXpress [®] software 5.3.01 using custom module tool to analyse three different channels (DAPI, GFP & Texas red) to identify nucleus, drug & cytoplasm of HCT 116 cells..... | 80 |
| | |
| Figure 3. 1.. A) DOPC liposome suspension before and after 200 membrane extrusion. B) AFM image of a DOPC liposome after extrusion entrapping crosslinked Sodium alginate (SA). | 84 |
| Figure 3. 2. (A) Schematic representation of the three synthesized nanocarriers entrapping different ratios of silk fibroin (SF) to sodium alginate (SA). (B) TEM images of the synthesized nanocarriers. (C) AFM images of the nanocarriers showing the polymeric core and the lipid shell in dry mode. (D) Height profiles of the nanocarriers obtained by AFM. (E) 3D AFM images of the nanocarriers. | 86 |

| | |
|---|-----|
| Figure 3. 3. (A) The maximum absorbance of ASC-J9 using UV spectroscopy. (B) ASC-J9 calibration curve in PBS..... | 88 |
| Figure 3. 4. Characterization of the synthesized nanocarrier formulations with varying properties. | 88 |
| Figure 3. 5. (A) Schematic representation of silk fibroin (SF) structural transformation in the designed nanocarriers as a result of blending with sodium alginate (SA). (B) FTIR spectra of SF and SF/SA blend with a different ratio in the nanocarrier core..... | 90 |
| Figure 3. 6. Representative force curves for extend and retract processes with a single nanocarrier formulation. (A) SF:SA (3:7). (B) SF:SA (1:1). (C) SF:SA (7:3). | 92 |
| Figure 3. 7. Characterization of the synthesized nanocarrier formulations by force mapping mode of the AFM (A) Schematic illustration of high and low stiffness nanocarriers during Young’s moduli measurements. (B) The Young’s moduli of the nanocarriers characterized in liquid mode by AFM calculated using Hertz model. | 93 |
| Figure 3. 8. High content fluorescent microscope images of HCT-116 showing cellular uptake of the free ASC-J9 and different ASC-J9 loaded nanocarriers (SF:SA=7:3, 1:1, & 3:7) after 24 hrs (×20 magnification, the scale bar represents 40 μm). | 96 |
| Figure 3. 9. (A) Relative cellular uptake of ASC-J9 loaded nanocarriers formulations and unformulated ASC-J9. (B) Fluorescence integrated intensity of ASC-J9 at multiple time points in unformulated form and in nanocarriers form. (C). The percentage of survived cells after ASC-J9 and ASC-J9 loaded nanocarriers treatments at multiple time points. (D) The effect of the unloaded nanocarrier formulations the cell population %. An asterisk denotes statistical significance as follows: *P < 0.05, **P < 0.01, ***P < 0.001..... | 97 |
| Figure 3. 10. (A) High content fluorescent microscope images showing uptake of ASC-J9 solution and ASC-J9 loaded nanocarrier formulations by HCT-116 tumour spheroids (×2 magnification, scale bars represent 400 μm). (B) The fluorescent intensity of ASC-J9 within the spheroids. | 98 |
| Figure 4. 1. Swirl mixer element: flow and concentration modeling at Re= 100. | 101 |
| Figure 4. 2. Syringe and flow system characteristics for FRR =3.0. (A) Swirl mixer with 4 mixing elements (4X). (B) The model T-mixer. | 102 |
| Figure 4. 3. Percentage yield of silk nanoparticles produced with Swirl mixer and T-mixer at two different TFR. | 104 |
| Figure 4. 4. The size distribution comparison of the two mixers operating at different TFRs and in laminar and transitional flow regime (Re> 3000). (A) Swirl mixer. (B) T-mixer..... | 105 |

| | |
|--|-----|
| Figure 4. 5. Mean flow patterns for turbulent flow in the tube mixer (left) and the swirl mixer (right). Streamlines are coloured with local concentration from red (pure Solution A) to blue (pure Solution B) with mid-green being the perfect mixture between the two..... | 107 |
| Figure 4. 6. The size distribution comparison of the two mixers operating at different TFRs and in fully turbulent flow regime ($Re < 3700$). (A) Swirl mixer. (B) T-mixer..... | 108 |
| Figure 4. 7 (A) The flow pattern modelling of the T-mixer. (B) The flow pattern modelling of the Swirl mixer (Mesh modelling). (C & D) The mean particle size and standard deviation produced by the T-mixer and swirl mixer using different TFR. (E & F) The mean particle size at different mixing time in T-mixer and swirl mixer. (G & H) Stability of silk nanoparticles generated by T-mixer (G) and swirl mixer (H) using the same Total flow rate (TFR = 50 ml/min). The particle size of the silk nanoparticles stored at 4 °C and 37 °C was measured in DI water over 30 days. | 110 |
| Figure 4. 8. Atomic force microscopy (AFM) scans of silk particles produced at (TFR = 50 ml/min, mixing time = 7.25 ms) using T-mixer and swirl mixer. (I & J) TEM images of silk nanoparticles produced at (TFR = 50 ml/min, mixing time = 7.25 ms) using T-mixer and swirl mixer..... | 112 |
| Figure 4. 9. (A) The effect of the number of swirl mixing elements in the chip on the mean size particle and the standard deviation. (B) Microscopic images of the swirl mixing elements of mixing chips.. | 113 |
| | |
| Figure 5. 1. (A) Formation of magnetic silk nanoparticles (MSNP) using the microfluidic platform followed by G3 functionalisation to prepare (G3-MSNP). (B) AFM scans of G3-MSNP. (C) The helical wheel projection of G3 peptide[404]..... | 118 |
| Figure 5. 2. (A) FTIR absorbance spectra of unpressed silk and silk nanoparticles produced by microfluidic device using Methanol or Acetone as the organic phase. (B) Silk fibroin secondary structure analysis of the nanoparticles generated by the microfluidic device by changing the organic phase and the total flow rate. | 121 |
| Figure 5. 3. AFM scans of the different steps involved in production and functionalisation of MSNPs using methanol or acetone as the organic phase. (A) MNP Scans before mixing with silk solution in the microfluidic system. (B) AFM scans of MSNPs produced by the microfluidic system at TFR = 50 ml/min. (C) AFM scans of G3 functionalised MSNPs after 12 h incubation with G3 solution..... | 123 |
| Figure 5. 4. (A) the size and (B) zeta potential of the MSNPs produced by the microfluidic system before and after functionalisation with G3 peptide..... | 124 |
| Figure 5. 5 (A) The maximum absorbance and calibration curve of FITC labelled G3 peptide. (B) The percentage of G3 grafted on the surface of MSNP processed with acetone or methanol. | 125 |
| Figure 5. 6. (A) Encapsulation efficiency (EE%) of ASC-J9. (B) Drug release profile of ASC-J9. | 127 |

Figure 5. 7. The cellular uptake and cytotoxicity study of G3 and G3 grafted MSNP in cancer and non-cancer cell lines. (A & B) The cellular uptake of G3 and G3-grafted MSNPs in HCT 116 and HDF cells. (C &D) Cytotoxicity of G3 and G3-grafted MSNPs in HCT 116 and HDF cells. 129

Figure 5. 8. High content microscopy images of HCT 116 cells (A) and HDF cells (B) treated with FITC-labelled G3 (FITC-G3) or MSNPs grafted with FITC-labelled G3 (FITC-G3-MSNP) at the concentration of 25 μ M for 6 h. The nuclei are stained with Hoechst 33342 (blue), the cytoplasm is stained with Flash Phalloidin™ 594 (red) and the fluorescent from FITC is observed in green. \times 20 magnification, scale bars represent 50 μ m..... 130

Figure 5. 9. (A & B) Cellular uptake of MSNP and (G3)-MSNP loaded with ASC-J9 compared to free ASC-J9 in HCT 116 cells and HDF cells. (C & D) Cytotoxicity study of MSNP and (G3)-MSNP loaded with ASC-J9 compared to free ASC-J9 in HCT 116 cells and HDF cells. 132

Figure 5. 10. High content microscopy images of HCT 116 cells treated with free ASC-J9, MSNPs loaded with ASC-J9 and G3-MSNPs loaded with ASC-J9 for 6 h. The nuclei are stained with Hoechst 33342 (blue), the cytoplasm is stained with Flash Phalloidin™ 594 (red) and the fluorescent from ASC-J9 is observed in green. \times 20 magnification, scale bars represent 50 μ m..... 133

Figure 5. 11. High content microscopy images of HDF cells treated with free ASC-J9, MSNPs loaded with ASC-J9 and G3-MSNPs loaded with ASC-J9 for 6 h. The nuclei are stained with Hoechst 33342 (blue), the cytoplasm is stained with Flash Phalloidin™ 594 (red) and the fluorescent from ASC-J9 is observed in green. \times 20 magnification, scale bars represent 50 μ m..... 134

Figure 5. 12. Mean normalised fluorescence intensity of MSNP, G3-MSNP with and without magnetic field (+M) in comparison to free ASC-J9 after 12 h of treatment compared to the untreated controls. 135

Figure 5. 13. High content microscope images of HCT 116 three dimensional multicellular tumor spheroids 12 h after treatment with ASC-J9 loaded MSNP, ASC-J9 loaded G3-MSNP or free ASC-J9 in the presence (+M) and absence of magnetic field in comparison to untreated controls. \times 2 magnification, Scale bar represents 400 μ m. 136

Figure 6.1 Schematic representation of future in vivo experiments for further investigation of the activity and targetability of drug loaded magnetic silk nanoparticles. Created by BioRender.....141

Figure 6.2 . Schematic representation of design modifications of the current microfluidic system and additional characterizations equipment that should be considered for optimizing nanoparticle production. Created by BioRender.....142

Chapter 1

1.1 Introduction

This PhD project is focused on designing nanocarriers using newly developed formulations and manufacturing techniques for drug delivery. The physiochemical properties of the prepared nanocarriers were characterised using a wide range of techniques to investigate their ability to function as vectors for model hydrophobic drugs. The first objective is to evaluate the impact of the nanocarrier properties on controlling the loaded drug release and regulating cellular uptake in human 2D and 3-D cell culture. The next objective is to develop a new microfluidic device for controllable production of nanocarriers (biopolymeric nanoparticles) which allows for scaling up the process and address the limitations of the current designs. The final objective is to implement the developed microfluidic device in the process of preparing functionalized magnetic nanoparticles to target tumour tissues and minimize the multidrug resistance in cancer cells. Several experimental approaches were used; including microscopic imaging, high content screening and multiple in vitro assays in both cancer and normal cells. The findings presented in this thesis show the impact of formulating an anticancer model drug in nanocarriers on the cellular uptake, activity and targetability using biocompatible ingredients. In addition, the newly developed microfluidic device in this thesis provides an improved platform for fabricating nanocarriers with a great potential for translating the benchtop preparations to pharmaceutical industry.

In the following sections, an overview of the challenges, strategies and applications of nanocarriers as drug delivery systems in the field of nanomedicine. In addition, detailed reviews of the anticancer model drug (ASC-J9) and the biopolymers used in the studied nanocarrier formulations were provided. The recent advances in microfluidics for drug delivery were also discussed to cover the pros and cons of the current devices and the rational design approaches for controlling the nanofabrication process.

1.1.1 Nanocarriers for targeted drug delivery

The majority of anticancer agents are small molecules with unsuitable physiochemical properties for drug delivery, such as high lipophilicity and low aqueous solubility. The molecules of free hydrophobic drugs lack the ability to form hydrogen bonds with water and

the drug is classified as poorly soluble when the maximum dose strength is not soluble in 250 ml of water [1, 2]. The poor physiochemical properties of anticancer drugs limit the translations of many unformulated anticancer agents to clinical trials. The main approaches to improving the drug solubility include: preparation of prodrug by chemical modifications; addition of organic solvents, and encapsulating into a nanocarrier [3-5]. Among these strategies, nanocarriers emerged as the preferred approach because it was the most feasible and did not require a cytotoxic ingredient [4, 5]. In addition to aqueous solubility, other properties, such as controlled drug release, enhanced cellular uptake and tumour tissue targeting, are essential in cancer therapy. The recent advances in nanotechnology allows for preparation of drug delivery systems with desirable characteristics and modified properties to improve the quality of anticancer treatment [6]. To achieve this goal, a wide range of nanocarriers were developed as drug delivery systems, including: liposomes, micelles, polymer conjugates, and polymeric nanoparticles [7, 8]. These systems are considered efficient nanocarriers for a drug when they meet certain standards, such as (1) efficient drug loading, (2) controlled payload release at the site of action, and (3) biocompatibility and biodegradability [9, 10]. Moreover, preventing rapid clearance and opsonisation of therapeutic agents that leads to short half-life, is a key task for the nanocarriers to deliver [11]. The short half-life of anticancer agents such as doxorubicin (DOX) and ASC-J9 may require increasing the administered dose or the administration frequency to achieve the desired effect [12, 13]. Fracasso *et al.* [14] conducted phase I clinical trials on 14 patients to investigate the impact of pegylated liposomal doxorubicin (PEG-LD) [14]. The results demonstrated a moderate prolongation of total doxorubicin clearance and half-life, but did not increase its toxicity [14]. More nanocarrier formulations and production techniques are currently under study to obtain specific properties for efficient drug delivery. For example, recent studies investigated the impact of nanocarrier size, components, surface charge and elasticity on regulating cellular uptake, tumour targeting, and modifying drug release [15-19]. Nanoparticles and liposomes with a size range (100-200 nm) achieved higher tumour accumulation due to enhanced permeability and retention effect (EPR) [10, 20-22]. Therefore, designing a nanocarrier preparation technique that maintains the size below 200 nm is highly desirable in nanomedicine.

1.1.2 Barriers to clinical application of current nanocarriers

Insufficient encapsulation of hydrophobic drugs is one of the common obstacles in the current nanocarrier formulations to efficient drug delivery [10, 23]. In the case of low encapsulation efficiency, large quantities of the nanocarriers must be administered in order to achieve the minimum effective drug concentration. As a result, the risk of toxicity and immunogenicity can increase, especially when synthetic polymers are used [24, 25]. Although natural polymers such as polysaccharides and proteins are biodegradable with low risk of toxicity, these polymers can have low stability, uncontrolled release of the loaded drug, and complicated processing methods [26]. In addition to low drug encapsulation, undesirable drug release is a main challenge in nanocarrier formulations. Therefore, avoiding the burst release effect (uncontrolled sudden release of the loaded drug) in the medium after administration is a necessity in cancer therapy [27]. Otherwise, a large amount of the loaded drug will be lost before reaching the target tissue, which can compromise the overall treatment process [28]. The development and planning process of the new generation of the nanocarriers must consider biodistribution and cell targeting. Lack of ability to target cancer cells can cause several undesirable side effects. The physical and chemical stability is another important limitation to address when developing nanocarrier formulations. For example, hydrolysis and oxidation are the major degradation reactions in phospholipid-based nanocarriers [29]. These reactions may be promoted by pH of the media or the nature of the loaded drug [30]. Physical instability issues, including: fusion, aggregation, and drug leakage, can affect the particle size of the nanocarrier as well as its loaded drug [29, 31]. Preparing nanocarriers with an average size of >200 nm is not the only strategy to improving biodistribution. Surface modification using polymers or ligands can have a greater impact on drug distribution and the targeting ability of the nanocarrier [31-33]. In addition, high production rate and reproducibility of prepared nanocarriers are additional barriers to large scale production [34]. To overcome these barriers, chemically modified or multi-component (hybrid) nano-carriers have been developed using two or more classes of nanomaterials, mostly polymers and lipids [35]. Moreover, using fabrication techniques such as microfluidics increases controllability, production rate, and can help the translation to the pharmaceutical industry [36].

1.1.3 Strategies and developments in nanocarrier design

Design and functionalization strategies for multifunctional nanocarriers (e.g. nanoparticles, micelles, liposomes) based on biodegradable/biocompatible materials intended to be employed for active targeting and drug delivery evolved in the past decades [37]. Nanocarriers can be engineered to precisely control drug-release rates, or to target specific sites within the body with a specific amount of therapeutic agent [38]. The first generation of nanoparticles was designed in the 1960s using a biologically active polymer (divinyl ether-maleic anhydride) in liposomes [39]. However, this formulation was found to be toxic in clinical trials [40]. This example shed light on the importance of the rational design of nanocarrier formulation and utilisation of biomaterials to avoid toxicity. Particle size and surface charge were the main concerns of the early stage of the internalisation kinetics of nanoparticles due to the relationship between the cellular internalisation rate, and particle size and aspect ratio [41]. Serum protein adsorption of positively charged nanocarriers increases significantly in comparison to neutral or negatively charged particles [42]. The focus of nanotechnology shifted in the early 1990s, from manipulating the nanoparticle size and shape only, to more advanced nanoparticle engineering (**Figure 1.1**). This shift occurred when more studies revealed that relying on the passive targeting mechanism in tumour tissues alone was not enough in efficient cancer therapy [43]. Modifying size, shape and surface charge are limited to less than 1% tumour accumulation [44]. The trend in drug delivery to tumors is consequently directed toward integrated multifunctional carrier systems, providing selective recognition of cancer cells in combination with a sustained or triggered release (**Figure 1.1**) [38]. More tools are emerging to allow nanocarriers to avoid internalisation by phagocytic cells and enhance accumulation at the target tissues. For example, the chemical reduction of disulfid bonds of polymeric nanocarriers can trigger the release of the payload by increasing the porosity of the carrier and enhancing drug diffusion to the site of action. This process was used as targeting mechanisms to cancer tissues as they have a lower pH than normal tissues [45, 46]. Pradhan et al.[19] prepared liposomal nanocarriers with multiple targeting mechanisms including: thermosensitive lipid combination (decomposing at 42 °C), sensitive to a magnetic field, and PEG-folic acid coating (**Figure 1.1**) [19]. The successful design of targeted nanocarriers is also governed by the nature of the used polymers and functionalising ligands. Modifying the physical nature of the polymeric nanocarrier was used to regulate the

cellular uptake siRNA loaded nanoliposomes [15]. Only recently, studies were conducted to investigate a relationship between polymeric nanocarrier stiffness and cellular uptake [7]. Nanocarrier stiffness regulating cellular uptake was explained by the shift in the cell internalisation pathway. For low Young's modulus, liposomes can enter the cells via fusion, the low energy predominant pathway [47], and endocytosis. By increasing the Young's modulus, the only way to enter the cell is endocytosis, and this results in sustained release of the loaded drug [15]. The main loading mechanism of gene delivery systems is the electrostatic interaction between positively charged polymeric carriers and negatively charged nucleic acids (DNAs & RNAs) so they can reach their targeted destination and escape enzymatic degradation. The positively charged carriers can also enhance the cellular uptake of the genetic material by interacting with the negatively charged cell surface. The carrier surface charge can be manipulated to optimise gene loading and release by using cationic polymers such as polylysine and polyethyleneimine (PEI) [48, 49].

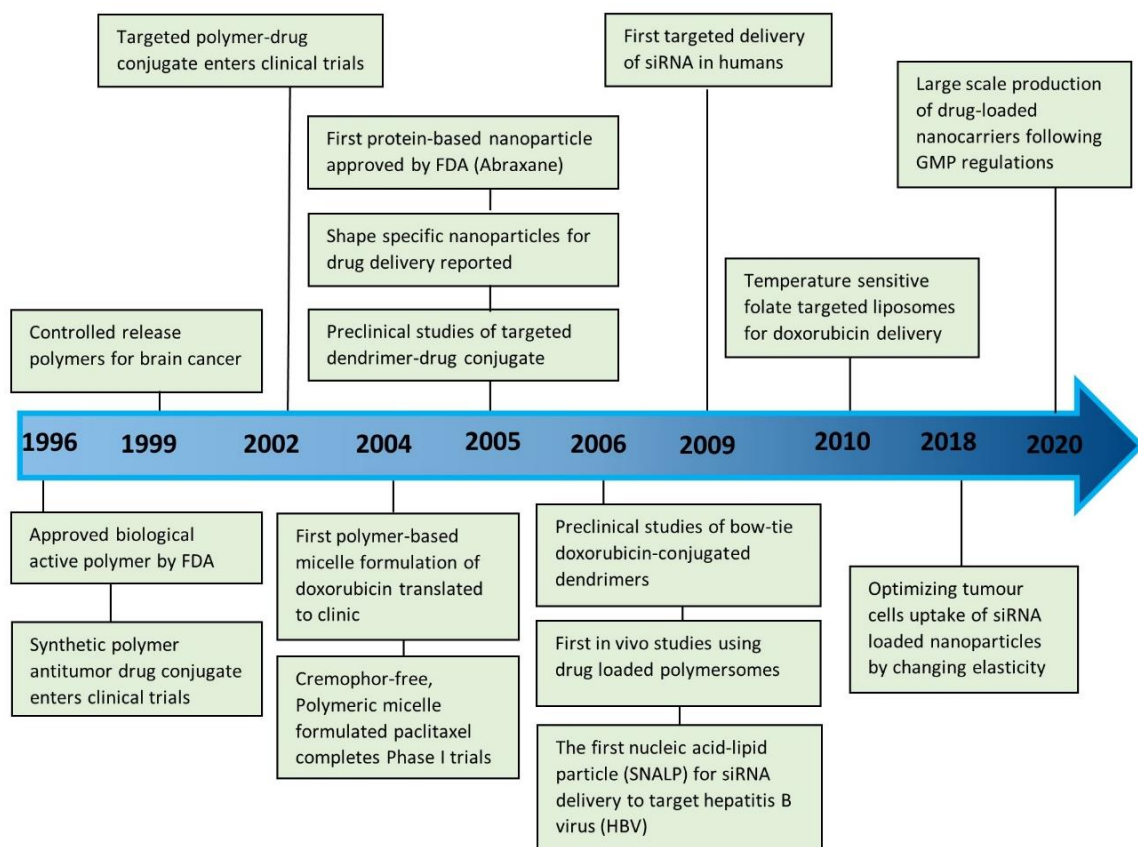


Figure 1.1. Timeline development of the main nanoparticles design strategies for drug and gene delivery in the past two decades [15, 31, 50-60].

1.1.4 Mechanisms of nanocarrier targeting

1.1.4.1 Organ or tissue targeting

Drug delivery systems with nanostructures promise numerous advantages for targeted drug delivery. One of the important properties for the nanocarriers to achieve effective concentration at the target tissue is maintaining the nanocarrier particle size below 200 nm. This particle size demonstrates a higher efficacy in cancer therapy in comparison to larger particles [21]. The enhanced permeability and retention effect (EPR) allows high accumulation of the nanocarriers in tumour tissue. The transport of the anticancer drug to a specific organ or tissue can be achieved by controlling the particle size. Due to cell-growth deregulation in tumour tissue, new blood vessels are formed that are a prerequisite for the survival of tumours larger than 2 mm in size (**Figure 1.2**) [38, 54]. To exploit tumour EPR effects, nanocarriers should not only maintain a specific size, but also have a stealthy surface to avoid renal clearance and cellular internalisation such as phagocytosis [61, 62].

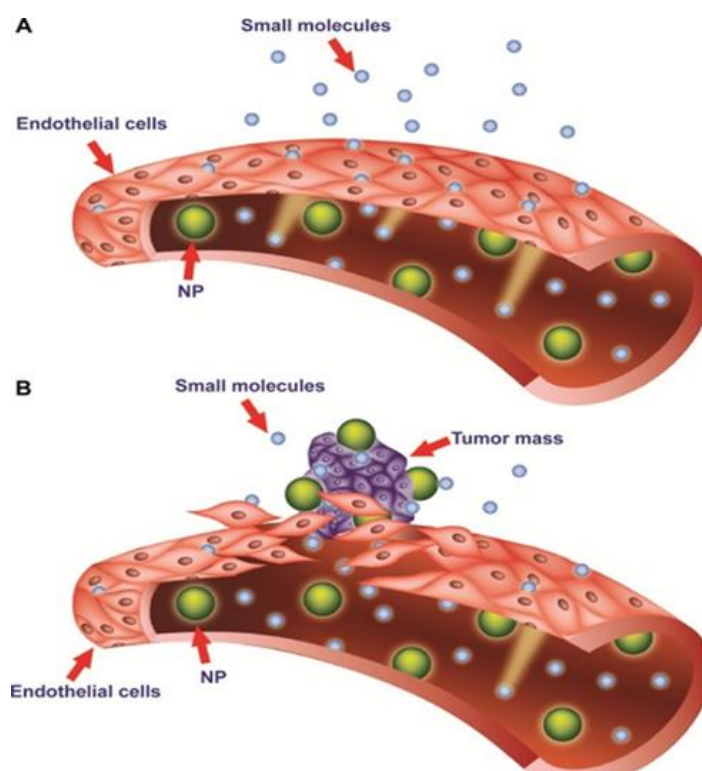


Figure 1.2. Schematic representation of tumor targeting by nanocarriers (the green particles) with particle size smaller than 200 nm following the enhanced permeability and retention effect (EPR).

(EPR) effect. Very low accumulation of nanocarriers was displayed at normal tissue (A) in comparison to tumour tissue (B) due to the EPR effect in the tumour vessels [54].

1.1.4.2 Folate-mediated targeting

Folate plays a key role in DNA replication and synthesis, cell division and growth, especially in rapidly proliferating cells [63]. Folate receptor (FR) is normally expressed at the luminal surface of epithelial cells to shield itself from direct contact with folate in the circulation [5,6]. However, the abnormal carcinoma cells allow FR to access folate via alteration of the trans-membrane region. Exploiting the overexpression of FR in cancer cells by functionalising nanocarrier surface with folate is one of the effective approaches in tumours targeting [22]. Recent studies demonstrated the possibility of delivering macromolecules into living cells by folate receptor endocytosis [64]. Nanoliposomes encapsulating doxorubicin were functionalised with folic acid to target folate receptors expressing tumour cell lines such as KB and HeLa cells [19, 65]. This approach was also used as a targeting technique towards tumours with haptens during cancer immunotherapy [66]. In another study conducted by Tong *et al.* [67] FA coupled PEGylated nanoliposomes were prepared to deliver Paclitaxel (PTX) to KOV3/TAX ovarian tumours [67]. This combination of FA-PEG-liposomes significantly prolonged the survival, and reduced the tumour nodule number in mice in comparison to free PTX or non-targeted nanocarriers [67].

1.1.4.3 Transferrin-mediated targeting

Transferrin receptor (Tfr) has low expression in normal cell membranes [68]. However, similar to FR, Tfr is overexpressed (100-fold) in many cancers including; ovarian, brain, breast, lung adenocarcinoma, and prostate due to the increased demand of iron for the survival of these tumours [69, 70]. Targeting cancer cells using (Tf) has become one of the common approaches in nanomedicine (**Figure 1.3**). For example, Riaz *et al.* [71] prepared T7 peptide-functionalised liposomes loaded with Quercetin (QR) to enhance the selectivity and anticancer activity of QR toward lung A549 cancer cells [71]. In gene delivery, Tf mediated liposomes were successfully delivered to rat brain cells. Surface modified liposomes with OX26 monoclonal antibodies for rat Tfr targeting have shown high bioavailability in brain microvascular endothelium [72].

1.1.4.4 Stimulated nanocarriers

Tumour tissues have different properties from normal body tissues as cancer cells have an uncontrollable proliferation of cancer cells and skip apoptosis. For example, tumour tissues have lower pH value and slightly higher temperature compared to healthy tissues. Nanocarriers that can utilise these conditions as a stimuli to discharge the loaded drug only in acidic environment and temperatures above 37 °C to target specific tumour tissues. The nanocarrier must be also uptaken by the cancer cells in large quantities or release the incorporated drug to exert the desired activity. Although liposomes functionalised with PEG have prolonged blood circulation time, drug release in the tumour tissue can be obstructed by the PEG coating. In order to improve the efficiency of these liposomes, the drug release should be triggered by the conditions at the site of action such as low pH. The PEG-lipid linkage can be formulated to cleave in the acidic media of the tumour [73]. In addition, liposomal formulations can be designed to release the therapeutic agent at a specific temperature. For example, the optimised ratios of phospholipids [1,2-dipalmitoyl-sn-glycero-3-phosphocholine (DPPC), cholesterol, and PEG 2000] demonstrated a significant increase in doxorubicin release when subjected to a temperature >40 °C due to decomposition of the lipid formulation [19, 74]. Another effective approach in tumour targeting is magnetic field stimuli, which can drive the nanocarrier to the targeted tissue simply by incorporating magnetic particles within the nanocarrier formula (**Figure 1.3**). Magnetic particles have demonstrated very promising results in enhancing tumour targeting and cell uptake of the hydrophobic drugs such as curcumin [49].

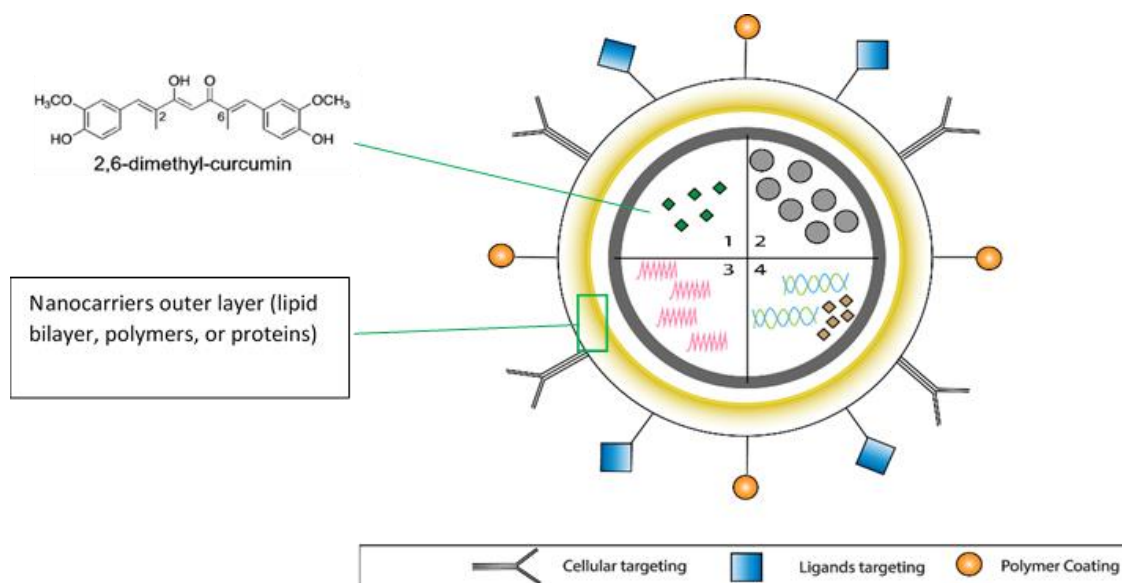


Figure 1.3. Schematic representation of nanocarriers with a modified surface using polymers, ligands, or antibodies for cellular targeting. The nanocarriers core can also be modified to load different APIs, control drug release, and target tumour tissues. (1) Encapsulating the hydrophobic drug in the carrier's core or the polymeric or lipid outer layer. (2) Incorporating magnetic particles within the nanocarrier core. (3) Entrapping one or more polymers to modify the physiochemical properties of the carrier. (4) Capturing DNA/ RNA within the carrier core using cationic polymers.

1.2 Curcumin and its Derivatives as Anticancer Agents

Cancer is the second most life-threatening disease and one of the main public health problems worldwide. In 2017 there were around 1.7 million new cases of cancer and more than 600 thousand deaths in the united states alone[75]. Despite the tangible advances in cancer therapy, the reported incidence of the disease and the mortality have not declined in the past 30 years[76]. Understanding the molecular alterations that contribute to cancer development and progression is a key factor in cancer prevention and treatment. There are several common strategies for targeting specific cancer cells to inhibit tumour development, progression and metastasis without causing severe side effects [77]. In addition to the chemically synthesized anticancer agents, several anticancer compounds with different modes of action have been extracted from plant sources such as *Taxus brevifolia*, *Catharanthus roseus*, *Betula alba*, *Cephalotaxus* species, *Erythroxyllum previllei*, *Curcuma longa*, and many others [78]. Among which, curcumin is the most active component of the

rhizomes of *Curcuma longa* L. (turmeric) [79] and it was extracted for the first time in a pure crystalline form from turmeric plant in 1870 [80]. Curcumin and its derivatives have received immense attention in the past two decades due to their bio-functional properties such as anti-tumour, antioxidant and anti-inflammatory activity [81]. These properties have been attributed to the key elements in the curcumin structure [82]. Therefore, a great deal of scientific work has shed light on the structure activity relationship (SAR) of curcumin in an attempt to improve its physiochemical and biological properties. Due to the importance of cancer as a leading cause of death, and the ongoing quest for more efficient and less toxic anticancer agents, this review has mainly focused on the anticancer activity of curcumin. The applications of curcumin in other diseases are beyond the scope of this review and have been reviewed elsewhere [78, 83]. The main mechanisms of action by which curcumin exhibits its unique anticancer activity include inducing apoptosis, inhibiting proliferation and invasion of tumours by suppressing a variety of cellular signalling pathways [84]. Several studies reported curcumin's antitumor activity on breast cancer, lung cancer, head and neck squamous cell carcinoma, prostate cancer and brain tumours [85], showing its capability to target multiple cancer cell lines. In spite of all the above mentioned advantages, curcumin's applications are limited due to low water solubility which results in poor oral bioavailability and also low chemical stability [81]. Another obstacle is the low cellular uptake of curcumin. Due to its hydrophobicity, curcumin molecule tends to penetrate into the cell membrane and bind to the fatty acyl chains of membrane lipids through hydrogen binding and hydrophobic interactions resulting in low availability of curcumin inside the cytoplasm [86, 87]. To overcome these obstacles and improve the overall anticancer activity of curcumin, several structural modifications have been suggested to enhance selective toxicity toward specific cancer cells[88], increase bioavailability, or enhance stability [78, 89].

1.2.1 Structural activity of curcumin and its derivatives

Chemical structure modification does not only affect the receptor binding and pharmacological activity of a drug molecule but also alters its pharmacokinetics and physiochemical properties [78]. Determining the essential pharmacophores within a drug molecule requires a thorough study of its natural and synthetic analogues[85]. The chemical structure of curcumin is depicted in **Figure 1.4 (A)**. As can be observed it consists of two phenyl rings substituted with hydroxyl and methoxyl groups and connected via a 7 carbon

keto-enol linker (C7). While curcumin is naturally derived, its derivatives are generally produced by a chemical reaction between aryl-aldehydes and acetylacetone. This assembly method can yield multiple chemical analogues such as compounds with alkyl substituents on the middle carbon of the linker (C7 moiety) [90, 91]. SAR study of curcumin derivatives demonstrates that the presence of a coplanar hydrogen donor group and a β -diketone moiety is essential for the antiandrogen activity for the treatment of prostate cancer [91]. In addition, scanning 50 curcumin analogues showed that shortening the linker from 7 carbon atoms (C7) to 5 carbon atoms (C5) improves the antiandrogenic activity[92]. As a result of introducing methyl group at both C2 and C6 positions, a new curcumin derivative has been produced (Figure 1 (B)). This derivative exhibits steric hindrance effect toward metabolizing enzymes such as alcohol dehydrogenase[88] and demonstrated significantly higher activity than curcumin in inhibiting endothelial cell proliferation and invasion both *in vitro* and *in vivo* [88]. Dimethylcurcumin or ASC-J9 (5-hydroxy-1, 7-bis (3, 4-dimethoxyphenyl)-1, 4, 6-heptatrien-3-one) is a newly developed curcumin analogue which enhances androgen receptor degradation and has been recently approved by FDA as anti-prostate cancer agent [93-95]. Moreover, it has also shown a significant antiproliferative effect against estrogen-dependent breast cancer cells [96]. Although methylation has enhanced the targetability and activity of the molecule, it has also increased its hydrophobicity massively compared to curcumin which has limited its administrable dose in cancer therapy [97].

Furthermore, studies on kinetic stability of synthetic curcumin derivatives have pointed out that glycosylation of the pharmacophore aromatic ring improves the compound's water solubility, which enhances its kinetic stability and leads to a better overall therapeutic response[98]. During phase I and phase II metabolism, the main routes of converting curcumin into a higher excretable form are oxidation, reduction, and conjugation (glucuronidation and sulfurylation). The conjugation reactions occur on the hydroxyl group (4-OH) attached to the two phenyl rings of curcumin. Thus, enhancing the curcumin kinetic stability can be achieved by masking the 4-OH group [99]. Another study has revealed a correlation between the hydrophobic property of the two benzyl rings and androgen receptor affinity [100]. The benzyl rings are also crucial for inhibiting tumour growth and adding hydrophobic substituents such as CH₃ groups on them (R1, R2, R3, R4 in figure 4(B)) have been linked to the increased antitumor activity of curcumin derivatives[100, 101]. O-methoxy

substitution was found to be more effective in suppressing nuclear factor kappa-light-chain-enhancer of activated B cells (NF- κ B), but this modification has also affected the lipophilicity of curcumin [102]. A summary of the potential sites of modification on the curcumin molecule is illustrated in **Figure 1.4 (B)**.

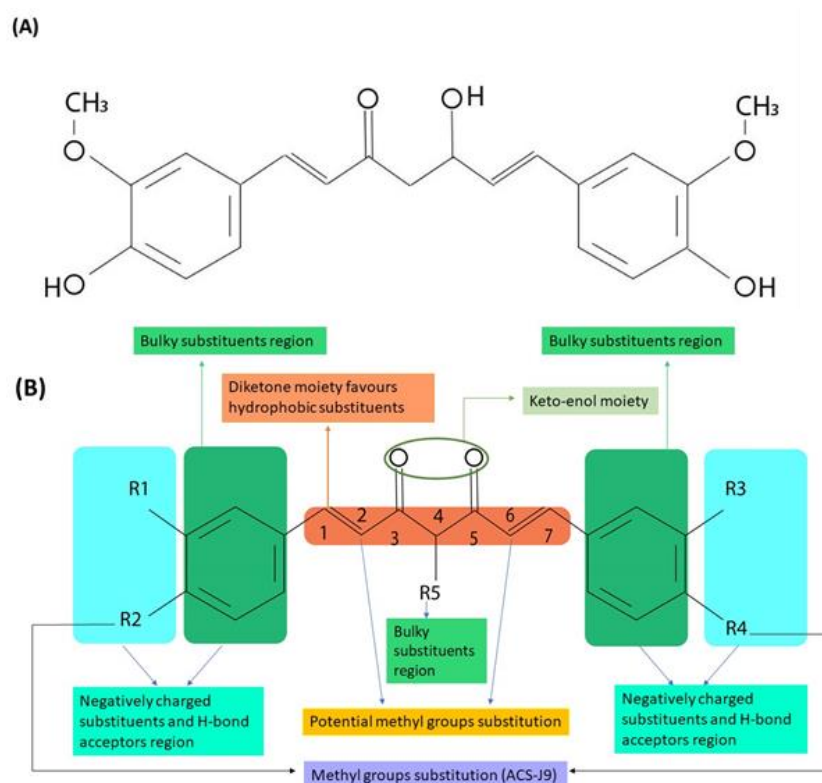


Figure 1.4. (A) Chemical structure of curcumin. (B) The main pharmacophore's structure activity relationship (SAR) of curcumin and potential substitution positions.

1.2.2 Different types of curcumin delivery systems used in cancer therapy

Various delivery systems for curcumin have been formulated using different nanotechnologies in order to improve curcumin properties and targetability. For rational design of the nanoformulations, several factors should be considered in order to enhance the efficacy and improve the cellular targeting of the anticancer agents. These factors include the nanoparticle size and shape, surface properties, and nanoparticle targeting ligands[103] as illustrated in **Figure 1.5**. A summary of the most commonly used curcumin delivery systems is introduced in this section.

1.2.2.1 Polymeric nanoparticles

Various polymers have been utilized to prepare nanoformulations for curcumin drug delivery to improve its biological activity [104]. The biocompatible and biodegradable polymers are preferred in the drug delivery systems due to lower risk of toxicity[105]. Therefore, biodegradable synthetic polymers such as PLGA (poly (D, L-lactic-co-glycolic acid) and natural polymers such as silk fibroin and chitosan have become widely used in drug delivery [49, 106, 107]. PLGA-Curcumin nanoformulation was found to be as effective as curcumin at 15-fold lower concentration in inhibiting mRNAs for inflammatory cytokines (CXCR3 and CXCL10), and increasing anti-inflammatory cytokine interleukin-10 (IL-10) in the brain[108]. *In vivo* study in rats showed that the bioavailability of curcumin-PLGA nanospheres was increased 9-fold in comparison to unprocessed curcumin administrated with alkaloid compound piperine. However, curcumin/ piperine co-administration enhanced curcumin activity by inhibiting hepatic and intestinal deactivation[109]. Another study compared the anticancer activity of curcumin-loaded PLGA nanoparticles (CUR-NPs) and curcumin-loaded PLGA nanoparticles conjugated to anti-P-glycoprotein (P-gp) (CUR-NPs-APgp). The latter formulation showed significantly more specific binding to cervical cancer cells KB-3-1 but lower entrapment efficiency compared to CUR-NPs [110]. Spherical PLGA nanospheres were also developed to encapsulate dimethyl curcumin (ASC-J9) and tested in breast cancer cells. The PLGA nanospheres were capable of releasing ASC-J9 intracellularly leading to growth inhibition of estrogen-dependent MCF-7 cancer cells[96].

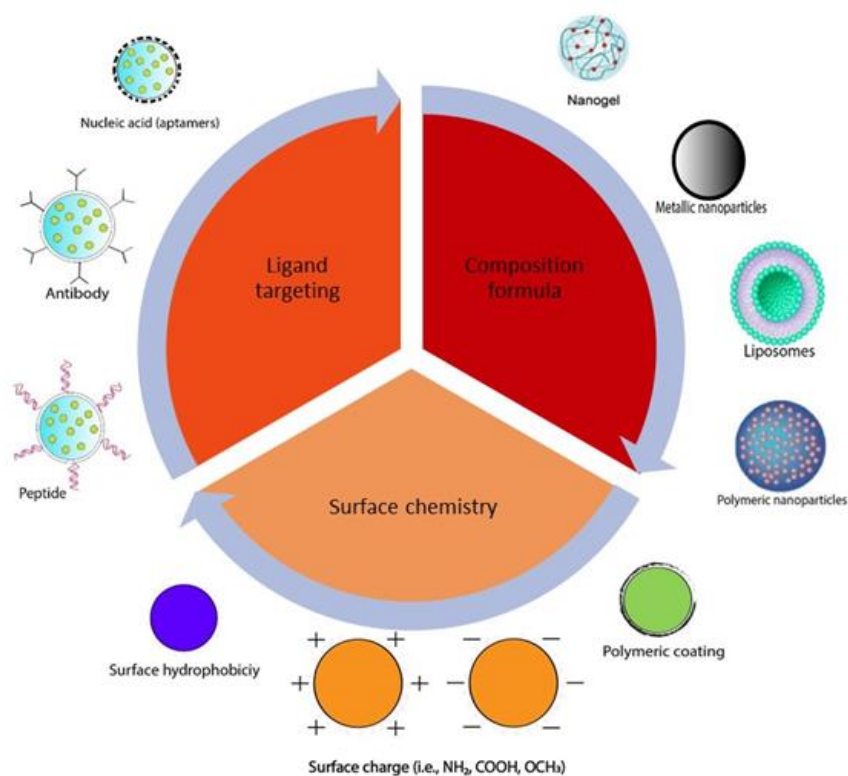


Figure 1.5. Examples of current nanoparticle design strategies for improving targeting.

1.2.2.2 Liposomes

Nanoscale liposomes are emerging as one of the most useful drug delivery systems for anticancer agents. Recent advances in liposome formulations have resulted in improved treatment for drug-resistant tumours and reduced toxicity [111]. A liposome consists of a phospholipid bilayer shell and an aqueous core which makes it an ideal carrier for encapsulating both hydrophobic and hydrophilic compounds. Several liposome preparations have been utilized to encapsulate curcumin (Table 2). Curcumin tends to solubilize in the liposomal lipid bilayer such as egg yolk phosphatidyl choline (EYPC), dihexyl phosphate (DHP) and cholesterol. This preparation was found to stabilize loaded curcumin proportionally to its content[112]. Another work on liposomes tested coating liposomes with lipid-polymer conjugate N-dodecyl chitosan-N-[(2-hydroxy-3-trimethylamine) propyl] (HPTMA) chloride. Positively charged nano-liposomes for curcumin delivery have also been developed by incorporating polyethylene glycol (PEG) and cationic polyethyleneimine (PEI) into the formulation. Despite low encapsulation efficiency (45%), this formulation has demonstrated 20-fold higher cytotoxic activity than unprocessed curcumin in various cell lines, including human HepG2 hepatocellular carcinoma, A549 lung carcinoma, HT29 colorectal carcinoma,

and cervical carcinoma [113]. In liposomal gene delivery, an interesting work conducted by Fujita *et al.* [114], utilized curcumin to control siRNA release. By incorporating curcumin into the liposomal formula, siRNA release showed a bell-shaped pattern due to the dose-dependent increase in liposomal permeability induced by curcumin. Curcumin-loaded liposomes were also used to inhibit the production of IL-6 in macrophages. The liposomes were prepared by mixing curcumin solution with human serum albumin (HSA) solution and subsequently adding this mixture to a lipid mixture containing 1, 2-dipalmitoyl-sn-glycero-3-phosphocholine (DPPC), 1, 2-dipalmitoyl-sn-glycero-3-phospho-L-serine sodium salt (DPPS) and cholesterol. The designed system induced significant IL-6 suppression and reduction in the total number of macrophages [115]

1.2.2.3 Nanogels

Although hydrogels and nanogels have gained considerable attention in the past decade as a promising drug delivery system, only a few studies investigated the curcumin-nanogel delivery in cancer therapy. There are several polymeric hydrogels nanoparticles that have been prepared recently using synthetic or natural polymers. Among the natural polymers, chitosan, chitin and alginate are the most studied for preparation of nanogels in drug delivery [116]. On the other hand, the most commonly used synthetic polymers are polyvinyl alcohol (PVA), polyethylene oxide (PEO), polyethyleneimine (PEI), polyvinyl pyrrolidone (PVP), and poly-N-isopropylacrylamide (PNIPAA) [117]. One of the main advantages of natural hydrogels over synthetic ones is biodegradability and biocompatibility when used in drug delivery [117, 118]. Additionally, nanogels possess unique features including large surface area for drug entrapment and porous structure for drug loading and release [118, 119]. Curcumin loaded chitin nanogel has been used as a transdermal system for treatment of skin cancer [118] (**Table 1.1**) and has shown more specific toxicity towards human skin melanoma (A375) in comparison to human dermal fibroblast (HDF) cells without compromising the antitumor activity of curcumin [118]. In another study, a hybrid nanogel system consisting of alginate, chitosan, and pluronic polymers was prepared via polycationic crosslinking method and tested on HeLa cell line [120]. This delivery system demonstrated very high entrapment efficiency and significant difference in cell proliferation was observed between the cells treated with unprocessed curcumin and the cells treated with curcumin loaded hybrid nanogel [120].

1.2.2.4 Peptide and protein formulations

As discussed earlier, hydrogels and polymeric materials have shown promising results in curcumin drug delivery. However, few limitations have arisen in processing clinical applications including toxicity of un-reacted monomers, post-crosslinking shrinkage or fragility of the polymer gels and rapid discharge of large amount of the loaded drug during the initial burst release in drug carrier [121]. In an attempt to address these limitations, self-assembling peptides systems have been developed. Peptides provide several benefits when introduced to delivery systems such as biocompatibility, desirable hydrophilicity and mild processing conditions [122]. A recent study investigated the physical properties and therapeutic efficacy of curcumin-loaded self-assembling (MAX8) peptide (β -hairpin) hydrogel system. This newly developed system has combined multiple advantages such as enhanced delivery, curcumin stabilization and controlled drug release by changing the MAX8 peptide concentration [123]. In another example, an amphiphilic polypeptide (β casein) was able to self-assemble into micelles. encapsulation of curcumin within the hydrophobic core of the β casein micelles, increased its aqueous solubility by 2500-fold [124]. Human serum albumin (HSA) is one of the most commonly used proteins in nanoparticle preparation due to its excellent biocompatibility [125]. Curcumin-loaded HSA nanoparticles have been produced through homogenization of aqueous HSA solution (to cross-link the HSA molecules) and curcumin dissolved in chloroform. This formulation improved the curcumin solubility by 300-fold but only achieved 7.2% curcumin loading efficiency which was likely due to entrapment of curcumin within albumin hydrophobic cavity through hydrophobic interactions [126]. Recently, silk fibroin (SF) protein has attracted tremendous attention due to its excellent biocompatibility and multiple biomedical applications [127]. Since it was approved by FDA, several studies have investigated its potential applications in drug delivery [128]. Magnetic silk nanoparticles (MSPs) were used to deliver curcumin to MDA-MB-231 breast cancer cells. As illustrated in **Figure 1.6**, these particles were fabricated using the salting out method to convert α -helix silk form to the β -sheet (the insoluble) form which provided a hydrophobic surface for curcumin loading. The nanoformulation managed to achieve small particle size (100-350 nm), cell internalization and provide the possibility for additional targeting using an external magnetic field on the target tissue [49].

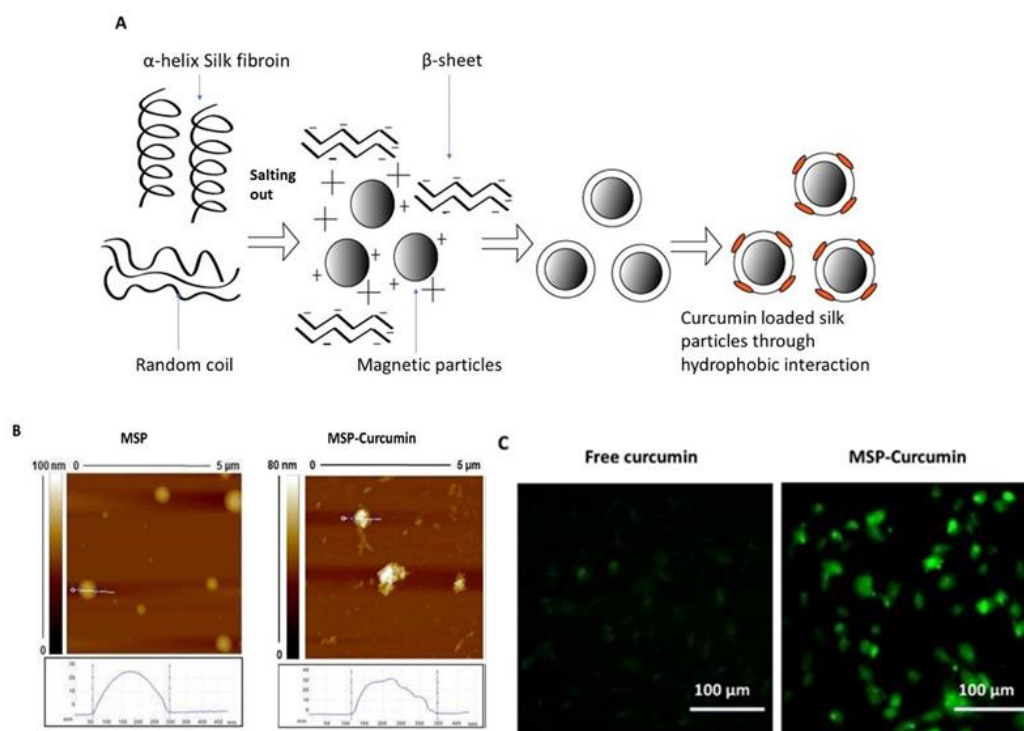


Figure 1.6. (A) Fabrication of magnetic silk particles (MSP) for curcumin delivery. (B) AFM images of MSP before and after curcumin loading. (C) Representative microscopic images of MDA-MB-231 cells incubated with free curcumin and curcumin loaded MSP showing a significant improvement of curcumin cellular uptake. [49].

Table 1.1. Examples of recent curcumin delivery systems

| Nano-formulation | Particle size | Application | Outcome | Reference |
|--|---------------|---|---|-----------|
| Curcumin loaded liposomal PMSA ^a antibodies | 100-150 nm | Human prostate cancer (LNCa, C4-2B) | Enhanced antiproliferative efficacy and targeting | [129] |
| Curcumin loaded Magnetic silk nanoparticles | 100-350 nm | Human breast cancer (MDA-MB-231) cells | Enhanced cellular uptake and growth inhibition | [49] |
| Curcumin/MPEG ^b -PCL ^c Micelles | 27 ± 1.3 nm | Colon carcinomas (C-26) cells | Enhanced cancer growth inhibition | [130] |
| Curcumin nanoemulsion | <200 nm | Human ovarian adenocarcinoma cells (SKV3) | Increased cytotoxicity | [131] |
| Curcumin loaded liposomes coated with N-dodecyl chitosan-HPTMA ^d chloride | 73 nm | Murine fibroblast (NIH3T3) and murine melanoma (B16F10) | Specific toxicity in murine melanoma (but not in fibroblasts) | [132] |
| Curcumin-PLGA ^e nanoparticles | 248 ± 1.6 nm | Erythroleukemia type 562 cells | Improved clinical management of leukaemia | [131] |
| Curcumin loaded lipo-PEG ^f -PEI ^g complexes | 269 nm | Melanoma (B16F10) and colon carcinoma (CT-26) | Increased cytotoxicity | [133] |
| Curcumin-Chitosan nanoparticles | 100-250 nm | Melanomas | Enhanced antitumor effect | [134] |
| ApoE ^h peptide-functionalized curcumin loaded liposomes | 132 nm | RBE4 cell monolayer | Increased accumulation in brain capillary endothelium | [135] |
| Curcumin-Crosslinked polymeric Nanogels | 10-200 nm | Breast and pancreatic cancers | Higher stability and enhanced antitumor effect | [118] |
| Curcumin loaded Chitin nanogels | 70-80 nm | Human skin melanoma (A385) and human dermal fibroblasts (HDF) | Specific toxicity in skin melanoma (lower toxicity in HDF) | [118] |
| Curcumin-loaded lipid-core nanocapsules | 196 ± 1.4 nm | Rats C6 and U251MG glioma cell lines | Decreased tumour size and prolonged survival | [136] |
| Liposome-encapsulated curcumin | Not reported | Head and neck cancer (HNSCC) cell lines (CAL27 and UM-SCC1) | Cancer growth suppression both in vitro and in vivo | [137] |

1.3 Silk Fibroin as a Functional Biomaterial for Drug and Gene

Delivery

Polymeric drug delivery systems have emerged as a new efficient alternative to the conventional formulations to provide a reservoir to the active pharmaceutical ingredients (APIs), improve their physicochemical properties, and overcome some of the major challenges in drug delivery including specific targeting, intracellular transport, and biocompatibility in order to improve the treatment efficiency and life quality of patients [138-141]. An ideal drug delivery system should stabilize the loaded API, allow for modulating its release kinetics and minimize its adverse effects by tissue-specific targeting, especially in the case of highly toxic drugs such as anticancer agents. Silk has been known as a valuable natural material for the fabric industry for centuries, but in the past decades it has attracted immense attention as a promising biopolymer for biomedical and pharmaceutical applications [142-144]. Silk protein possesses a unique combination of properties which is rare among natural polymers. It also enjoys desirable characteristics such as mild aqueous possessing conditions, high biocompatibility and biodegradability, and the ability to enhance the stability of the loaded APIs (e.g., proteins, pDNA, and small molecule drugs) [141, 142, 145, 146]. Moreover, silk fibroin (SF) solution can be processed by various methods to produce different types of delivery systems including hydrogels, films, scaffolds, microspheres, and nanoparticles [147]. SF exists in three different structural forms: Silk I, Silk II and Silk III. Silk I exists in water-soluble form and consists of a high percentage of α -helix domains in addition to random coils [148]. Contrarily, Silk II has mainly β -sheet structure and is more stable and water-insoluble, while Silk III prevails at the water/air interface [149]. The transformation from Silk I to Silk II can be tuned by different methods including organic solvent treatment, physical shear, electromagnetic fields, or chemical processing [150, 151]. These properties can be utilized in the pharmaceutical industry for producing micro- and nano particles and nano-fibrils or for coating other pharmaceutical preparations such as liposomes [152, 153]. Moreover, the availability of carboxyl and amino groups in the SF allows for bio-functionalization with various biomolecules or ligands which could be used for targeted drug delivery [128]. The two main strategies for functionalizing silk protein are chemical conjugation and genetic modification of silk by changing the amino acid composition or adding a fragment to obtain a specific function [154]. A large proportion of drug formulations including the vast majority of

anticancer drug formulations are prepared for parenteral administration, resulting in direct contact with the blood components. Thus, the drug carriers used in such formulations should not induce any haematological toxicity or immune responses [3], which necessitates the use of biocompatible polymers in the formulation. Furthermore, designing delivery systems for biological drugs such as vaccines and antibodies requires maintaining their physical stability as well as their biological activity, which is more crucial for the controlled release systems [155]. This is mainly due to the higher sensitivity of the biological compounds, especially the protein-based therapeutics, to many of the processing conditions throughout the delivery system preparation compared to small molecule drugs, which limits the processing strategies [156, 157]. Hence, loading the biological therapeutics into a compatible polymer can increase their stability and consequently their half-life [158]. Moreover, incorporating the APIs into a natural biocompatible protein such as SF has multiple advantages e.g., preserving the API [159], improving the mechanical properties of the formulation [143], modifying drug release kinetics [160-163], enhancing cell adhesion [153], and compatibility with blood components [161]. The versatility of SF protein processing and formulating methods allows the preparation of a wide range of drug carriers with different sizes and morphologies using unmodified or engineered SF (**Figure 1.7**). Unmodified SF carriers have been used to deliver various anticancer drugs such as doxorubicin [164], paclitaxel [165], curcumin [146, 166], and cisplatin [167].

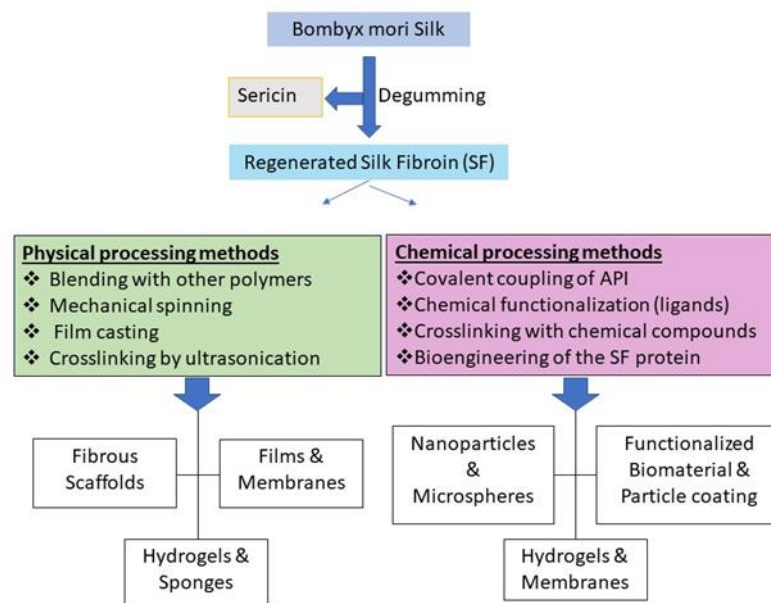


Figure 1.7. A diverse set of physical assemblies and chemical methods for preparing a variety of silk fibroin (SF) formats for pharmaceutical and biomedical applications.

1.3.1 Physiochemical Properties of Silk Fibroin

SF possesses a unique combination of mechanical and biological properties and exhibits special features of both synthetic and natural polymers [168, 169]. Typically, silk represents softness in the clothing industry, but it is considered one of the most robust natural biomaterials due to its tensile strength and modulus [170]. This feature is important for the polymers involved in bone tissue regeneration as mechanical performance of the polymer is of utmost importance for such applications [171]. SF demonstrates excellent stability under high thermal stress (higher than 250 °C) [172].

1.3.1.1 Biocompatibility

SF is a biocompatible material that has been officially recognized by the Food and Drug Administration (FDA) for the development of a plethora of nanotechnological tools [173]. The biocompatibility of silk has been studied extensively over the past two decades. The majority of the studies have reported excellent biocompatibility and relatively lower immunogenic response in comparison to other common degradable biological polymers in the pharmaceutical industry such as polylactide (PLA), poly(lactic-co-glycolic acid) (PLGA) and collagen [158, 174, 175]. Cytocompatibility studies on SF formats revealed high compatibility with different cell lines including hepatocytes, osteoblasts, fibroblasts, endothelial cells and mesenchymal stem cells (MSCs) [176, 177]. During SF processing, organic solvents such as methanol and hexafluoroisopropanol (HFIP) are used to crosslink SF via inducing structural transformation (α helix to β sheet), which has been found responsible for the inflammatory potential of SF formulations [178]. However, mild processing conditions that avoid the use of organic solvents have been used to avoid these inflammatory responses [49]. An evaluation of the levels of lymphocyte activating factor IL-1 β and inflammatory cyclooxygenase-2 (COX-2) gene expression in relation to SF stimulation did not show any significant differences from those of collagen or PLA, indicating very low immunogenicity [179]. Another study has evaluated the biocompatibility of scaffolds consisting of a combination of calcium polyphosphate (CPP) and SF used for the reconstruction of cartilage and bone defects [180]. The results showed a tangible increase in tissue biocompatibility and osteogenicity of SF-CPP scaffolds in comparison to CPP scaffolds [180].

1.3.1.2 Mechanical Properties

Mechanical stiffness is a key property of SF-based formulations for pharmaceutical and biomedical applications. The SF material used in tissue engineering, for example, must match the stiffness of the targeted tissue. The stiffness can also affect the stability and degradability of the SF polymer [181]. Many polymers that have been used in drug delivery devices, such as PLGA and collagen, lack sufficient mechanical strength. A common strategy to enhance the mechanical strength of the biopolymers such as collagen is crosslinking. However, the crosslinking reaction could result in undesirable consequences such as cellular toxicity and immunogenicity [182]. SF possesses robust β -sheet structure which provides excellent mechanical properties without the need for any harsh crosslinking procedures. Based on the β -sheet content, SF can transform into different formats including liquid, hydrogels, or scaffolds [142]. Measurements of mechanical strength are usually obtained from Young's modulus using nanoindentation techniques [183]. SF exhibits high tensile strength and resistance to compressive force making it a very suitable material for drug delivery and tissue engineering [184]. Moreover, the removal of sericin during the degumming process results in a 50% increase in tensile strength [185] which makes SF more stable during physical pharmaceutical processing.

1.3.1.3 Stability

The stability of the polymeric materials is one of the most important factors in the production of pharmaceutical formulations. Although biopolymers are preferred to their synthetic counterparts for clinical applications due to their biocompatibility and biodegradability, they must also meet certain stability standards to be considered for utilisation in the pharmaceutical industry. One of the common stability problems of pure SF solution is aggregation or gelation during long-term storage. SF is available in soluble form (with high content of α -helix and random coil) and insoluble form (with high content of β -sheet). Depending on the pharmaceutical preparation, either form should be used and maintained. Storing the soluble SF in highly humid conditions results in a transformation from α -helix and random coil to β -sheet which could lead to gelation and a decrease in the stability of the SF solution [186, 187]. SF shows excellent stability under thermal stress compared to other proteins. The best indicator for protein thermal stability is the glass transition temperature (T_g) which in the case of SF is affected by its β -sheet content. The T_g of SF films is

approximately 175 °C and the protein remains stable up to 250 °C which is desirable for formulation processing. On the other hand, T_g of the frozen SF solution can go to -34 °C [188] which is also advantageous in low temperature pharmaceutical processing. Furthermore, the degree of crystallinity and porosity of SF films are also affected by T_g [189]. The increase in β -sheet content of SF causes a transformation from Silk I to Silk II, reflected by a significant change in T_g which changes the degree of crystallinity. Stability of the SF in physiological fluids is another important issue for its biomedical applications. SF could be protected from enzymatic degradation within the body by coating with polymers such as polyethylene glycol (PEG) in order to improve the delivery of the associated drugs to the site of action.

1.3.1.4 Degradability

Degradability is an important property of biological materials. Although biodegradability is a main advantage of SF in clinical applications, this property makes pure SF particles liable to proteolytic enzymes. The degradation rate of SF can be regulated by modifying the molecular weight, the degree of crystallinity, morphological features, or crosslinking [190]. However, the degree of crystallinity and crosslinking are not the only approaches to stabilization of SF against degradation. For example, an in vitro enzymatic degradation experiment revealed that SF sheets slightly transformed from Silk II to Silk I crystalline structure when exposed to collagenase IA. However, when protease XIV was used, the majority of the SF sheets transformed to Silk I leading to a higher degree of crystallinity. Although the degradation time was 15 days in both cases, the degradation rate was significantly lower for protease XIV compared to collagenase IA [191]. Another study reported a predictable loss of mechanical integrity due to SF degradation [192]. Incubation with protease led to an exponential decrease in the SF filament diameter to 66% of the initial diameter after 10 weeks. Gel electrophoresis indicated a decreasing amount of the silk 25 kDa light chain and a shift in the molecular weight of the heavy chain with increasing incubation time with protease XIV [192].

1.3.2 SF-Based Drug Delivery Systems

Delivery of APIs in sustained and controlled release forms is important for many clinical applications. Selection of the particle size, composition, and other features depends on the type of the delivery system and the route of administration. Moreover, using biocompatible and mechanically durable polymers with mild fabrication and processing conditions in such

delivery systems is advantageous for preserving the bioactivity of the loaded APIs. As discussed earlier, SF meets all these requirements which makes it a promising candidate for drug delivery [142, 193]. SF-based drug delivery systems can be fabricated by different methods, each resulting in a delivery system with unique properties such as modified release kinetics, stability, and other features which could be of benefit in various applications. Various types of SF-based drug delivery systems have been designed including hydrogels, films, micro- and nanoparticles, nanofibers, lyophilized sponges as well as SF-coated polymeric particles. In the following section, some of the most widely studied SF-based drug delivery systems are reviewed.

1.3.2.1 Hydrogels

SF aqueous solution was used to generate hydrogels by different methods. The transition from solution to gel can be triggered by physicochemical or chemical processes using natural polymers or synthetic reagents [194]. The physicochemical processes include shearing (spinning), water exclusion via evaporation or osmotic stress, electric field, and heating [195]. The gel form is stabilized because of thermodynamically stable β -sheets which result in a stable gel form in physiological conditions unless extensively degraded by enzymes or oxidative reactions [195]. One recent study used curcumin-loaded gel scaffolds prepared by electrogelation for wound healing [196]. The prepared gel formulation not only improved protein adsorption and sustained the release of curcumin, but also enhanced bacterial growth inhibition by 6-fold against *S. aureus* [196]. Since protein adsorption on substrates is a key factor for cell growth and proliferation, SF gel scaffolds can serve in wound healing by promoting cell proliferation. Sundarakrishnan *et al.* [197], adapted a chemical approach using horseradish peroxidase (HRP) and hydrogen peroxide to prepare SF hydrogels that were subsequently crosslinked with di-tyrosinase, and loaded with phenol red in order to develop a self-reporting pH system for *in vitro* environment [197]. Addition of phenol red during di-tyrosine crosslinking resulted in stable entrapment of phenol red within SF hydrogel network due to covalent interactions between phenol red and tyrosine and also prevented leaking [197].

1.3.2.2 Silk Films

Film preparation from SF has attracted more attention recently due to its huge potential as a biomaterial in pharmaceutical formulations and tissue engineering [198]. SF films can be

simply prepared by casting an aqueous SF solution [199]. However, there are other reported SF film preparation techniques such as vertical deposition [200], spin coating [201], centrifugal casting [198], and spin assisted layer-by-layer assembly [202]. Terada et al. [201] investigated the behavior of spin-coated SF films treated with different ethanol concentrations. Alcohol concentrations of 80% or less resulted in a jelly-like hydrogel layer while treatment with more than 90% alcohol provided a rigid film surface. This change in morphology affected the attachment of the fibroblast cells to the SF films. Fibroblasts aggregated on the rigid surface rather than attaching individually to the hydrogel surface [201]. Another study found that blending SF with other polymers such as sodium alginate (SA) before casting the film results in a miscible and transparent film and also induces a structural change in SF [203]. Manipulating the SF/SA blending ratio shifted the SF conformation to the higher β -sheet content. Moreover, mixing SA with SF enhanced water permeability, swelling capacity and tensile strength of SF films [203]. Hence, SF/SA blend can provide unique tunable characteristics that can be beneficial in pharmaceutical applications.

1.3.2.3 Silk Particles

As discussed earlier, there are an increasing number of SF-based systems that have been used for encapsulating APIs and achieving modulated drug delivery among which nanoparticle delivery systems have been studied the most, especially for anticancer drugs. One example of such systems is the lysosomotropic SF nanoparticles designed by Seib et al. [164] for pH-dependent release of the anticancer drug doxorubicin in order to overcome drug resistance. SF nanoparticles are largely employed for controlled release of the loaded drug at the site of action. SF nanoparticles can be fabricated by various methods, for example polyvinyl alcohol (PVA) blends, which are used for fabricating SF spheres with controllable sizes and shapes [204] (**Table 1.2**). The determinant factors for drug distribution and encapsulation efficiency in such systems are their charge and lipophilicity. Modifying these factors results in different drug release profiles [205]. Furthermore, addition of PVA results in a tangible improvement in the morphology of the SF-particles [206]. One of the popular methods for fabrication SF particles is the salting-out method. For example, Lammel et al. [207] produced SF particles with controllable sizes ranging from 500 nm to 2 μ m using potassium phosphate as the salting out agent. The β -sheet structure and zeta potential of the SF particles were affected by the pH of the potassium phosphate solution [199, 207]. In another study conducted by Tian et al.

[208] SF nanoparticles were prepared using the salting out method, loaded with a combination of doxorubicin and Fe₃O₄ magnetic nanoparticles and driven to the target tissue using an external magnetic field to achieve tissue-specific targeted delivery [208]. It was also found that the entrapment efficiency of doxorubicin can be tuned by changing the concentration of Fe₃O₄ in the formulation [208]. However, the size of SF particles produced by potassium phosphate was over 500 nm, which is not ideal for drug delivery. Recently, Song *et al.* [49] produced magnetic SF nanoparticles (MSNPs) with size range of 90–350 nm by using sodium phosphate. The size and morphology of the MSNPs were governed by the SF concentration, the ionic strength and pH of the salting-out agent [49]. Compared to potassium phosphate, sodium phosphate produced smaller particles and the size did not increase significantly with increasing SF concentration and ionic strength, providing a promising method to produce smaller particles with high concentration for drug delivery. The size of the particles can be further reduced by increasing the pH of the salting-out agent. Although salting-out and PVA methods are preferred over other methods due to their simplicity and low toxicity, purifying the SF nanoparticles from excess polymers or salting-out agent is required. Therefore, Mitropoulos *et al.* [209] managed to prepare SF particles with spherical shape using a co-flow capillary device with PVA as the continuous phase and silk solution as the discrete phase. This device allows for generation of SF spheres (2 μm in size) without the requirement for any further purification steps. Moreover, the diameter of the spheres can be simply adjusted by changing the concentration of the polymers, the flow rate, and the molecular weight of the selected polymer [209]. However, the size of the particles produced is not within the desired size range for drug delivery. A more recent study on the microfluidics has used a microfluidic setup (nano-assembler) to produce smaller sizes of SF particles (150–300 nm) by a desolvation method [210] (**Table 1.2**). It was found that the characteristics of the SF nanoparticles are controlled by two main factors: Flow rate and flow rate ratio [210]. The use of microfluidic instrument enabled rapid, reproducible and controlled production of SF nanoparticles with desirable sizes for drug delivery. However, solvent residues within the particles and the cost of the equipment should also be taken into account. The properties of the SF particles can also be manipulated by blending with other polymers. For example, Song *et al.* [146] have recently produced SF nanoparticles blended with different amounts of polyethyleneimine (PEI). The size of the SF nanoparticles was found to increase with increasing SF percentage, while the zeta potential of the particles decreased with increasing

SF amount. This allows to fine tune the drug delivery through controlling the size and zeta potential of the particles.

Table 1.2. Preparation techniques of SF micro- and nanoparticles

| Preparation Technique | Advantages | Disadvantages | Particle Size |
|--|---|---|--------------------------------------|
| Self-assembly | Simple and safe procedure Does not require toxic reagents | Sensitive to temperature and vigorous mixing | 100–200 nm [211] |
| Salting out | Low cost method The active ingredient can be loaded during the particle formation | Salting out agent residue Relatively high particle size polydispersity | 100–350 nm [49] 500 nm–2 μm [207] |
| Emulsification | Controllable particle size Low cost method | Organic solvent or surfactant residues | 170 nm [212] |
| Desolvation | Simple and quick method Small particle size Reproduceable technique | Particle aggregation Organic solvent residue | 35–170 nm [213] |
| Electrospraying | High purity particles Very good monodispersity | Requires additional step to insolubilize SF | 59–80 nm [214] 600–1800 nm [205] |
| Microfluidic methods | Rapid procedure Mild operation conditions Controllable particle yield and particle size | Relatively expensive Residual salting agent or organic solvents | 150–300 nm [210] |
| Capillary microdot | Simple procedure | Organic solvents residue | 25–140 nm [215] |
| Freeze drying | Porous particles | Large particle size | 490–940 μm [128] |
| Supercritical fluids | High drug loading | Expensive technique Not easy to operate Requires additional step to insolubilize SF | 50–100 nm [216] |
| PVA Blending method | Time and energy efficient No use of organic solvent | PVA residue | 5–10 μm [204] 300–400 nm [204] |
| Nano-imprinting and inject printing | Tunable dimensions of different nanostructures | Complicated method Not easy to scale up Not easy to prepare particles | 180 nm–50 μm [217] |

1.3.3 Applications of Silk Fibroin for Drug and Gene Delivery

Silk has been used as a carrier for delivery of a wide range of therapeutic agents including small molecule drugs [140], biological drugs [218], and genes [219]. For each class of therapeutic agents, different formulations have been designed using various silk processing technologies [220]. One of the main criteria of the SF-based delivery systems is to stabilize the loaded API and manipulate its circulation time to achieve the required therapeutic effect. In addition, the designed formulations are usually optimized to obtain a particular application in drug delivery including stabilising the loaded drug, controlling drug release, and improving cell adhesion [153]. In the following section, an insight into SF applications in drug and gene delivery will be provided a summary of which is presented in **Tables 1.3**.

1.3.3.1 Drug and Gene Stabilization by SF

One of the main goals of incorporating active ingredients such as small molecules or peptides into SF-based carriers is to stabilize them by different mechanisms including adsorption, covalent interaction, and/or entrapment [221]. Without a stable interaction between the drug and the SF-based carrier to maintain the drug activity, sustained drug release cannot be achieved. Aside from a few exceptions such as growth factors, the majority of the stabilization approaches rely on entrapping the drug within the SF-matrix or SF-particles in an equally distributed manner [158]. SF-based biomaterials are generally stable to changes in temperature [159], humidity [222], and pH [223]. Therefore, they have been widely studied for enhancing the stability of other materials, for example, encapsulation of antibiotics such as erythromycin, which has very low stability in water. However, porous SF sponges managed to sustain its release and maintain its antimicrobial activity against *Staphylococcus Aureus* for up to 31 days at 37 °C [140]. SF films have also been used for stabilization of biological compounds. For example, enhanced stability of horseradish peroxidase (HRP) when loaded on SF films or mixed with SF solutions has been reported. The enzymatic activity of SF-loaded HRP was increased by 30–40%, while its half-life showed a tremendous increase from 2 h to 25 days at ambient conditions in comparison to free HRP [224]. A greater improvement in enzymatic activity (80%) was observed in glucose oxidase (GOx) when loaded on SF films [225]. Moreover, SF-loaded GOx demonstrated enhanced thermal and pH stability [226]. Topical application of SF lyogels (gel system in which the pores are filled with both organic and non-organic solvents) containing hydrocortisone in a mouse model of atopic eczema

resulted in decreased expression of IgE and enhanced the efficacy of hydrocortisone compared to the commercially available hydrocortisone cream [227]. Moreover, SF lyogels have also been used for stabilizing monoclonal antibodies. The lyogels achieved sustained release of IgG1 over 160 days and the release rate was found to be inversely proportional to the SF concentration [155]. In addition to drug stabilization, SF has also been investigated for DNA preservation in order to protect the DNA from the potential destabilizing conditions such as temperature and UV radiation. In a recent study porous cellulose paper was coated with SF and used to preserve the DNA extracted from human dermal fibroblast cells [159]. The results showed that the DNA integrity was maintained for 40 days following 10 h of UV radiation at relatively high temperature (37–40 °C) [159].

1.3.3.2 Controlled Drug Release

Controlled release drug delivery systems are aimed at releasing the encapsulated API in specified amounts over a specified period of time. One application of such systems is sustained drug release to maintain the therapeutic concentrations of the drug in the blood or site of action for a longer duration which is of great importance for the treatment of chronic diseases. Moreover, sustained drug release reduces the administration frequency and the adverse drug reactions which results in increased patient compliance [158]. Most of the currently available controlled release formulations in the market are composed of synthetic polymers such as PEG and PLGA because they provide desirable pharmacokinetic and pharmacodynamic properties [228]. Although PLGA is approved by FDA as a safe ingredient in pharmaceutical products, the processing requirements might restrict its utilization in certain controlled release formulations. Therefore, more recently, natural polymers such as SF which offer tunable sustained release kinetics and stabilization of the loaded APIs have gained more attention for use in controlled drug release systems.

One of the unique properties of SF is its ability to undergo diverse structural transformations at the molecular level. The most investigated structural transformation in SF is the change in the ratio of α -helix to β -sheet content. For example, the permeability and release kinetics of the SF films are affected by the percentage of β -sheet structure [144]. The mechanism of controlled release from SF films was studied previously by Hines and Kaplan using different models [229]. The release kinetics of FITC-dextran from methanol-treated and untreated SF films was evaluated as a function of molecular weight of FITC-dextran. The methanol-treated

films maintained higher percentage of the loaded FITC-dextran compared to the untreated films which was directly proportional to the molecular weight of FITC-Dextran [229]. In a more recent study, the release profile of the anticancer drug epirubicin from five Heparin-SF films (HEP-SF) treated with methanol (MeOH) or glycerol was investigated and it was found that using different ratios of glycerol in the HEP-SF nanofilm formulation affects the β -sheet content of the nanofilm leading to a modification in the release profile of epirubicin from the nanofilm (**Figure 1.8**). This mechanism-causal relationship between SF conformation and release profile also influenced the degree of degradation [144].

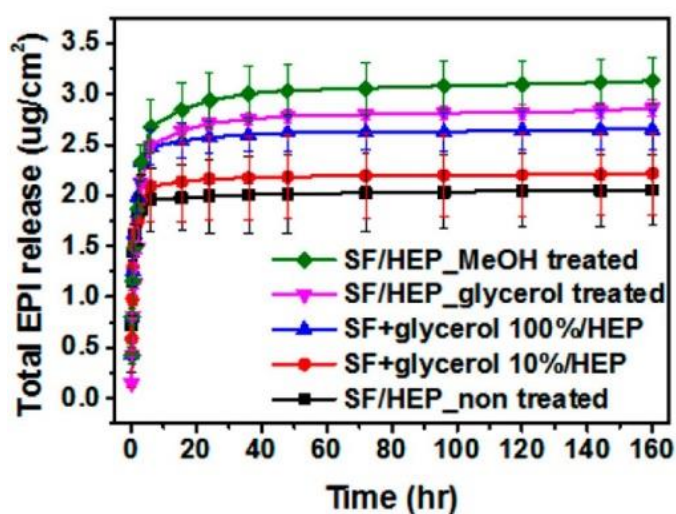


Figure 1.8. Total epirubicin (EPI) release profile from SF nanofilm depending on the ratio of the added glycerol and the solvent treatment. Reprinted from Reference [144].

In a novel study conducted by Yavuz et al. [163] SF was formulated into insertable discs that can encapsulate either IgG antibody or human immunodeficiency virus (HIV) inhibitor 5P12-RANTES. Three different formulations were prepared by SF layering, water vapor annealing, and methanol treatment. These formulations managed to stabilize the protein cargo and to modify its release profile. High concentrations of IgG were released in a relatively short time from the formulation treated with methanol due to the highly porous structure in comparison to the other two formulations that demonstrated a slower and more controlled release. In the case of 5P12-RANTES, the water vapor annealing showed a sustained release for 31 days and this released protein could inhibit HIV infection in both blood and human colorectal tissue [163].

Controlled release from SF nanoparticles and microspheres has been studied extensively in the past decade. In an attempt to control SF particle features, a recent study conducted by Song et al. [49] demonstrated pH-controlled release of curcumin from SF nanoparticles for up to 20 days with lower pH promoting the release. Moreover, the SF nanoparticles had higher cellular uptake and induced significantly higher growth inhibitory effect in MDA-MB-231 cells compared to curcumin solution. Another study developed SF microspheres (2 μm) using DOPC (1,2-dioleoyl-*sn*-glycero-3-phosphocholine) lipid vesicles as a templates [230]. The physically cross-linked β -sheet structure of SF and the residual DOPC in the microspheres played key roles in controlling the release of loaded enzyme (HRP) [230].

Table 1.3. SF-based drug delivery systems

| Type of Drug Delivery System | Associated API | Results | References |
|------------------------------|-----------------------------------|---|------------|
| SF sponges | Erythromycin | Sustained drug release and prolonged antimicrobial activity against Staphylococcus Aureus | [140] |
| SF films | Horseradish peroxidase (HRP) | Enhanced stability | [172] |
| | Glucose oxidase (GOx) | Increased enzymatic activity | [225] |
| | FITC-dextran | Controlled drug release | [229] |
| | Epirubicin | Controlled drug release | [144] |
| SF hydrogels | Hydrocortisone | Enhanced efficacy | [218] |
| | IgG | Enhanced stability and sustained release | |
| Insertable SF discs | IgG and HIV inhibitor 5P12-RANTES | Enhanced stability and modified release profile | [163] |
| SF nanoparticles | Curcumin | Modified release profile and enhanced cellular uptake | [49] |
| SF microspheres | Horseradish peroxidase (HRP) | Modified the release profile | [230] |
| SF-coated PCL microspheres | Vancomycin | Modified the release profile | [231] |
| SF-coated liposomes | Ibuprofen | Enhanced adhesion to human corneal epithelial cells, tunable drug release | [153] |
| | Emodin | Selective targeting of keloid cells | [232] |

1.3.4 Modification of SF for Enhanced Delivery

1.3.4.1 SF Bioconjugates

There are many protein-based drugs that have shown a very short half-life in the body. In order to enhance their *in vivo* stability, an approach has been designed to utilize SF by forming bioconjugates. A covalent bond between the protein or enzyme and SF can be formed by the cross-linking reagents [142]. SF consists of 18 different amino acids among which 10% are polar amino acids such as serine and lysine with hydroxyl and amino groups in their side chains. These functional groups in SF can be covalently conjugated to polar groups in other proteins such as insulin using bifunctional reagent glutaraldehyde [233]. SF-insulin (SF-Ins) bioconjugate not only demonstrated higher *in vitro* stability than bovine serum albumin-insulin (BSA-Ins) conjugate, but also prolonged the pharmacological activity 3.5 times in comparison to native insulin [233]. Covalent conjugation of growth factor BMP-2 to SF using carbodiimide chemistry preserved BMP-2 activity and also reduced its degradation rate due to reduction in its unfolding rate as well as protecting it from proteases [234]. Immobilization of enzymes on silk particles has also been studied recently to enhance the catalytic efficiency of enzymes by improving enzymatic stability. SF has several active amino groups that have the potential for covalent binding to several enzymes to immobilize them (**Figure 1.9**) such as catalase immobilization on SF particles via tyrosinase crosslinking [235]. SF films have been also used to immobilize antibodies such as mouse IgG simply through the conformational transition to fabricate biocompatible biosensors [236]. The immobilization was achieved by slowly drying concentrated SF solution to reach the semisolid state and then blending it with antibody solution before complete drying. It was found that more antibody was immobilized on the surface of SF film by controlling the conformational changes during the drying process in comparison to covalent methods [236]. These results indicate that SF can be functionalized with antibodies with or without crosslinking agents, offering a wide range of biomedical applications.

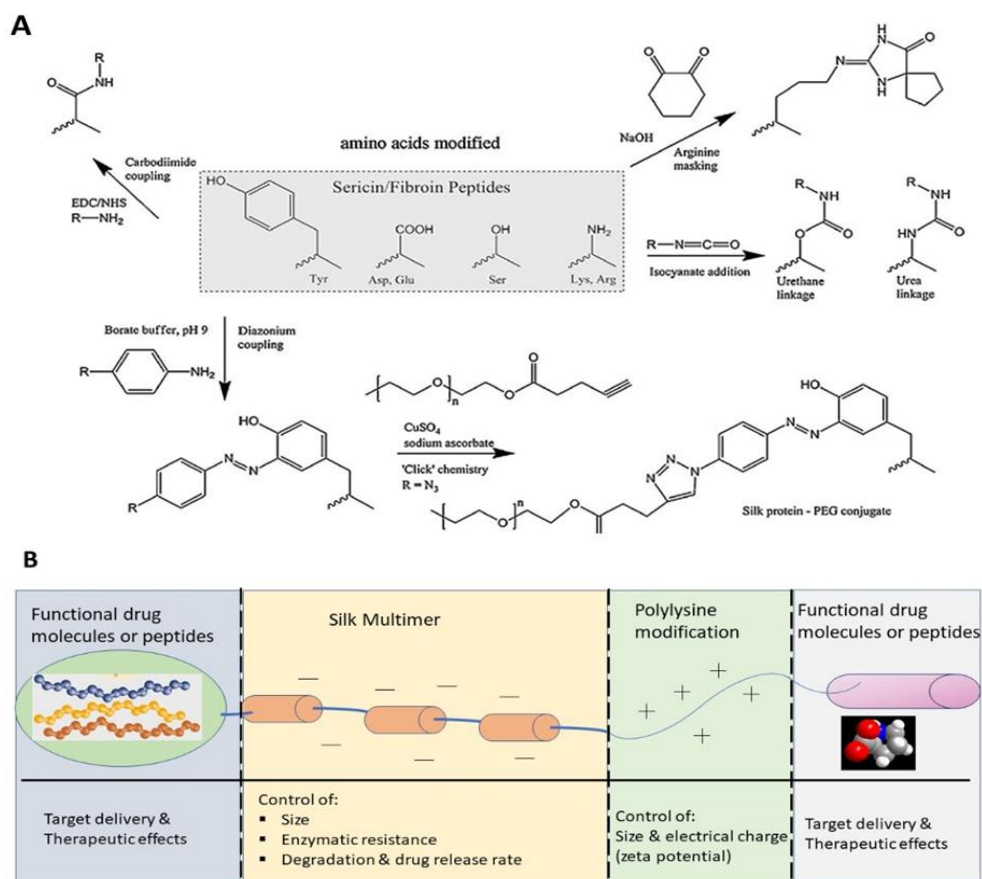


Figure 1.9. (A) Possible routes toward chemical modification of amino acids of silk proteins. Reprinted from [185]. **(B)** The new properties obtained by SF when functionalised or modified in different positions.

1.3.4.2 Functionalisation of SF with Ligands

One of the fundamental advantages of nanoparticles is the greater surface area to the volume ratio compared to larger particles. This property is essential for encapsulating the APIs such as anticancer agents and delivering them to the site of action. Moreover, the loaded APIs must be delivered at a proper concentration to cause the required effect on the target cells and minimise the damage to other cells [237]. However, recent studies have found that engineered particles with the optimum size and shape are limited to less than 1% tumor tissue accumulation [44]. Therefore, decorating polymeric nanocarriers with a targeting molecule has emerged as an effective approach to increase the specificity of the nanoparticles for the targeted cell lines [238]. As mentioned earlier SF has several active amino groups (**Figure 1.9**) which can be used for binding to other macromolecules [239]. For example, Arg-Gly-Asp (RGD) sequence that acts as a ligand for cell surface integrin receptors can be linked to SF

particles to enhance their attachment to the certain cancer cells that overexpress integrins [240]. In a similar fashion, due to the overexpression of folate receptors (FR) in a wide range of tumor cells, modifying the surface of the silk nanoparticles with folate could be used as a tumor-targeting strategy [22]. Folate-conjugated SF particles (SF-FA) were used to enhance targeted delivery of doxorubicin (DOX) to human breast adenocarcinoma cell line (MDA-MB-231) [240]. Folate decoration on silk particle not only increased the retention of the nanoparticles at the tumor site but also promoted cellular uptake of the particles [241]. DOX incorporated in SF-FA nanoparticles demonstrated 3-fold higher cytotoxic activity in comparison to free DOX *in vitro*. Moreover, conjugation of folate to SF nanoparticles changed their cellular uptake mechanism from passive diffusion (free DOX) to endocytosis [239]. Another example of specific targeting using functionalised SF is modification of SF with human epidermal growth factor receptor 2 (Her2) which is overexpressed in 30% of breast carcinomas for targeted drug delivery to breast cancer cells [242]. An alternative functionalisation approach involves using tumor-specific ligands such as nucleic acid sequences like CpG-siRNA [243].

1.4 Microfluidics for preparation of drug and gene delivery systems

In the past decade, enormous advancement in the field of nanotechnology was achieved to produce nanoformulations for drug and gene delivery [244-246]. Employing this nanotechnological advancement in nanomedicine opened doors for improving some of the most challenging therapies such as cancer treatments. Designing nanoformulations with controlled size and features offers many advantages including enhanced drug encapsulation, controlled release of the payloads, improved targetability and enhanced cellular uptake [247, 248]. In addition, encapsulating the active pharmaceutical ingredients (APIs) such as anticancer drugs within nanocarriers can enhance *in vivo* stability, and increase their blood circulation time [249]. In spite of all these advantages, only few nanoformulations have made to clinical trials such as Doxil[®], Caelyx[®], Myocet[®] and Abraxane[®] due to technical challenges in formulating many pharmaceutical materials [250]. Fabricating pharmaceutical nanomaterials can be achieved using top-down or bottom-up approaches. In general, top-down approach is not suitable for processing many (APIs) due to high shear forces involved in the mechanical milling [251-253]. In the bottom-up approach, the formation of nanostructures is performed by converting the molecular matter dissolved in liquid to particulate forms. Based on the nature and composition of the fabricated drug delivery systems (DDSs), the nanostructures are formed by self-assembly, emulsification or precipitation [254-260]. One of the main considerations in formulating different types of polymers or APIs, is to maintain the dimensions of the designed particles within a range of 100-300 nm which is desirable for pharmaceutical applications [261]. A frequently used technique to prepare DDSs with controlled size is mixing amphiphile (e.g., liposomes or micelles) solutions with antisolvent or polyelectrolyte solutions (e.g., cationic polymers or nucleic acids) [262, 263]. DDSs will precipitate or self-assemble as a result of the hydrophobic or electrostatic interactions. Despite the great potential that nano-sized DDSs possess *in vitro*, they demonstrated slow translation to clinical applications. This limitation is due to challenges such as production of large quantities and reproducibility of prepared nanostructures of the DDSs [264]. Many studies have shed more light on the mixing kinetics in order to control the properties of the fabricated DDSs such as size, polydispersity and the API encapsulation efficiency [265-268]. Among several mixing techniques, microfluidic systems have received the most attention due to their ability to control mixing, low running cost and amenability to

modifications [269]. In comparison to bulk production methods, microfluidic synthesis/formulation of single or multicomponent nanoparticles (NPs) has shown higher controllability and reproducibility [34, 36, 270]. The newly developed microfluidic devices provided a platform for preparing different formulations of DDSs including multiple emulsions [271, 272], protein-based nanoparticles [210, 273], liposomes [274, 275] and polymeric nanoparticles [276]. There are several reported microfluidic devices that have implemented the principles of rapid and controlled mixing for preparing a myriad of DDSs. In addition, the microfluidic platform has helped overcoming some obstacles in DDSs fabrication such as purification, functionalization and large-scale production [277, 278]. This review presents the recent developments in microfluidics and its application in drug and gene delivery. In the first part, the basic principles of controlled mixing and flow regimes are summarized to provide a theoretical background for rational design of microfluidic devices. Subsequently, the most common microfluidic design strategies are discussed with an emphasis on recent applications in pharmaceutical preparations. The properties of the DDSs that can be controlled by the microfluidics were discussed followed by a summary of different types of the DDSs prepared by the microfluidics for drug and gene delivery applications. The challenges for the industrial application of microfluidics for DDS fabrication were also included.

1.4.1 Principles of mixing under controlled conditions

1.4.1.1 Rapid nanoprecipitation

Fast precipitation is a widely used process in the pharmaceutical field as a bottom-up approach to prepare small molecule drug nanoparticles or to formulate multicomponent nanocarriers for drug delivery. The basis of nanoparticle formation has been explained by the classical crystallization theory [252, 279]. In single phase system, rapid precipitation occurs when a highly supersaturated condition is reached as a result of sudden change in precipitation dependant conditions such as concentration or temperature. The precipitation process begins with nucleation when solid seeds emerge from the liquid phase to achieve thermodynamic stability. This phase separation is governed by the force generated by the reduction from the high Gibbs free energy (ΔG) of supersaturation state to low ΔG which is more favourable thermodynamically. The nucleation rate (B) can be calculated using this energy difference according to Equation (1) [280]:

$$B = A \exp\left(\frac{-\Delta G}{kT}\right) \quad (1)$$

Where A is a constant, k is Boltzmann's constant, T is the absolute temperature and ΔG is the Gibbs free energy of nucleation. Assuming the outcome of nucleation is spherical particles with critical radius (r_c), the nucleation rate can also be given by Equation (2) [281]:

$$B = A \exp\left(\frac{-16\pi\gamma^3 v^2}{3k^3 T^3 [\ln(S_r)]^2}\right) \quad (2)$$

Where A is a constant, γ is the surface tension, v is the molar volume, k is Boltzmann's constant, T is the absolute temperature and S_r is the supersaturation ratio. Both equations 1&2 demonstrate that nucleation and particle growth are governed by supersaturation, as well as temperature [279, 281]. Therefore, the mechanism by which supersaturation is achieved can control particle formation and growth at a given temperature. The nanoprecipitation of particles requires creating the supersaturation condition by rapid mixing of two or more miscible liquids. When one solution containing the solute (drug or polymer) meets an anti-solvent in the mixer channels, nucleation and particle growth of the solute are triggered (**Figure 1.10**). Optimizing mixing parameters between solution and anti-solvent such as reducing mixing time (t_{mix}), selecting the mixer geometry and flow regime can cause the least variation in supersaturation conditions and thus the least variation in particle properties. However, there are several other parameters that must be considered to modify the properties of the nanoparticles produced by nanoprecipitation. These involve: (1) the hydrophobicity of the drug or polymer, (2) the selection of the solvent and anti-solvent, (3) addition of stabilizers to minimize agglomeration [279, 281, 282].

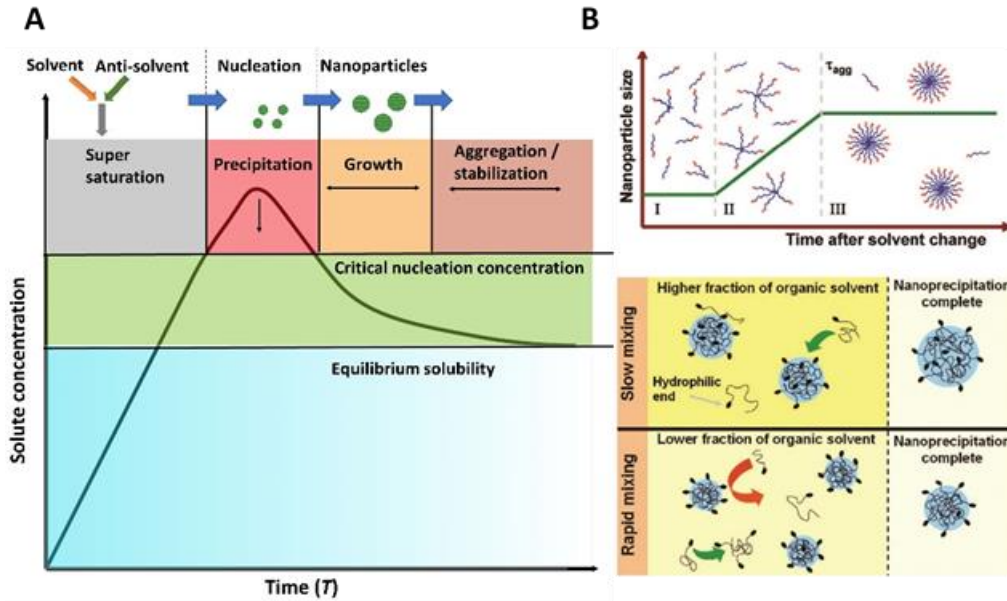


Figure 1.10. A) Schematic representation of solute concentration trend during the nanoprecipitation and nanoparticle formation steps. B) The staged assembly process of block copolymers to form nanoparticles and the effect of rapid mixing on the properties of the produced nanoparticles. Reprinted from [283].

1.4.1.2 Flow regimes and Reynolds number

The production of nanoformulations using nanoprecipitation of small molecules, controlled crosslinking of polymers, or structural transformations of proteins requires rapid mixing [210, 284]. In nanoprecipitation, mixing in small timescale (milliseconds to microseconds) can create uniform local high supersaturation leading to nanoprecipitation of any molecule above the saturation level regardless of its nature [281, 285]. This mechanism has been exploited to formulate many hydrophobic drugs in pharmaceutical industry [283]. The interaction of two fluids can be classified into two regimes: laminar and turbulent. Laminar flow occurs when the mixed fluids flow in parallel layers or paths without forming perpendicular or opposite currents to the main flow. On the other hand, turbulent flow takes place when the fluids undergo irregular fluctuation leading to continual mixing in both magnitude and direction [252]. The type of flow within the mixer chamber is governed by viscous forces and inertial forces (resistance and driving forces) which is measured by Reynolds number (Re) in Equation (3)[286]:

$$Re = \frac{\rho u D h}{\mu} = \frac{u D h}{\nu} \quad (3)$$

where ρ is fluid density; μ is dynamic viscosity; ν is the fluid kinematic viscosity; u is a mean fluid velocity and D_h is a hydraulic diameter of the channel of the mixer. The design and geometry of the mixing channels is correlated to its hydraulic diameter, and is given by Equation (4)[286]:

$$Dh = \frac{4A}{P_{wet}} \quad (4)$$

where A is the channel cross-sectional area and P_{wet} are wetted perimeter. Turbulent flows regime dominates at relatively high Reynolds number ($Re > 4000$) and the range between $Re=2100$ and 4000 is unsteady flow and its complexity is highly dependent on the mixer geometry. As a result of the random motion of fluid streams in multiple directions in time and space, the mass transfer by advection occurs in all spatial directions in the turbulent flow regime [287]. On the contrary, laminar flow is associated with low Reynolds number ($Re < 2100$) and the advective mass transport can only happen in the direction of the main flow [286]. The majority of microfluidic devices use low Re and which corresponds to laminar flow. In this regime, mixing relies on passive diffusion and advection. The molecular movement from high concentration to a lower concentration domain is defined as Diffusion-based mass transfer and can be calculated using Fick's laws Equation (5) [288]:

$$J = -D \frac{d\varphi}{dx} \quad (5)$$

Where φ is the concentration; D is the diffusion coefficient and x represent the spatial coordinates. The diffusion coefficient is given by Stokes–Einstein Equation (6)[289]:

$$D = \frac{kT}{6\pi\mu r} \quad (6)$$

Where k is Boltzmann's constant; T is the absolute temperature; r is the particle radius and μ is the fluid viscosity. For small molecules dissolved in water at constant ambient temperature, D can be considered as $10^{-10} \text{ m}^2\text{s}^{-1}$ [290]. Diffusion does not happen at once; but it is a gradual process which takes into account the time factor t and fluids are non-linearly diffuse over distance x . Therefore one-dimensional diffusion process follow the Equation (7) [291]:

$$x^2 = 2Dt \quad (7)$$

Where x^2 is the mean square distance diffused in time t . Since many microfluidic systems use laminar flow, diffusion has become the main consideration for manipulating rapid mixing and

controlling particle production. Based on Equations (5 & 6), modifying the diffusion process can be done by altering the viscosity (changing the solvent quality) by changing one or more of the mixed solvents. Moreover, reducing the diffusion distance x in the microchannels of the mixer results in shorting the time required for mixing (Equation 7) [292]. Therefore, these factors have provided guidelines for the design of microfluidic device and optimization of particle production by rapid mixing.

1.4.2 Microfluidic techniques control the properties of the DDSs

1.4.2.1 Size

The size uniformity and reproducibility of the nanoformulation are essential requirements for pharmaceutical applications. Controlling molecular assembly and particle growth (t_{agg}) plays the key role in obtaining the desirable size of DDSs. Studies revealed that the determinant factor for nucleation time is the precursors concentration in the microfluidic production of nanoformulations, while t_{agg} is govern by Re , total flow rate (TFR) and the flow rate ratio (FRR) between aqueous and organic phase [293, 294]. Increasing the FRR can reduce the mixing time which results in reducing the diameter of the liposomes prepared by HFF mixer [295, 296]. One or more of these parameters can be manipulated in the microfluidic system to achieve the required size range. For example, Ghazal et al. [275] has assessed the dependence of multilamellar vesicles (MLVs) size and monodispersity on Hydrodynamic flow focusing (HFF) device geometry and FRRs [275]. This study found that FRR has a significant role in modulating the size distribution of the produced MLVs, while TFR exhibited much less impact (**Figure 1.11 A&B**). Increasing the FRR from 10 to 50 at constant TFR (100 μ L/min) results in 27% reduction in both mean size and PDI (**Figure 1.11B**). The design of the microfluidic chip has also shown a tangible effect on the MLVs size due to the impact of the channel length and geometry on diffusion [275]. Another study conducted by Lim et al. [297] investigated the impact of Re on various types of nanoparticle production including PLGA-PEG, lipid vesicles, iron oxide nanoparticles and polystyrene nanoparticles [297]. This work has shown a significant reduction in the size of all tested formulation (from 150 to 20 nm) when Re was increased from 500 to 3500 [297]. These results implied that the size and PDI of nanoparticles can be easily controlled by microfluidic parameters.

1.4.2.2 Shape and structure

The shape of DDSs is one important factor for regulating cellular uptake and enhancing API encapsulation [298]. Moreover, modifying the structure such as increasing the porosity and pore size in NPs were associated with increasing the drug release rate. Mesoporous silica nanomaterial was successfully prepared using spiral-shaped microfluidic devices. By changing the flow rate, it was possible to transform the morphology of mesoporous silica from nanofibers to spherical nanoparticles [299]. In another research, the compactness of chitosan nanoparticles was tuned by applying different FRR and changing the hydrophobicity of the chitosan chains [300]. Liu et al. [301] have successfully prepared nanocarriers that enjoy desirable features including high stability, biodegradability, pH-responsive and fast dissolution. These nanocarriers were fabricated by integrating sorafenib (SNF) or itraconazole (ICZ) nanocrystal drug core into a polymeric shell which made of acetylated dextran functionalized with folic acid (ADS-FA) using a microfluidic platform (**Figure 1.11 C&D**) [301].

1.4.2.3 Surface engineering

One of the most common approaches for improving the targetability of DDSs to cancer cells is surface modification. For example, Di Santo et al. [263] prepared hybrid nanoparticles consisting of graphene oxide (GO) flakes coated with cationic lipids using microfluidic mixing. The resulting particles had a size of (>150 nm) and charge of ($\xi = +15$ mV) that are suitable for delivering plasmid DNA (pDNA) to human cervical cancer cells (HeLa) and human embryonic kidney (HEK-293) cells [263]. One of the challenges in fabricating functionalized nanocarriers is the lack of approaches for isolation and purification. In a study conducted by Wang et al. [277], chemically modified exosomes were prepared for active targeted drug delivery to cancer cells [277]. This study used three-dimensional (3D) nanostructured microfluidic chip consists of an ordered series of micropillars functionalized with multiwall carbon nanotubes (MWCNTs) to efficiently capture exosomes [277]. Capture efficiency can be optimized by changing height, spacing distances and flow rate (**Figure 1.11 E&F**).

1.4.2.4 Elasticity

Recent studies have found that mechanical properties such as elasticity of the DDSs have a significant influence on cellular uptake, drug release, and stability [248]. The precise manipulation of the flow and flow regime within the microfluidic system can modify the

particle elasticity. Sun *et al.* [302] designed nanocarriers made of polymeric core (PLGA) and lipid shell with tuneable rigidity for regulating cellular uptake (Figure 3G&H) [302]. In this study, the particle elasticity was modulated in the microfluidics device by altering the injection order of organic solutions containing PLGA and lipid-PEG. This technique allows for variation in the water content leading to variation in Young's modulus which influences the internalization mechanism in Hela cells [302].

1.4.3 Industrial application

Pharmaceutical products have a very high value with estimated global market of one trillion US\$ [303]. However, the process required from discovery, formulation to manufacturing the final product is costly and time consuming [303]. Therefore, one of the main priorities of pharmaceutical companies is to implement new strategies for rapid and controlled manufacturing of pharmaceutical products to achieve cost effectiveness, sustainability and on-demand production [304]. In microfluidics, the translation from bench-top instrument to the industrial scale requires high production rate and compliance with good manufacturing practice (GMP)[60]. Increasing the production rate by increasing the fluid velocity within the microfluidic channel is undesirable due to the significant increase in the pressure drop across the fabrication device. Therefore, generating a cumulative flow by increasing the number of identical devices at the same fluid velocity is a better alternative strategy for production at industrial level [252, 305]. In addition, using a multiple pressure sources (pumps) for each microfluidic device can provide more control, thus more uniform size distribution but it is not cost-efficient. Distributing a uniform flow from a main pressure source is more convenient and practical for industrial applications and substantial research and development are required in this area [306-308]. NanoAssembler GMP system is one of the recent development in large scale production of pharmaceutical formulations using microfluidic platforms[60]. This system offers a replaceable cartridge, which has the mixing elements, and is equipped with custom pumps. Changing the cartridge is not only beneficial for maintaining the mixing quality and sterility, but also allows for switching the mixer type (SHM & TrM)[60]. Switching to continuous flow production using microfluidics still has many challenges in regard to quality control and cost efficiency. By implementing new approaches and modifying the current designs, microfluidics can play a key role in large scale production of pharmaceuticals, especially in nanomedicine.

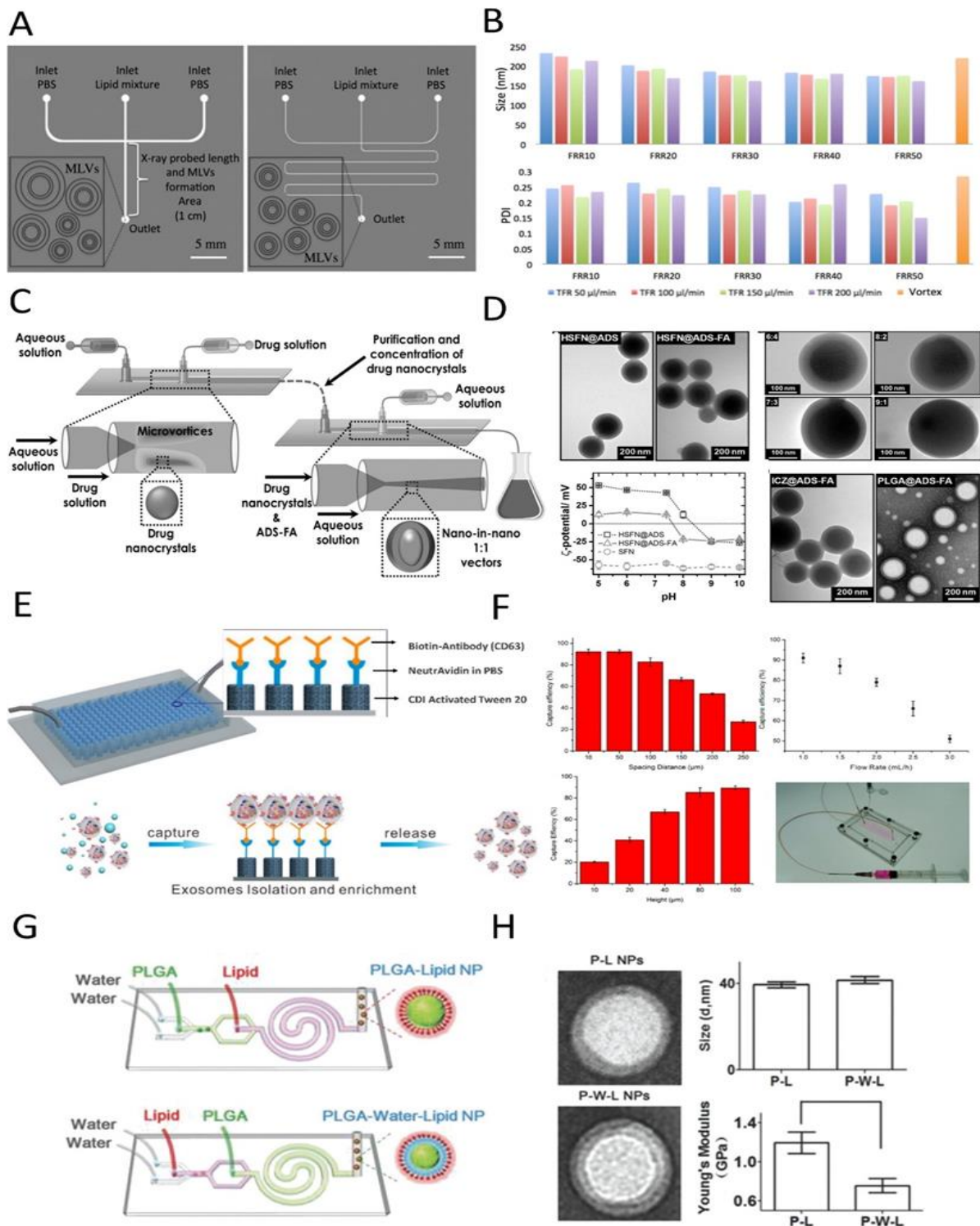


Figure 1.11. Examples of microfluidic fabrication of DDSs. **A)** A schematic representation of the impact of two chip designs on the production of MLVs. **B)** DLS results for the MLVs produced showing the effects of FRR and TFR on size and polydispersity. Reprinted from [275]. **C)** Schematics of the process to formulate the nano-in-nano vectors through the multistep microfluidic nanoprecipitation. **D)** TEM images of nano-vectors prepared by multistep microfluidic nanoprecipitation (HSFN@ADS) and (HSFN@ADS-FA), the effect of SFN and ADS-FA weight ratio (6:4 to 9:1) on shell thickness and ζ -Potential of SFN nanocrystals in terms of

pH values of the dispersion media. Reprinted from [301]. E) Schematics describing the process of electroless plating and functionalizing MWCNT for capturing exosomes. F) The effect of pillars height, pillars spacing distance and the flow rate on the capturing efficiency. Reprinted from [277]. G) Assembling PLGA–lipid nanoparticles with varying amounts of interfacial water to modify the particle rigidity, P-L nanoparticles (without interfacial water layer, top) and P-W-L nanoparticles (with interfacial water layer, bottom). H) Size and Young’s modulus of P-L nanoparticles and P-W-L nanoparticles from TEM and AFM scanning. Reprinted from [302].

1.5 Research motivation

The main purpose of this research project is to develop efficient nanocarriers for the delivery of small molecule hydrophobic anticancer drugs (e.g. ASC-J9). The development of nanocarriers as successful anticancer drug delivery systems requires a simple and scalable preparation technique, tunable physiochemical properties, modified release kinetics and the ability to target tumor tissue. In order to meet these requirements, in-depth investigation of novel formulations of nanocarriers and production techniques have been studied. The impact of the stiffness of biopolymeric nanocarriers has been evaluated in terms of drug release, encapsulation efficiency and cellular uptake in 2D and 3D cell culture in different biological conditions. In addition, a new geometric design of microfluidic mixer has been developed to improve the quality of mixing during the microfabrication process of protein nanoparticles. The new design (swirl mixer) was compared to conventional microfluidic system (T-mixer) in terms of percentage of yield, particle shape and particle size distribution. Finally, the new microfluidic system was also employed to produce magnetic silk nanoparticles which was functionalised with a short amphiphilic peptide (G(IKK)3I-NH₂) for targeted delivery of ASC-J9 to cancer cells. The results obtained from characterization, cellular uptake and cytotoxicity studies provide a complete evaluation of the nanocarriers properties, efficiency as drug delivery system and the potential application in cancer therapy.

1.6 Thesis outline

Chapter 1: provides a background of nanocarriers in nanomedicine and the chronological development of the formulation strategies and applications. It also covers the potential use of biopolymeric materials in pharmaceutical preparations and the strategies and applications of microfluidic techniques.

Chapter 2: demonstrates the detailed methodology used in the experimental sections of this PhD thesis. This chapter also explains the theoretical principles of the instruments and techniques used in the experimental sections.

Chapter 3: presents original experimental research covers the design, preparation and characterization of stiffness-tunable nanocarrier formulations for controlled drug delivery of the hydrophobic anticancer agent (ASC-J9) to colorectal cancer cells.

Chapter 4: reveals the design and evaluation of novel microfluidic device (swirl mixer). Silk nanoparticles were used as a model biopolymeric particle to assess the performance of swirl mixer in nanoparticle production. A conventional T-mixer design was used as comparison to investigate the impact of the mixer geometry on nanoparticle formation.

Chapter 5: presents a new nanoparticle formulation prepared by microfluidic platform. These nanoparticles consist of a magnetic silk nanoparticle which were functionalised by short amphiphilic cationic peptide with anticancer activity. This chapter characterize and evaluate the prepared nanoparticles in both cancer and normal cells to investigate the augmented effect and the selective anticancer activity.

Chapter 6: is the conclusive chapter of this thesis where all the discussed data are highlighted and summarised. It also describes the challenges and the future work in the field of nanomedicine and microfluidics.

2 Chapter 2: Materials and Methods

2.1 Materials

Bombyx mori silk was obtained from Jiangsu, P.R. China. Sodium carbonate was purchased from Alfa Aesar. 1,2-dioleoyl-sn-glycero-3-phosphocholine (DOPC) was purchased from Avanti Polar Lipids (Alabaster, AL, USA). ASC-J9 was obtained from Changzhou University, China. Sodium alginate, sodium salicylate, ammonium hydroxide, calcium chloride and foetal bovine serum, (FBS) were purchased from SIGMA-ALDRICH (Gillingham, UK). DMEM (Dulbecco's Modified Eagle Medium) and Trypan blue dye 0.4% were sourced from GIBCO®, Thermo Fisher Technologies & Invitrogen™, Thermo Fisher Scientific. Hoechst 33342 and Flash Phalloidin™ 594 stains were purchased from Thermo Fisher Scientific and biolegend respectively. 96 well plates were purchased from Greiner Bio One.

HCT-116 epithelial cancer cells derive from a colorectal carcinoma extracted from an adult male and provided by Dr. Spencer Collis CRUK Senior Cancer Research Fellow at Department of Oncology & Metabolism, University of Sheffield Medical School. This line has a mutation in codon 13 of K-Ras proto-oncogene on chromosome 12 and is positive for transforming growth factor β 1 (TGF- β 1) and β 2. HDFs (normal human primary dermal fibroblasts) obtained from healthy human foreskin or adult skin (a kind gift of Dr. Zoe Hewitt, Project Manager UKRMP Pluripotent Stem Cell Platform, Centre for Stem Cell Biology, University of Sheffield). All cell lines used in this research were not directly obtained from patients and therefore ethics approval for handling patients' samples was not required.

2.2 Methods

2.2.1.1 Preparation of the nanocarriers stiffness-tunable nanocarriers

2.2.1.2 Preparation of silk fibroin (SF) solution and sodium alginate (SA) solution

The extraction of SF from silk cocoon was reported previously[309]. Briefly, the cocoons were boiled in 0.02M Na₂CO₃ solution for 30 min. The cocoons were rinsed in UHQ water to remove any traces of the dissolved sericin. After drying, the degummed fibres of SF were dissolved in Ajisawa's reagent (CaCl₂/ Ethanol/ water = 1: 2: 8 molar ratio) at 80 °C for 90 min before dialysed in a cellulose tube (MWCO 12 kDa) against UHQ water for 2 days to remove CaCl₂. The last step was to purify the solution from impurities by centrifugation (12,000 rpm) and filtering the solution with a 0.45 μ m filter. The resulting solution was stored at 4 °C.

The SA solution was prepared by dissolving SA powder in UHQ water at 30 °C (20 mg/ml) and kept on constant stirring overnight under sterilised conditions. The solution was then transferred to a 20 ml bottle and stored at room temperature.

2.2.1.3 Synthesis of SF/SA incorporated nanocarriers

1,2-Dioleoyl-sn-glycero-3-phosphocholine (DOPC) 10 mg) was dissolved in chloroform (1 ml) in a 25 ml round bottom flask [19]. The solvent was evaporated using a rotary evaporator to form a thin layer of lipid. One millilitre of SF/SA mixture (different ratio for each formulation) was added to hydrate the lipid layer at 40 °C for 10-15 min and form multilamellar lipo-gel vesicles (MLV). MLVs were extruded through 200 nm polycarbonate membrane using Avanti Mini Extruder for 8 times at 35 °C to form a uniform and small size distribution (**Figure 2.1**). Unencapsulated SF/SA was removed by gel filtration using Sephadex G50 in PBS as eluent.

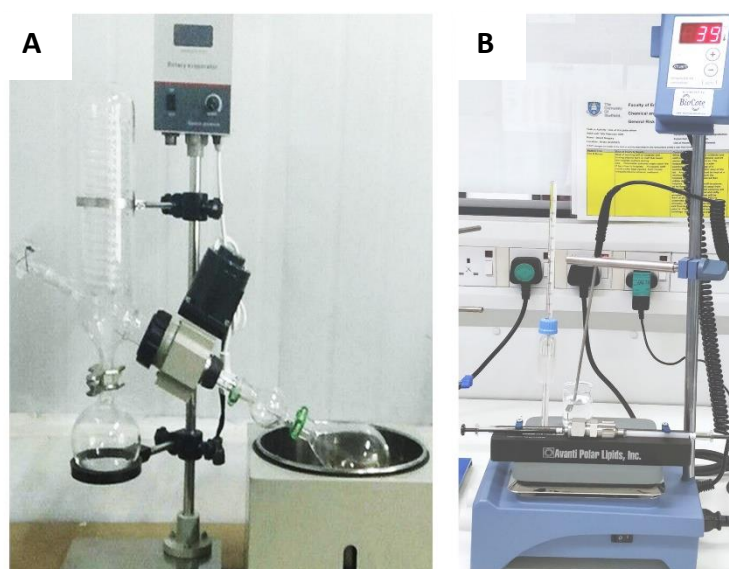


Figure 2. 1. A) Formation of multilamellar lipo-gel vesicles (MLVs) by hydration of the thin lipid layer using a rotary evaporator. **B)** Extrusion of MLVs using Avanti Mini Extruder.

2.2.1.4 Preparation of ASC-J9 loaded nanocarriers

Three formulations of nanocarriers containing different ratios of the biopolymers (SF:SA 7:3, 1:1, 3:7) were prepared and loaded with the hydrophobic anticancer drug ASC-J9. The drug loading and crosslinking of the SA monomers within the biopolymeric core were performed simultaneously by adding the drug and crosslinker solution (ASC-J9 & CaCl₂ (10 mM))

dropwise to the nanocarrier solutions (1:1, v:v). After 1 h incubation with constant stirring at 30 °C, the crossed-linked nanocarriers were dialyzed in FLOAT-A-LYZER G2 dialysis tubing (MWCO 1000 kDa) in PBS for 8 h at 4 °C to remove the remaining CaCl₂.

2.2.1.5 Encapsulation efficiency measurement of SF/SA nanocarriers

To measure the encapsulation efficiency (EE%), the unencapsulated drug was removed by gel filtration using Sephadex G50 in a HR 10/30 column with UHQ water as eluent at flow rate of 1 mL/min. Next, 50 µL of the sample was diluted with DMSO in an eppendorf tube and vortexed for 1 min. The encapsulated drug was quantified by UV-Vis spectrometry (JENWAY 6715, Bibby Scientific, UK) at λ=435 nm using standard calibration curves for ASC-J9 in DMSO and PBS. Each sample was assayed in triplicate. The EE% was determined by equation (1)

$$EE\% = \frac{\text{The encapsulated Dimethylcurcumin (ASC-J9) concentration}}{\text{The initial added Dimethylcurcumin (ASC-J9) concentration}} \times 100 \quad (1)$$

2.2.1.6 In vitro drug release of SF/SA nanocarriers

The *in vitro* drug release profile of the ASC-J9 loaded nanocarrier solutions was determined by transferring aliquots of ASC-J9 solution (63 µM) into FLOAT-A-LYZER G2 dialysis tubing (MWCO 1000 kDa). The tubes were dialyzed against 50 mL sodium salicylate solution (1 M) at 37 °C with rotation at 150 rpm. The concentration of ASC-J9 released at various time points was measured by UV-Vis spectrometry at 435 nm. The drug release profile of ASC-J9 solution was determined under identical conditions for comparison.

2.2.2 Preparation of SF nanoparticles and SF-magnetic nanoparticles by microfluidic platform

2.2.2.1 Fabrication of microfluidic device

The microfluidic devices used in this study have a swirl microchannel consisting of 1,2 or 4 elements. The geometry of the designed swirl mixer approximates the proportions of the element (**Figure 2.2**), with elements on 1.2 mm centres having a nominal chamber of diameter 0.8 mm, depth 0.4 mm, and with orifice diameter 0.4 mm. It was manufactured by removing material from a 1 mm thick Polyether ether ketone (PEEK) sheet using laser ablation (Layer Micromachining Ltd). One chamber of each element and the connecting channels were created by cutting from one side of the PEEK sheet and then the other chambers and the connecting orifices are cut from the other (**Figure 2.2**). The volume of each element of this mixer is estimated to be 0.612 µL. The mixer is completed by clamping the chip between two

opposing blocks fitted with connection holes and fitting threads and accommodating O-rings to seal the unit. Flow through the mixer was generated by connecting the two mixer inlets to a dual syringe pump (Fusion 4000, Chemyx Inc.) (**Figure 2.2**). This pump has a maximum linear speed (V_{MAX}) of 17.8 1cm/min and 289 N maximum force in each syringe.

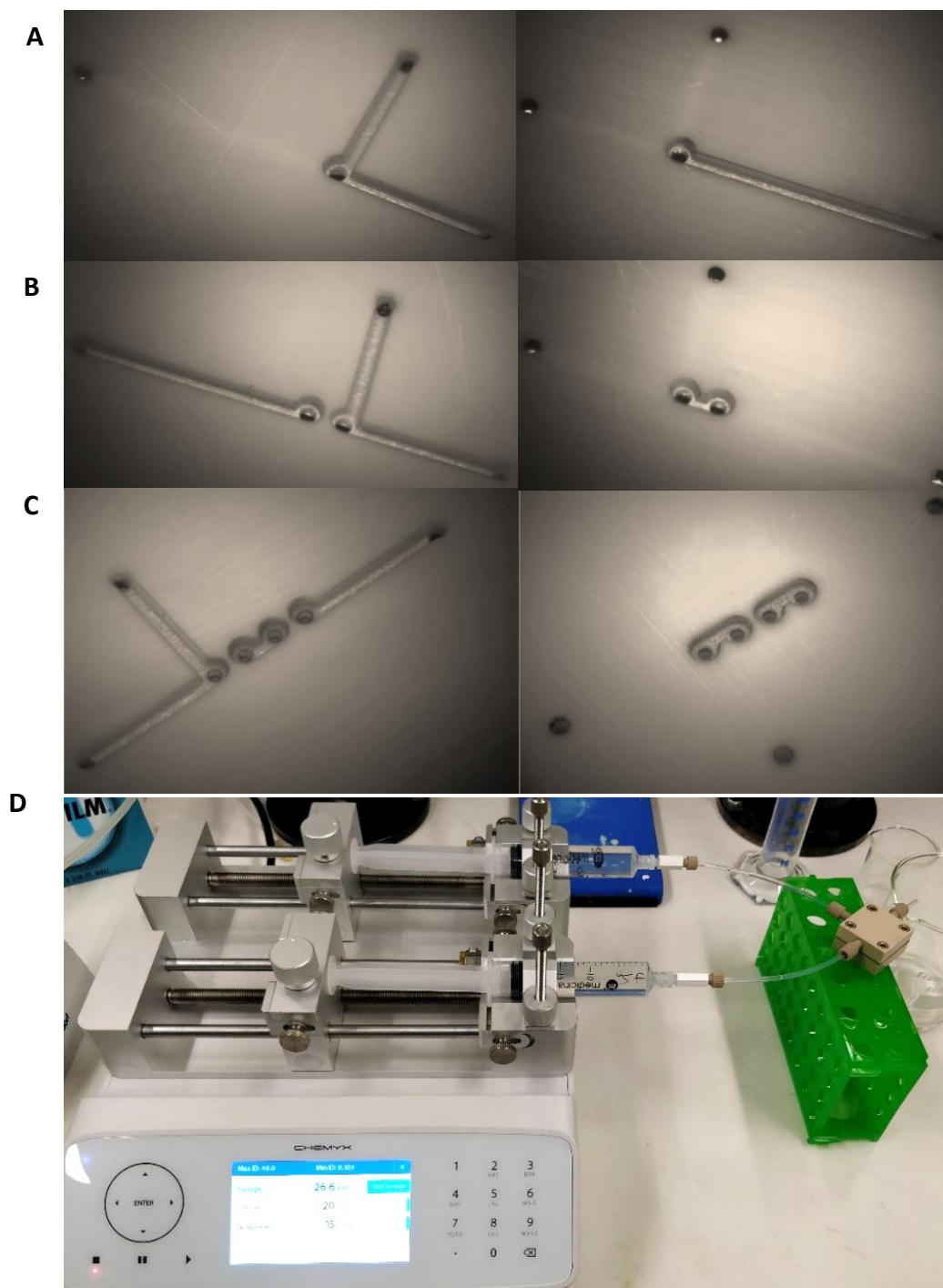


Figure 2. 2. Angled view of the swirl mixer pattern from the two sides of the PEEK chip. **A)** One mixing element. **B)** Two mixing elements. **C)** Four mixing elements. **D)** The complete swirl mixer setup connected Chemyx syringe pump.

2.2.2.2 Computation and modelling

A continuum computational method is used to determine and evaluate the performance of the swirl mixer in comparison to standard tube mixer. The computations were by Dr Jordan MacInnes using a previously reported approach [310] using Ansys 2019.R2 software. The modelling software used in the study is Ansys 2019.R2 (Engineering Simulation & 3D Design Software) which generates modelling of the flow patterns by providing several precise inputs including; the length, width and geometry of the microfluidic channels and mixing chambers of the device.

2.2.2.3 Preparation of magnetic nanoparticles (MNP)

Production of magnetic particles has been reported previously [49]. Briefly, 4 g of FeCl_3 and 4.5 g FeCl_2 were dissolved in UHQ water. The resulting solution was transferred to 500 ml round-bottom flask and kept for 30 min under nitrogen. Then, 15 ml of NH_4OH was mixed with the solution and kept at 25 °C under constant stirring. To collect the particles, Neodymium magnets (20x10 mm) was used (**Figure 2.3**) and then washed multiple times with UHQ water to ensure they are free from impurities. The last step was rinsing with 2 ml of ethanol and dried overnight.

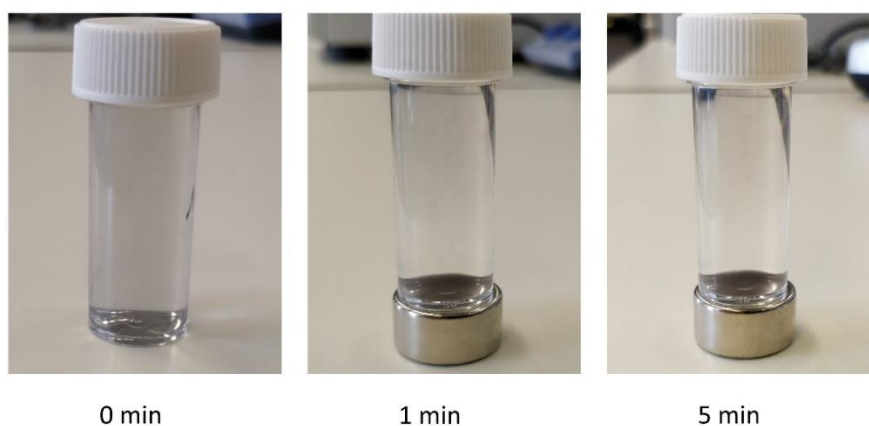


Figure 2. 3. *Magnetic nanoparticles collected using Neodymium magnet (20 x10 mm).*

2.2.2.4 Preparation of SF nanoparticles using the microfluidic system

SF nanoparticles were manufactured using the microfluidic system equipped with the swirl mixer (**Figure 2.2**). A 1.5 mg/ml aqueous silk solution and organic solvent (either methanol or acetone) were loaded into the two syringes connected to the two inlets of the mixer. The SF

nanoparticles were generated within the mixer channels by desolvation and collected by an eppendorf tube at the outlet. In the study conducted on swirl mixer and tube mixer in Chapter 4, the total flow rate and was varied as shown in **Table 2.1 & 2.2**.

For the magnetic silk nanoparticles prepared in Chapter 5, the total flow rate (TFR) of the solvent and silk solution was varied, from 1 to 50 ml/min. The flow rate ratio (FRR) was also varied at 1:3 and 1:1. To remove the organic solvent, the formed SF nanoparticles were centrifuged at 12000 rpm and the supernatant was discarded. The pellets were resuspended in UHQ water and sonicated for 5 min to allow full homogenous dispersion in the suspension.

Table 2. 1 Expermental planner for the production of silk nanoparticle in the model Tube mixer.

| Total flow rate | Silk Solution flow rate | Organic Solvent flow rate | Flushing time | Volume (Silk solution) | Volume (Organic solvent) | Mixing time | Re |
|------------------------|--------------------------------|----------------------------------|----------------------|-------------------------------|---------------------------------|--------------------|-----------|
| (mL/min) | (mL/min) | (mL/min) | (s) | (mL) | (mL) | (ms) | |
| 8.154 | 6.116 | 2.0386 | 8 | 3.90 | 1.03 | 45.46 | 439 |
| 10.601 | 7.950 | 2.650 | 6 | 3.90 | 1.03 | 34.97 | 571 |
| 13.781 | 10.336 | 3.445 | 5 | 3.90 | 1.03 | 26.90 | 742 |
| 17.915 | 13.436 | 4.479 | 4 | 3.90 | 1.03 | 20.69 | 964 |
| 23.290 | 17.467 | 5.822 | 3 | 3.90 | 1.03 | 15.92 | 1254 |
| 30.28 | 22.707 | 7.569 | 2.1 | 3.90 | 1.03 | 12.24 | 1630 |
| 39.36 | 29.52 | 9.840 | 1.6 | 3.90 | 1.03 | 9.42 | 2119 |
| 51.17 | 38.38 | 12.792 | 1.3 | 3.90 | 1.03 | 7.24 | 2754 |
| 66.52 | 49.89 | 16.629 | 1.0 | 4.06 | 1.09 | 5.57 | 3580 |
| 86.47 | 64.85 | 21.618 | 0.7 | 4.56 | 1.25 | 4.29 | 4655 |
| 112.41 | 84.31 | 28.10 | 0.6 | 5.21 | 1.47 | 3.30 | 6051 |
| 146.14 | 109.60 | 36.53 | 0.4 | 6.05 | 1.75 | 2.54 | 7866 |

Table 2. 2 Experimental planner for the production of silk nanoparticle in the Swirl mixer.

| Total flow rate | Silk Solution flow rate | Organic Solvent flow rate | Flushing time | Volume (Silk solution) | Volume (Organic solvent) | Mixing time | Re |
|-----------------|-------------------------|---------------------------|---------------|------------------------|--------------------------|-------------|------|
| (mL/min) | (mL/min) | (mL/min) | (s) | (mL) | (mL) | (ms) | |
| 2.20 | 1.65 | 0.549 | 28.4 | 3.84 | 1.02 | 16.72 | 94 |
| 2.86 | 2.14 | 0.714 | 21.8 | 3.84 | 1.02 | 12.86 | 123 |
| 3.71 | 2.78 | 0.93 | 16.8 | 3.84 | 1.02 | 9.89 | 159 |
| 4.83 | 3.62 | 1.21 | 12.9 | 3.84 | 1.02 | 7.61 | 207 |
| 6.27 | 4.70 | 1.57 | 9.9 | 3.84 | 1.02 | 5.85 | 269 |
| 8.2 | 6.12 | 2.04 | 7.6 | 3.84 | 1.02 | 4.50 | 350 |
| 10.6 | 8.0 | 2.65 | 5.87 | 3.84 | 1.02 | 3.46 | 455 |
| 13.8 | 10.3 | 3.45 | 4.52 | 3.84 | 1.02 | 2.66 | 592 |
| 17.9 | 13.4 | 4.48 | 3.48 | 3.84 | 1.02 | 2.05 | 769 |
| 23.3 | 17.5 | 5.82 | 2.67 | 3.84 | 1.02 | 1.58 | 1000 |
| 30.3 | 22.7 | 7.57 | 2.06 | 3.84 | 1.02 | 1.21 | 1300 |
| 39.4 | 29.5 | 9.8 | 1.58 | 3.84 | 1.02 | 0.93 | 1691 |
| 51.2 | 38.4 | 12.8 | 1.22 | 3.84 | 1.02 | 0.72 | 2198 |
| 66.5 | 49.9 | 16.63 | 0.94 | 4.00 | 1.07 | 0.55 | 2857 |
| 86.5 | 64.9 | 21.6 | 0.72 | 4.50 | 1.24 | 0.42 | 3714 |
| 112.4 | 84.3 | 28.1 | 0.55 | 5.15 | 1.46 | 0.33 | 4828 |

2.2.2.5 Preparation of magnetic SF nanoparticles using the microfluidic system

The magnetic particles were mixed with organic solvent (either methanol or acetone) to make a 0.05 mg/ml suspension. Silk solution of 1.5 mg/ml and the magnetic suspension was injected in the two mixer inlets and the magnetic silk nanoparticles were collected in an eppendorf tube. TFR was set at 30 ml/min and FRR (3:1).

2.2.2.6 Yield measurement of SF nanoparticles

To measure the percentage of the SF nanoparticles produced by the microfluidic device, the volume of SF nanoparticle suspension collected from the mixer outlet was determined. Next, 10 empty Eppendorf tubes (1.5 ml) were weighed (*W1*). The fabricated SF nanoparticles were added to the tubes and dried in the oven at 40 °C for 24 h and the total weight of the

nanoparticles and tubes was determined (W2). The yield percentage can be calculated using equation (2)

$$\% \text{ Yield of the silk nanoparticles} = \frac{(W2 - W1) \times \text{Total suspension volume}}{\text{The original amount of introduced SF} \times \text{sample volume}} \times 100 \quad (2)$$

2.2.2.7 Preparation of FITC-labelled G3

The synthesis of the fluorescent version of (G3) peptide was performed using a standard Fmoc based solid-phase protocol. To minimize degradation during the last cleavage step of the N-terminals FITC labelling, a 6-46 aminohexanoic acid (Ahx) group was introduced between the last amino acid (A or G) and the fluorescein motif [311].

2.2.2.8 Preparation of (G3)- SF magnetic nanoparticles

Biofunctionalization of MSNP with G3 was performed by mixing 75 μM G3 solution with (5-15 mg/ml) MSNP stock. The mixture was kept under constant stirring for 12 hrs in a dark environment at 4 $^{\circ}\text{C}$. The absorbance of the supernatant was measured at 495 nm after collecting the G3-MSNP using in Neodymium magnet. A calibration curve of FITC-G3 was used to determine the G3 grafted percentage on MSNP.

2.2.2.9 Preparation ASC-J9 loaded SF magnetic nanoparticles

ASC-J9 was dissolved in DMSO with a concentration of 50 mg/ml ACS-J9 DMSO solution. This solution was diluted with UHQ water to make (100-50) μM of ASC-J9 solution. SF magnetic nanoparticles produced by the microfluidic system were mixed with ACS-J9 for 50 min to allow drug loading. Then, unencapsulated ASC-J9 was removed by collecting the ASC-J9 loaded SF magnetic nanoparticles with Neodymium magnet (20 x10 mm) and the supernatant was analysed to determine residual ASC-J9 concentration by UV-Vis spectrometry (JENWAY 6715, Bibby Scientific, UK). The maximum peak absorbance was identified by obtaining ASC-J9 spectrum and slandered calibration curves in PBS, UHQ water were used. The encapsulation (EE%) was calculated using equations (3)

$$EE\% = \frac{\text{Amount of Dimethylcurcumin (ASC - J9) in nanoparticles}}{\text{The initial Dimethylcurcumin (ASC - J9) added}} \times 100 \quad (3)$$

2.2.2.10 Release profile of ASC-J9 from SF and magnetic SF nanoparticles (MSNP)

The *in vitro* ASC-J9 release from SF and magnetic SF nanoparticles was measured by suspending 5 mg of the nanoparticles in PBS (pH 7.4) in 5 ml vials and kept in the incubator at 37 °C under constant agitation. At various time points, the nanoparticles were centrifuged at 15000 rpm and the supernatant was collected for measuring the concentration of the released ASC-J9. The removed supernatant was replaced with fresh PBS to measure the ASC-J9 at the next time point. The experiments were performed in triplicate and the values were reported as mean \pm SE

2.2.3 Characterization

2.2.3.1 Particle size and zeta potential analysis

The particle size and zeta potential of the SF/SA nanocarriers were obtained by Dynamic light scattering (DLS) ((NanoBrook 90 plus Pals Particle size Analyzer, Brookhaven Instrument, NY, USA). The prepared carriers were diluted 10 times in DI water and transferred to DLS cuvette before placing it in the instrument sample cell. The DLS is equipped with 660 nm wavelength laser and the refractive index was set to 1.331 & 1.540 for DI water and the nanocarriers respectively. All measurements were carried out at 20 °C using a circulation bath. The experiments were performed in triplicate and the values were reported as mean \pm SE.

The size distributions of SF nanoparticles produced by the microfluidic system were acquired using nanoparticles tracking analysis (NTA, Nanosight LM 10, UK). SF nanoparticles samples were diluted 15 times in DI water before carefully injecting the sample using 1 ml syringe into the scattering cell to ensure that the cell is bubble-free, and the measurements were performed at 20 °C. The tracking video was recorded for 1 min (1800 frame) and the valid particles were tracked for a minimum of 5 frames.

2.2.3.2 Secondary structure measurements of SF/SA nanocarriers and SF nanoparticles

Fourier transform infrared (FTIR) spectroscopy (IR Prestige-21, Shimadzu, UK) was used to investigate the chemical interaction between SF and SA and to detect the SF structural transformations. Nanocarrier formulations were mixed with 1% Triton X-100 to disturb the lipid shell and then centrifuged using 30k Amicon Ultra Centrifugal Filters at 10,000 rpm to remove the remaining lipid. The samples were allowed to air dry on the diamond attenuated total reflectance (ATR) attachment (ATR apparatus, Pike Technologies, USA) of the

spectrophotometer. The range of wave numbers was set from 500 to 3000 cm^{-1} and the spectrum was read using the Happ-Genzel apodisation function over 64 scans with a resolution of 4 cm^{-1} . Each peak in the spectrum is assigned to either SF or SA (**Table 2.1**). The region (1575 - 1750 cm^{-1}) which is assigned to amide I was investigated to determine the secondary structural changes of SF.

Table 2. 3. FTIR absorption peaks of silk fibroin (SF), sodium alginate (SA), and SF/SA mixture in the nanocarrier [203].

| 100% SF | SF/SA mixture | 100% SA | Attribution of absorption peaks |
|---------|---------------|---------|--|
| - | 1731.9 | 1731.9 | C=O stretching |
| 1620.1 | 1622.0 | 1635.5 | Amide I and antisymmetric =COO= stretching overlap |
| 1505.2 | 1522.0 | - | Amide II |
| 1228.5 | 1236.2 | 1238.2 | Amide III and C=O stretching overlap |
| - | 1080.0 | 1076.2 | O-H bending |
| - | 1029.9 | 1027.9 | O-H bending |
| - | 927.7 | 927.7 | C-O vibration |

The SF nanoparticle suspension samples were dried at 40 °C for 24 h. The samples were subjected to secondary structure analysis by Fourier transform infrared (FTIR) spectroscopy (IR Prestige-21, Shimadzu, UK). Each sample was run for 128 scans at a 4 cm^{-1} resolution and the wavenumber range was set from 400 to 4000 cm^{-1} , and the spectra were interpreted by Happ-Genzel apodisation function. Unlike the nanocarrier, all FTIR absorption peaks are visible in the SF nanoparticle analysis. To measure the secondary structure transformation, the amide I region (1595 -1705 cm^{-1}) of the SF protein was investigated. Other SF regions were identified and deconvoluted including side chain (1605-1615 cm^{-1}), random coil (1638-1655 cm^{-1}), α -helical bands (1656-1662), β -sheet structure (1616-1637 cm^{-1} & 1697-1703 cm^{-1}) and turns (1663-1696 cm^{-1}) [312]. OriginPro 9.2 Software was used to correct the baseline and plot the data.

2.2.3.3 Atomic Force Microscopy (AFM) analysis

The size, shape and morphology of the SF/SA nanocarriers and SF nanoparticles were characterized using AFM (Dimension FastScan with ScanAsyst, Bruker corporation, USA) (**Figure 2.8**). Two drops of the nanocarrier or SF nanoparticles suspension were dropped on mica substrates and dried with gentle air at room temperature before placing it on the

instrument sample stage. The measurements were run using SCANASYST-AIR tips and tapping mode. The resulting data were deconvoluted and analysed by NanoScope 1.5 software (**Figure 2.9**).

All Young's modulus measurements were carried out under the same ScanAsyst-Fluid probe. The AFM, with a 10 µm piezoelectric scanner, was set to ScanAsyst-Fluid mode to acquire images. By navigating the image, the force-distance curves of selected nanocarriers were obtained subsequently and 8-50 shooting target measurements were performed. The Young's modulus of samples was calculated according to the Hertz model (Equation 4)[313].

$$F = \frac{4}{3} \frac{E}{(1-\nu^2)} \sqrt{R\delta^3/2} \quad (4)$$

where F is the force from force curve, E is Young's modulus, ν is Poisson's ratio, R is the radius of the indenter tip, and δ is the indentation depth. The original force curves were analysed using NanoScope Analysis software (version 1.9).

2.2.3.4 Transmission electron microscope (TEM)

Transmission electron microscopy (TEM) images were obtained using a FEI Tecnai BioTWIN G2 sprint. The accelerating voltage was set to 80 Kv. 10 µL of the nanocarrier solution was deposited onto carbon-coated copper grids for 1 min and blotted with a filter paper. The grids were left to dry at 25 °C and stained with 0.1% (w/v) phosphotungstic acid for 1 min and blotted again with a filter paper. Finally, the samples were washed with DI water and kept for measurement at room temperature. Images were recorded using a Gatan Orius SC1000B bottom-mounted digital camera and Gatan Digital Micrograph software.

2.2.3.5 Cellular uptake

Cellular uptake studies were carried out using HCT-116 human colorectal adenocarcinoma cells. The cells were cultured in DMEM supplemented with 10% FBS and 1% penicillin/streptomycin in 37 °C and under 5 % CO₂. The HCT-116 cells were cultured in 96 well plates at a seeding density of 4 x 10³ cells per well and were incubated for 24 hr. To accurately calculate the seeding density, the cells were trypsinized following the regular passaging protocol and resuspended in fresh DMEM. Then, the concentration of the cell suspension was determined using an automated cell counter device Countess® II Automated Cell Counter to find out the dilution factor required for achieving the desired seeding density.

20 µL of the cell suspension was mixed of trypan blue dye (1:1) and injected in Countess® Cell Counting Chamber Slide and repeated twice to take the average number of cells per ml before performing dilution. The diluted cell suspension was transferred to the 96 well plates (90 µL per well). The plates were kept in the incubator at 37 °C overnight to allow for attachment of the cells and used for cell uptake experiments the next day. In the next stage, the cells were treated with the drug solution, the drug-loaded nanocarriers, or drug-loaded SF nanoparticles according to predesigned experimental plan (**Table 2.2**) and incubated for 6 hr before replacing the media with fresh DMEM.

In the case of SF/SA nanocarriers, the experiment was carried out in two different conditions. The first set of experiments were performed in the cells growing in DMEM supplemented with 10% FBS. In the second set of experiments, the cells were starved in serum-free media for 4 hr prior to addition of the drug solution or drug-loaded carriers, and then the media were replaced with media supplemented with 10% FBS. At designated time points, the cells were fixed with 3.7% formaldehyde, stained with Hoechst 33342 and Flash Phalloidin™ 594 and imaged with the high content fluorescent automated widefield microscope (ImageXpress® Micro System). The images were analysed using MetaXpress® software 5.3.01 (Molecular Devices). Two algorithms were used to determine the cellular uptake: one for quantifying the drug or drug-loaded objects within the cell, and one for measuring the average integrated intensity of the drug within the cytosol.

Table 2. 4. Experimental plan of silk magnetic nanoparticles prepared using the microfluidic system using Methanol or Acetone and on 96-well plate seeded with HCT 116.

| | 1 | 2 | 3 | 4 | 5 | 6 | 7 | 8 | 9 | 10 | 11 | 12 |
|---|------------------------------------|---|---|------------------------------------|-----------------------|---|---|------------------------------------|---|----|----|----|
| A | FITC-labeled G3 | | | (FITC-labeled G3) loaded MSNP-MEOH | | | | (FITC-labeled G3) loaded MSNP-ACE | | | | |
| B | ASC-J9 (50 µM) | | | ASC-J9 (25 µM) | | | | ASC-J9 (10 µM) | | | | |
| C | FITC-labeled MSNP-MEOH | | | | FITC-labeled MSNP-ACE | | | | | | | |
| D | ASC-J9 (50 µM) loaded MSNP-MEOH | | | ASC-J9 (25 µM) loaded MSNP-MEOH | | | | ASC-J9 (10 µM) loaded MSNP-MEOH | | | | |
| E | ASC-J9 (50 µM) loaded MSNP-ACE | | | ASC-J9 (25 µM) loaded MSNP-ACE | | | | ASC-J9 (10 µM) loaded MSNP-ACE | | | | |
| F | ASC-J9 (50 µM)&G3 loaded MSNP-MEOH | | | ASC-J9 (25 µM)&G3 loaded MSNP-MEOH | | | | ASC-J9 (10 µM)&G3 loaded MSNP-MEOH | | | | |
| G | ASC-J9 (50 µM)&G3 loaded MSNP-ACE | | | ASC-J9 (25 µM)&G3 loaded MSNP-ACE | | | | ASC-J9 (10 µM)&G3 loaded MSNP-ACE | | | | |
| H | Control | | | | | | | | | | | |

2.2.3.6 Uptake in 3D spheroids

In the domain of cancer therapy, investigating the activity of nanocarriers loaded with anticancer drug in 3D cultures provides a better understanding of the extent of tumour

penetration and drug activity in a 3D environment. Unlike the conventional 2D cellular monolayers, the 3D culture can give a better insight into drug-tumour and nanocarrier-tumour interactions due to its ability to mimic the complex heterogeneity of solid tumours in patients[314, 315].

The 3D spheroids were prepared by growing HCT-116 cells in ultra-low attachment 96 well plates at a seeding density of 8×10^3 cells per well for 48 hr. The spheroids were treated with 25 or 40 μM ASC-J9 solution or ASC-J9 loaded nanocarriers (lipid shell nanocarrier of magnetic silk nanoparticles MSNP) for 12 hr and then fixed with 3.7% formaldehyde and stained with Hoechst 33342 and imaged with the high content microscope. For the investigation of the impact of magnetic field on the uptake of MSNP in HCT-116 spheroids, a magnetic plate was placed under the cell culture plate for 30 min to drive the nanoparticles from the media toward the spheroids in the bottom of the wells (**Figure 2.4**). This magnetic force was used previously for drug and gene delivery to target tumor tissue or enhance transfection efficiency [257, 316].

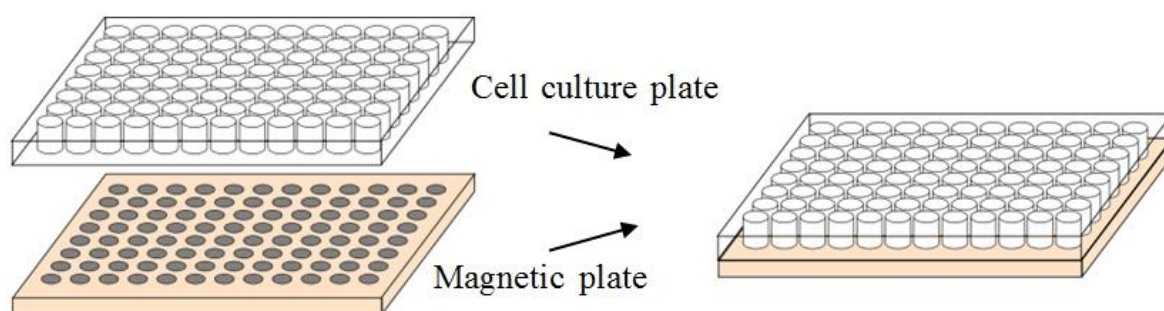


Figure 2. 4. Schematic representation of the testing process of magnetic silk nanoparticles (MSNP) under magnetic field [317].

2.2.3.7 Statistical analysis

The statistical analysis of the data was carried out using GraphPad Prism 7.04. The Student's t-test was used for comparison between two groups, and the one-way ANOVA was used for the comparison between multiple groups. All data were presented as the mean \pm standard error unless otherwise mentioned. Statistical significance was considered when the p value was less than 0.05.

2.3 Techniques and instrumental principles

2.3.1 Dynamic light scattering (DLS)

DLS is one of the earliest and the most common technique to characterise the particle size and zeta potential for nanostructures. DLS is a physical technique that can measure hydrodynamic quantities, translational and/or rotational diffusion coefficients. Combining these measurements allows for determining sizes of the measured nanostructures via theoretical relations [318, 319]. The DLS equipped with a laser source which generates monochromatic light passes through the sample cuvette (**Figure 2.5**). When the light encounters particles, it scatters in multiple directions and the scattering intensity fluctuates due to Brownian motion of the particles [320]. The relatively large particles tend to have slower Brownian motion in comparison to smaller particles [319]. The scattered light was measured by a photon detector which can identify the intensity fluctuation and correlate it to the particle size (**Figure 2.5**). For perfectly monodisperse sample, the algorithms that analyse the data should produce identical results. However, most of the tested samples are unlikely to be perfectly monodisperse and hence, the collected results from these algorithms tend to differ. The polydispersity (PDI) reflects the scattered light by various fractions of particles with various sizes and is calculated by $(\text{width}/\text{mean})^2$ for every individual peak [320]. PDI values smaller than 0.1 is considered as monodisperse and (0.1-0.4) are moderately polydisperse while values larger than 0.4 are considered as highly polydisperse [320]. The zeta potential of nanocarriers and SF nanoparticles was also measured using DLS using Zeta Pals function. Zeta potential, also known as electrokinetics potential, is the potential difference between electric double layer (EDL) of electrophoretically moving particles and the layer of dispersant around them at the slipping plane (**Figure 2.5**) [320, 321]. To measure zeta potential, an electric field is applied by the instrument electrode to induce the electrophoretic mobility of the tested particles. The particles mobility generates different frequencies of the scattered light from the laser source. The DLS detector can correlate the frequency shift to the particles speed and measure the zeta potential through theoretical relations [320].

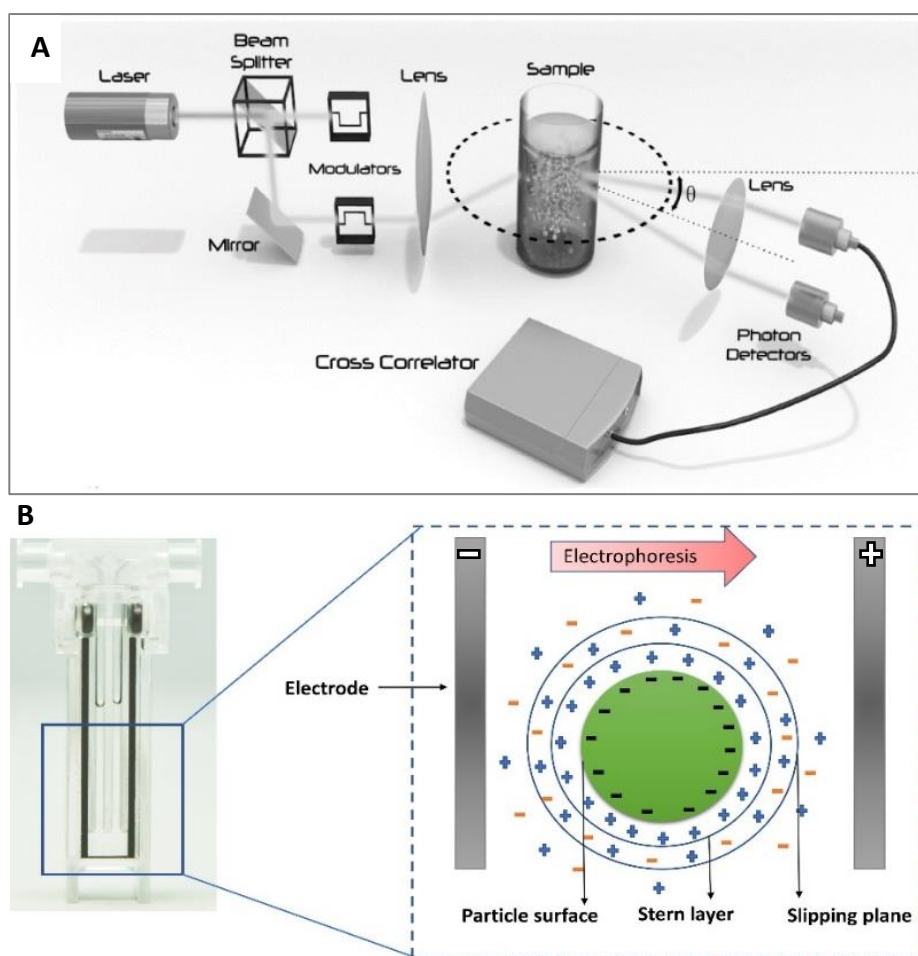


Figure 2. 5. A) Schematic representation of the dynamic light scattering (DLS) instrument. Reprinted from [322]. **B)** Schematic representation of the layers surrounding the surface of negatively charged particles during Zeta potential measurement.

2.3.2 Nanoparticle tracking analysis (NTA)

Nanoparticle tracking analysis (NTA) was first introduced in 2006 as an innovative system for measuring the nanoparticle size (30 to 1000 nm) and size distributions [323]. This technique enjoys a lower detection limit that is dependent on the reflective index of the nanoparticles. Unlike DLS, NTA records the light scattering from the laser source using a microscope equipped with a (CCD) camera (**Figure 2.6**). The basic principle of NAT is illustrated in **Figure 2.6**, where the laser beam passes through the sample chamber at a low angle causing illumination of the nanoparticles in the sample suspension [324]. Using the NAT software, the mobility of nanoparticles can be recorded, and the Brownian motion of each recorded nanoparticles is tracked on a frame-by-frame basis. To ensure accuracy, nanoparticles that

are recorded for a small number of frames will be excluded. NAT software can relate the nanoparticle movement to particle size following the Stokes-Einstein equation (5).

$$(x, y)^2 = \frac{2KBT}{3\pi\eta r} \quad (5)$$

Where $(x, y)^2$ is the mean squared speed of a particle at temperature, T , in solvent viscosity, η , and hydrodynamic radius, r .

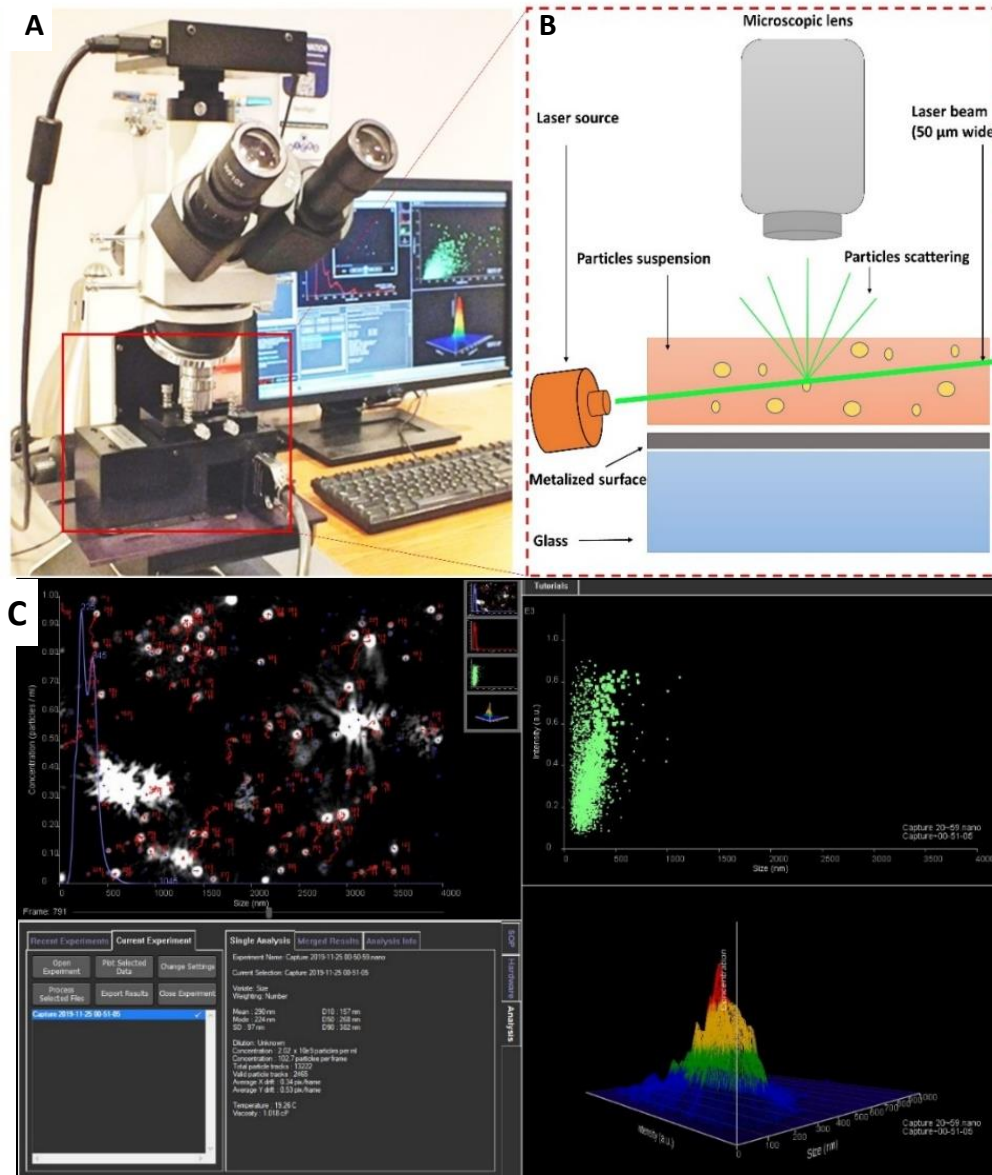


Figure 2. 6. A) Nanosight for nanoparticle tracking analysis (NTA). B) Schematic representation of the NTA instrument configuration. C) Nanoparticle Tracking Analysis software (NTA 3.1) using the scattered light in the recorded video for measuring the size distribution and determining the standard deviation SD.

2.3.3 Transmission electron microscopy (TEM)

Transmission electron microscope (TEM) is a very powerful technique for imaging a wide range of micro and nanostructures. TEM allows for analysing the size, shape and inner structure of nanomaterials, and it has been used for imaging the SF/SA nanocarriers and SF nanoparticles. The TEM in its current form was invented in 1986 by Ernst Ruska [325]. The principle of TEM relies on the ability of the electron beam to deflect and concentrate using electrostatic and magnetic fields. Similar to the light microscope, TEM collects a detailed image of the scanned sample. However, instead of detecting visible light (photons) from a light source, TEM uses an electron beam which has a much smaller wavelength to allow for higher magnification and more detailed information of the scanned sample [326]. To calculate the wavelength of the electron beam, Louis de Broglie derived an equation (6)

$$\lambda = \frac{h}{mv} \quad (6)$$

where h is Planck's constant, m is the mass of a particle, and v is the velocity of a particle. This equation showed that the electron beam accelerated by the energy of 60,000 volts would have a wavelength of 0.05 Å. TEM is equipped with an electron gun to launch the electron beam into free space, and condenser lenses are used to generate a focused thin beam (**Figure 2.7**). The most important part of the TEM is the lens system (Ruska's design), which can create an extremely short focal length by concentrating the magnetic field. TEM utilizes the lens system to collect electrons upon the specimen and series of lenses (diffraction, intermediate, and projector) is employed to magnify the specimen image and reflect it on the fluorescent screen [325, 326]. The objective aperture is designed to restrict high angle diffracted electrons to provide better clarity and enhance the contrast of the collected image. The bright areas in the sample image correspond to a relatively high number of electrons transmitted. While the darker areas represent a denser material that restricts the electron transmission.

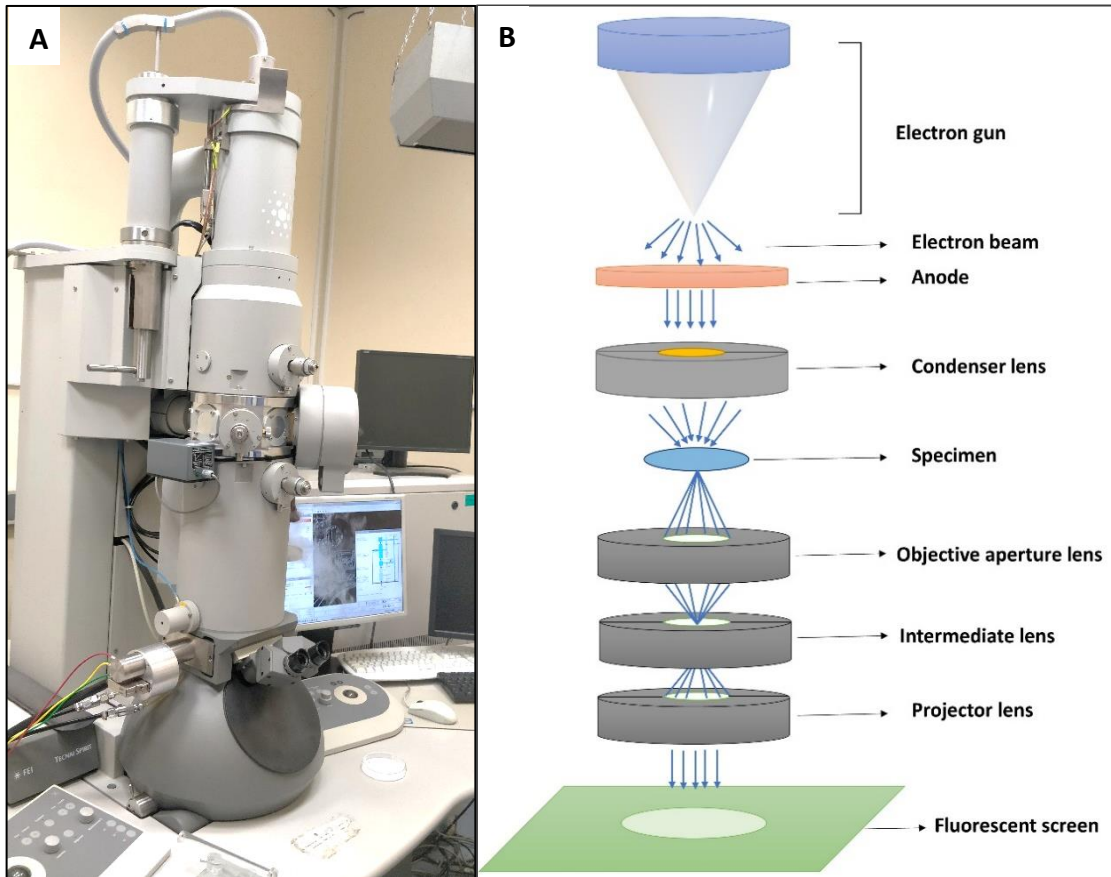


Figure 2. 7. A) Transmission electron microscopy (TEM), FEI Tecnai BioTWIN G2 sprint (USA) (the University of Sheffield). **B)** Schematic representation of the working principle of TEM.

2.3.4 Atomic force microscopy (AFM)

Atomic force microscopy (AFM) has evolved into one of the most advanced techniques for performing in-depth characterisation of nano and microstructures. AFM is capable of revealing the intramolecular forces at the nanoscale level with atomic resolution [327]. This allows for studying a wide range of synthetic materials, polymers and biomaterials. AFM has more capabilities than TEM, AFM provides further detailed information when scanning nanomaterials [328, 329]. In addition to sample imaging, AFM has been used extensively in the past two decades to characterize the mechanical properties, morphology and homogeneity of the tested material. AFM system has a micro-machined cantilever probe equipped with a tip which is mounted to a Piezoelectric (PZT) actuator (**Figure 2.8**) [327]. A laser beam is reflected off the cantilever and detected by a sensitive photon detector. During sample scanning, the tip moves over the sample surface at a constant force or constant height above the surface. The deflected laser beam determines the difference in the intensities

between upper and lower photon detector [327]. The acquired information from the cantilever tip corresponds to the force between the probe tip and the surface of the sample, and the force is related to the distance between the scanned sample and the tip following Hook's Law (equation 7)

$$F = -kx \quad (7)$$

where F is the force between the sample and the tip, k is the spring constant of the cantilever and x is the spring stretch or compression (the deflection of the cantilever) [330].

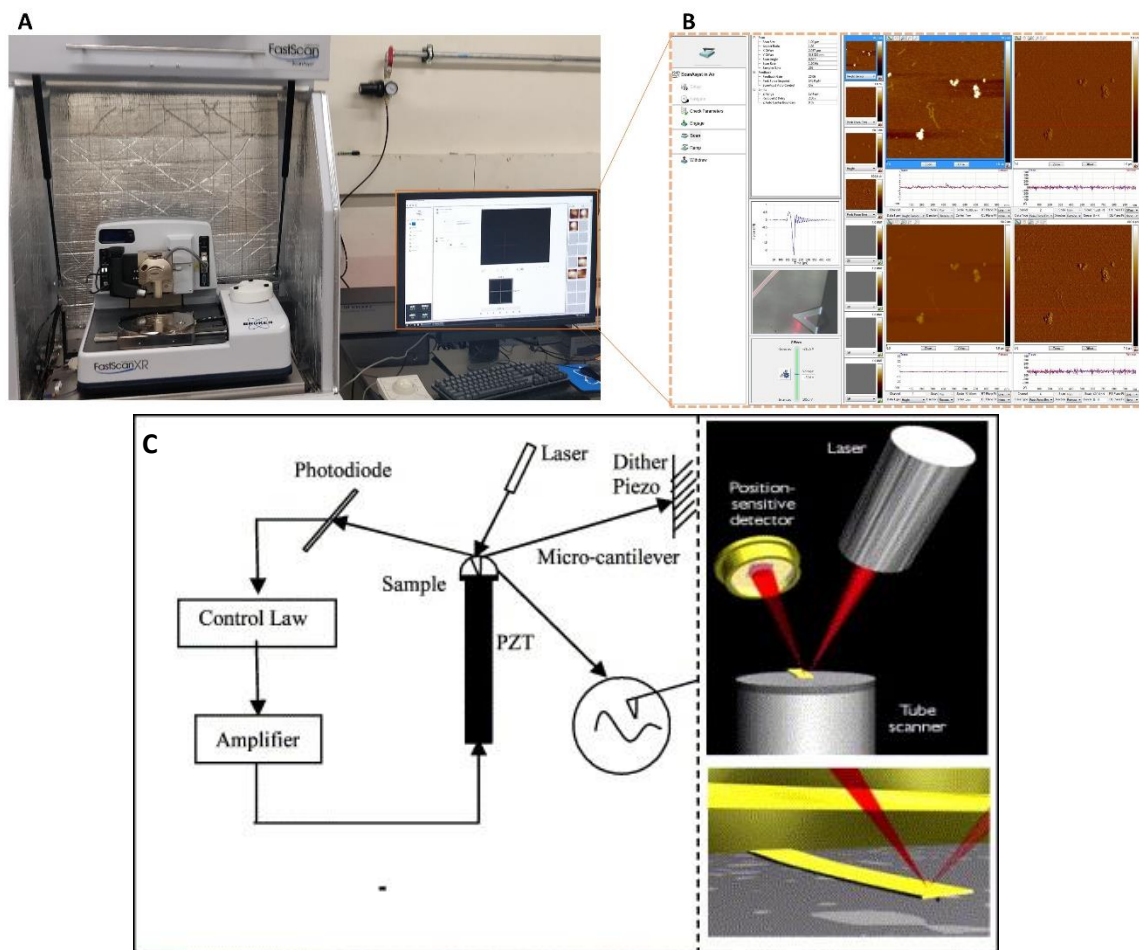


Figure 2. 8. A) Atomic Force Microscopy (AFM) Dimension FastScan with ScanAsyst, Bruker (University of Sheffield). **B)** SCANASYST-AIR in PeakForce and Tapping Mode operating software. **C)** Schematic representation of AFM basic principles (left), real micro-cantilever and components (right) Reprinted from [327] with permission from Elsevier.

The difference in the detected signal is recorded and analysed by a special AFM software which also assists in operating the instrument in different modes (**Figure 2.8**). In contact

mode, the tip will be in a close contact with the sample throughout the scan, leading to repulsive interaction forces (Van der Waals forces). In this mode, the surface profile can be acquired either by fixing the height (constant height) or the force between the tip and the sample (constant force). The main disadvantage in contact mode is the resulting shear force which can damage soft samples [327].

Tapping mode is the most frequently used mode in the AFM technology due to its ability to generate high-resolution images of relatively soft samples. Tapping mode avoids common problems such as friction and adhesion. Instead of constant contact with the sample, tapping mode applies a force on the cantilever tip to induce vibration. This vibration allows for the probe tip to touch the sample and lift off at a specific frequency. The energy losses occurred during intermittent contacting of the tip with the surface determines the surface topography of the sample [327, 330]. The collected samples can be deconvoluted by using a specific analysis software provided by the AFM manufacturer. In this study, NanoScope 1.5 (**Figure 2.9**) was used to obtain images of the tested samples in addition to size and morphology.

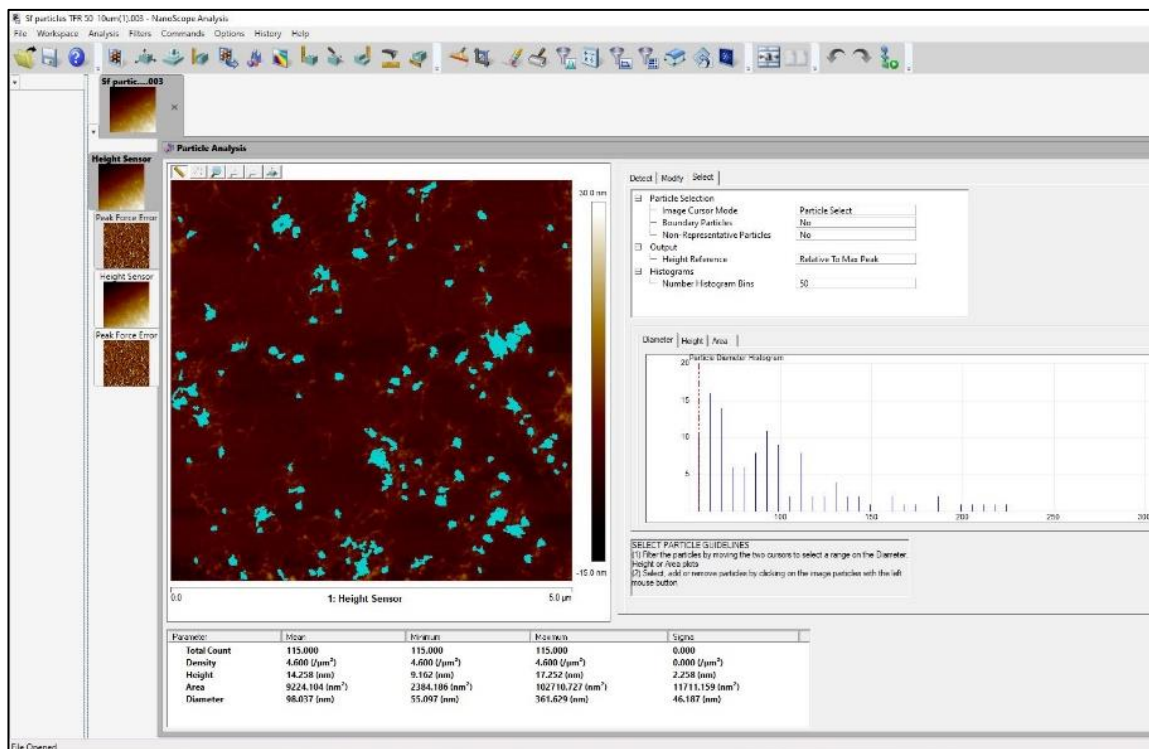


Figure 2. 9. AFM data analysis software (NanoScope 1.5) for measuring the size, shape and morphology of the scanned sample.

2.3.5 Fourier transform infrared (FTIR) spectroscopy

Fourier transform infrared (FTIR) is an analytical technique which can detect the infrared radiation (IR) absorbance of the dipole bonds within the functional group of the tested material. IR radiation can induce vibration (bending or stretching motion) of the molecular bonds by exciting the electrons within these bonds[331, 332]. Most compounds have a dipole moment except molecules such as N₂ and O₂, and therefore can be characterized qualitatively using FTIR[333, 334]. The structural information of the tested molecules can be obtained from the frequency and intensity of the peaks in the IR spectrum. As shown in **Figure 2.10** the principle of FTIR relies on utilizing the interference between two IR beams to generate a signal known as interferogram using a Michelson interferometer. This signal is degraded later into frequencies using Fourier Transform algorithms[335]. Michelson interferometer consists of IR source, a semi-reflecting beamsplitter and two perpendicular mirrors. The IR beam is divided equally by the beamsplitter and reflected back to the beamsplitter by the two mirrors to recombine and interfere before reaching the detector (**Figure 2.10**). Depending on the path length determined by the moving mirror, this interference can be destructive or constructive[332, 334, 335]. FTIR reveal the absorbance of unknown sample by converting the optical path length into wavenumbers and the sample and the light intensity into transmittance.

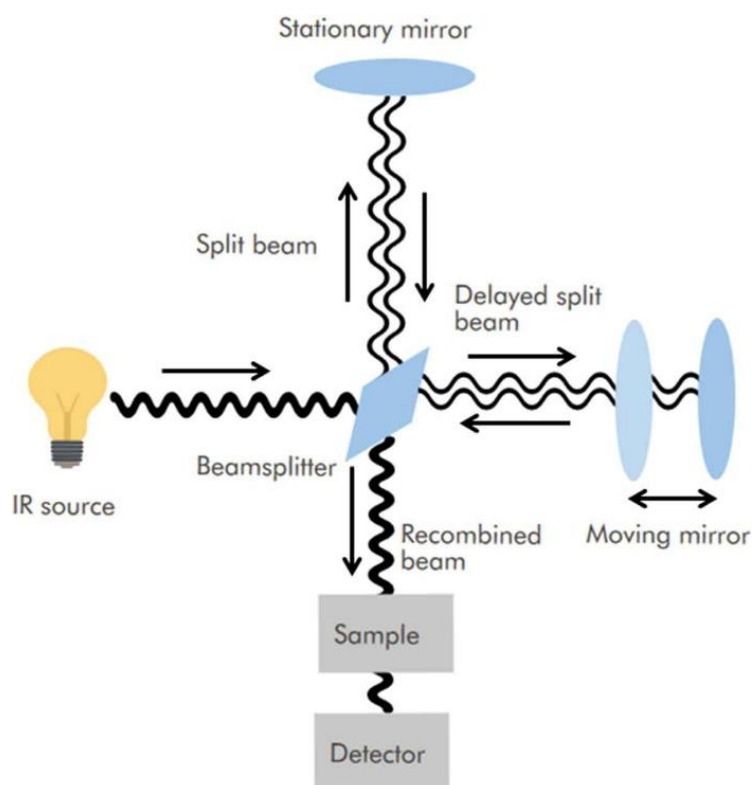


Figure 2. 10. Schematic representation of the principle of a Michelson interferometer. Reprinted from [336] with permission from Taylor & Francis.

2.3.6 High content fluorescent imaging microscope

The high content fluorescent automated widefield microscope (ImageXpress® Micro System) shown in **Figure 2.11** was used to acquire fluorescent images of 96 well plates of HTC 116 cells incubated with drug-loaded nanocarriers solutions. Three channels were used (DAPI, Texas red & GFP) to identify the cells' nucleus, cytoplasm, and ASC-J9 (location and intensity). The images were then analysed using MetaXpress® software 5.3.01 (Molecular Devices) to obtain, the cell population, drug fluorescent intensity and drug relative uptake. Using custom module function in MetaXpress®, it was possible to design an algorithm to quantify the cell population by selecting the approximate size and shape of HCT 116 nucleus as the target object (**Figure 2.11**). Similarly, the drug fluorescent intensity in 3D spheroids was analysed by designing an optimized algorithm.

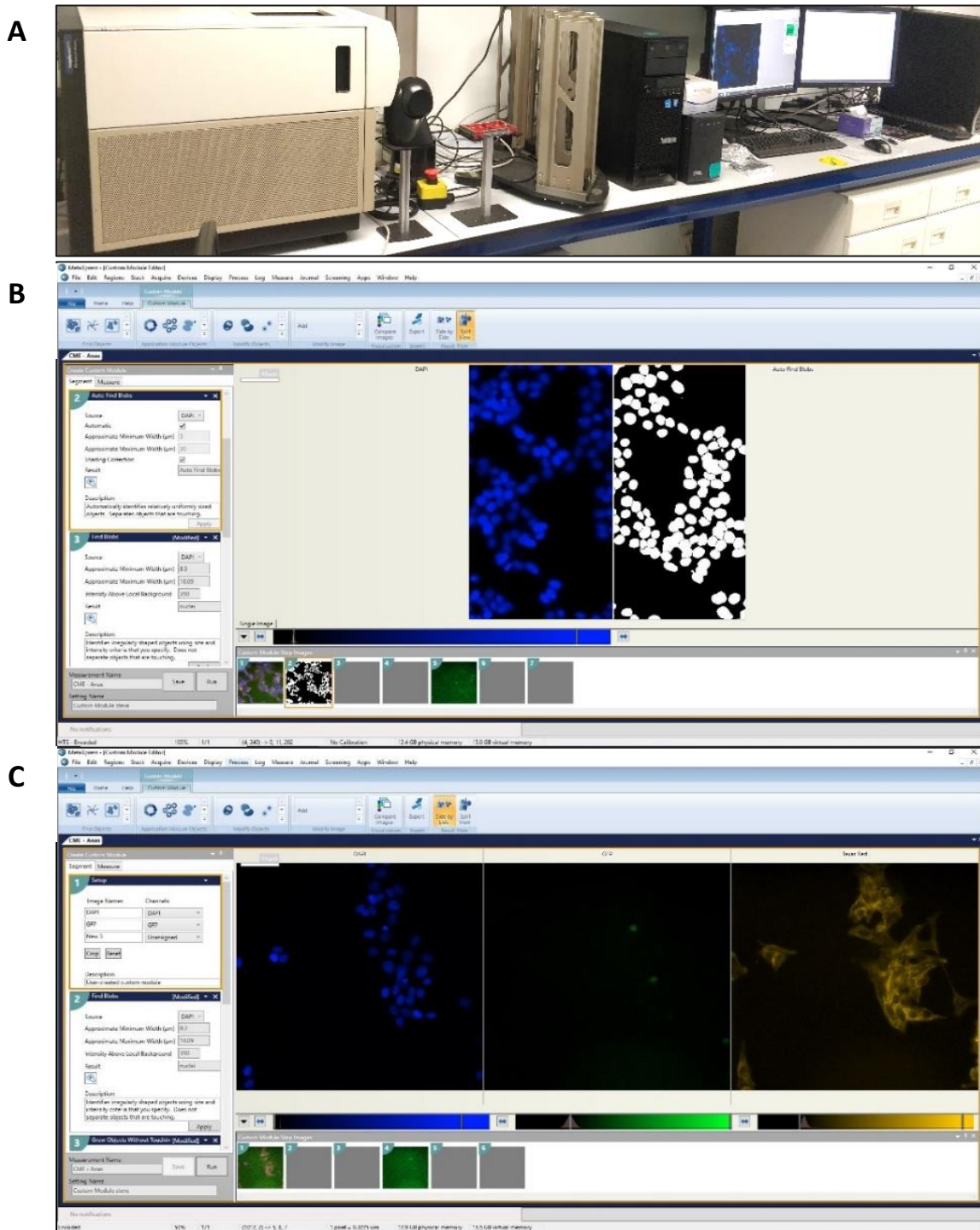


Figure 2. 11. A) ImageXpress® Micro System. B) MetaXpress® software 5.3.01 using custom module tool to design an algorithm that can find nucleus of HCT 116 cells and determine cellular population. C) MetaXpress® software 5.3.01 using custom module tool to analyse three different channels (DAPI, GFP & Texas red) to identify nucleus, drug & cytoplasm of HCT 116 cells.

3 Chapter 3: Stiffness-tuneable nanocarriers for controlled delivery of ASC-J9 into colorectal cancer cells

Abstract

Development of highly efficient and non-toxic drug delivery systems for hydrophobic anticancer drugs is one of the main challenges in cancer therapy. The poor water solubility of these drugs often leads to low bioavailability and low concentrations in the tumour tissue. Although various types of polymer-based drug delivery systems have been developed for such purpose, they often suffer from low encapsulation efficiency, uncontrolled release and lack of long-term stability. Herein, we report the development of a novel core-shell nanocarrier system with tunable stiffness and controlled release for the delivery of hydrophobic anticancer agent ASC-J9. The nanocarriers were prepared from two naturally derived biocompatible polymers silk fibroin (SF) and sodium alginate (SA) using a simple method which does not require any organic solvents, excessive heat or changes to pH. The synthesized nanocarriers had a high encapsulation efficiency (62-78%) and were physically stable for up to 5 months at 4 °C. The stiffness of the nanocarriers dictated the release profile of the drug which was easily tunable by changing the ratio of SF to SA in the core. Loading ASC-J9 into the designed nanocarriers enhanced its cellular uptake and its anticancer activity in HCT-116 colorectal cancer cells as well as 3D tumour spheroids. Hence, the designed nanocarriers could be considered as a highly efficient drug delivery system for enhanced bioavailability and controlled release of hydrophobic anticancer drugs.

Keywords: *nanocarrier; silk fibroin; stiffness tunable; controlled release; hydrophobic anticancer drug; ASC-J9.*

3.1 Introduction

One of the main obstacles to overcome in cancer therapy is designing non-toxic and biodegradable carriers for safe and efficient anticancer drug delivery. Recent advances in nanotechnology and polymer engineering have opened doors to new more efficient approaches to cancer therapy using nano-formulations [6]. However, the inherent low solubility of many anticancer agents in water and biological fluids complicates their formulation process and hinders their clinical application [337]. Moreover, the low local

concentration of these drugs in the tumour tissue due to insufficient diffusion and/or short elimination half-life ($t_{1/2}$) may result in multidrug resistance (MDR) which is one of the major challenges in cancer treatment especially in the case of metastatic cancers such as breast and colon cancers [338-340]. For example, $t_{1/2}$ of the hydrophobic anticancer agent ASC-J9 was found to be less than 6 hrs following an intravenous injection in mouse, which reduces the bioactivity in certain tissues [13]. Increasing the exposure time of ASC-J9 to the cancer cells reduces the half-maximal inhibitory concentration (IC_{50}) values due to cumulative cytotoxic effect [94]. Therefore, development of novel drug delivery systems for efficient loading enhanced aqueous solubility, and improved cellular uptake of hydrophobic anticancer agents within the elimination time window has received more attention over the past decade [49, 96, 341].

In order to design effective nano-carriers, several factors must be taken into consideration such as size, geometric shape, elasticity, and surface charge [7, 42, 342-344]. Recently, nanoformulations, such as liposomes [19, 22], micelles [344], polymer conjugates, and polymeric nanoparticles [96], have been prepared to function as vectors for many hydrophobic anticancer agents showing great potential for delivering these agents to the target cells. Although engineered nanoparticles with optimized size and shape can improve drug delivery, they still lack efficient targeting and their accumulation in the tumour tissue is limited to less than 1% [44]. Other limitations of the conventional nano-carriers include low encapsulation efficiency (EE), uncontrolled release, “initial burst effect” (rapid release of the loaded drug within the first few minutes) and lack of long-term stability [344-346]. Most of the currently available literature has focused on improving the properties of the nanoparticles and nanoliposomes through modifying their surface or their outer shell respectively [19, 347] and only few recent studies have investigated the impact of modifying the physical characteristics of the particle core on their properties such as EE, release profile, and cellular uptake. In the present work, we present novel nanocarriers with tuneable physical properties through incorporation of a combination of silk fibroin (SF) and sodium alginate (SA). Unlike the previous studies, the focus is on modification of the physical properties of the core in order to enhance the EE, improve the cellular uptake and achieve controlled drug release.

Silk fibroin (SF) is an FDA approved naturally derived biopolymer obtained from cocoons of *bombyx mori* silkworm which exhibits unique features such as biocompatibility,

biodegradability, and the ability to enhance the stability of the loaded drug [33, 145, 348]. SF can undergo diverse structural transformations at the molecular level. The most studied transformation is the shift in the ratio of α -helix to β -sheet [144]. This transformation results in insolubilizing SF to form micro and nanoformulations that can be employed for drug and gene delivery [33]. Furthermore, SF can be easily processed by various techniques to prepare a variety of micro and nanostructures including sponges, microspheres, nanogels, and nanoparticles for biomedical applications [128]. The physical properties of silk can be improved by blending it with other polymers. A recent study by De Moraes et al. [203] have reported modified physical characteristics of SF when blended with polysaccharides such as sodium alginate (SA) [203]. SF/SA blends have almost no toxicity, high miscibility, less heterogeneity and restricted phase separation due to the interaction between SA carboxyl groups and SF amino groups [203]. Furthermore, mixing SA with SF allows SF to shift to β -sheet predominant form (Silk II) which can provide a platform for loading poorly water-soluble compounds through hydrophobic interactions [33, 203]. Therefore, the combination of SF and SA has been selected in this study to form the core of the nanocarriers. This combination of polymers also allows for controlling the elasticity of the nanocarriers.

Particle elasticity hypothesis has drawn increasing attention in the field of nanomedicine in the past few years [349]. Modifying the rigidity of the nanoparticles can alter their cellular uptake pathways (e.g. fusion and/or endocytosis), as well as other properties such as EE and drug release [7, 15, 302]. For example, Sun et al. [302] developed modified PLGA-lipid nanoparticles with different rigidity by altering the injection order of PLGA and PEG-lipid solutions in the microfluidic system to vary the amounts of water in between the polymeric core and the lipid shell [302]. However, this method involves synthetic polymers and organic solvents which is not desirable for biomedical applications. In a more recent study conducted by Guo et al. [15] the elasticity of the crosslinked nanogel cores was altered by changing the crosslinker concentration [15]. In the present study, nanocarriers consisting of a lipid shell and a core composed of a combination of SF and SA have been developed using a simple procedure that does not require any organic solvents, synthetic polymers or high concentrations of the crosslinkers, and used for delivery of highly hydrophobic anticancer agent ASC-J9 to HCT-116 colorectal adenocarcinoma cells. ASC-J9 has been used for the treatment of different types of cancer including the prostate cancer and breast cancer due to

its ability to enhance the degradation of androgen receptors (AR) and increase the downstream apoptotic markers [94, 96]. However, there are no reports of the use of ASC-J9 for treatment of colorectal cancer. The stiffness of the designed nanocarriers was simply tuned by changing the ratio between SF and SA. To the best of our knowledge, using the combination of SF and SA for tuning the stiffness of the nanocarriers, regulating their cellular uptake and drug release has not been reported elsewhere.

3.2 Results & Discussion

Due to its strong activity to cancer cells, curcumin has been one of the most studied natural compounds for cancer therapy [30]. Recently, curcumin analogues with higher anticancer efficacy such as ASC-J9 have been developed through structural modifications such as methylation [30, 31]. Nonetheless, these structural changes have led to a tangible increase in the hydrophobicity of the resulting drug molecules [32]. ASC-J9 increases the downstream apoptotic markers to a higher extent compared to curcumin which results in enhanced anticancer activity [7]. On the other hand, ASC-J9 is more hydrophobic than curcumin, and has relatively short elimination time ($t_{1/2} < 6$ hrs) which can limit its anticancer activity in the tumour tissue [6]. The present work was aimed at developing nanocarriers (**Figure 3.1**) with tuneable properties for enhanced loading, improved aqueous solubility and enhanced cellular uptake of ASC-J9 before it is cleared from the body.

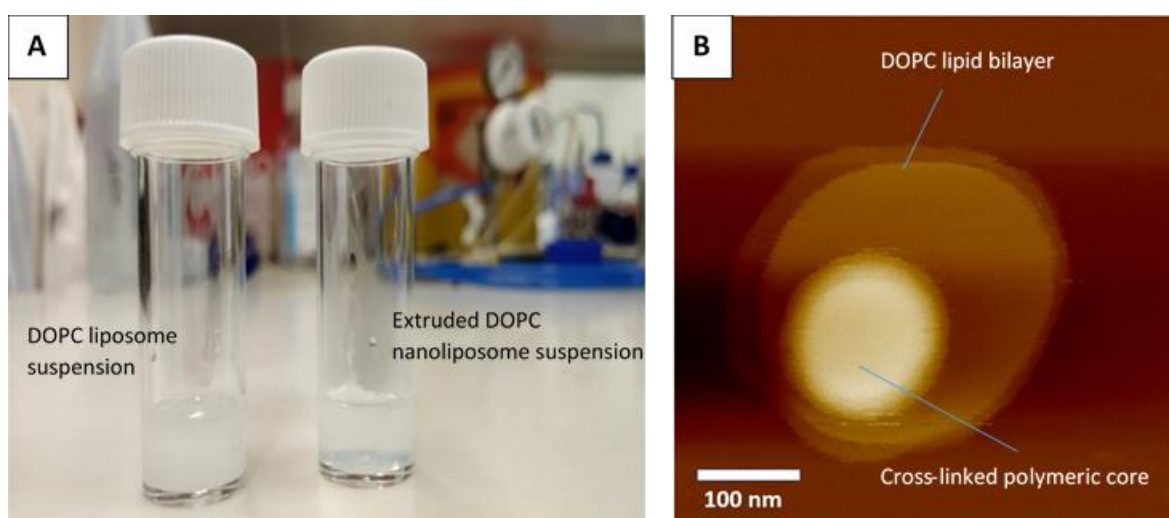


Figure 3. 1.. A) DOPC liposome suspension before and after 200 membrane extrusion. B) AFM image of a DOPC liposome after extrusion entrapping crosslinked Sodium alginate (SA).

3.2.1 Physical characterization of the ASC-J9 nanocarriers

The designed nanocarriers consist of a lipid bilayer shell and a biopolymeric core which serves as a vector for ASC-J9. After extrusion through the polycarbonate membrane, the liposomal suspension becomes more transparent and less turbid due to the difference in the light scatter between the heterogenous liposomes and the extruded homogeneous liposomes (**Figure 3.1**). Crosslinking SA with calcium within the core transforms the core into a hydrogel. The rigidity of the resulting hydrogel core is modulated by blending SA with SF which alters the amount of the SA monomers required to make the hydrogel network (**Figure 3.2.A**). The DOPC lipid shell provides a template for controlling the overall size of the nanocarriers via extrusion method [33]. This shell maintains the size of the nanocarrier in the aqueous phase as shown in **Figure 3.4.A**. The DLS characterization showed a similar hydrodynamic diameter of ~170 nm for all three formulations. The zeta potential was slightly negative in the nanocarrier formulation SF:SA (3:7). However, the zeta potential became more negative when the ratio of SF to SA was increased in the nanocarrier formulation (**Figure 3.4.C**). SF is negatively charged protein and therefore increasing the ratio of SF to SA allows more SF molecules to incorporate in the lipid shell and alters its charge. The three nanocarrier formulations demonstrate size stability for up to 5 months when stored at 4 °C (**Figure 3.4.F**). After 6 months, significant variation in the size of the nanocarriers was observed in the SF:SA (7:3) formulation which is supposed to be due to aggregation.

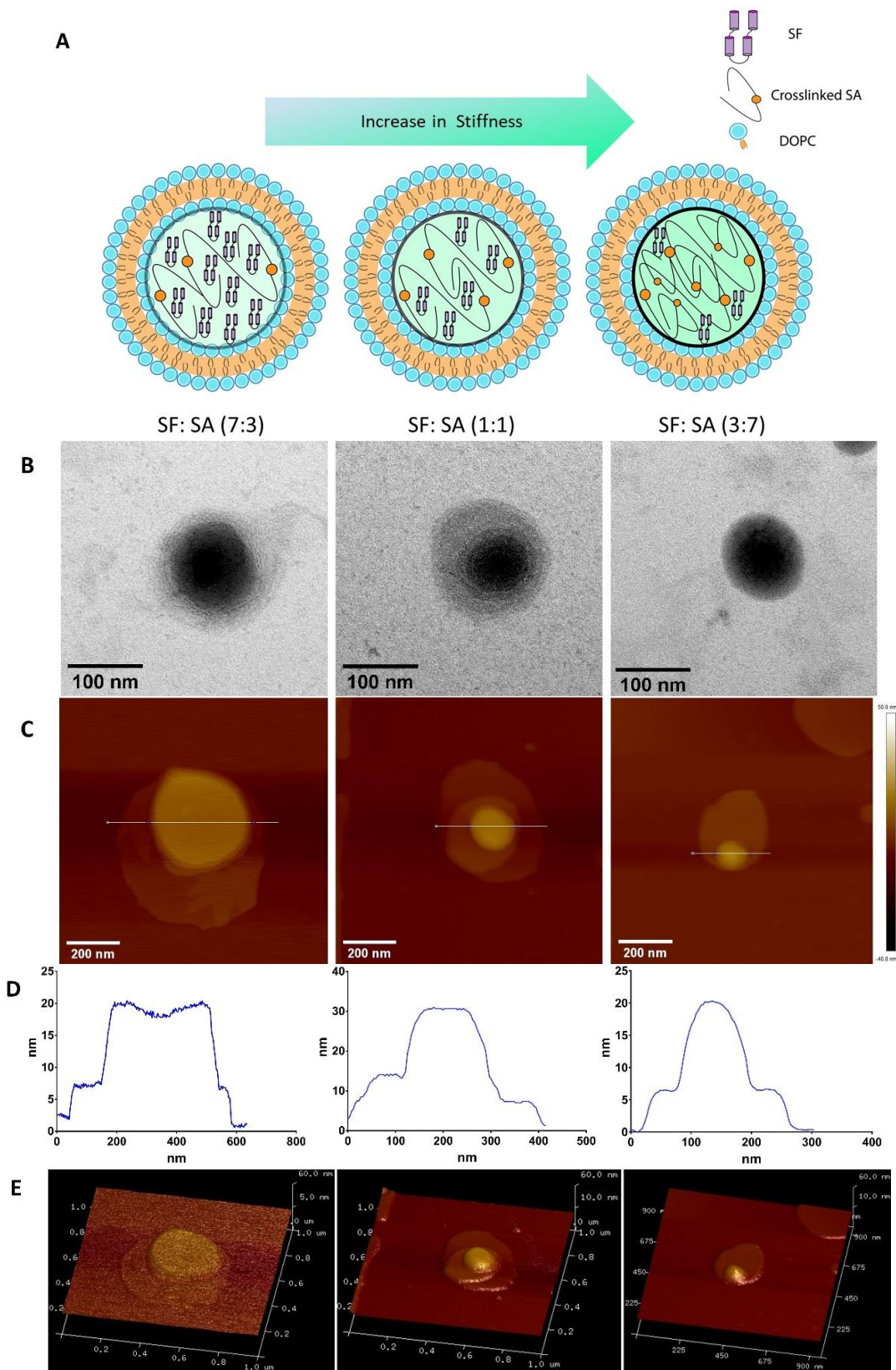


Figure 3. 2. (A) Schematic representation of the three synthesized nanocarriers entrapping different ratios of silk fibroin (SF) to sodium alginate (SA). (B) TEM images of the synthesized nanocarriers. (C) AFM images of the nanocarriers showing the polymeric core and the lipid

shell in dry mode. (D) Height profiles of the nanocarriers obtained by AFM. (E) 3D AFM images of the nanocarriers.

The nanocarrier cores were made of multiphase blends of SF and SA which can exhibit different morphological states. Typically, dispersing one polymer in the matrix of another causes changes in the properties of the mixture, and these changes are mainly controlled by the matrix properties [34]. TEM and AFM were used to provide a clearer insight into the interior structure of the nanocarriers. As shown in **Figure 3.2**, spherical nanocarriers were formed in the three formulations. The dense hydrogel core appears darker than lipid bilayer in the TEM image (**Figure 3.2.B**). The AFM scanning was carried out to determine the morphology of the nanocarriers. The stiffness of the cores correlates to the ratio of SA to SF in the nanocarrier formulation. The AFM scans revealed that the formulation with low SA to SF ratio (low stiffness) has an increase in the core size in comparison to the formulation with high SA to SF ratio when scanned in the dry mode (**Figure 3.2.C & Figure 3.4.B**). This can be explained by higher core deformation during scanning due to less SA hydrogel network which maintains the structure of the core. The height profiles obtained by AFM show an increase in the surface roughness of the core structure by increasing the SF to SA ratio (**Figure 3.2.D**). On the other hand, high SA content provides a smooth core surface because of forming a tighter hydrogel network. The Young's modulus was measured using AFM in liquid mode (**Figure 3.6 & 3.7**). The stiffness of the prepared formulations of the nanocarrier was quantified by applying Hertz model (**Equation 5**) using the values obtained from the force curves (**Figure 3.6**). The calculated Young's modulus increased by increasing the amount of sodium alginate (SA) in the formulation (**Figure 3.7**). The maximum acquired Young's modulus is 43.7 MPa, which is higher than previously reported nanolipogels entrapping SA only [15]. These results indicate that a larger stiffness range can be obtained by using a combination of biopolymers in the nanocarrier formulation. Unlike conventional approach which modifies nanocarrier stiffness by changing the crosslinker concentration, the approach used in this study allows for adjusting the stiffness by adding another polymer (SF protein) which also increases the β -sheet percentage, modifies zeta potential and nanocarrier enzymatic degradation in the biological environment [313, 350].

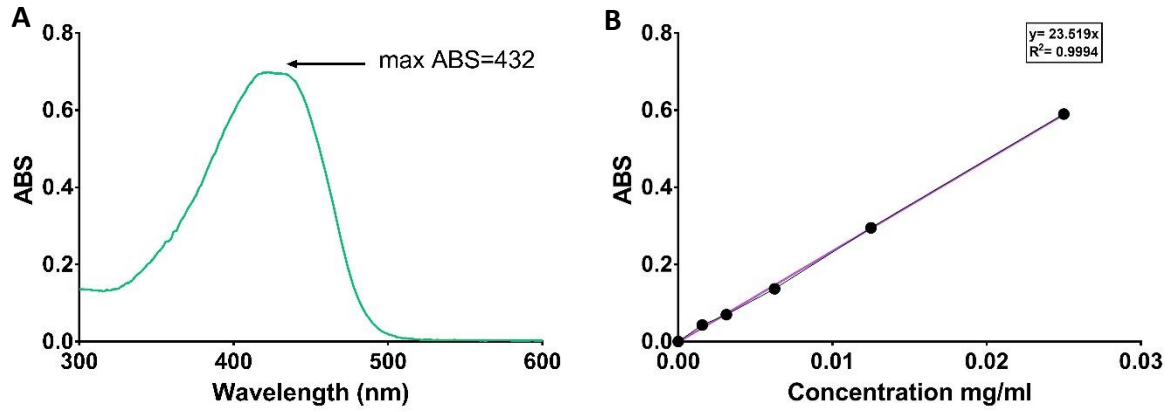


Figure 3.3. (A) The maximum absorbance of ASC-J9 using UV spectroscopy. (B) ASC-J9 calibration curve in PBS.

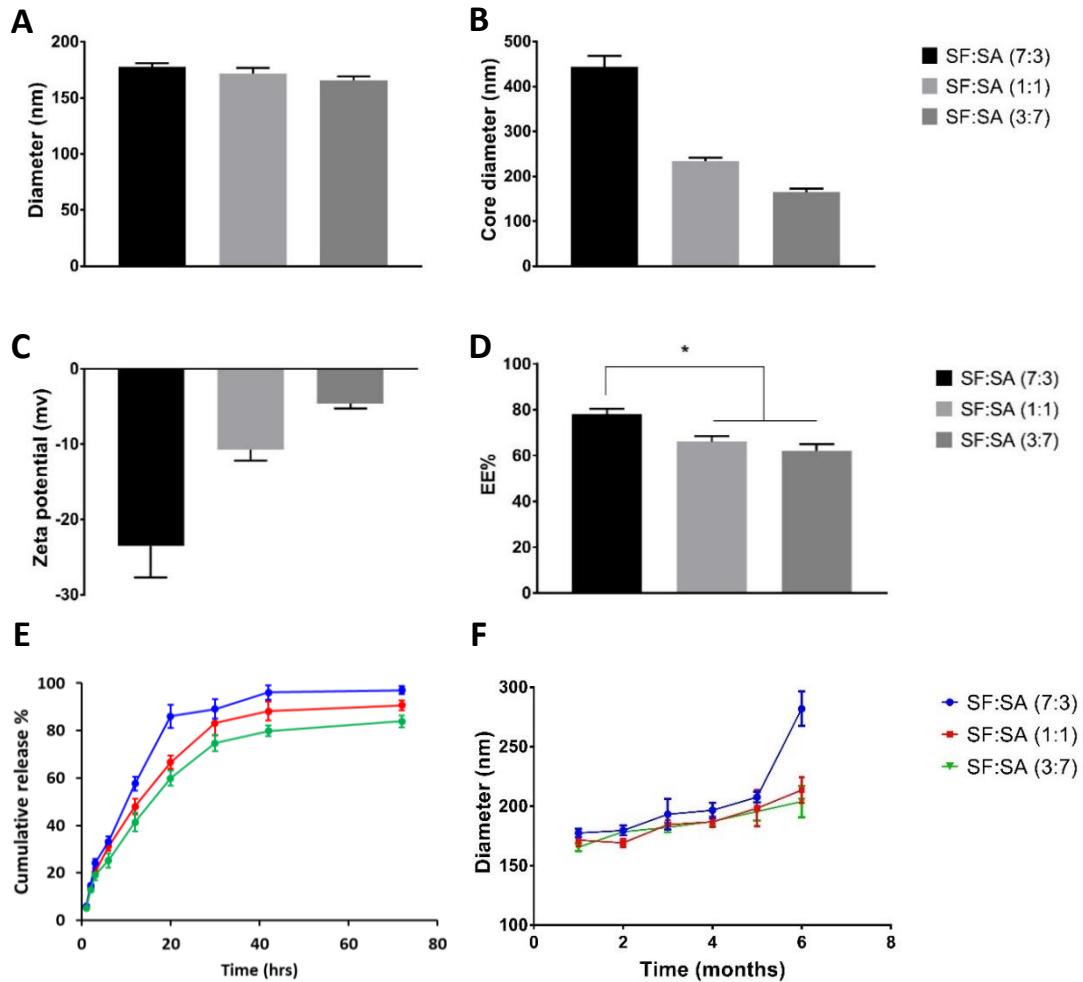


Figure 3.4. Characterization of the synthesized nanocarrier formulations with varying properties. (A) the particle size of the nanocarriers measured by dynamic light scattering. (B) The core size of the nanocarriers obtained by AFM scans in dry mode. (C) zeta potential of the

*nanocarriers measured by dynamic light scattering. (D) Encapsulation efficiency (EE) of ASC-J9 in different nanocarrier formulations. (E) Release profiles of ASC-J9 encapsulated in different nanocarrier formulations. (F) Changes to the diameters of nanocarriers over 6 months measured by dynamic light scattering. * Denotes values of $P < 0.05$.*

FTIR spectroscopy has been a useful technique to investigate the transformation of SF to β -sheet predominant SF. The main absorption peaks for unprocessed SF and SF blends in the nanocarrier formulations are presented in **Figure 3.5**. The FTIR spectrum of unprocessed SF shows the absorption bands assigned to amide I (1616.2 cm^{-1}) and II (1508.2 cm^{-1}) that correspond to β -sheet predominant (silk II) [27]. Amide III absorption band (1228.5 cm^{-1}) corresponds to silk I conformation with α -helix predominance. The nanocarrier formulations containing blends of SF and SA (7:3, 1:1 & 3:7) present spectra similar to the unprocessed SF with additional absorption bands that are assigned to the C=O, O-H, and C-O stretching in the SA structure [27, 35]. SF amide I and III absorption bands are overlapping with structural groups of SA; therefore, the amide II band was used to analyse the spectra and detect the transformation to silk II. As illustrated in **Figure 3.5**, the amide II band clearly shifted to higher wavelength and was detected at 1528.2 cm^{-1} indicating silk II conformation.

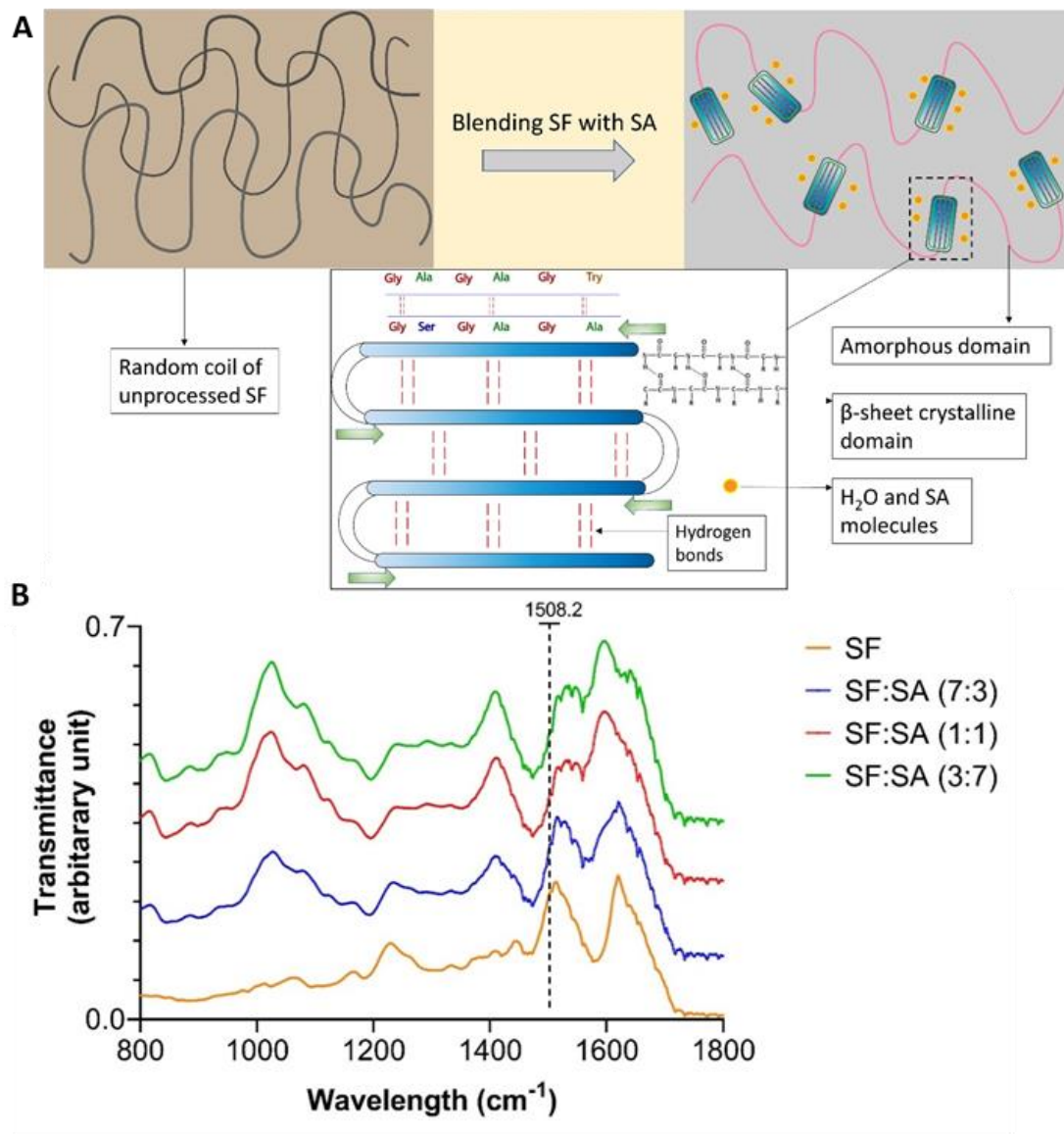


Figure 3. 5. (A) Schematic representation of silk fibroin (SF) structural transformation in the designed nanocarriers as a result of blending with sodium alginate (SA). (B) FTIR spectra of SF and SF/SA blend with a different ratio in the nanocarrier core

3.2.2 ASC-J9 encapsulation and release

Drug encapsulation efficiency (EE) is one of the most important features for determining the effectiveness of the designed delivery system as drug carrier especially in nanoformulations [20]. To calculate the ASC-J9 EE, the maximum absorbance was measured, and a calibration curve was produced (**Figure 3.3**). For efficient entrapment of ASC-J9 in the polymeric core matrix, the drug and the crosslinking agent (CaCl₂) were added simultaneously. The drug molecule enters the matrix with calcium ions that are transforming the structure of SA to form

the hydrogel network. Changing the nature of the core from liquid state to polysaccharide hydrogel during crosslinking can restrict the Brownian motion of the ASC-J9 molecules and enhance their retention in the nanocarrier. A previous study has shown a significant increase in the encapsulation efficiency as a result of hydrogel network formation. However, no significant change in EEs was observed in different hydrogel stiffness when one polymer was used [28]. In the current study, two polymers have been used (SF & SA) and the interaction between the two during crosslinking allows SF to transform to β sheet providing a platform for hydrophobic interaction with ASC-J9 molecules. This can explain the higher EE observed in high SF content nanocarrier formulation (SF:SA=7:3) in comparison to the formulation with lower SF content (SF:SA=1:1, 3:7) (**Figure 3.4.D**).

The effect of modifying the nanocarrier stiffness on the drug release kinetics was also investigated. The nanocarrier formulation with higher stiffness (higher young's modulus) exhibited slower drug release (**Figure 3.4.E**). The high percentage of SA results in a tighter hydrogel network and smaller pore size (**Figure 3.2.D**) which consequently results in higher retention and slower release of the encapsulated drug (**Figure 3.4.E**). These results suggest enhanced EE and tunable drug release.

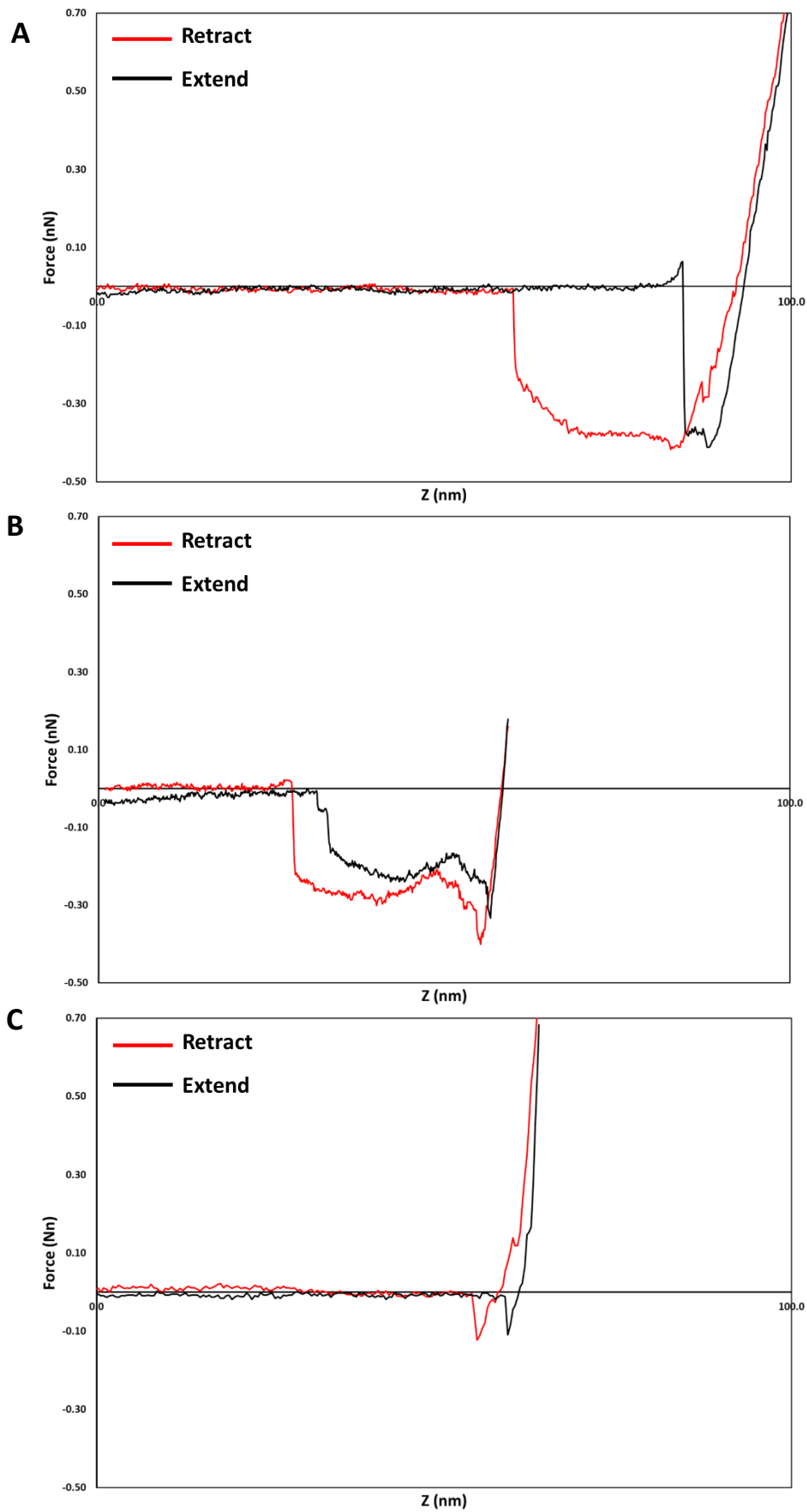


Figure 3. 6. Representative force curves for extend and retract processes with a single nanocarrier formulation. (A) SF:SA (3:7). (B) SF:SA (1:1). (C) SF:SA (7:3).

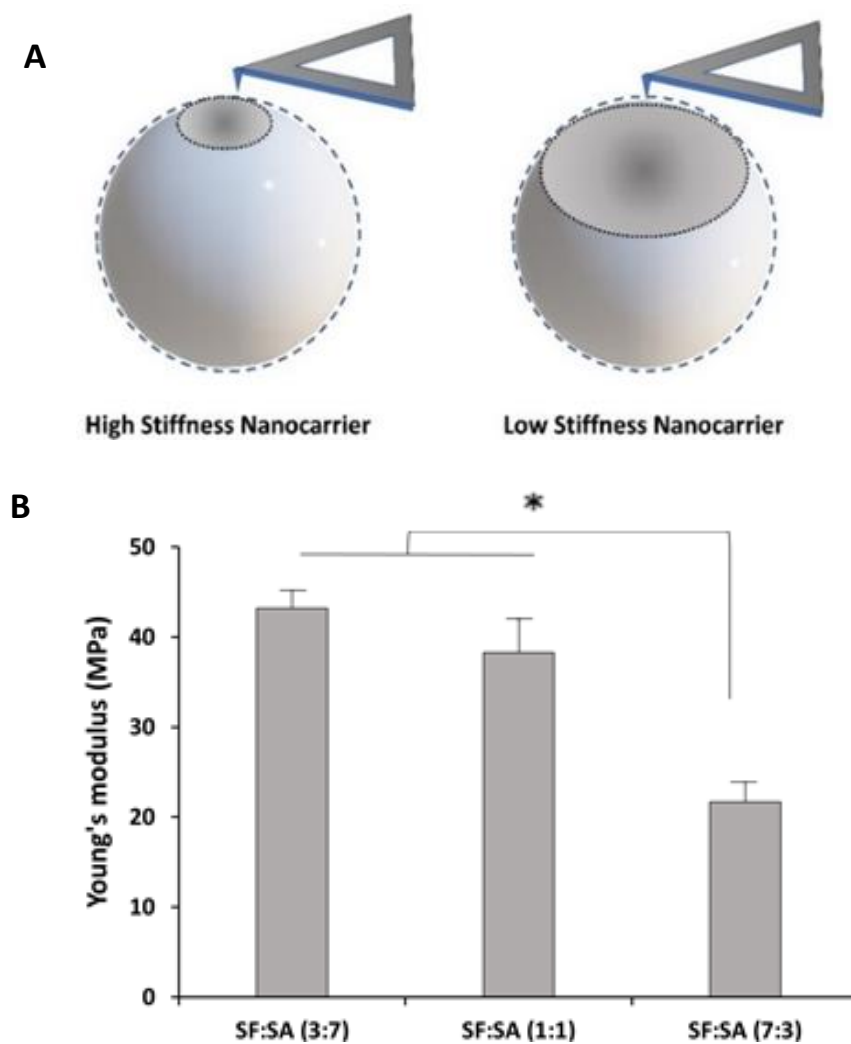


Figure 3. 7. Characterization of the synthesized nanocarrier formulations by force mapping mode of the AFM **(A)** Schematic illustration of high and low stiffness nanocarriers during Young's moduli measurements. **(B)** The Young's moduli of the nanocarriers characterized in liquid mode by AFM calculated using Hertz model. * Denotes values of $P < 0.05$.

3.2.3 *In vitro* cellular uptake study

The designed nanocarriers consist of a combination of biopolymers that are individually approved by FDA for pharmaceutical applications and regarded as biocompatible, nonimmunogenic, and nontoxic polymers [33, 351]. To confirm the lack of toxicity of the unloaded nanocarrier formulations, the cell population was evaluated after treatment with unloaded (SF:SA=7:3, 1:1 & 3:7) (**Figure 3.9.D**). The reduction in the cell population ranged between 1-11% indicating very low toxicity.

To investigate the internalization of the nanocarriers and their payload release in HCT-116 colorectal adenocarcinoma cells, the cells were treated with ASC-J9 (25 μ M) or ASC-J9 loaded nanocarriers for 6 hrs to simulate the drug availability time *in vivo* before elimination. The quantitative cellular uptake study was carried out in two conditions (10% FBS & 0% FBS) to mimic different *in vivo* physiological conditions. The treatments were removed after 6 hrs by replacing the media to ensure that the intensity measurements are assigned only to the uptaken drug. Like curcumin, ASC-J9 molecule is auto-fluorescent (λ_{exc} = 432 nm; λ_{emi} = 522 nm) and this property has been used previously for cell tracking and measuring cellular uptake [49, 96, 352]. The enhanced cellular uptake by HCT-116 is evident from the high content images presented in **Figure 3.8**. A weaker fluorescent signal was observed in cells treated with unprocessed ASC-J9 in comparison to ASC-J9 loaded nanocarriers. As it could be observed in **Figure 3.9** the relative uptake of the ASC-J9 was significantly enhanced when it was loaded into the different nanocarrier formulations. Moreover, the ASC-J9-loaded nanocarriers remained in the cells for up to 72 hrs after internalization serving as a reservoir for the drug and providing sustained drug release whereas the amount of free ASC-J9 within the cells showed a reduction after 72 hrs. This is supposed to be due to cellular efflux mediated by transporters such as P-glycoprotein [340].

The anticancer activity of the drug was assessed by measuring the percentage of cells within a population that survived treatment with the free drug and the drug-loaded nanocarriers at different time points (**Figure 3.9.C**). The free ASC-J9 showed higher activity at 12 hrs than the drug-loaded into the nanocarriers, causing a 50-60% reduction in the number of cancer cells. However, due to the low concentration of the drug within the cells resulting from lower cellular uptake compared to the drug-loaded nanocarriers, the cells recovered from the drug treatment and restarted growing after 24 hrs. In the case of drug-loaded nanocarriers, on the other hand, the antiproliferative activity started more slowly but was maintained over a longer period of time (72 hrs) resulting in a considerable reduction in the cell population (**Figure 3.9.C**). A variation in the anticancer activity was observed among the three nanocarrier formulations at 12 hrs especially in the absence of FBS. However, all nanocarriers formulations showed similar pattern after 24 hrs. This behaviour can be explained by the different drug release trend exerted by different formulations. Overall, it can be conferred from these data that the anticancer activity of the ASC-J9 in HCT-116 cells was enhanced by

loading into the designed nanocarriers and that the sustained release of the drug from the nanocarriers resulted in a prolonged antiproliferative activity which prevented the cells from recovering.

3.2.4 Uptake in 3D tumour spheroids

3D tumour spheroids were used as a mimic of the tumours tissue in the human body. 3D cell cultures are very useful in cancer research as they can study the efficiency and activity of drug-loaded nanoformulation in tumour tissues, where the 2D cellular monolayers can't simulate the complex organisation and heterogeneity of solid tumours found in patients [314, 315]. Spheroids generated from HCT-116 cells (with a diameter of 600-800 μm) were used to assess the penetration and anticancer effect of the ASC-J9 loaded into the designed nanocarriers into the tumours. As it could be clearly observed in **Figure 3.10.A** the drug fluorescence appears to be quite uniformly distributed across the spheroids. A drastic increase in the fluorescent intensity was detected in the spheroids treated with ASC-J9 loaded nanocarriers in comparison to the spheroids treated with the free drug. Furthermore, there was a significant difference in the fluorescence intensity of the drug within the spheroids treated with different nanocarrier formulations (**Figure 3.10.B**). The SF:SA (7:3) formulation (with low stiffness) had the highest fluorescence intensity followed by SF:SA (1:1) and SF:SA (3:7) respectively. The observed difference in the drug penetration into tumour spheroids is attributed to the different elasticity of the nanocarrier formulations providing a tool for tuning the cellular uptake of the drug-loaded nanocarriers through changing the composition of the nanocarrier cores.

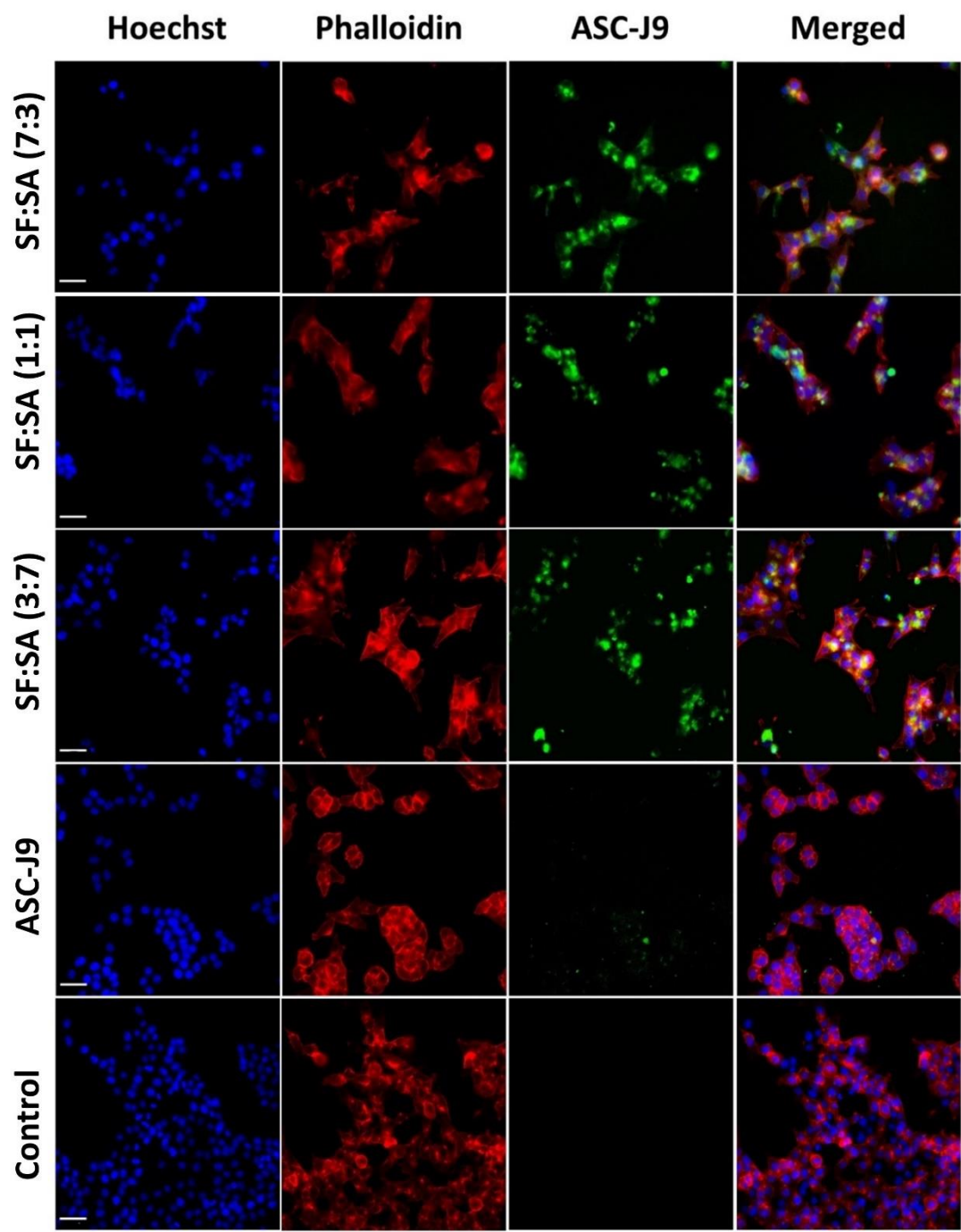


Figure 3. 8. High content fluorescent microscope images of HCT-116 showing cellular uptake of the free ASC-J9 and different ASC-J9 loaded nanocarriers (SF:SA=7:3, 1:1, & 3:7) after 24 hrs ($\times 20$ magnification, the scale bar represents 40 μm).

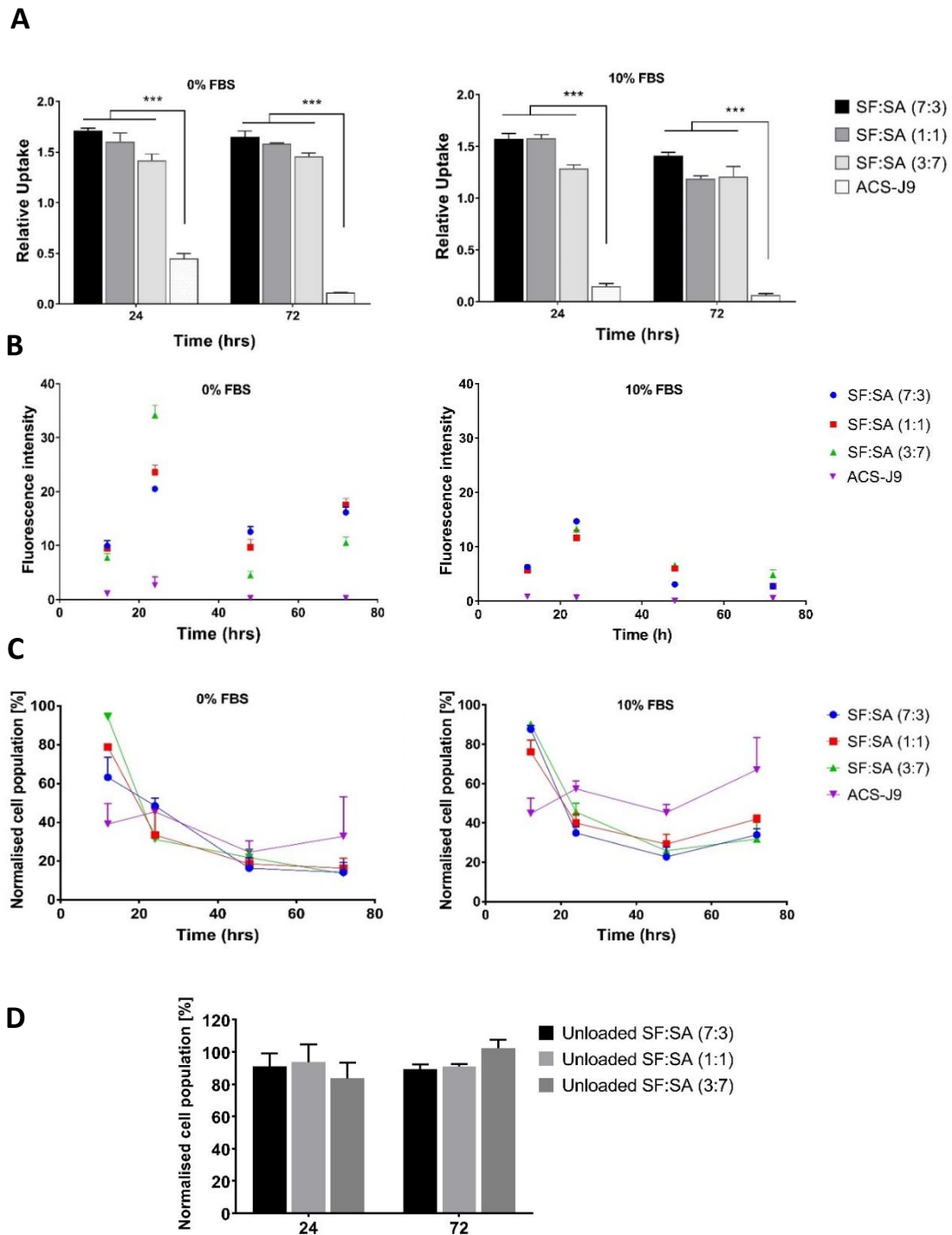


Figure 3. 9. (A) Relative cellular uptake of ASC-J9 loaded nanocarriers formulations and unformulated ASC-J9. (B) Fluorescence integrated intensity of ASC-J9 at multiple time points in unformulated form and in nanocarriers form. (C). The percentage of survived cells after ASC-J9 and ASC-J9 loaded nanocarriers treatments at multiple time points. (D) The effect of the unloaded nanocarrier formulations the cell population %. An asterisk denotes statistical significance as follows: * $P < 0.05$, ** $P < 0.01$, *** $P < 0.001$.

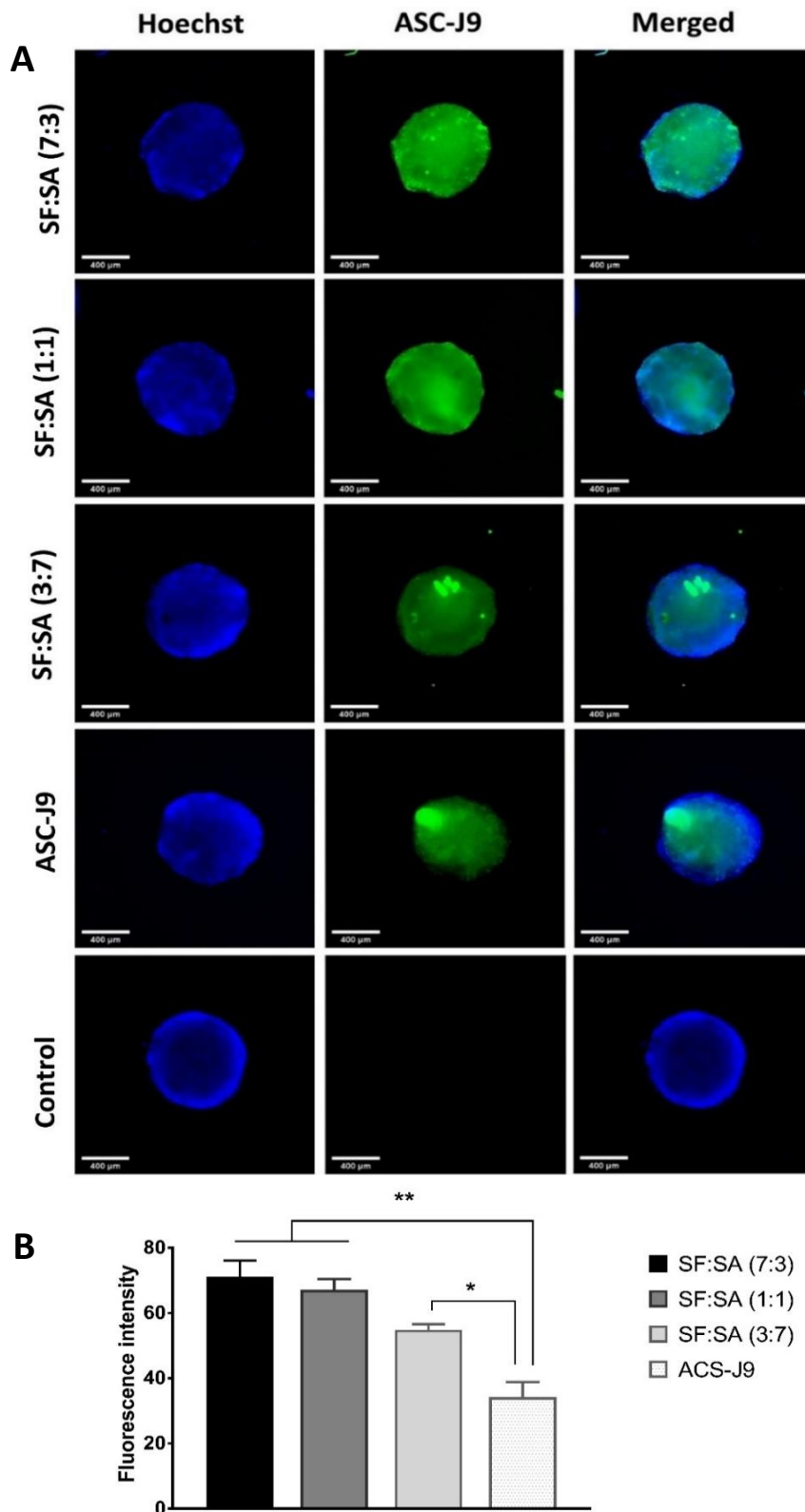


Figure 3. 10. (A) High content fluorescent microscope images showing uptake of ASC-J9 solution and ASC-J9 loaded nanocarrier formulations by HCT-116 tumour spheroids ($\times 2$ magnification, scale bars represent $400\ \mu\text{m}$). (B) The fluorescent intensity of ASC-J9 within the spheroids. An asterisk denotes statistical significance as follows: $*P < 0.05$, $**P < 0.01$, $***P < 0.001$.

3.3 Conclusion

SF is a biocompatible biopolymer which has been approved by FDA for pharmaceutical applications. Therefore, it has gained great attention as the main ingredient in various drug delivery systems. Although the nature of SF protein is desirable, formulating SF as stable nanocarriers with controllable properties remains a challenge. Herein, we report the development of a very versatile, stable nanocarrier system using a blend of SF and SA for enhanced encapsulation and controlled release of the hydrophobic anticancer agent ASC-J9. The designed nanocarriers were prepared using a simple method which avoids harsh preparation conditions such as extreme heat, pH or organic solvents and enjoyed controllable size (using the extruded lipid template technique) and tunable stiffness (via changing the SF/SA ratio). Tuning the stiffness of the nanocarriers resulted in changes to the drug release and anticancer activity of the ASC-J9 in HCT-116 colorectal cancer cells. Our findings also display a significant increase in cellular uptake of ASC-J9 within the $t_{1/2}$ window when loaded into the nanocarrier systems and prolonged anticancer activity resulting in the prevention of the cancer cell recovery in comparison to the free drug which may be of significance in preventing MDR. Modifying the nanocarrier properties also affected their penetration into the 3D tumour spheroids which serve as a model for solid tumours. Despite the large number of factors that govern the mechanism of cellular uptake in tumours, this study results suggest that tailoring the stiffness of the anticancer nanocarriers should be considered in the rational design process of anticancer drug delivery systems.

4 Chapter 4: Swirl mixer for the production of silk fibroin nanoparticles

Abstract

Drug delivery systems (DDSs) have great potential for improving treatment of several diseases, especially microbial infections and cancers. However, the formulation procedures of DDSs remain challenging at the nanoscale. Reducing batch-to-batch variation and enhancing production rate are some of the essential requirements for accelerating the translation of DDSs from small scale to the industrial level. Microfluidic technologies have emerged as an alternative to the conventional bench methods to address these issues. By providing precise control over the fluid flows and rapid mixing, microfluidic systems can be used to fabricate and engineer different types of DDSs with specific properties for efficient delivery of a wide range of drugs and genetic materials. Here, we demonstrate the potential of the newly developed microfluidic device (Swirl mixer) for the continuous production of silk nanoparticles with tuned particle characteristics. Our new microfluidic design demonstrated efficient mixing of organic and aqueous phases, which allows for controlled production of silk nanoparticles.

4.1 Introduction

In the past decade, there has been significant development in microfluidic devices for nanoparticle production [353]. Rapid mixing within the microfluidic system generates nanoparticles by fast nanoprecipitation and this process is simple, scalable, and convenient for the pharmaceutical industry [354]. The ability to incorporate more than one component in the nanostructure and control the particle formation by changing the processing parameters, is an important feature for drug delivery applications [355]. The high precision control of flow rates, flow regime (Reynold's number), and mixing time allows for optimizing the properties of the prepared nanoparticles such as size, shape, and size distribution. Creating a supersaturated solution of constituent molecules is an important route to nanoparticle synthesis [356]. Approaches to date have relied either on the rapid distortion of the aqueous particle component stream by acceleration into adjacent diluent solvent streams [357] or by folding the streams together in mixer elements [210]. In the first approach particles necessarily form under conditions of highly non-uniform composition, while mixer

designs employed in the second are far less effective than the best available again resulting in formation in a non-uniform particles [310, 358, 359]. To generate uniform particles under controlled conditions, a microfluidic mixer must be designed to achieve a uniform mixture in a time shorter than the time scales required for particle growth and aggregation as previously discussed (Chapter 1, section 1.4.1).

The current microfluidic designs (e.g. Staggered herringbone) that can achieve uniform mixing are limited by the pressure drop which takes place in the microchannel [358]. This problem makes the majority of the current microfluidic mixers costly, unsuitable for scaling up, and inconvenient for processing many pharmaceutical ingredients. Although increasing the size of the channel of the mixer can reduce the pressure drop, it can also reduce the uniformity of the resulting mixture. Therefore, the preferred mixer in pharmaceutical processing should have a geometric design that generates the lowest pressure drop, which allows for a high total flow rate, without affecting mixing uniformity and residence time. To obtain the desired particle size and narrow size distribution, specific mixing time (t_m) and mixture uniformity must be reached [310]. Rapid mixing is likely to require flow in the high Reynolds number regimes in which inertial effects are large. The mixer used in this study has a novel swirl design for the efficient preparation of nanoparticles. It consists of one or more mixing elements, each with an initial chamber for generating angular momentum, followed by an orifice leading into a second chamber as illustrated in **Figure. 4.1**. The flow pattern and concentration are shown for computation at $Re = 100$. The swirling flow in the initial chamber is evident and one can see the complex flow produced in the second chamber.

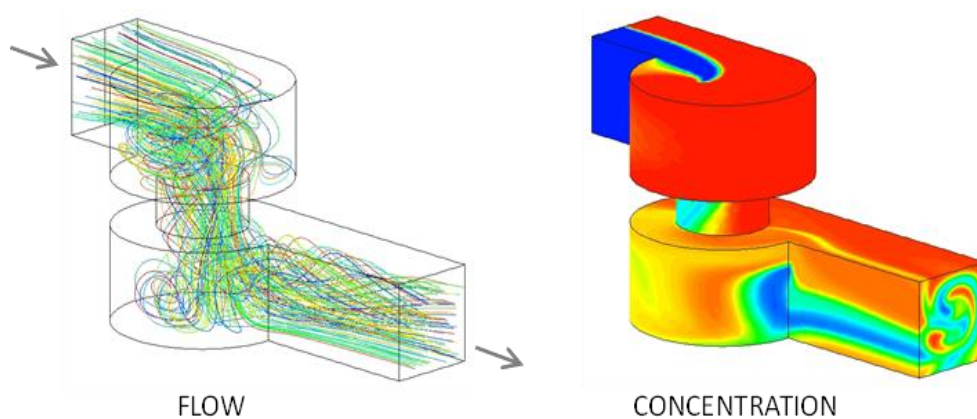


Figure 4. 1. Swirl mixer element: flow and concentration modeling at $Re= 100$.

In this study, four-elements, two-elements and one element swirl mixers were designed and tested using the example of silk nanoparticle production. The objective is to achieve the smallest possible mixing time with this particular mixer using a dual syringe pump and to document the effect of flow rate, Reynold’s number and mixing time, on particle size distribution. To evaluate the performance of the developed swirl mixer in terms of mean size and particle size distribution, a T-mixer operating at the same conditions was used. Size distribution measurement was obtained using nanoparticle tracking analysis (NTA).

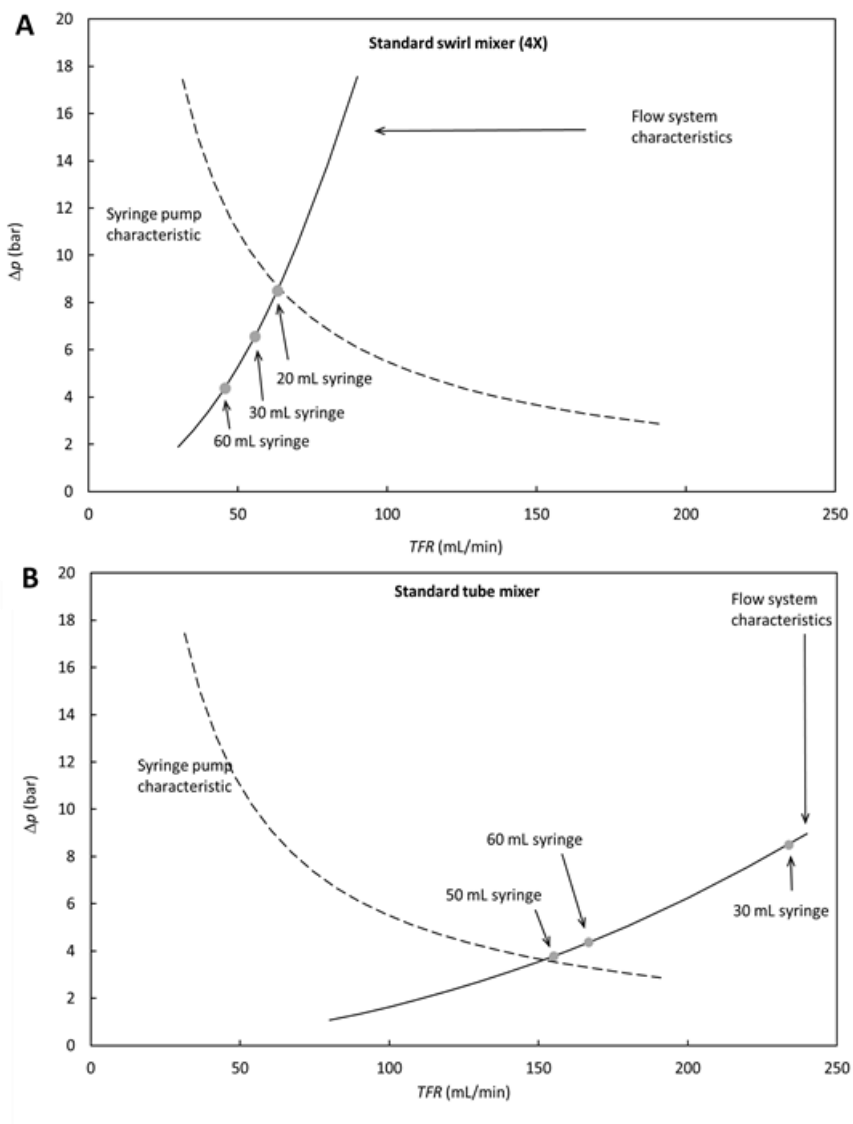


Figure 4. 2. Syringe and flow system characteristics for FRR =3.0. **(A)** Swirl mixer with 4 mixing elements (4X). **(B)** The model T-mixer.

4.2 Result and discussion

Protein-based nanoparticles (e.g. silk fibroin) emerge as promising nanomaterials for drug and gene delivery [261]. Although silk-based nanoparticles are increasingly reported in cancer therapy research, most of these particles are produced in the conventional precipitation methods [360]. These methods are batch-based and provide no in-process control of the nanoparticle properties. The development of microfluidic systems to produce pharmaceutical nanostructures and fine tune their properties has been explored by several studies [246]. In fluid mixing, there are two main flow regimes: turbulent flow and laminar flow. Either flow can occur depending on Reynold's number which is determined by the velocity and viscosity of the fluid in the mixer microchannels [361]. Most microfluidic platforms uses laminar flow (low Re) which initiate mixing only by molecular diffusion, this is inefficient for producing a uniform mixture in the available microfluidic devices [361-363]. The channel geometry and the design of the microfluidic designs have been modified to optimize the mixing, and produce particles with desirable properties [60]. For example, the staggered herringbone design creates chaotic flow by forcing the streams to pass over a herringbone structure, which creates transverse vortices to produce a uniform mixture [364]. Although this design has been used to produce size control nanostructures (e.g. silk nanoparticles and liposomes), it has few limitations, such as complicated fabrication of the device channels and high pressure drop which limits the TFR to 20 ml/min [60]. Therefore, increasing the maximum TFR is one of the issues to address to scale up the microfluidic device, and to comply with Good Manufacturing Practice (GMP) standards. The alternative design that is developed in this study offers maximum TFR (112 ml/min) with novel swirl design to produce a uniform nanoparticle size at different TFRs and different flow regimes. To evaluate the performance of the swirl mixer, a standard T-mixer is operating at the same conditions was also used for comparison.

The flow through the swirl mixer and T-mixer was generated using dual syringe pumps (Fusion 4000, Chemyx Inc.) one for aqueous phase and the other for organic phase. Although each pump is capable of 17.8 cm/min maximum linear speed (V_{max}) and 289 N maximum force (F_{max}), the force used to generate the flow is affected by the volume of mounted syringes. Part of the force is required to drive against the syringe plunger, and therefore the allowed pressure and flow rate are dependent on syringe diameter and the pump characteristic. This characteristic is plotted in **Figure. 4.2**, together with the flow system characteristic estimated

using a simple network model, for the flow ratio. The maximum flow states corresponding to the maximum pressure allowed for each of three available syringe sizes (**Figure 4.2**). Since all are below the pump characteristic (dashed curve) the flow states indicated are possible and specify the maximum flow rate that can be achieved with each of these syringes. With the 20 mL syringe, the maximum total flow rate is 83 mL/min ($t_m = 0.44$ ms). As the 20 mL syringe is on the borderline for this preliminary study the 30 mL syringe is used (TFR =50 mL/min and ($t_m = 0.73$ ms) to avoid difficulties associated with operating at the limits of the syringe pump. In the case of the standard tube mixer (T-mixer), the channels geometry allows for larger syringes (60 ml) to be used (**Figure 4.2**).

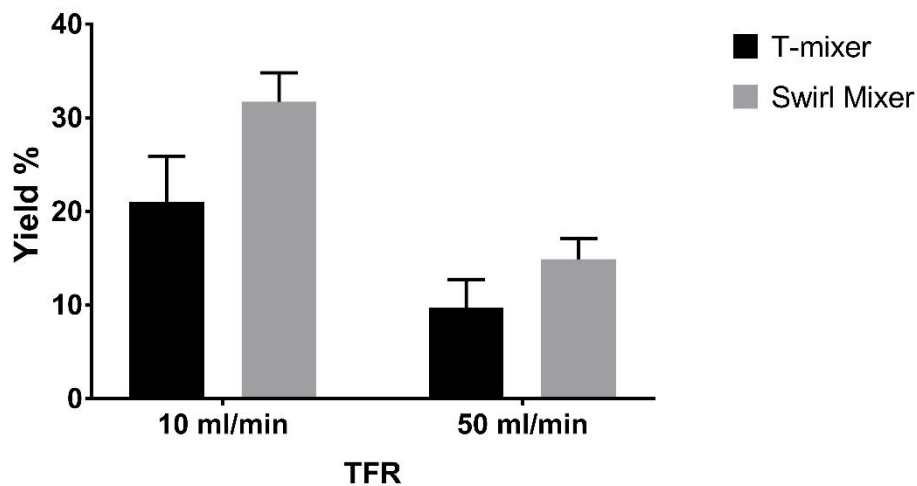


Figure 4. 3. Percentage yield of silk nanoparticles produced with Swirl mixer and T-mixer at two different TFR.

The percentage yield of the silk nanoparticles that is manufactured using the swirl mixer and the T-mixer is dependent on the applied TFR in both microfluidic platforms (**Figure 4.3**). The production efficiency for the manufacturing of silk nanoparticles demonstrates that relatively low TFR has higher nanoparticle yield. Slow TFR allows more time for silk solution to interact with organic solvent and induce the structural changes required for more nanoparticles [210]. The developed swirl mixer showed a higher percentage yield than the T-mixer in both tested TFR (10 & 50 ml/min) (**Figure 4.3**). The higher mixing efficiency which takes place in the swirl mixer, in comparison to the T-mixer, enhances the removal of the water molecules and ultimately high precipitation of silk nanoparticles.

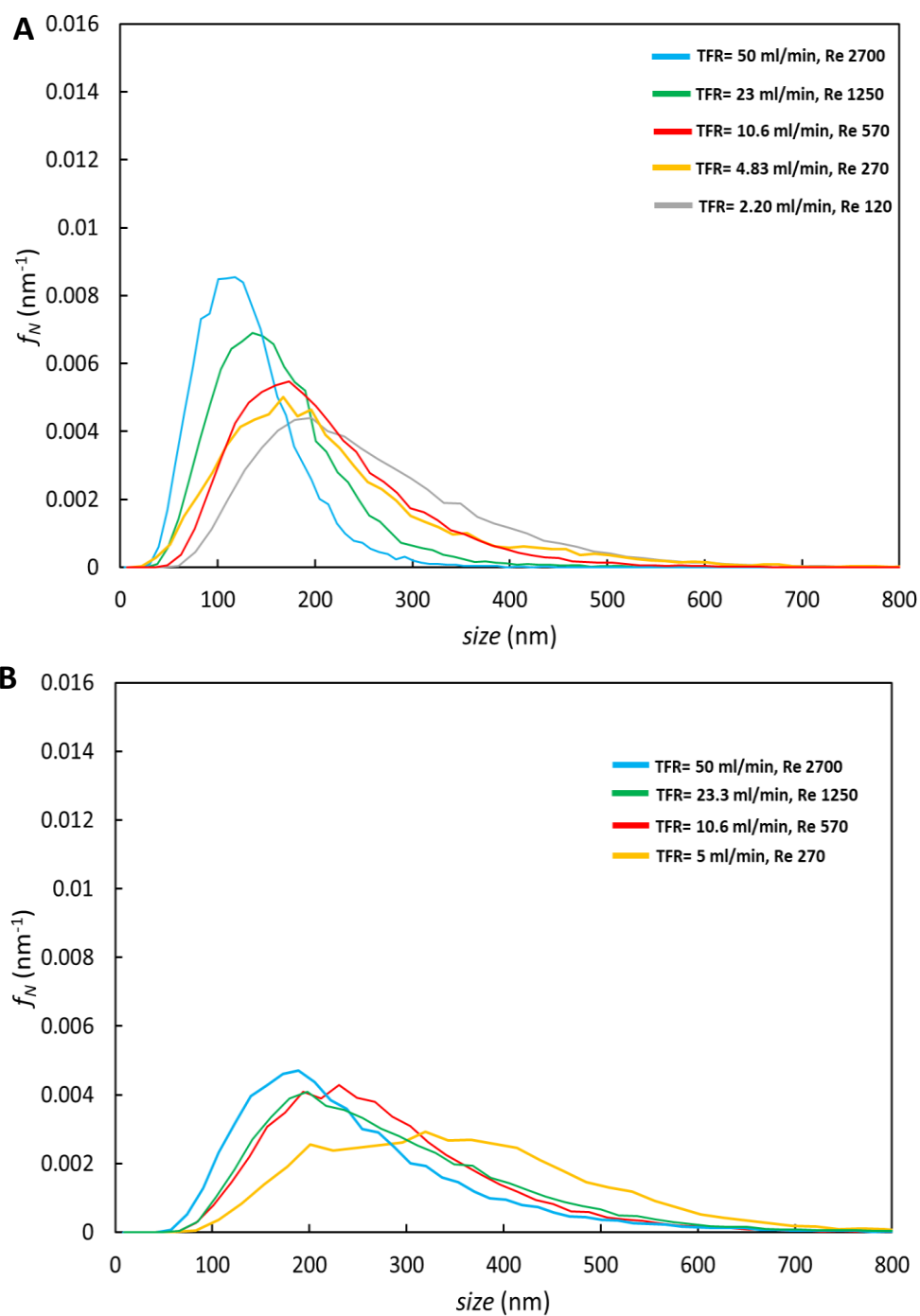


Figure 4. 4. The size distribution comparison of the two mixers operating at different TFRs and in laminar and transitional flow regime ($Re > 3000$). **(A)** Swirl mixer. **(B)** T-mixer.

The mixing element within the swirl mixer produces a complex flow pattern that helps to fold the two solutions (Silk solution and methanol) together. It functions by creating angular momentum in the first chamber of the mixing element, using the tangential inlets, and creating a complex flow in the second chamber when the high angular momentum fluid is then passed to it through a small passage. This flow pattern brings the first solution in contact with other and triggers rapid precipitation of homogenous silk particles even at low Re (**Figure 4.1 & 4.4**). On the other hand, T-mixer requires much high Re and TFR to achieve homogeneous nucleation and rapid precipitation of the nanoparticles [354, 356]. **Figure 4.4** shows that varying the TFR in the transitional and laminar flow (Re 100 to 2700) affects the size distribution in both mixers. Increasing the TFR reduces the mixing time (t_{mix}) and this minimize the available time for the particles to grow and aggregate (t_{agg}) [356]. Therefore, at TFR = 50 ml/min in the swirl mixer, the size distribution becomes significantly sharper with smaller average size than lower TFR. However, the picture that emerges from T-mixer is completely different. Even at the highest TFR investigated within the transitional flow regime (TFR= 50 ml/min, Re=2700), the T-mixer demonstrates much wider distribution in comparison to the developed swirl mixer. Varying the TFR in the T-mixer also shows very little effect of the mixing performance in the flow regime.

Before experimentally investigating the performance criteria in the turbulent flow, a computational study using Ansys 2019 R2 software was conducted to look qualitatively at the flow pattern and associated mixing of two solutions in both T- mixer and swirl mixer. **Figure 4.5** shows mean flow patterns computed using a turbulence model to represent the effect of fluctuating motions, for the tube mixer on the left and a swirl mixer on the right, each at Reynolds number 5000 (based on average velocity in the tube and connecting hole, and on those diameters). The streamlines shown are coloured by local mean concentration, which ranges from red for pure solution A, through green to blue for pure solution B. The flow rates of the two solutions in this example are the same. The main two observations are: (1) The swirl mixer volume is much smaller than that of the tube mixer, (2) the outlet of the tube length shows the mean concentration remains highly non-uniform, with both slight orange and blue colouring of some of the streamlines evident. The swirl mixer, with the very compact space occupied, has produced an apparently uniform (green) mixture of the two solutions.

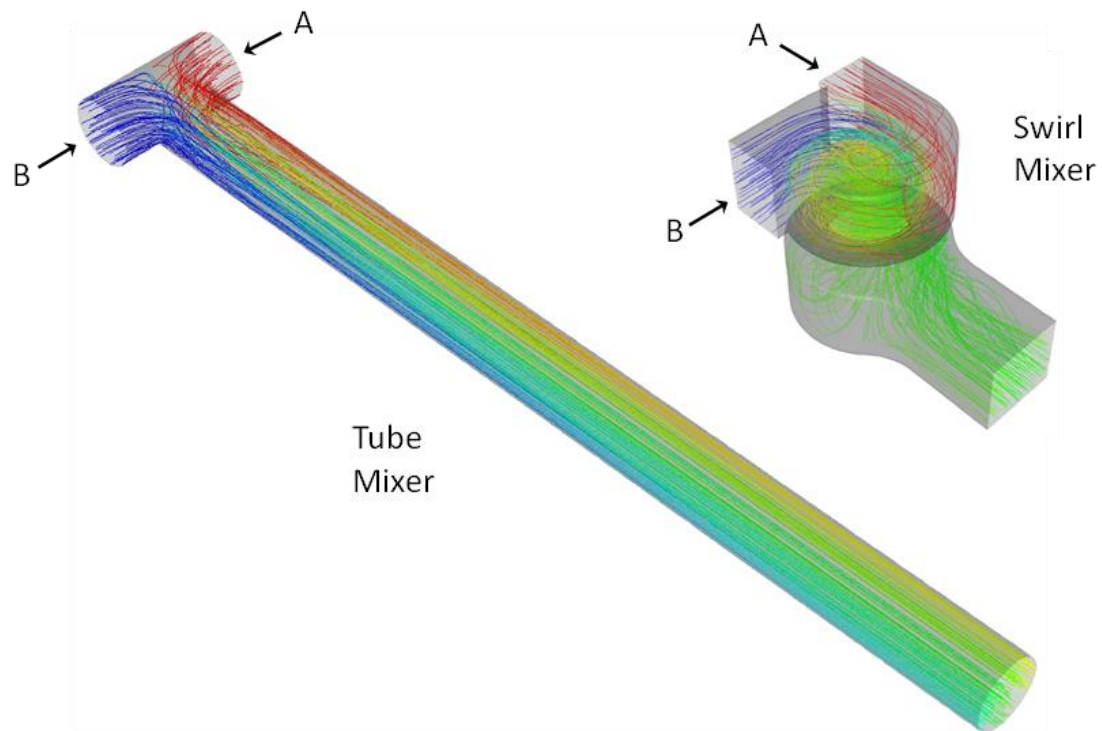


Figure 4. 5. Mean flow patterns for turbulent flow in the tube mixer (left) and the swirl mixer (right). Streamlines are coloured with local concentration from red (pure Solution A) to blue (pure Solution B) with mid-green being the perfect mixture between the two. Produced by Ansys 2019 R2 software.

To investigate the performance of the swirl and T-mixer in fully turbulent flow ($Re > 3700$), the size distribution is measured at relatively high TFR (86, 112 ml/min) as seen in **Figure 4.6**. Overall, the distributions gradually shift in a regular manner towards smaller particle size as the TFR increases in both mixers. Although the performance of T mixer improves in the turbulent flow, the swirl mixer continues to show sharper distributions at the same TFRs in fully turbulent regime.

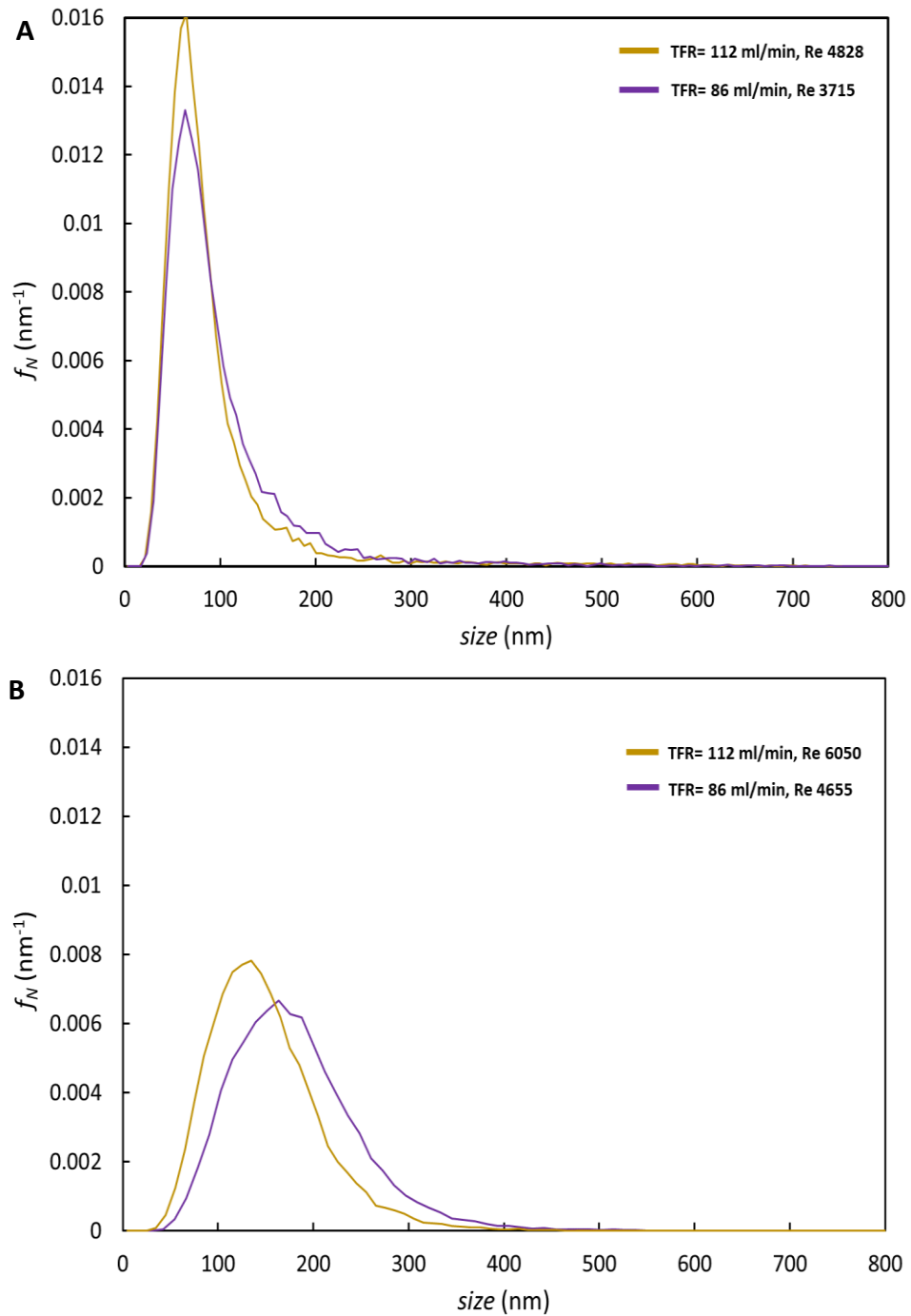


Figure 4. 6. The size distribution comparison of the two mixers operating at different TFRs and in fully turbulent flow regime ($Re < 3700$). **(A)** Swirl mixer. **(B)** T-mixer.

By comparing **Figures 4.4A** and **4.6B**, the size distribution produced by swirl mixer at TFR= 50 ml/min ($Re = 2700$) is almost identical to the size distribution produced by the T-mixer at TFR= 112 ml/min ($Re = 6050$). Generating this high flow rate in the turbulent flow requires much higher pressure than the swirl mixer at laminar flow that produces the same size distribution.

Although both mixers respond to the increase in TFRs by producing smaller particle size, the standard deviation trend in case of the T-mixer is dependent on the TFR. This means that the smaller standard deviation can only be achieved at high TFR. Due to the efficient mixing that takes place in the swirl mixer, the standard deviation trend is independent from the TFR, as seen in (**Figure 4.7 C & D**). This allows for particle size tuning by changing the TFR without risking large standard deviation (undesirable large particles). Solomun et al.[365] produced silk nanoparticles using a commercial Staggered herringbone micromixer (Nanoassembler) at maximum TFR= 12 ml/min [365]. The silk nanoparticle size produced by this mixer is in the range (110-310 nm). At the same flow rate ratio (3:1) organic phase: aqueous phase, the swirl mixer produces silk nanoparticles in the range (230- 95 nm) with maximum TFR of 112 ml/min observed in **Figure 4.7C**.

To understand the influence of mixing on the trend of mean particle size and shape of the size distribution, with increasing TFR and Re , mixing time should be considered. As shown in **Figure 4.7C & D**, T-mixer doesn't produce particles size below 200 nm until it is operating in the chaotic turbulent flow with mixing time > 4 ms. On the other hand, the designed swirl mixer produces particle size below 200 nm in the transitional and turbulent flow (mixing time > 8 ms) and performs significantly better even in the laminar flow. Due to the difference in geometric design, laminar and transitional flow can occur at shorter time in the swirl mixer than in the T-mixer. This property allows for a larger margin to reduce the mixing time without shifting to another flow regime, this can be extremely useful in tuning the formation and maintain reproducibility.

The silk nanoparticle stability was also investigated in water over 30 days, because the nanoparticles prepared for biomedical applications are required to possess long-term stability during storage and transportation. Silk nanoparticles were produced at the same total flow rate (TFR 50 ml/min, $Re = 2700$) in the two tested mixers (swirl mixer & T-mixer). The particle size of the silk nanoparticles produced by swirl mixer retained their size at 4 °C, and have an increase of only 10 to 20 nm at 37 °C (**Figure 4.7 H**). On the other hand, the silk nanoparticles

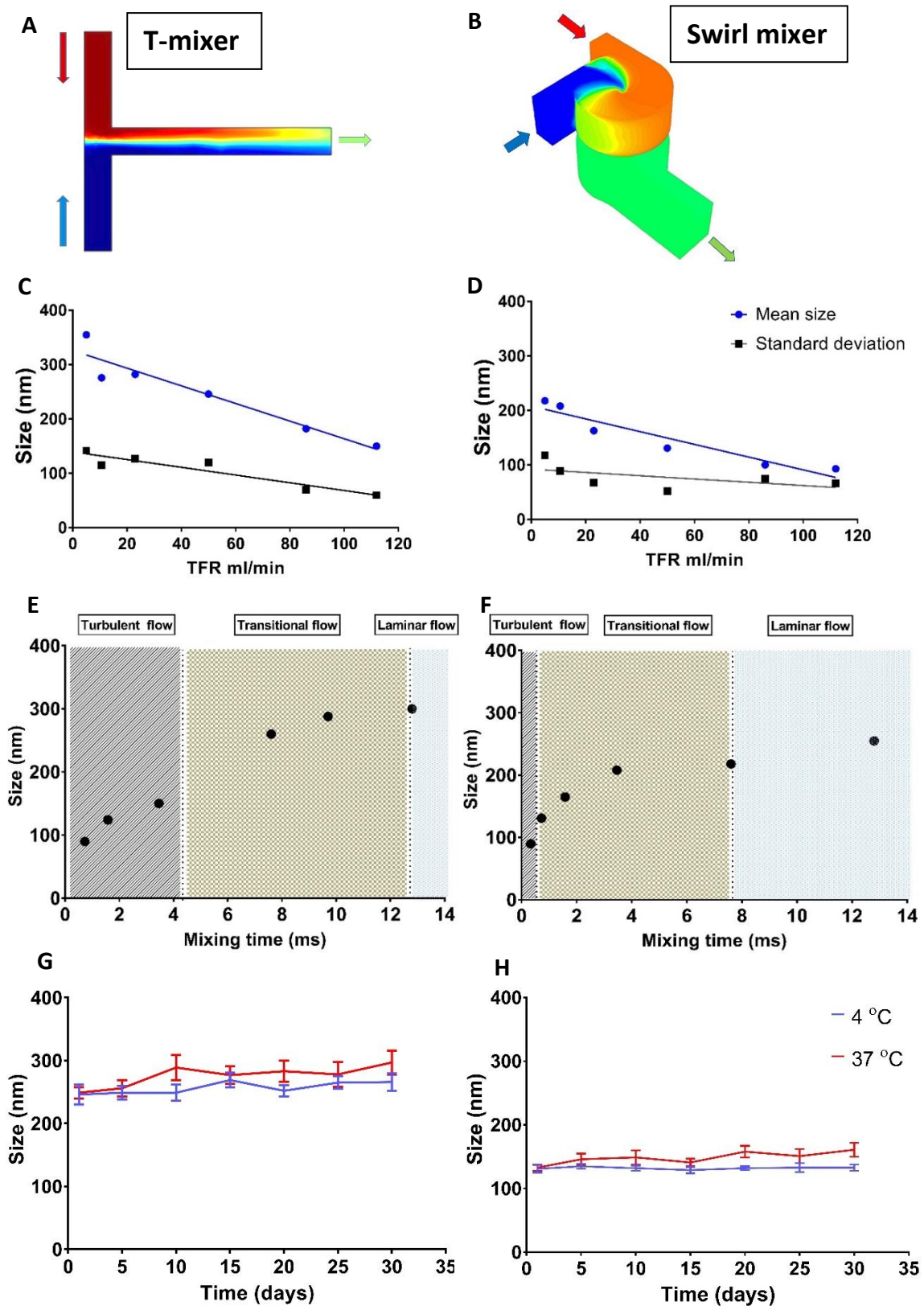


Figure 4. 7 (A) The flow pattern modelling of the T-mixer. **(B)** The flow pattern modelling of the Swirl mixer (Mesh modelling). **(C & D)** The mean particle size and standard deviation produced by the T-mixer and swirl mixer using different TFR. **(E & F)** The mean particle size at different mixing time in T-mixer and swirl mixer. **(G & H)** Stability of silk nanoparticles generated by T-mixer (G) and swirl mixer (H) using the same Total flow rate (TFR = 50 ml/min). The particle size of the silk nanoparticles stored at 4 °C and 37 °C was measured in DI water over 30 days.

generated by the T-mixer showed an increase in the particle size ranging from 30 to 50 nm over the tested time period (**Figure 4.7 G**). The difference in stability between the particles produced by T-mixer and those produced by the designed swirl mixer can be explained by the difference in their size distribution. In the case of the swirl mixer, the distribution is sharper and narrower than the distribution of the particles produced by the T-mixer with the same processing conditions (**Figure 4.4**). The wide distribution indicates very low size uniformity in the case of T-mixer, which can increase the tendency of small particles to aggregate on the larger ones with time leading to a shift in the mean size during the stability test.

The shape and morphology of the silk nanoparticles produced by the swirl and the T-mixer at TFR =50 ml/min are analysed by AFM and TEM (**Figure 4.8**). The silk nanoparticles generated by the swirl mixer have spherical shapes and uniform size distribution, which correlates with the NTA measurements (**Figure 4.4**). More irregular shapes and larger sizes with wide distribution are observed in the nanoparticles produced by the T-mixer. This difference in the nanoparticles produced by the two mixers can be explained by the inefficient mixing that is generated by the T-mixer during the particle formation. This results in loose fusion and aggregation of the silk nanoparticles. The silk protein has a relatively high molecular weight (390 KD) which requires a sufficient amount of organic solvent to encounter the silk solution, and rapid removal of water molecules to produce packed and uniform silk particles. These conditions are achieved in the swirl mixer, which can induce more efficient rapid mixing than the T-mixer.

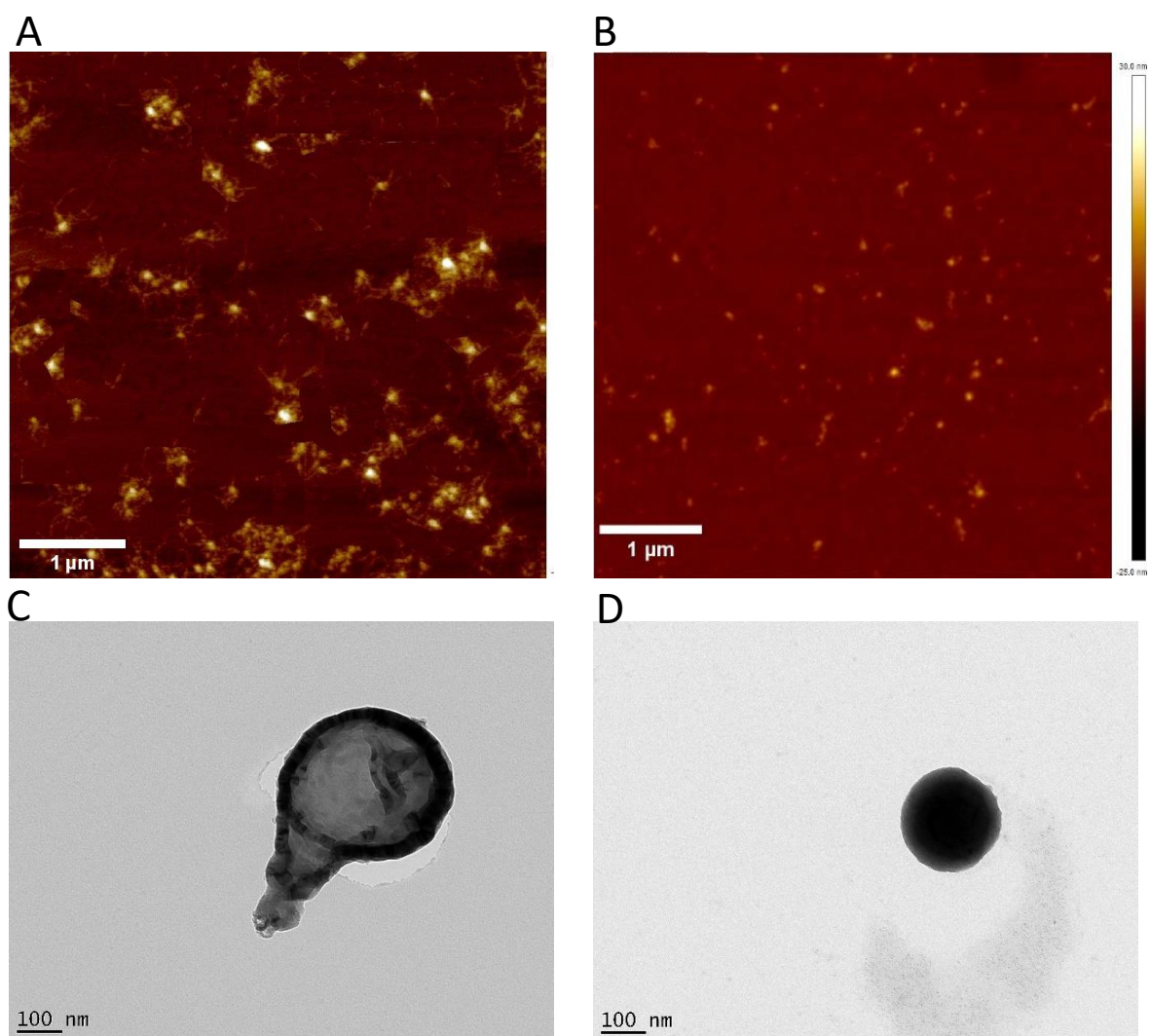


Figure 4. 8. Atomic force microscopy (AFM) scans of silk particles produced at (TFR = 50 ml/min, mixing time = 7.25 ms) using T-mixer and swirl mixer. (I & J) TEM images of silk nanoparticles produced at (TFR = 50 ml/min, mixing time = 7.25 ms) using T-mixer and swirl mixer.

The impact of the number of mixing elements in the swirl mixer on the mean size and standard deviation is also investigated at two different TFRs (10 & 50 ml/min) (**Figure 4.9**). At the relatively high TFR (50 ml/min), no significant difference in the mean size or standard deviation is recorded among 1, 2 & 4 mixing elements. However, the lower tested TFR (10 ml/min) shows a tangible increase in the mean size and standard deviation of the silk nanoparticles produced by the 4 mixing elements, in comparison to the 1 & 2 elements (**Figure 4.9**). The impact of the number of mixing elements can vary depending on the concentration and the composition of the nanoformulation (**Figure. S.1 in Supplementary data**).

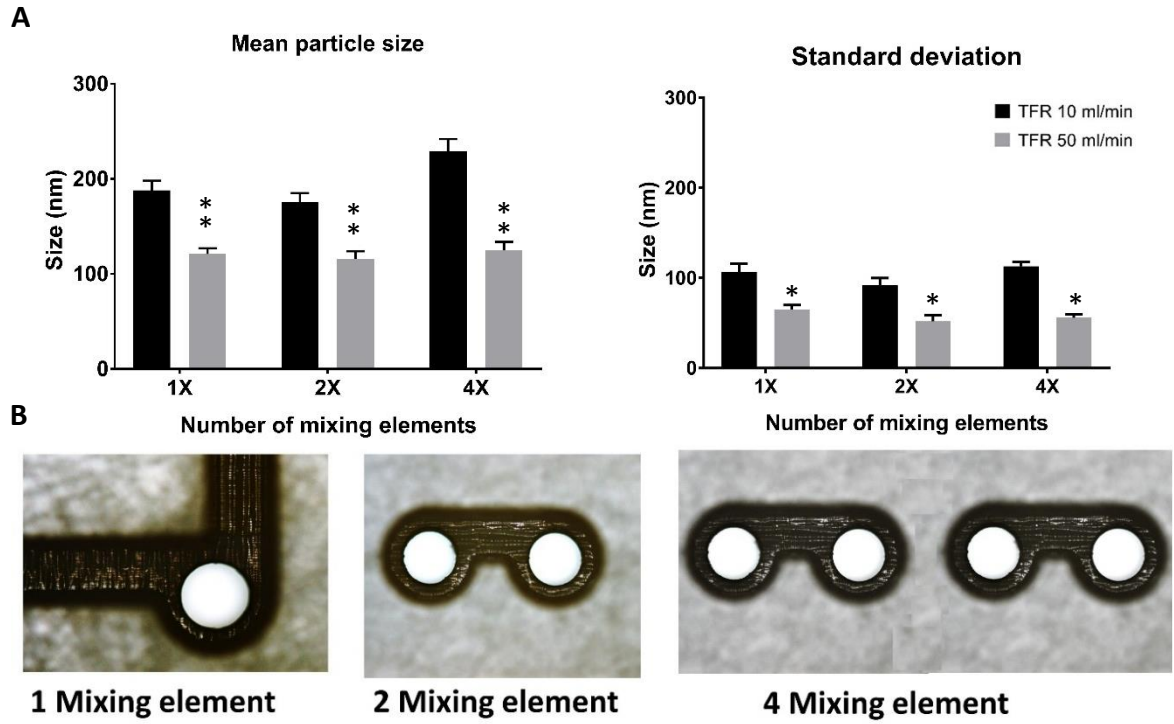


Figure 4. 9. (A) The effect of the number of swirl mixing elements in the chip on the mean size particle and the standard deviation. **(B)** Microscopic images of the swirl mixing elements of mixing chips.

4.3 Conclusion

Biopolymeric nanoparticles are a well-recognised drug delivery system for their ability to enhance the drug activity, improve cellular uptake, and reduce off-target toxicity by increasing accumulation at the target tissue. There is an increasing demand for nanoparticles as nanocarriers for several active pharmaceutical ingredients, especially hydrophobic anticancer drugs. Therefore, controlled and large-scale production of nanoparticles with desirable properties have become an important strategy in pharmaceutical industry. Microfluidic platform allows for controlled preparation of nanoparticles with specific properties, thereby reducing the risk of their application as formulation in nanomedicine. Although several microfluidic devices address the limitations of the conventional methods, such as reproducibility and tunable properties, the main remaining challenge is scaling up production without using very high pressure. These challenges slow down the translation of many nanoparticle formulations from bench-top to pharmaceutical industry. In this study, we present a new microfluidic swirl mixer which has higher TFR than many of the current complicated designs (e.g. Staggered herringbone) and better performance than the common simple designs (e.g. T-mixer). The findings presented in this study showed that the swirl mixer is more efficient than the T-mixer in mixing two solution in different flow regimes. Moreover, the swirl mixer can be optimized by adding additional mixing elements and inlets and has achieved higher mixing performance than the T-mixer, despite having a much smaller size. The swirl mixer design enables size tuning of silk nanoparticles (220-95 nm), and can reach a TFR of 112 ml/min making it a promising microfluidic platform for the pharmaceutical industry.

5 Chapter 5: G3-Functionalised magnetic silk nanoparticles produced by the swirl mixer for enhanced anticancer activity

Abstract

Silk fibroin is an FDA approved biopolymer for clinical applications with a great potential use in nanomedicine. However, silk-based nanoformulations are still facing several challenges in processing (e.g., Reproducibility) and drug delivery efficiency (e.g., Targetability) especially in cancer therapy. To address these challenges, robust and controllable production methods are required for generating nanocarriers with desired properties. The aim of this study was to develop a novel method for production of peptide-functionalized magnetic silk nanoparticles with higher selectivity for cancer cells for targeted delivery of the hydrophobic anticancer agent ASC-J9. A new microfluidic device with a swirl mixer was designed to fabricate magnetic silk nanoparticles (MSNP) with desired size and narrow size distribution. The surface of MSNPs was functionalized with a cationic amphiphilic peptide, G(IKK)₃I-NH₂ (G3), to enhance their selectivity towards cancer cells. The G3-MSNPs increased the cellular uptake and anticancer activity of in colorectal cancer cells HCT 116 compared to free G3. Moreover, the G3-MSNPs exhibited considerably higher cellular uptake and cytotoxicity in HCT 116 colorectal cancer cells compared to normal cells (human dermal fibroblasts). Encapsulating ASC-J9 in G3-MSNPs resulted in augmented anticancer activity compared to free ASC-J9 and ASC-J9 loaded MSNPs. These results show that functionalizing MSNPs with enhanced the selectivity and anticancer activity of ASC-J9 within its biological half-life.

Keywords: *Drug delivery, Magnetic silk nanoparticles, Microfluidics, G3- peptide and targeted cancer therapy.*

5.1 Introduction

Cancer is one of the main causes of deaths worldwide [366]. In the United States, colorectal cancer (CRC) is the second cause of cancer death and was estimated to be responsible for 53,200 deaths in 2020 out of 147,950 newly diagnosed individuals with CRC [367]. To fight this life-threatening disease, tremendous efforts in nanomedicine research were devoted in the past few decades [208]. Drug delivery systems (DDSs) have improved the treatment efficiency in terms of targetability, drug resistance and controlled release of the payload [6, 368, 369]. Engineered nanoparticles (NPs) for targeted drug delivery have emerged as effective drug nanocarriers in cancer therapy [6]. Many recent studies have focused on modifying the properties of NPs to improve drug selectivity, minimize side effects, prolong blood circulation, and reduce drug resistance in tumours [208, 370]. Nanoparticles are suitable for tumor targeting due to their ability to take advantage of the leaky neovasculatures of solid tumours which allows for their passive accumulation [371]. This accumulation is a result of enhanced permeability and retention (EPR) effect which attracted more attention to the production of nanostructures with specific size distribution (>200 nm) [356, 372, 373]. The remote control of the properties (size, shape & charge) of the generated nanocarrier is a key factor in enhancing the loaded drug activity and determining the *in vivo* fate of the nanocarrier [374-377]. Therefore, many nanoparticles with different properties and compositions are currently in clinical trials for a wide range of applications in drug and gene delivery [378, 379].

Due to the low solubility, short half-life and poor targetability many anticancer drugs such as curcumin and ASC-J9 have shown limited activity in tumor tissues [49, 166]. Loading the anticancer agent to a nanocarrier with specific properties can deliver the drug to the target tumor microenvironment and exert the required anticancer activity [16, 380]. Since the majority of anticancer agents are prepared for parenteral administration, it is essential to prevent drug opsonization in the bloodstream or elimination before reaching the target tissue at effective concentration. Low drug concentration at the tumor tissue is one of the main reasons for multidrug resistance (MDR) in metastatic cancers [338-340]. For example, the half-life ($t_{1/2}$) of ASC-J9 is less than 6 hrs following an intravenous injection in mouse [13]. A common strategy to overcome these limitations is to design drug nanocarriers that reduce immune response and enhance cellular uptake within the $t_{1/2}$ of loaded drug [381-383].

Biopolymeric nanoparticles such as silk fibroin (SF) particles are preferred in drug delivery due to their biocompatibility, biodegradability and low immunogenicity [33, 49]. SF-based nanoparticles have shown strong ability to capture and release several model drugs [165, 209, 384, 385]. Seib *et al.*, produced SF nanoparticles for pH dependant release of doxorubicin to overcome drug resistance in human breast cancer cells MCF-7 [386]. In addition, SF nanoparticles can be decorated or functionalized with different ligands in multiple ways to promote cellular uptake and improve the delivery of the loaded drug [239]. However, low tumor targeting is one of the main issues that undermine the efficacy of many anticancer formulations due to insufficient tumor accumulation [6]. To enhance tumor-specific delivery of the anticancer agents and minimize off-target effects, active targeting approach using functionalised nanocarriers has shown promising results [387]. This approach formulates nanocarriers (liposomes or nanoparticles) by functionalising a targeting ligand (monoclonal antibody, or peptide) on the carrier surface to favour specific tissue or cell line [388-391]. Riaz *et al.* [71] augmented the therapeutic efficacy of quercetin for lung cancer therapy by using liposomes functionalised with T7 (HAIYPRH) peptide which targets the overexpressed transferrin receptors in Lung tumors [71]. The use of magnetic field is another effective strategy to drive the anticancer formulation toward the targeted tissue and enhance drug accumulation at the tumor sites [392, 393].

Producing nanoparticles with controllable properties using a robust method remains a challenge. Although SF nanoparticles can be produced in a broad spectrum of methods, desolvation method using microfluidic devices is found to be the most robust and reproducible technique [33, 210, 365]. Size variation can affect several performance factors in drug delivery such as loading efficiency, targetability, cellular uptake and pharmacokinetics [394]. The recent advances in microfluidics allow for precise manipulation of fluids mixing through modifying the geometric designs of the microfluidic device, and altering the process parameters such as total flow rate (TFR) and flow rate ratio (FRR) between different phases (organic & aqueous) [395, 396]. For example, staggered herringbone was utilized to prepare SF nanoparticles (100-300 nm) with controllable properties at a maximum production rate of 12 ml/min [210, 365]. In this paper, we present a new microfluidic device (swirl mixer) which provides a relatively high production rate (100 ml/min) and controlled preparation of

5.2 Results and discussion

In cancer therapy, combining two therapeutics is a common strategy to maximize treatment outcomes. Pharmacokinetics, elimination time and intracellular concentration are mainly affected by the physiochemical properties of anticancer drugs which can be modified by formulating the drug in nanocarriers. Recent studies suggest that cellular drug concentrations are essential for maximizing not only the drug activity but also the synergetic effect when combining more than one active pharmaceutical ingredient [405]. For example, liposomes loaded with a combination of cytarabine and daunorubicin have been used in clinical trials for treating patients with acute myeloid leukaemia (AML) [405]. The use of nanocarriers that modify the drugs' properties to improve their efficiency in the body is an effective approach in cancer treatment. However, the preparation of suitable, reliable, and reproducible nanocarriers at a large scale is one of the main challenges for moving many drug-carrier formulations from proof of concept to clinical applications. The microfluidic technologies have been employed previously to produce different types of drug delivery systems such as liposomes and polymeric nanoparticles [34, 355, 406, 407]. In this study, magnetic silk nanoparticles (MSNPs) were fabricated in a controlled manner using a newly developed microfluidic device. These MSNPs served as nanocarriers for the hydrophobic anticancer drug (ASC-J9) to enhance its intracellular concentration within the tumour tissue. To improve ASC-J9 activity and selectivity toward cancer cells, G3 peptide was grafted on the surface of the nanoparticles. Although using cationic helical peptides with anticancer activity such as G3 has been reported [399], functionalising G3 on nanoparticles and combining G3 with an anticancer agent has not been reported elsewhere and is studied here for the first time.

5.2.1 Characterization and surface analysis of MSNP and (G3)-MSNP

The rapid nanoprecipitation generated by the microfluidic device produced magnetic silk nanoparticles with a size range (129-232 nm). The size and zeta potential were characterized by dynamic light scattering (DLS) (**Table 5.1**). The net charge of the MSNPs was negative with zeta potential ranging from -36 mV to -19 mV in DI water depending on the processing conditions such as TFR, FRR, and the organic phase selection. Two FRRs (3:1) and (5:1) (organic phase: aqueous phase) were used in this study. The MSNPs prepared using acetone at FRR acetone: aqueous (3:1) and (5:1) demonstrated the smallest particle size (~130 nm).

Table 5. 1. Dynamic light scattering characterization of MSNP produced by the microfluidic device by varying total flow rate (TFR) and flow rate ratio (FRR).

| Sample (TFR: ml/min) | Organic phase (FRR) | Size (nm) | PDI | Zeta potential (mV) |
|----------------------|---------------------|-----------|------|---------------------|
| MSNP (10) | Methanol (3:1) | 232 ±11 | 0.22 | -26.3 ±4.0 |
| | (5:1) | 219 ±13 | 0.20 | -29.1 ±2.9 |
| MSNP (50) | Methanol (3:1) | 190 ±14 | 0.18 | -21.2 ±2.2 |
| | (5:1) | 172 ±9 | 0.19 | -22.5 ±1.8 |
| MSNP (10) | Acetone (3:1) | 211 ±17 | 0.26 | -15.8 ±3.3 |
| | (5:1) | 218 ±21 | 0.24 | -16.2 ±3.8 |
| MSNP (50) | Acetone (3:1) | 132 ±15 | 0.21 | -12.9 ±3.9 |
| | (5:1) | 129 ±18 | 0.22 | -12.3 ±4.3 |

The high solvent ratio and low total flow rate enable better removal of water molecules from the silk structure which results in rapid nanoparticle formation [408]. Miscible organic solvents that can form hydrogen bonds with water (aqueous phase) are the suitable solvents for microfabrication of nanomaterials using the microfluidic platform. However, the ability to form hydrogen bonds with water is not the same among organic solvents. The polar protic organic solvent such as methanol and isopropanol have a higher capacity to form hydrogen bonds with water than aprotic organic solvents such as acetone and DMSO [210]. Therefore, methanol and acetone were used to investigate their impact on the nanoparticle production and to select the solvent which provides desirable nanoparticle properties for drug delivery. In agreement with a previous study on silk nanoparticle production using microfluidic systems [210], the higher organic solvent to silk solution ratio (5:1) generated smaller particle size and zeta potential in both tested organic solvents than the lower ratio (3:1). As speculated, the nanoparticles produced using methanol showed a larger particle size than the ones processed with acetone under the same microfluidic parameters (TFR). This can be explained by the difference in the ability of the two solvents to strip the silk structure of water molecules when rapidly mixed with the silk solution in the mixer chambers. The type of the organic solvent is not the only factor that affects the particle size and surface charge. The applied TFR plays a key role in controlling the properties of nanoparticles. Although swirl mixer can initiate uniform mixing at low TFR (low Reynolds number), the mixing time at high TFR (50 ml/min) is significantly smaller than low TFR (10 ml/min). This may shorten the available time for the

nanoparticle growth and change packing arrangement leading to different particle size and surface charge.

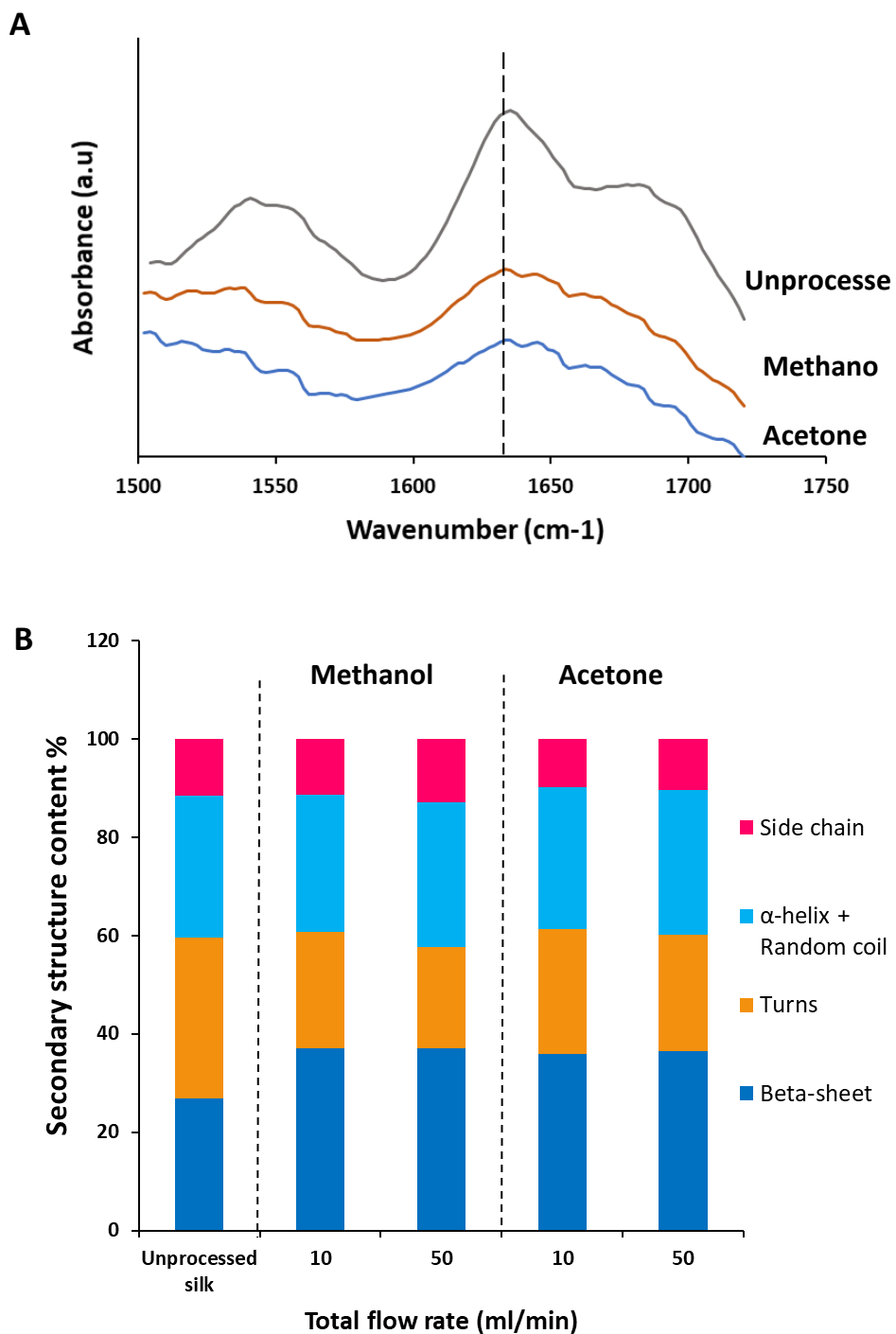


Figure 5. 2. (A) FTIR absorbance spectra of unpressed silk and silk nanoparticles produced by microfluidic device using Methanol or Acetone as the organic phase. (B) Silk fibroin secondary structure analysis of the nanoparticles generated by the microfluidic device by changing the organic phase and the total flow rate.

The structural transformation of the silk fibroin when processed under different microfluidic conditions was assessed using FTIR. The FTIR spectra of the amide I region (1610-1650) of SF was used for comparing the fabricated nanoparticles with unprocessed SF (**Figure 5.2 A**). The spectra were normalized and the areas under the curve of the amide I region were analysed as reported previously [312, 409]. Overall, the secondary structure of the nanoparticles produced by the microfluidic system showed a higher percentage of β -sheets and a lower percentage of α -helices than unprocessed water-soluble SF (**Figure 5.2 B**). However, the silk nanoparticles processed with methanol showed a slightly higher percentage of β -sheet (37.1%) than the particle processed with acetone (35.8%) at TFR 10 ml/min. This can be due to the stronger ability of methanol to reach silk molecules and induce structural transformation.

To investigate the changes in size and shape of the nanoparticles during production and functionalisation, morphological assessment using atomic force microscopy (AFM) was performed after every processing step (**Figure 5.3**). The magnetic nanoparticles (MNP) were scanned before being loaded to the organic phase syringe. Then, the magnetic silk nanoparticles (MSNPs) produced by the microfluidic system at TFR=50 ml/min were analysed. In agreement with DLS size measurement, the size and morphological assessment by AFM showed smaller MSNPs produced by acetone. However, more irregular shapes were observed in the sample processed by acetone. On the other hand, the nanoparticles produced using methanol showed more size and shape uniformity (**Figure 5.3 B**). After functionalisation with G3 peptide, the nanoparticles demonstrated slightly larger size and completely different morphology from the unfunctionalised nanoparticles. We speculate G3 functionalisation occurs through electrostatic interaction between the MSNP and G3 peptide. This is confirmed by the AFM scans in the G3-MSNP produced using methanol and acetone (**Figure 5.3 C**).

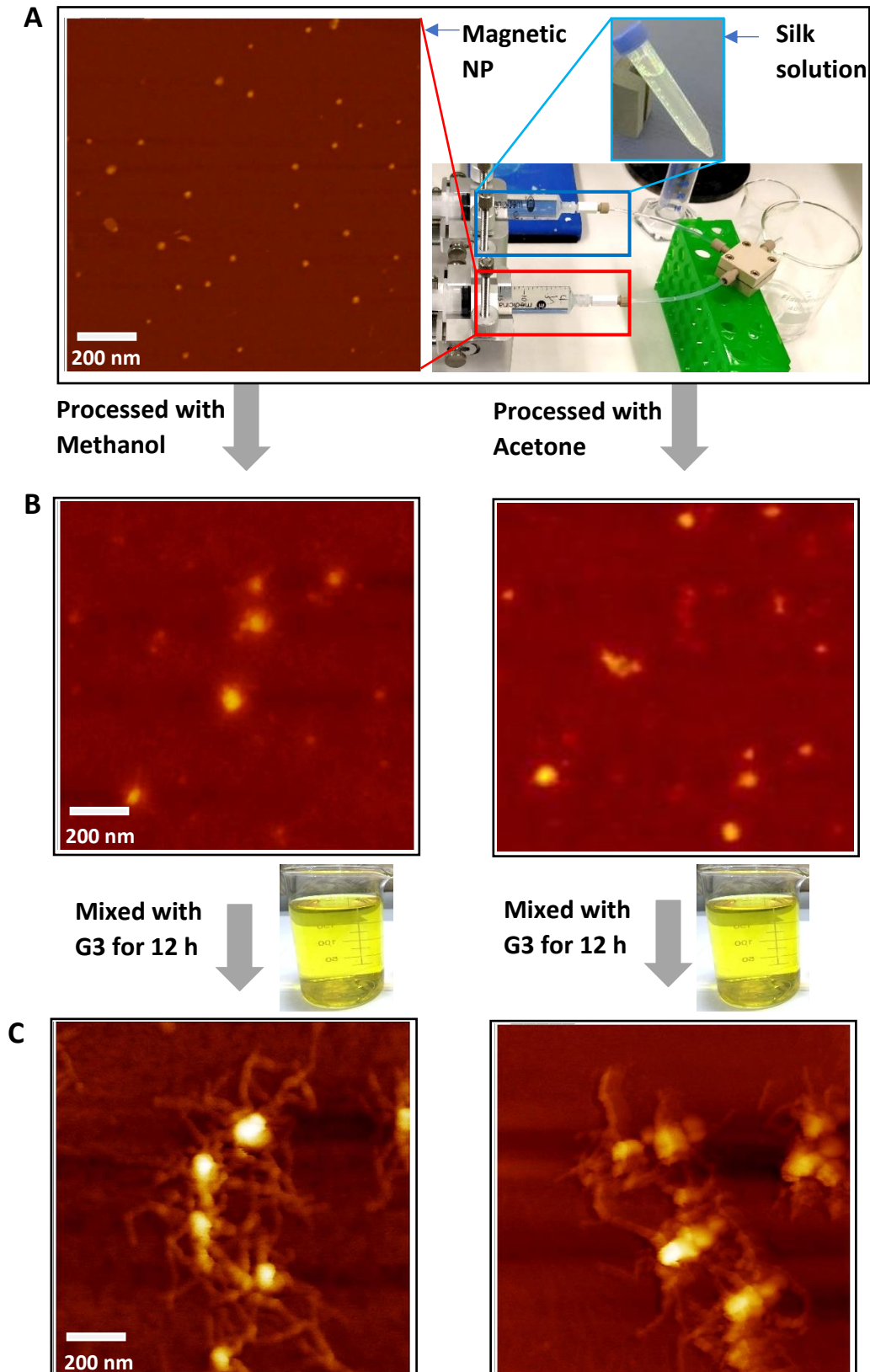


Figure 5. 3. AFM scans of the different steps involved in production and functionalisation of MSNPs using methanol or acetone as the organic phase. (A) MNP Scans before mixing with silk solution in the microfluidic system. (B) AFM scans of MSNPs produced by the microfluidic system at TFR = 50 ml/min. (C) AFM scans of G3 functionalised MSNPs after 12 h incubation with G3 solution.

Due to the substantial difference in zeta potential between the positive G3 peptide ($\sim +6$ mV) and the negative biopolymeric surface of MSNPs, it was possible to functionalise the MSNPs surface with G3 peptide through electrostatic interactions. This functionalization results in a significant increase in the surface charge between MSNP and G3-MSNP associated with a slight increase in the size of the G3-MSNP as shown in the DLS measurements (**Figure 5.4**). The change in zeta potential value and mean size of the nanocarriers after interaction with the peptide was used previously as indicators to confirm the functionalisation of mApoE and dApoE peptides on the surface of nanoliposomes [135].

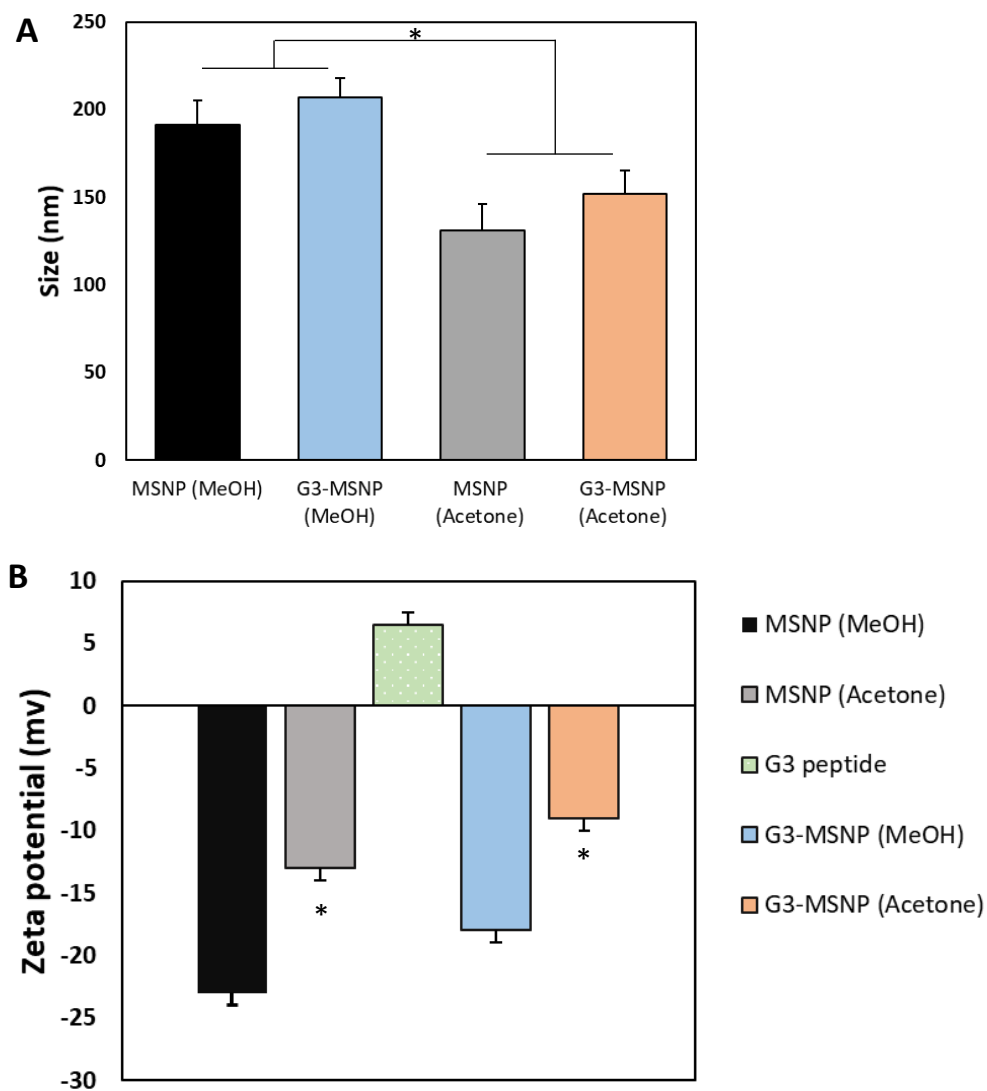


Figure 5. 4. (A) the size and (B) zeta potential of the MSNPs produced by the microfluidic system before and after functionalisation with G3 peptide.

The amount of peptide grafted on the surface of MSNPs was calculated by measuring the concentration of the peptide before and after incubation with MSNPs using the UV absorbance calibration curve **Figure 5.5 A**. The grafting efficiency of MSNPs produced with the desired size range (at TFR 50 ml/min) using either acetone or methanol was measured. The G3 peptide grafting efficiency of the MSNPs processed with methanol was slightly higher than MSNPs processed with acetone **Figure 5.5 B**. This can be a result of the difference of the surface charge between the particles generated by the two solvents **Table 5.1**. Therefore, the MSNPs batch produced by methanol at TFR: 50 ml/min was routinely used for all subsequent studies.

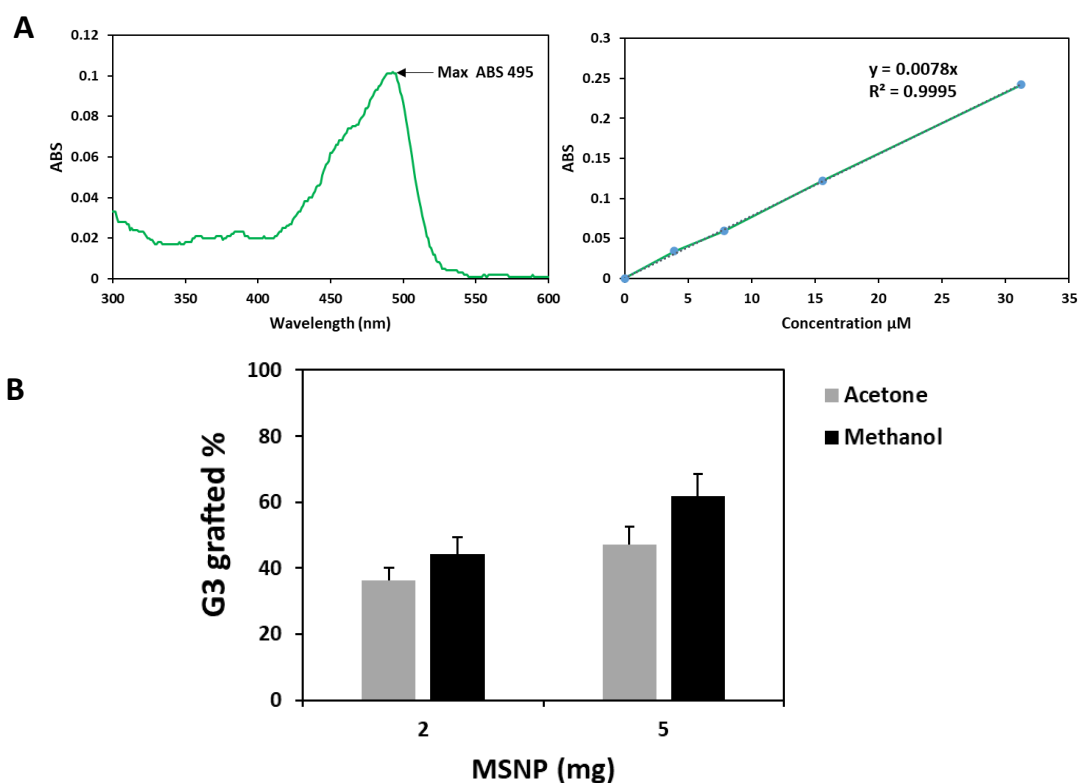


Figure 5. 5 (A) The maximum absorbance and calibration curve of FITC labelled G3 peptide. (B) The percentage of G3 grafted on the surface of MSNP processed with acetone or methanol.

To investigate the MSNP encapsulation efficiency (EE%) 90 μ M of ASC-J9 and 2 mg or 5 mg of nanoparticles were used (**Figure 5.6.A**). The encapsulation efficiency was lower with 2 mg of MSNP compared to 5 mg of MSNP (61% vs. 84% respectively) but there was no statistically significant difference between the encapsulation efficiency of MSNPs and G3-MSNPs. Compared to other protein-based nanoparticles, MSNPs demonstrate very high encapsulation efficiency for hydrophobic model drugs [257, 410, 411]. The release behaviour of ASC-J9 was also studied to obtain information about drug diffusion timing. Also, this study typically allows for investigating the impact of modifying the polymeric matrix of the nanoparticles on the interaction between the drug molecules and the nanoparticles. Similar to curcumin, there are multiple steps involved in the release of ASC-J9 from the surface of the nanoparticles including initial diffusion, water penetration to release the entrapped drug and the nanoparticle degradation [412]. In agreement with a previously reported study [96], more than half of the loaded drug was released in the first 12 hours of incubation at 37 °C (**Figure 5.6**). This was followed by a slower release with 70-74% of the loaded drug released after 72 h. The cumulative drug release reached a plateau, suggesting a continuous and sustained release by MSNPs and G3-MSNPs with no statistically significant difference between the two (**Figure 5.6**).

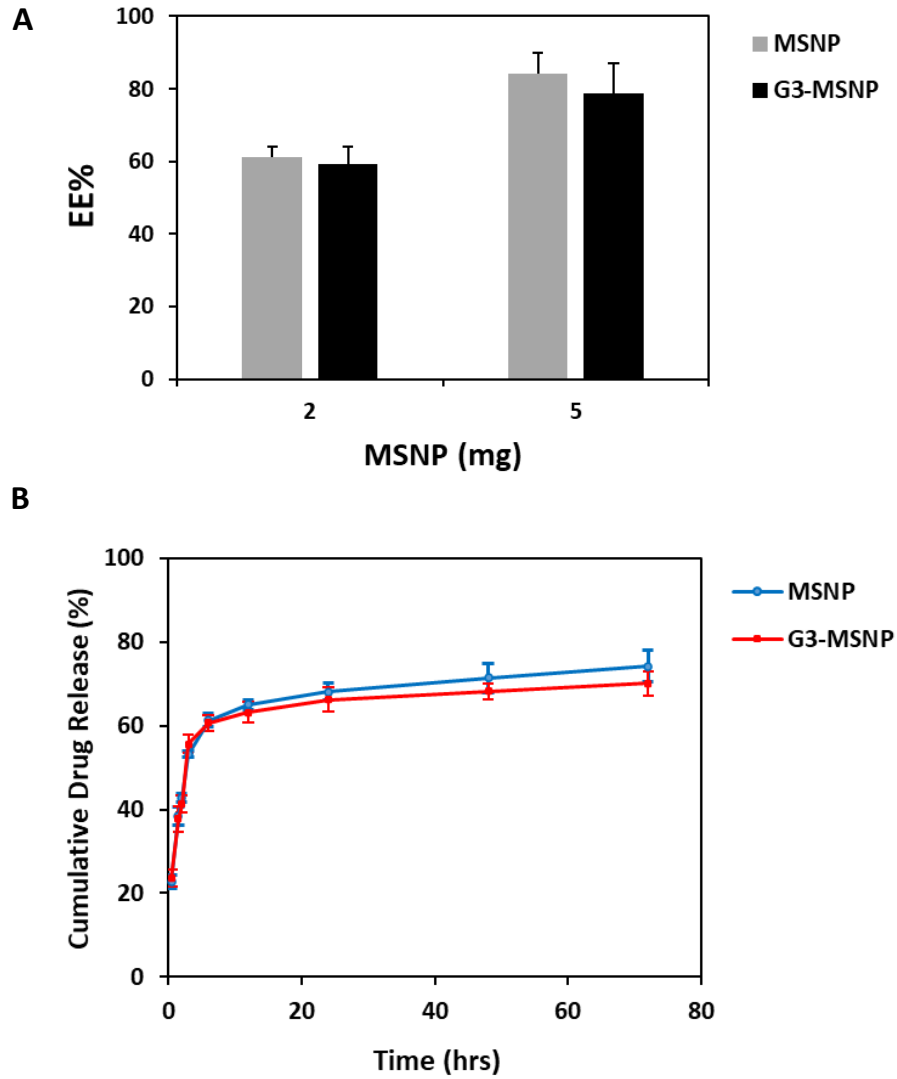


Figure 5. 6. (A) Encapsulation efficiency (EE%) of ASC-I9 demonstrates the amount of drug loaded to the nanoparticles to the amount of drug that initially mixed with the nanoparticles. (B) Drug release profile of ASC-I9 shows the amount of released drug (unloaded) from the nanoparticles with time at 37 °C.

5.2.2 Cellular uptake and cytotoxicity study

Naturally occurring or synthetic cationic amphiphilic peptides with the ability to penetrate the cell membranes have been widely used for drug delivery and targeting [413]. Many of these peptides have α -helical structures or can form transmembrane α -helices [414]. Recent mechanistic simulation studies reported that the formation of transmembrane helix allows for a firm amphiphilic structure that can enhance membrane interaction and promote permeability [415, 416]. Recently, a short α -helical cationic amphiphilic peptide named G3, with the structure G(IKK)₃I-NH₂, has been designed by Hu et al with the ability to penetrate into the cancer cells and selective anticancer activity [404]. The higher selectivity of G3 for cancer cells over normal mammalian cells has made it a promising tool for targeted drug or gene delivery to cancer cells [399, 403]. However, the cellular uptake of the peptide was found to be concentration and time-dependent [403]. In our cellular uptake study, the impact of grafting G3 on MSNP on cellular uptake was evaluated and the corresponding cytotoxicity was also assessed (**Figure 5.7**).

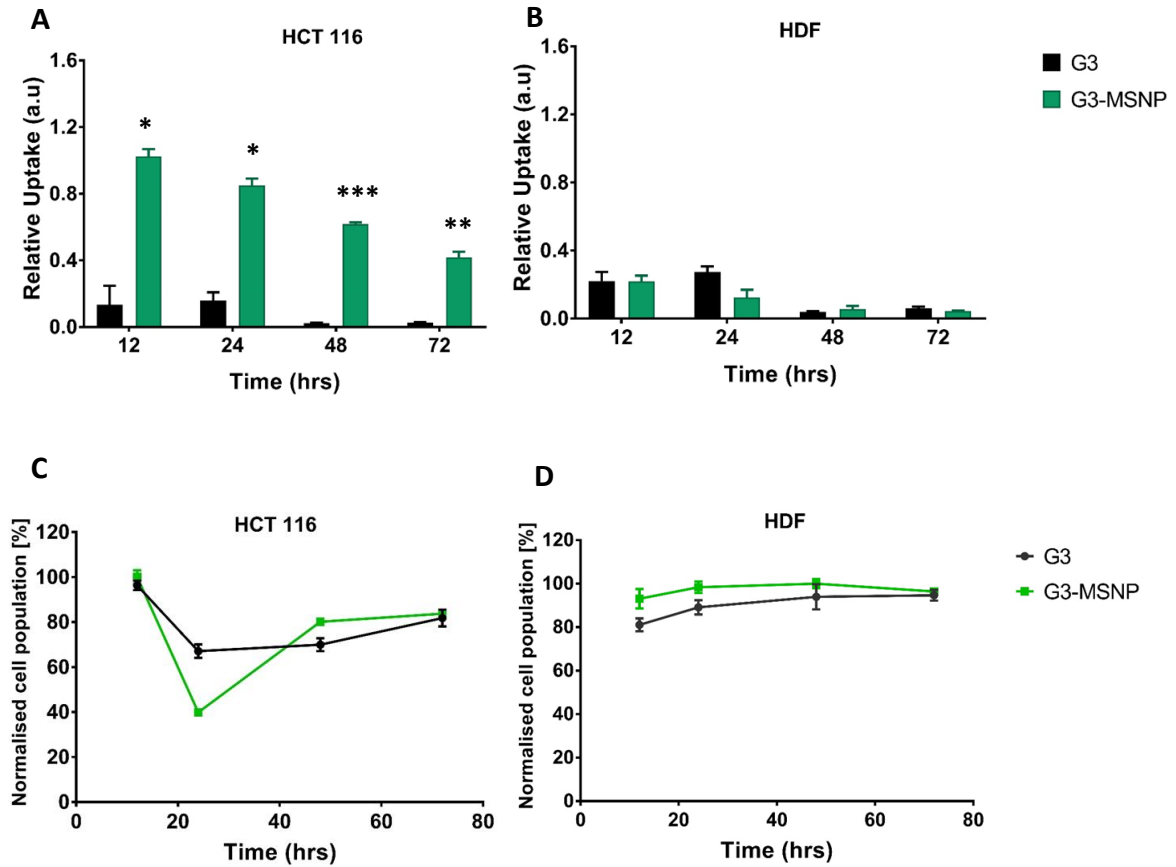


Figure 5. 7. The cellular uptake and cytotoxicity study of free G3 peptide and magnetic silk nanoparticles grafted with G3 peptide (G3-MSNP) assessed in both cancer and non-cancer cell lines to investigate the impact of G3-MSNP on the activity of G3 peptide in the cellular microenvironment. (A & B) The cellular uptake of free G3 and G3-MSNPs in colorectal cancer cells (HCT 116) and normal human dermal fibroblast cells (HDF). (C & D) Cytotoxicity of free G3 peptide and magnetic silk nanoparticles grafted with G3 peptide (G3-MSNPs) in HCT 116 and HDF cells. An asterisk denotes statistical significance as follows: * $P < 0.05$, ** $P < 0.01$, *** $P < 0.001$.

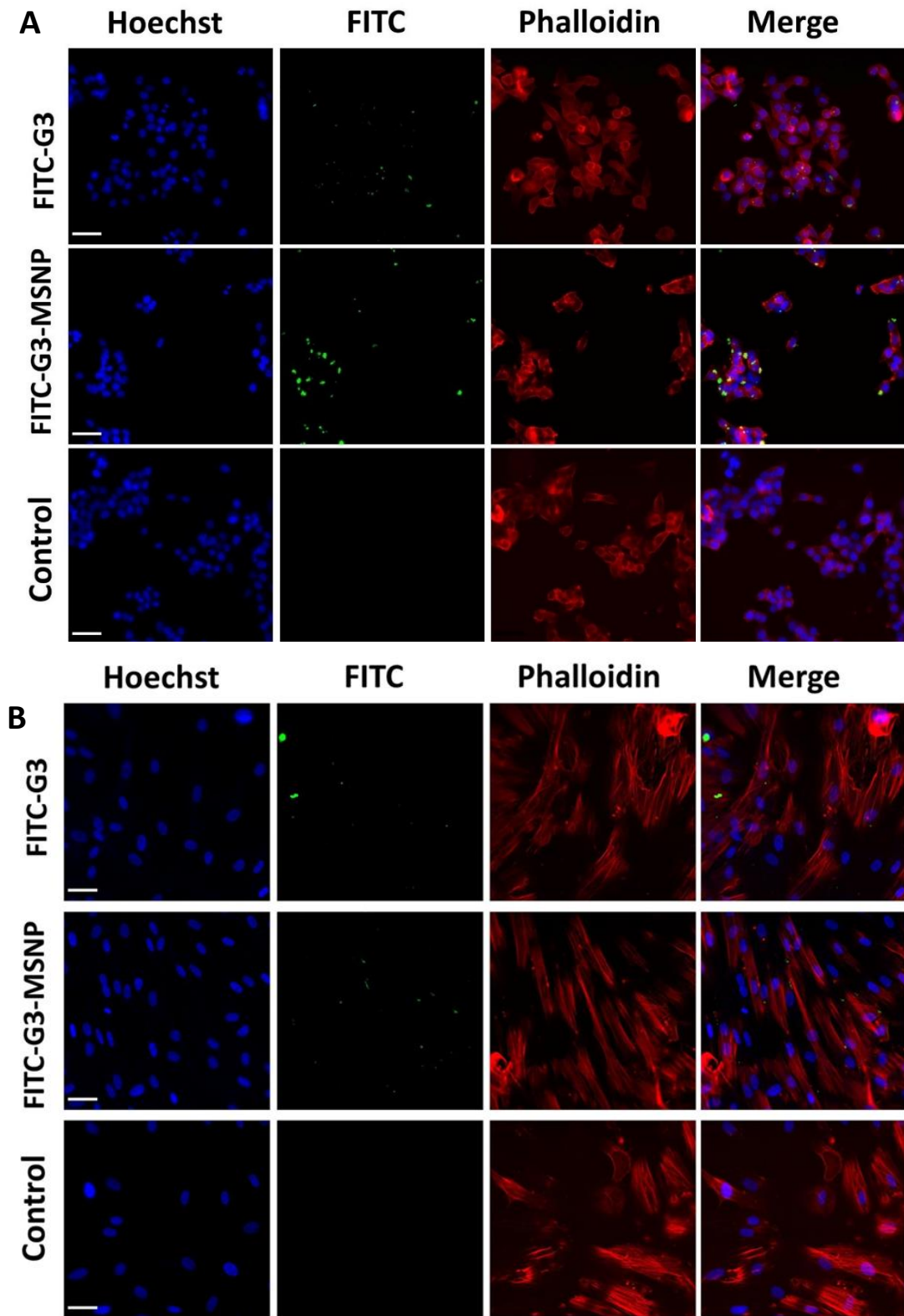


Figure 5. 8. High content microscopy images of colorectal cancer cells (HCT 116) **(A)** and normal human dermal fibroblast (HDF) cells **(B)** treated with fluorescently labelled G3 peptide (FITC-G3) or magnetic silk nanoparticles grafted with FITC-labelled G3 (FITC-G3-MSNP) at the concentration of 25 μ M for 6 h. The nuclei of the cells are stained with Hoechst 33342 stain (blue), the cytoplasm is stained with Flash Phalloidin™ 594 (red) and the fluorescent from FITC

is observed in the green channel of the fluorescence microscope. ×20 magnification, scale bars represent 50 μm.

The cellular uptake of the free FITC-labelled G3 and FITC-labelled G3 grafted on magnetic silk nanoparticles (FITC-G3-MSNP) was studied by measuring the fluorescence intensity of FITC using high content microscopy. After 6 hrs incubation, higher cellular uptake was observed in the FITC-G3-MSNP in comparison to free FITC-G3 (**Figure 5.7 & 5.8**). This tangible increase in the cellular uptake of FITC-G3 can indicate that MSNPs facilitate the peptide internalization by the HCT 116, thereby allow for a higher accumulation of G3 peptide in the cell's cytoplasm in the exposure time window (6 hrs) (**Figure 5.7 A&B**). Although the relative uptake of FITC-G3 was reducing with time, the FITC-G3-MSNP uptake remained higher than free FITC-G3 in all tested time points. The uptake of FITC-G3 and FITC-G3-MSNP was significantly lower in HDF cells in comparison to HCT 116 which is consistent with the results of previous studies [403]. The cytotoxicity study was performed by measuring the reduction in the cell population using high content microscope. The cells proliferation plots showed a significant reduction in the cell population in both treatments before it starts to show recovery after 24 hrs (**Figure 5.7 C&D**). However, FITC-G3-MSNP demonstrated higher growth suppression than free FITC-G3 which might be a result of the difference in their cellular uptake.

The cellular uptake study of the tested anticancer drug (ASC-J9) was also performed on HCT 116 and HDF cells after 6 hrs incubation at 37 °C with MSNP and G3-MSNP, both loaded with ASC-J9 (40 μM). In this case, the fluorescence from ASC-J9 ($\lambda_{exc} = 432 \text{ nm}$; $\lambda_{emi} = 522 \text{ nm}$) was used to measure the cellular uptake [96] and the G3 was not fluorescently labelled to allow for accurate detection of the cellular uptake of the drug. Due to its high hydrophobicity and relatively short half-life (less than 6 hrs), free ACS-J9 has low cellular uptake. Similar to FITC-G3 cellular uptake study, the two nanoparticle formulations (MSNP-ASC-J9 and G3-MSNP-ASC-J9) demonstrated significantly higher uptake in HCT-116 than free ASC-J9 (**Figure 5.9 & 5.10**). On the other hand, all the tested treatment of ASC-J9 showed very low cellular uptake in HDF (**Figure 5.11**). The two formulations of ASC-J9 loaded nanoparticles suppressed the HCT 116 growth more strongly than free ASC-J9. In addition, the G3-MSNP-ASC-J9 showed the highest anticancer activity among all of the treatments, reducing the cell population to

less than 10 percent and preventing recovery (**Figure 5.9**). These results indicate that G3-MSNP-ASC-J9 has an augmented anticancer effect compared to ASC-J9 and G3 alone.

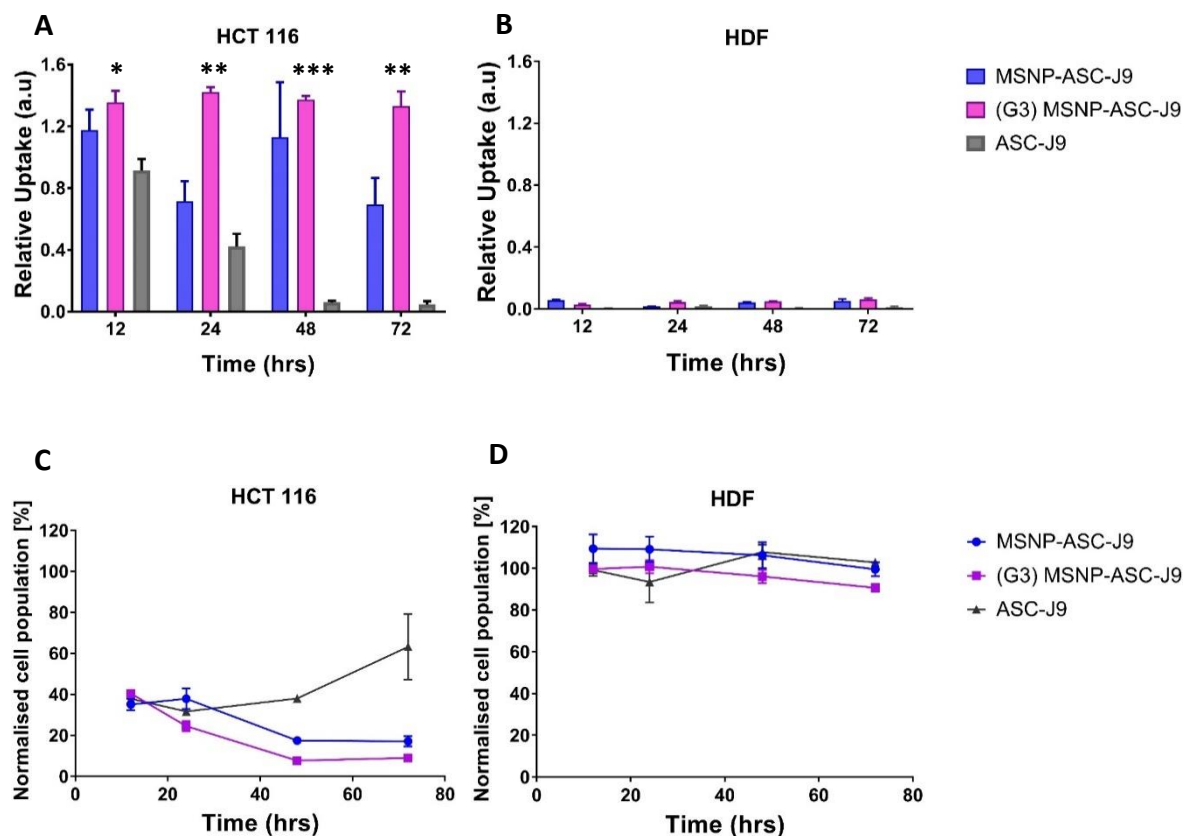


Figure 5. 9. (A & B) Cellular uptake of MSNP and (G3)-MSNP loaded with ASC-J9 compared to free ASC-J9 in HCT 116 cells and HDF cells. (C & D) Cytotoxicity study of MSNP and (G3)-MSNP loaded with ASC-J9 compared to free ASC-J9 in HCT 116 cells and HDF cells. An asterisk denotes statistical significance as follows: * $P < 0.05$, ** $P < 0.01$, *** $P < 0.001$.

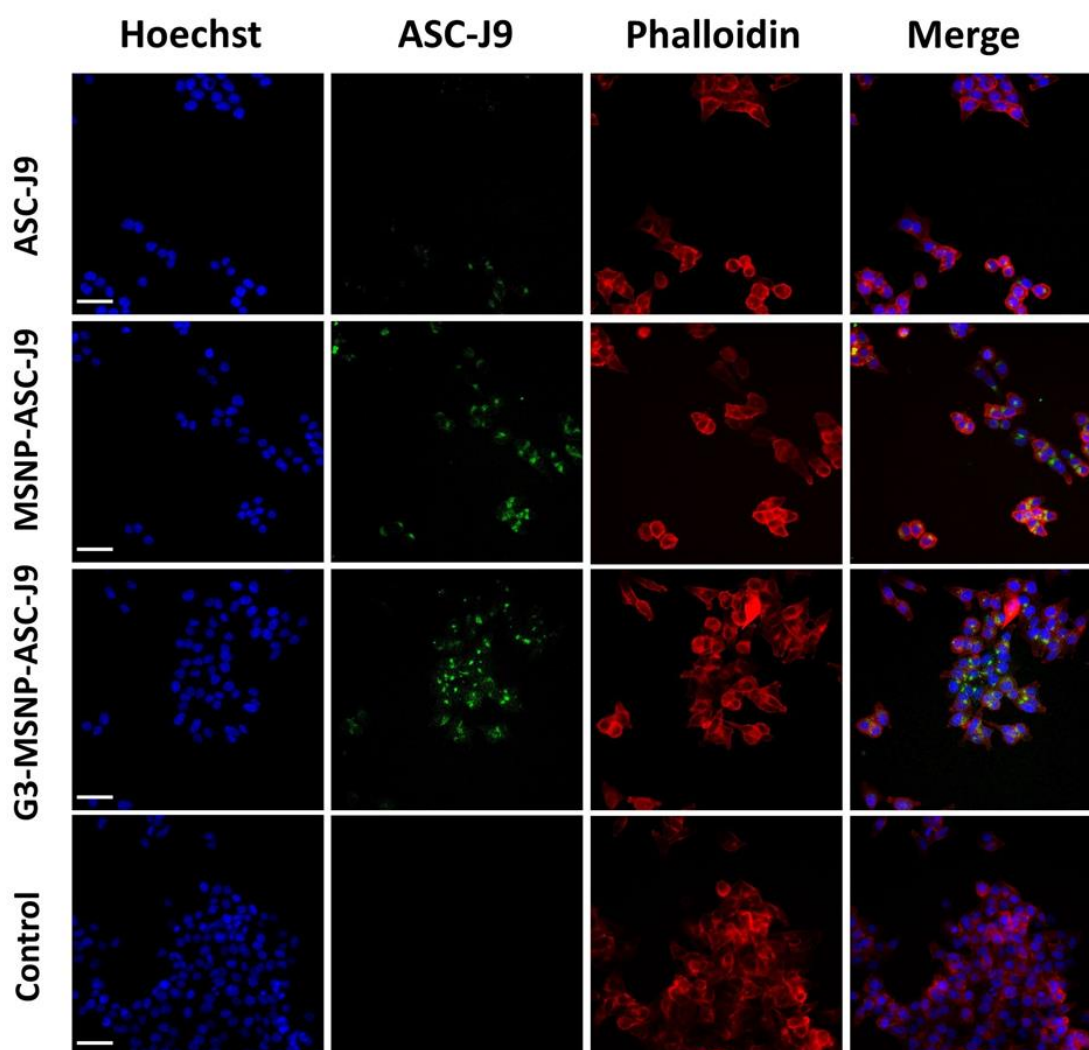


Figure 5. 10. High content microscopy images of HCT 116 cells treated with free ASC-J9, MSNPs loaded with ASC-J9 and G3-MSNPs loaded with ASC-J9 for 6 h. The nuclei are stained with Hoechst 33342 (blue), the cytoplasm is stained with Flash Phalloidin™ 594 (red) and the fluorescent from ASC-J9 is observed in green. $\times 20$ magnification, scale bars represent 50 μm .

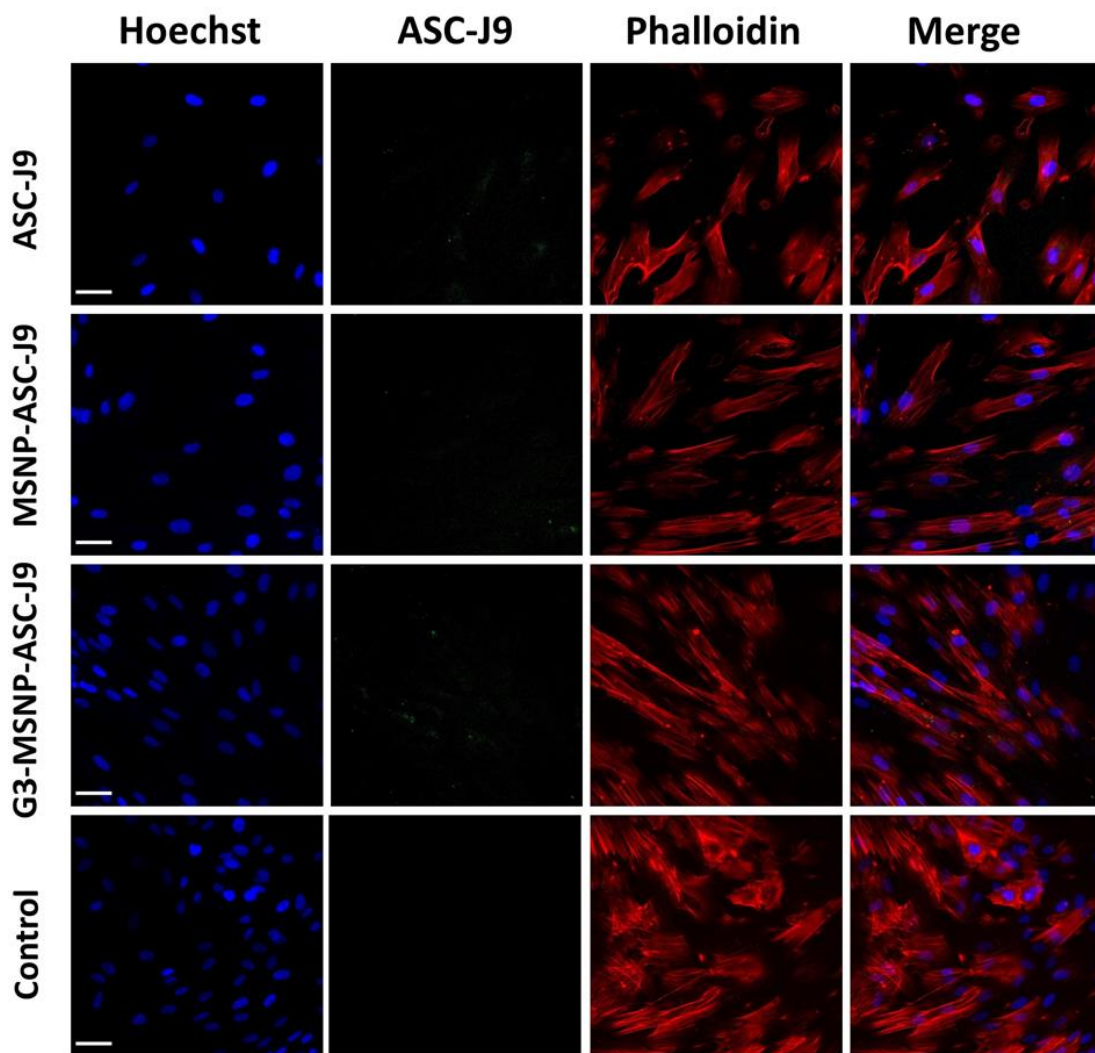


Figure 5. 11. High content microscopy images of HDF cells treated with free ASC-J9, MSNPs loaded with ASC-J9 and G3-MSNPs loaded with ASC-J9 for 6 h. The nuclei are stained with Hoechst 33342 (blue), the cytoplasm is stained with Flash Phalloidin™ 594 (red) and the fluorescent from ASC-J9 is observed in green. $\times 20$ magnification, scale bars represent 50 μm .

5.2.3 Tumor-spheroid penetration study

Three-dimensional spheroids are typically used in *in vitro* studies, but they can resemble the *in vivo* microenvironment more closely than the 2D monolayer cell culture system. 3D spheroids can serve as *in vitro* models for simulating drug penetration into the tumor tissue [417]. In this study, the 3D colorectal tumor spheroids were formed after 48 hrs incubation of 8×10^3 HCT 116 cells in each well of ultra-low attachment 96 well plates. 10 μ l treatments containing 40 μ M of free ASC-J9 or ASC-J9 loaded into MSNP were added to the designated wells and incubated for 12 hrs. For the investigation of the impact of the magnetic field on the spheroid penetration, a Neodymium magnet (120 x 80 mm) was placed under the plate for 30 min. The spheroids were then fixed and stained for further analysis in the high content microscopy. Due to the inherent fluorescence of ASC-J9, the analysis of cellular uptake and penetration in spheroids is feasible using the high content microscopy. The spheroids treated with free ASC-J9 showed less fluorescence than all tested formulations (**Figure 5.12 & 5.13**). In agreement with the results from 2D cell culture (**Figure 5.9**), both MSNP and G3-MSNP enhanced ASC-J9 cellular uptake and penetration in HCT 116 spheroids. Further cellular uptake and penetration in both nanoparticle formulations (MSNP & G3-MSNP) was observed when magnetic field was applied (**Figure 5.12 & 5.13**).

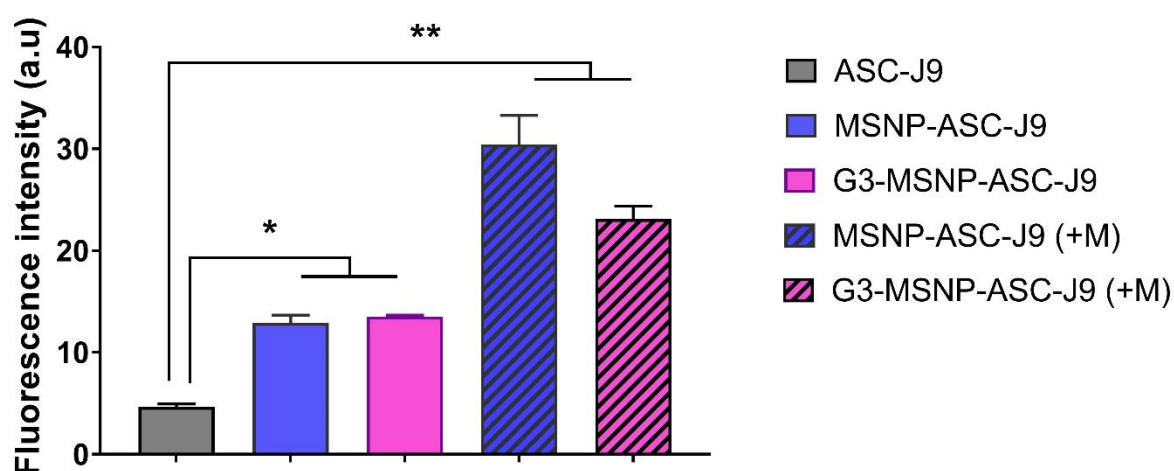


Figure 5. 12. Mean normalised fluorescence intensity of MSNP, G3-MSNP with and without magnetic field (+M) in comparison to free ASC-J9 after 12 h of treatment compared to the untreated controls. Data are presented as mean \pm SD (n=3). An asterisk denotes statistical significance as follows: * $P < 0.05$, ** $P < 0.01$, *** $P < 0.001$.

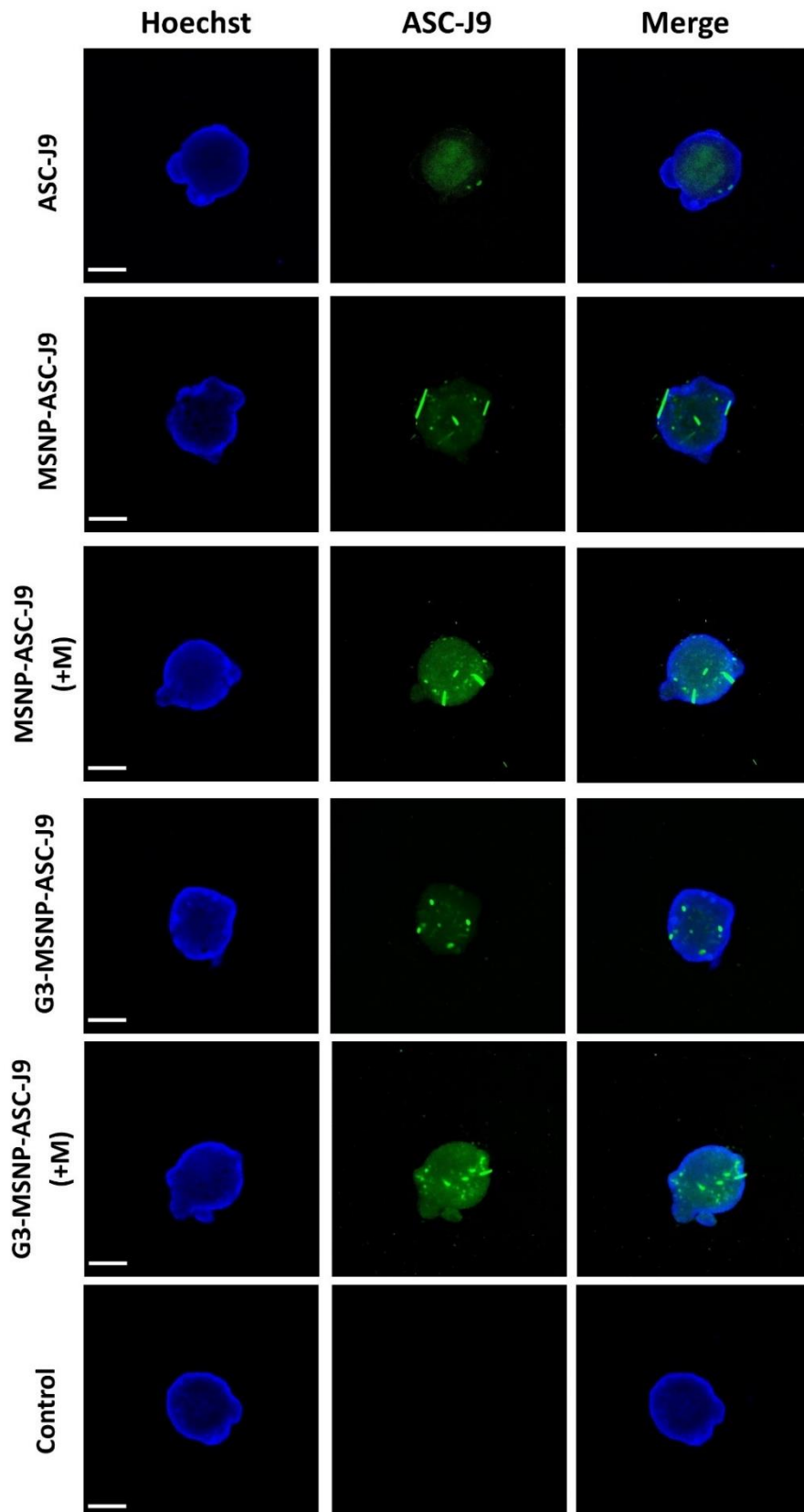


Figure 5. 13. High content microscope images of HCT 116 three dimensional multicellular tumor spheroids 12 h after treatment with ASC-J9 loaded MSNP, ASC-J9 loaded G3-MSNP or free ASC-J9 in the presence (+M) and absence of magnetic field in comparison to untreated controls. $\times 2$ magnification, Scale bar represents 400 μm .

5.3 Conclusion

In summary, this study reports magnetic silk nanoparticles (MSNP) with tunable properties prepared by microfluidic platform (swirl mixer) and functionalised with G3 peptide for the delivery of ASC-J9. The developed nanoparticles were characterized and evaluated as a potential drug delivery system with augmented anticancer activity. The G3 peptide, which is known for its anticancer activity, was successfully grafted on the surface of the microfabricated MSNPs. The anticancer activity of the formulated nanoparticles was investigated in colorectal cancer cells HCT 116 and fibroblast HDF. The G3 functionalised MSNP demonstrated significantly enhanced cellular uptake and cytotoxicity compared to non-functionalised MSNP despite the limited incubation time 6 hrs. However, no significant variation was recorded in HDF following treatment with either MSNP or G3-MSNP. Loading ASC-J9 onto the two formulations, enhanced the anticancer activity and cellular uptake leading to a steeper reduction in the cancer cell population and lower cancer cell recovery than free ASC-J9. These findings indicate a selective and augmented anticancer effect as a result of combining G3 with ASC-J9. Incorporating magnetic particles in prepared nanoformulations made the MSNPs and G3-MSNPs responsive to the magnetic field which could enhance the loaded drug accumulation in the tumor tissue. This was confirmed in the tumor-spheroid penetration study that did not only show an enhanced penetration of MSNPs and G3-MSNPs in comparison to free ASC-J9, but also higher penetration was observed in both nanoformulations when a magnetic field was applied. The reported data support the advantages of formulating short amphiphilic peptides with anticancer agents for cell selective and targeted anticancer therapy.

6 Chapter 6: Conclusion and the future perspective

6.1 Conclusion

In this thesis, several formulations were designed and manufactured using different biomaterials and proteins including silk fibroin, lipids, sodium alginate, magnetic particles and cationic short amphiphilic peptides. These nanoformulations served as nanocarriers for the model hydrophobic drug ASC-J9 and the efficiency of these nanocarriers was evaluated in terms of batch to batch variation, stability, encapsulation efficiency, drug release, cellular uptake and 3D tumor penetration. The formulations were rationally designed to modify the characteristics, the physicochemical properties of the nanocarriers, and improve their efficiency in drug delivery. Moreover, the preparation methods were designed and optimized to allow a suitable size for nanomedical application (<200 nm), reproducibility and high stability. In addition, a new microfluidic device was introduced using a novel design (swirl mixing elements) to provide a platform for microfabrication of nanomaterials at a high production rate. This microfluidic platform was employed in the production of two types of nanostructure (silk particles and magnetic silk particles).

The implementation of nanocarrier rational design for overcoming drug delivery barriers is the key for improved cancer therapy. As mentioned previously, the majority of studies have considered the common barriers for targeted drug delivery in their strategies to optimize several nanocarrier design parameters (e.g. size, shape and surface charge) [31]. However, recent studies have started recently investigating the impact of other factors such as deformability and biodegradability of the nanocarriers on drug delivery [15, 418]. The *in vivo* fate of the designed nanoparticle is important to assess for frequently used therapeutics. The lack of degradability of the administrated nanoformulation can accumulate in the body organs, causing undesirable side effects or toxicity. On the other hand, particles stability from time of administration to site of action has a major impact on the delivery performance of the loaded drug. For example, the degradation in blood circulation, before reaching the targeted tissue, can affect the drug release kinetics, which reduces the amount of drug at the site of action and increases the side effects. Therefore, using a biodegradable material, such as silk fibroin as the building block of many nanocarriers has been studied as they provide the desired stability in the body without causing toxicity or immunogenicity. Building on that,

biodegradable natural polymers, such as silk fibroin, sodium alginate or cationic peptides were used in the designed nanocarrier formulations introduced in this thesis.

More recently, deformability and stiffness modification of nanocarriers for optimizing the payload kinetics and regulating cellular uptake have been considered in the design strategy of nanostructures for nanomedical application. This feature has been studied in the formulations in Chapter 3, using a combination of biopolymers to change the stiffness of the nanocarrier. The findings from the stiffness-tunable nanocarriers showed an impact of changing rigidity on the drug encapsulation efficiency, drug release and cellular uptake. The stability study conducted on of the nanocarrier formulations also showed that rigidity minimized liposomal fusion and aggregation during storage.

Silk is a versatile biomaterial with great potential for drug and gene delivery applications. SF has been used as a naturally derived biopolymer for development of various types of drug delivery systems, including hydrogels, SF films, microparticles and nanoparticles using a variety of fabrication methods. Each of these SF-based systems have shown promising features for different biomedical applications. In this project, SF was formulated into lipid shell-nanogel drug carriers, SF nanoparticles and peptide-SF magnetic nanoparticles. In addition, these silk-based nanoformulation was used previously to load hydrophobic drugs and stabilise biological agents, such as horse radish peroxidase (HRP), glucose oxidase, vaccines and monoclonal antibodies, in order to enhance their shelf life. Functionalisation of SF with biological recognition elements, such as RGD sequence, folate and Her2, has been used for tissue-specific drug delivery. The findings reported in Chapters 3 & 5 confirm the ability of SF-based formulations to encapsulate active pharmaceutical ingredients (ASC-J9 & the G3 peptide), control drug release and enhance cellular uptake. The results presented in the thesis show the impact of combining SF with other ingredients (polysaccharides, lipids and crosslinkers) and the processing conditions on the properties of the SF-based formulations. Unlike previously reported work, the methods developed for producing SF formulations (extrusion of lipid templates and microfluidic platform) were robust and minimized batch to batch variation.

Nanoformulations that utilize biopolymers and lipids are the preferred drug and gene delivery systems in nanomedicine as they possess many advantages over viral vectors. The virus-mediated methods for gene delivery are easy to use and demonstrated high transfection

efficiency [419]. However, viral vectors have a potential risk of infecting healthy cells leading to undesirable side effects. Some viral vectors such as adenovirus can initiate a strong inflammatory immune response which can cause death in patients [420]. Moreover, the amount of the delivered genetic material is limited by the capacity of the viral vector to carry and insert this material into the cells. Electroporation is another gene delivery method that has been studied as an alternative method for viral vectors. Electroporation is a phenomenon that occurs in the cellular membrane allowing it to perforate and deliver exogenous nucleic acids (DNA or RNA) to the cell when a sufficient electrical field is applied [421]. Although this technique can target large number of cells with low toxicity, it is an invasive method that causes short-term pain and tissue damage [420, 421]. On the other hand, biopolymeric and lipid-based nanoparticles can open doors for a wide range of formulations that can be adjusted and modified according to the loaded material and the type of therapy. As discussed in this thesis, using biodegradable and natural ingredients prevent inducing an undesirable immune response and avoid any risk of toxicity. In addition, the ability to modify the properties (size, shape, charge, etc.) of nonviral vectors by using combinations of lipids and biopolymers or changing the processing parameters allows for optimizing the encapsulation and transfection efficiencies. Moreover, the recent advances in fabrication techniques of biopolymeric and lipid nanoformulations made scaling up production easier in comparison to conventional viral vectors.

The recent innovations and developments in microfluidic technology have offered a better alternative to many conventional techniques for designing and producing nanoparticles. The new designs of microfluidic systems have many functionalities that address many limitations of the early designs. This substantial improvement has made the microfluidic platform an effective tool in fabricating a wide range of formulations for drug and gene delivery. The main obstacles facing formulation development in nanomedicine are reproducibility and tunability of the nanoparticles' parameters. These challenges affect the translation of many potential nanocarriers from benchtop to large-scale production. Most of the nanocarriers that are formulated to load and deliver anticancer drugs are produced by rapid nanoprecipitation or self-assembly. Both mechanisms are difficult to control in conventional bulk preparation methods, especially when dealing with protein-based preparations, leading to a lack of uniformity of the produced particles, and large batch-to-batch variation. The rapid

microfluidic mixing is a robust alternative technique allowing for controlled microfabrication conditions that can tune the size, shape and maintain reproducibility. Changing the processing parameters and the mixer geometric design does not only manipulate the flow regime of the mixed solutions, but also alters the properties of the produced nanoparticles. In Chapter 4, a novel swirl mixer design was introduced as an improved microfluidic platform for large scale production of nanostructures. The new design showed an improved production rate with total flow rate 112 ml/min, this is much higher than the previously reported mixer designs (e.g. Staggered herringbone). The swirl mixer performance and mixing efficiency was evaluated in comparison to a typical microfluidic design (T-mixer) with same channel dimensions and operating at the same processing conditions using silk fibroin as a model precursor. The swirl mixer performed significantly better in controlling particle size than the T-mixer under different flow regimes. The swirl mixer results show a great potential for large scale production of nanomaterials in the pharmaceutical industry.

6.2 Future work

The findings presented in the experimental chapters of this thesis indicate a significant impact of the nanocarrier properties and composition on targeted drug delivery. Modifying the stiffness, adding magnetic nanoparticles or functionalising the surface of nanocarriers showed a tangible effect on, cellular uptake, tumor penetration and targetability. These results were obtained from 2 D and 3 D *in vitro* cellular studies. However, *in vivo* studies are required for further investigation of the impact of nanocarrier formulation, and the overall performance on drug delivery. The animal studies using animal models, such as rats or mice, can provide a better insight into the changes in circulation time of the nanocarriers in the blood stream and tumour accumulation (**Figure 6.1**). In the animal study, it is possible to monitor the tumour size with time after each of the animals under study are injected with a different nanocarrier formulation. The ability of the nanocarrier to penetrate and accumulate in the tumour tissue can be evaluated more precisely in the biological environment. Moreover, targetability of nanocarriers such, as magnetic silk nanoparticles (MSNP) can be investigated more closely by using a magnetic field on the tumour induced tissue in a model animal (**Figure 6.1**).

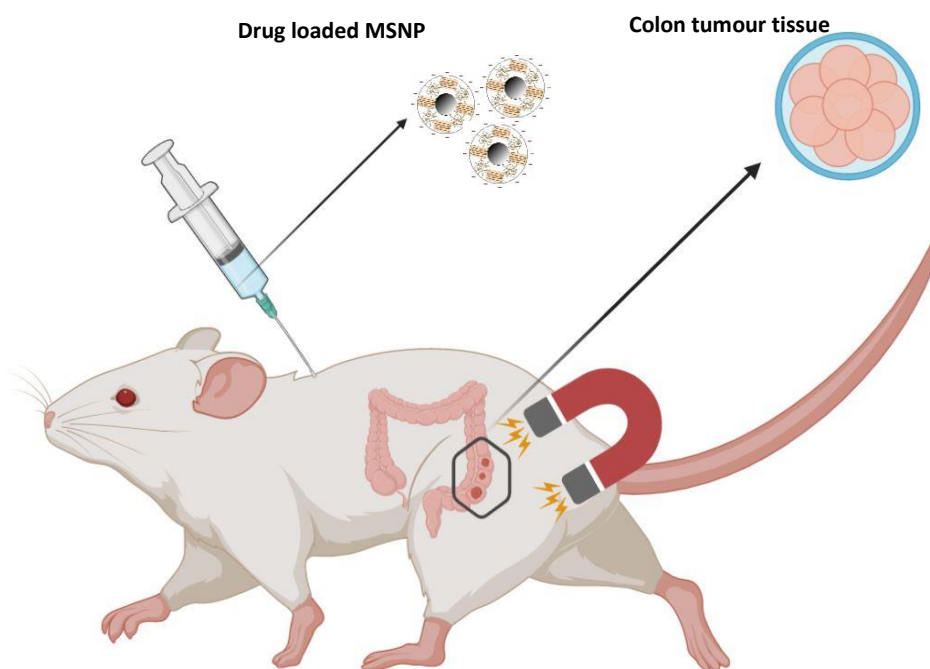


Figure 6. 1. Schematic representation of future in vivo experiments for further investigation of the activity and targetability of drug loaded magnetic silk nanoparticles. Created by BioRender.

The designed nanoformulation in Chapter 3 (lipid shell and biopolymeric core) can be used for the delivery of DNA or RNA to the target cells. In order to capture genetic material, a cationic lipid such as Dioleoyl-3-trimethylammonium propane (DOTAP) should be added in an appropriate molar ratio with the zwitterionic lipid (DOPC) to make a lipid mixture before forming the thin lipid layer by rotary evaporator as described in section 2.2.1.3. This modification in the formulation allows for forming positively charged nanocarriers that are capable of capturing the negatively charged genetic material (RNA or DNA). The encapsulation and the transfection efficiencies can be evaluated in macrophages or in cancer cell lines depending on the type of RNA or DNA used. In addition, the impact of the nanocarriers' stiffness on gene delivery can be assessed in a similar manner to the study presented in Chapter 3. As shown in Figure S2 (Supplementary information) the presented microfluidic device (Chapter 4 & 5) can produce lipid nanoparticles with different size and size distributions. As discussed earlier, the large scale production of RNA loaded lipid nanoparticles has attracted more attention recently to meet the increasing demand for RNA-

based vaccines. Different lipid combinations and processing conditions including; aqueous phases (buffers) and organic phases (water-miscible organic solvents) can be screened to optimize the production of lipid nanoparticles for gene delivery by using the swirl mixer.

There are many hurdles for microfluidic mixing to become widely applicable in the pharmaceutical industry. In Chapter 4, the swirl mixer addressed one of the most common limitations such as low production rate and inefficient mixing. However, the single step microfabrication induced by this microfluidic system is not suitable for all types of nanoformulations. For example, layer-by-layer assembly and coating protocols require completely different mixing conditions from the ones that are taking place in swirl or T-mixer (fast nanoprecipitation). Instead of using only two inlets, the biggest room for improvement of the current swirl mixer design is to include additional inlets (**Figure 6.2**). These additional inlets can be used to terminate the mixing process by adding a new fluid to the system, encapsulating active ingredients or to fabricate a more complicated drug delivery system by coating or functionalising the generated particles. In Chapter 5, the G3 peptide can be added to the formulation by introducing a third solution through an additional inlet. Another modification to consider for the future work on the swirl mixer is to combine advance characterization techniques such as dynamic light scattering, confocal Raman microscopy, and fluorescence resonance energy transfer (FRET) to the outlet of the current system (**Figure 6.2**). Introducing a camera system and using transparent materials (glass) in the mixer chips allows for monitoring the flow, the formation of bubbles, and blockage of a certain part of the channels. Implementing these techniques in the microfluidic system allows for a real-time characterization of the formed nanoparticles inside the microfluidic device. It can also help in providing the required feedback for optimizing the processing parameters directly such as total flow rate and flow rate ratio.

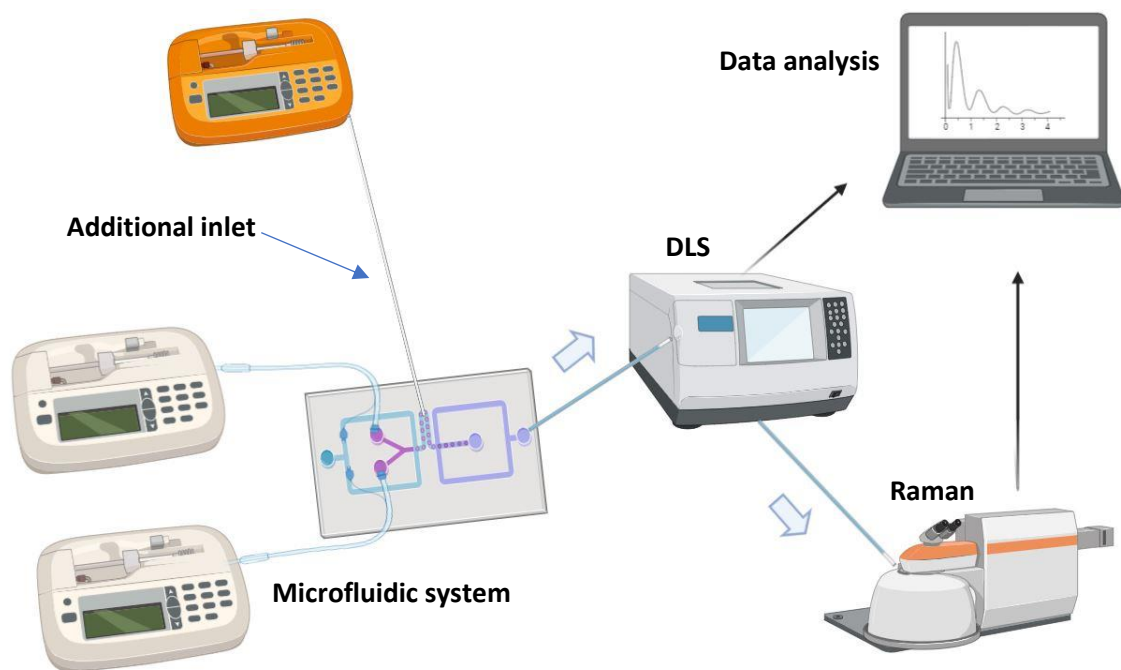


Figure 6. 2. Schematic representation of design modifications of the current microfluidic system and additional characterizations equipment that should be considered for optimizing nanoparticle production. Created by BioRender.

7 References

- [1] J.E. Kipp, The role of solid nanoparticle technology in the parenteral delivery of poorly water-soluble drugs, *Int J Pharm*, 284 (2004) 109-122.
- [2] A.N. Lukyanov, V.P. Torchilin, Micelles from lipid derivatives of water-soluble polymers as delivery systems for poorly soluble drugs, *Advanced Drug Delivery Reviews*, 56 (2004) 1273-1289.
- [3] P. Ettmayer, G.L. Amidon, B. Clement, B. Testa, Lessons Learned from Marketed and Investigational Prodrugs, *Journal of Medicinal Chemistry*, 47 (2004) 2393-2404.
- [4] H. Gelderblom, J. Verweij, K. Nooter, A. Sparreboom, Cremophor EL: the drawbacks and advantages of vehicle selection for drug formulation, *European Journal of Cancer*, 37 (2001) 1590-1598.
- [5] K.T. Savjani, A.K. Gajjar, J.K. Savjani, Drug solubility: importance and enhancement techniques, *ISRN Pharm*, 2012 (2012) 195727.
- [6] D. Peer, J.M. Karp, S. Hong, O.C. Farokhzad, R. Margalit, R. Langer, Nanocarriers as an emerging platform for cancer therapy, *Nature Nanotechnology*, 2 (2007) 751.
- [7] X. Banquy, F. Suarez, A. Argaw, J.-M. Rabanel, P. Grutter, J.-F. Bouchard, P. Hildgen, S. Giasson, Effect of mechanical properties of hydrogel nanoparticles on macrophage cell uptake, *Soft Matter*, 5 (2009) 3984-3991.
- [8] V.P. Torchilin, Targeted pharmaceutical nanocarriers for cancer therapy and imaging, *Aaps j*, 9 (2007) E128-147.
- [9] P. Horcajada, T. Chalati, C. Serre, B. Gillet, C. Sebrie, T. Baati, J.F. Eubank, D. Heurtaux, P. Clayette, C. Kreuz, J.-S. Chang, Y.K. Hwang, V. Marsaud, P.-N. Bories, L. Cynober, S. Gil, G. Férey, P. Couvreur, R. Gref, Porous metal–organic-framework nanoscale carriers as a potential platform for drug delivery and imaging, *Nature Materials*, 9 (2009) 172.
- [10] M. Narvekar, H.Y. Xue, J.Y. Eoh, H.L. Wong, Nanocarrier for Poorly Water-Soluble Anticancer Drugs—Barriers of Translation and Solutions, *AAPS PharmSciTech*, 15 (2014) 822-833.
- [11] F. Alexis, E. Pridgen, L.K. Molnar, O.C. Farokhzad, Factors Affecting the Clearance and Biodistribution of Polymeric Nanoparticles, *Molecular Pharmaceutics*, 5 (2008) 505-515.
- [12] E. Blanco, H. Shen, M. Ferrari, Principles of nanoparticle design for overcoming biological barriers to drug delivery, *Nature biotechnology*, 33 (2015) 941-951.
- [13] S.F. Soh, C.K. Huang, S.O. Lee, D. Xu, S. Yeh, J. Li, E.L. Yong, Y. Gong, C. Chang, Determination of androgen receptor degradation enhancer ASC-J9((R)) in mouse sera and organs with liquid chromatography tandem mass spectrometry, *J Pharm Biomed Anal*, 88 (2014) 117-122.
- [14] P.M. Fracasso, K.A. Blum, M.K. Ma, B.R. Tan, L.P. Wright, S.A. Goodner, C.L. Fears, W. Hou, M.A. Arquette, J. Picus, A. Denes, J.E. Mortimer, L. Ratner, S.P. Ivy, H.L. McLeod, Phase I study of pegylated liposomal doxorubicin and the multidrug-resistance modulator, valspodar, *British Journal of Cancer*, 93 (2005) 46-53.
- [15] P. Guo, D. Liu, K. Subramanyam, B. Wang, J. Yang, J. Huang, D.T. Auguste, M.A. Moses, Nanoparticle elasticity directs tumor uptake, *Nature Communications*, 9 (2018) 130.
- [16] T. Wongpinyochit, P. Uhlmann, A.J. Urquhart, F.P. Seib, PEGylated Silk Nanoparticles for Anticancer Drug Delivery, *Biomacromolecules*, 16 (2015) 3712-3722.
- [17] Y. Dong, P. Dong, D. Huang, L. Mei, Y. Xia, Z. Wang, X. Pan, G. Li, C. Wu, Fabrication and characterization of silk fibroin-coated liposomes for ocular drug delivery, *European Journal of Pharmaceutics and Biopharmaceutics*, 91 (2015) 82-90.
- [18] N. Li, C. Zhuang, M. Wang, X. Sun, S. Nie, W. Pan, Liposome coated with low molecular weight chitosan and its potential use in ocular drug delivery, *Int J Pharm*, 379 (2009) 131-138.
- [19] P. Pradhan, J. Giri, F. Rieken, C. Koch, O. Mykhaylyk, M. Doblinger, R. Banerjee, D. Bahadur, C. Plank, Targeted temperature sensitive magnetic liposomes for thermo-chemotherapy, *J Control Release*, 142 (2010) 108-121.

- [20] F. Yuan, M. Dellian, D. Fukumura, M. Leunig, D.A. Berk, V.P. Torchilin, R.K. Jain, Vascular Permeability in a Human Tumor Xenograft: Molecular Size Dependence and Cutoff Size, *Cancer Research*, 55 (1995) 3752.
- [21] P. Couvreur, R. Gref, K. Andrieux, C. Malvy, Nanotechnologies for drug delivery: Application to cancer and autoimmune diseases, *Progress in Solid State Chemistry*, 34 (2006) 231-235.
- [22] V.P. Torchilin, Recent advances with liposomes as pharmaceutical carriers, *Nature Reviews Drug Discovery*, 4 (2005) 145.
- [23] G.H. Altman, F. Diaz, C. Jakuba, T. Calabro, R.L. Horan, J. Chen, H. Lu, J. Richmond, D.L. Kaplan, Silk-based biomaterials, *Biomaterials*, 24 (2003) 401-416.
- [24] R.H. Muller, K. Mader, S. Gohla, Solid lipid nanoparticles (SLN) for controlled drug delivery - a review of the state of the art, *Eur J Pharm Biopharm*, 50 (2000) 161-177.
- [25] M.J. Alonso, P. Couvreur, Historical view of the design and development of nanocarriers for overcoming biological barriers, in: *Nanostructured Biomaterials for Overcoming Biological Barriers*, The Royal Society of Chemistry Cambridge, UK, 2012, pp. 3-36.
- [26] A.O. Elzoghby, W.M. Samy, N.A. Elgindy, Albumin-based nanoparticles as potential controlled release drug delivery systems, *Journal of Controlled Release*, 157 (2012) 168-182.
- [27] X. Huang, C.S. Brazel, On the importance and mechanisms of burst release in matrix-controlled drug delivery systems, *J Control Release*, 73 (2001) 121-136.
- [28] A.M. Grumezescu, *Design and development of new nanocarriers*, William Andrew, 2017.
- [29] M. Brandl, Liposomes as drug carriers: a technological approach, in: *Biotechnology Annual Review*, Elsevier, 2001, pp. 59-85.
- [30] R. Moog, M. Brandl, R. Schubert, C. Unger, U. Massing, Effect of nucleoside analogues and oligonucleotides on hydrolysis of liposomal phospholipids, *Int J Pharm*, 206 (2000) 43-53.
- [31] R.A. Petros, J.M. DeSimone, Strategies in the design of nanoparticles for therapeutic applications, *Nature Reviews Drug Discovery*, 9 (2010) 615.
- [32] H. Yin, R.L. Kanasty, A.A. Eltoukhy, A.J. Vegas, J.R. Dorkin, D.G. Anderson, Non-viral vectors for gene-based therapy, *Nat Rev Genet*, 15 (2014) 541-555.
- [33] M.A. Tomeh, R. Hadianamrei, X. Zhao, Silk Fibroin as a Functional Biomaterial for Drug and Gene Delivery, *Pharmaceutics*, 11 (2019).
- [34] J.-M. Lim, N. Bertrand, P.M. Valencia, M. Rhee, R. Langer, S. Jon, O.C. Farokhzad, R. Karnik, Parallel microfluidic synthesis of size-tunable polymeric nanoparticles using 3D flow focusing towards in vivo study, *Nanomedicine: Nanotechnology, Biology and Medicine*, 10 (2014) 401-409.
- [35] Z. Yang, X. Luo, X. Zhang, J. Liu, Q. Jiang, Targeted delivery of 10-hydroxycamptothecin to human breast cancers by cyclic RGD-modified lipid-polymer hybrid nanoparticles, *Biomed Mater*, 8 (2013) 025012.
- [36] M.H.M. Leung, A.Q. Shen, Microfluidic assisted nanoprecipitation of PLGA nanoparticles for curcumin delivery to leukemia jurkat cells, *Langmuir*, 34 (2018) 3961-3970.
- [37] J. Nicolas, S. Mura, D. Brambilla, N. Mackiewicz, P. Couvreur, Design, functionalization strategies and biomedical applications of targeted biodegradable/biocompatible polymer-based nanocarriers for drug delivery, *Chemical Society Reviews*, 42 (2013) 1147-1235.
- [38] W. Cui, J. Li, G. Decher, Self-Assembled Smart Nanocarriers for Targeted Drug Delivery, *Advanced Materials*, 28 (2016) 1302-1311.
- [39] A.D. Bangham, R.W. Horne, Negative staining of phospholipids and their structural modification by surface-active agents as observed in the electron microscope, *Journal of Molecular Biology*, 8 (1964) 660-IN610.
- [40] D.S. Breslow, BIOLOGICALLY ACTIVE SYNTHETIC POLYMERS++Hercules Research Center Contribution No. 1674, in: H. Eisenberg (Ed.) *Macromolecular Chemistry*—11, Pergamon, 1977, pp. 103-113.
- [41] S.E. Gratton, P.A. Ropp, P.D. Pohlhaus, J.C. Luft, V.J. Madden, M.E. Napier, J.M. DeSimone, The effect of particle design on cellular internalization pathways, *Proc Natl Acad Sci U S A*, 105 (2008) 11613-11618.

- [42] Y. Yamamoto, Y. Nagasaki, Y. Kato, Y. Sugiyama, K. Kataoka, Long-circulating poly(ethylene glycol)-poly(D,L-lactide) block copolymer micelles with modulated surface charge, *J Control Release*, 77 (2001) 27-38.
- [43] F. Danhier, To exploit the tumor microenvironment: Since the EPR effect fails in the clinic, what is the future of nanomedicine?, *Journal of Controlled Release*, 244 (2016) 108-121.
- [44] S. Wilhelm, A.J. Tavares, Q. Dai, S. Ohta, J. Audet, H.F. Dvorak, W.C.W. Chan, Analysis of nanoparticle delivery to tumours, *Nature Reviews Materials*, 1 (2016) 16014.
- [45] J.K. Oh, D.J. Siegwart, H.-i. Lee, G. Sherwood, L. Peteanu, J.O. Hollinger, K. Kataoka, K. Matyjaszewski, Biodegradable Nanogels Prepared by Atom Transfer Radical Polymerization as Potential Drug Delivery Carriers: Synthesis, Biodegradation, in Vitro Release, and Bioconjugation, *Journal of the American Chemical Society*, 129 (2007) 5939-5945.
- [46] R.A. Petros, P.A. Ropp, J.M. DeSimone, Reductively Labile PRINT Particles for the Delivery of Doxorubicin to HeLa Cells, *Journal of the American Chemical Society*, 130 (2008) 5008-5009.
- [47] C. François-Martin, J.E. Rothman, F. Pincet, Low energy cost for optimal speed and control of membrane fusion, *Proceedings of the National Academy of Sciences*, 114 (2017) 1238.
- [48] K. Numata, D.L. Kaplan, Silk-based delivery systems of bioactive molecules, *Advanced Drug Delivery Reviews*, 62 (2010) 1497-1508.
- [49] W. Song, M. Muthana, J. Mukherjee, R.J. Falconer, C.A. Biggs, X. Zhao, Magnetic-Silk Core-Shell Nanoparticles as Potential Carriers for Targeted Delivery of Curcumin into Human Breast Cancer Cells, *ACS Biomaterials Science & Engineering*, 3 (2017) 1027-1038.
- [50] L.W. Seymour, D.R. Ferry, D. Anderson, S. Hesslewood, P.J. Julyan, R. Poyner, J. Doran, A.M. Young, S. Burtles, D.J. Kerr, Hepatic drug targeting: phase I evaluation of polymer-bound doxorubicin, *J Clin Oncol*, 20 (2002) 1668-1676.
- [51] M.E. Davis, The first targeted delivery of siRNA in humans via a self-assembling, cyclodextrin polymer-based nanoparticle: from concept to clinic, *Mol Pharm*, 6 (2009) 659-668.
- [52] S. Danson, D. Ferry, V. Alakhov, J. Margison, D. Kerr, D. Jowle, M. Brampton, G. Halbert, M. Ranson, Phase I dose escalation and pharmacokinetic study of pluronic polymer-bound doxorubicin (SP1049C) in patients with advanced cancer, *Br J Cancer*, 90 (2004) 2085-2091.
- [53] J.P. Rolland, B.W. Maynor, L.E. Euliss, A.E. Exner, G.M. Denison, J.M. DeSimone, Direct Fabrication and Harvesting of Monodisperse, Shape-Specific Nanobiomaterials, *Journal of the American Chemical Society*, 127 (2005) 10096-10100.
- [54] G. Bozzuto, A. Molinari, Liposomes as nanomedical devices, *International Journal of Nanomedicine*, 10 (2015) 975-999.
- [55] J.F. Kukowska-Latallo, K.A. Candido, Z. Cao, S.S. Nigavekar, I.J. Majoros, T.P. Thomas, L.P. Balogh, M.K. Khan, J.R. Baker, Jr., Nanoparticle targeting of anticancer drug improves therapeutic response in animal model of human epithelial cancer, *Cancer Res*, 65 (2005) 5317-5324.
- [56] T.Y. Kim, D.W. Kim, J.Y. Chung, S.G. Shin, S.C. Kim, D.S. Heo, N.K. Kim, Y.J. Bang, Phase I and pharmacokinetic study of Genexol-PM, a cremophor-free, polymeric micelle-formulated paclitaxel, in patients with advanced malignancies, *Clin Cancer Res*, 10 (2004) 3708-3716.
- [57] C.C. Lee, E.R. Gillies, M.E. Fox, S.J. Guillaudeu, J.M. Frechet, E.E. Dy, F.C. Szoka, A single dose of doxorubicin-functionalized bow-tie dendrimer cures mice bearing C-26 colon carcinomas, *Proc Natl Acad Sci U S A*, 103 (2006) 16649-16654.
- [58] F. Ahmed, R.I. Pakunlu, G. Srinivas, A. Brannan, F. Bates, M.L. Klein, T. Minko, D.E. Discher, Shrinkage of a Rapidly Growing Tumor by Drug-Loaded Polymersomes: pH-Triggered Release through Copolymer Degradation, *Molecular Pharmaceutics*, 3 (2006) 340-350.
- [59] D.V. Morrissey, J.A. Lockridge, L. Shaw, K. Blanchard, K. Jensen, W. Breen, K. Hartsough, L. Machemer, S. Radka, V. Jadhav, N. Vaish, S. Zinnen, C. Vargeese, K. Bowman, C.S. Shaffer, L.B. Jeffs, A. Judge, I. MacLachlan, B. Polisky, Potent and persistent in vivo anti-HBV activity of chemically modified siRNAs, *Nat Biotechnol*, 23 (2005) 1002-1007.
- [60] C. Webb, N. Forbes, C.B. Roces, G. Anderluzzi, G. Lou, S. Abraham, L. Ingalls, K. Marshall, T.J. Leaver, J.A. Watts, J.W. Aylott, Y. Perrie, Using microfluidics for scalable manufacturing of

- nanomedicines from bench to GMP: A case study using protein-loaded liposomes, *International Journal of Pharmaceutics*, 582 (2020) 119266.
- [61] J. Rejman, V. Oberle, I.S. Zuhorn, D. Hoekstra, Size-dependent internalization of particles via the pathways of clathrin- and caveolae-mediated endocytosis, *Biochem J*, 377 (2004) 159-169.
- [62] S.D. Conner, S.L. Schmid, Regulated portals of entry into the cell, *Nature*, 422 (2003) 37.
- [63] L. Xu, Q. Bai, X. Zhang, H. Yang, Folate-mediated chemotherapy and diagnostics: An updated review and outlook, *Journal of Controlled Release*, 252 (2017) 73-82.
- [64] C.P. Leamon, S.R. Cooper, G.E. Hardee, Folate-liposome-mediated antisense oligodeoxynucleotide targeting to cancer cells: evaluation in vitro and in vivo, *Bioconjug Chem*, 14 (2003) 738-747.
- [65] S. Ni, S.M. Stephenson, R.J. Lee, Folate receptor targeted delivery of liposomal daunorubicin into tumor cells, *Anticancer Res*, 22 (2002) 2131-2135.
- [66] Contributors to Volume 391, in: *Methods in Enzymology*, Academic Press, 2005, pp. ix-xii.
- [67] L. Tong, W. Chen, J. Wu, H. Li, Folic acid-coupled nano-paclitaxel liposome reverses drug resistance in SKOV3/TAX ovarian cancer cells, *Anti-Cancer Drugs*, 25 (2014) 244-254.
- [68] H. Hatakeyama, H. Akita, K. Maruyama, T. Suhara, H. Harashima, Factors governing the in vivo tissue uptake of transferrin-coupled polyethylene glycol liposomes in vivo, *Int J Pharm*, 281 (2004) 25-33.
- [69] L. Han, R. Huang, S. Liu, S. Huang, C. Jiang, Peptide-Conjugated PAMAM for Targeted Doxorubicin Delivery to Transferrin Receptor Overexpressed Tumors, *Molecular Pharmaceutics*, 7 (2010) 2156-2165.
- [70] M. Singh, Transferrin as a targeting ligand for liposomes and anticancer drugs, *Current pharmaceutical design*, 5 (1999) 443-452.
- [71] M.K. Riaz, X. Zhang, K.H. Wong, H. Chen, Q. Liu, X. Chen, G. Zhang, A. Lu, Z. Yang, Pulmonary delivery of transferrin receptors targeting peptide surface-functionalized liposomes augments the chemotherapeutic effect of quercetin in lung cancer therapy, *International journal of nanomedicine*, 14 (2019) 2879-2902.
- [72] J. Huwlyer, D. Wu, W.M. Pardridge, Brain drug delivery of small molecules using immunoliposomes, *Proceedings of the National Academy of Sciences of the United States of America*, 93 (1996) 14164-14169.
- [73] X. Guo, F.C. Szoka, Jr., Steric stabilization of fusogenic liposomes by a low-pH sensitive PEG--diortho ester--lipid conjugate, *Bioconjugate chemistry*, 12 (2001) 291-300.
- [74] T.L. Andresen, S.S. Jensen, K. Jorgensen, Advanced strategies in liposomal cancer therapy: problems and prospects of active and tumor specific drug release, *Progress in lipid research*, 44 (2005) 68-97.
- [75] R.L. Siegel, K.D. Miller, A. Jemal, Cancer statistics, 2017, *CA: A Cancer Journal for Clinicians*, 67 (2017) 7-30.
- [76] A.P. Gupta, P. Pandotra, R. Sharma, M. Kushwaha, S. Gupta, Chapter 8 - Marine Resource: A Promising Future for Anticancer Drugs, in: R. Atta ur (Ed.) *Studies in Natural Products Chemistry*, Elsevier, 2013, pp. 229-325.
- [77] A. Umar, B.K. Dunn, P. Greenwald, Future directions in cancer prevention, *Nature Reviews Cancer*, 12 (2012) 835.
- [78] A.P. Gupta, S. Khan, M.M. Manzoor, A.K. Yadav, G. Sharma, R. Anand, S. Gupta, Chapter 10 - Anticancer Curcumin: Natural Analogues and Structure-Activity Relationship, in: R. Atta ur (Ed.) *Studies in Natural Products Chemistry*, Elsevier, 2017, pp. 355-401.
- [79] F. Alibeiki, N. Jafari, M. Karimi, H. Peeri Dogaheh, Potent anti-cancer effects of less polar Curcumin analogues on gastric adenocarcinoma and esophageal squamous cell carcinoma cells, *Scientific Reports*, 7 (2017) 2559.
- [80] A. Goel, A.B. Kunnumakkara, B.B. Aggarwal, Curcumin as "Curecumin": from kitchen to clinic, *Biochem Pharmacol*, 75 (2008) 787-809.

- [81] K. Nagahama, T. Utsumi, T. Kumano, S. Maekawa, N. Oyama, J. Kawakami, Discovery of a new function of curcumin which enhances its anticancer therapeutic potency, *Scientific Reports*, 6 (2016) 30962.
- [82] B.B. Aggarwal, L. Deb, S. Prasad, Curcumin differs from tetrahydrocurcumin for molecular targets, signaling pathways and cellular responses, *Molecules (Basel, Switzerland)*, 20 (2014) 185-205.
- [83] M. Gera, N. Sharma, M. Ghosh, D.L. Huynh, S.J. Lee, T. Min, T. Kwon, D.K. Jeong, Nanoformulations of curcumin: an emerging paradigm for improved remedial application, *Oncotarget*, 8 (2017) 66680-66698.
- [84] A.B. Kunnumakkara, D. Bordoloi, G. Padmavathi, J. Monisha, N.K. Roy, S. Prasad, B.B. Aggarwal, Curcumin, the golden nutraceutical: multitargeting for multiple chronic diseases, *Br J Pharmacol*, 174 (2017) 1325-1348.
- [85] P. Anand, C. Sundaram, S. Jhurani, A.B. Kunnumakkara, B.B. Aggarwal, Curcumin and cancer: an "old-age" disease with an "age-old" solution, *Cancer Lett*, 267 (2008) 133-164.
- [86] J. Barry, M. Fritz, J.R. Brender, P.E. Smith, D.K. Lee, A. Ramamoorthy, Determining the effects of lipophilic drugs on membrane structure by solid-state NMR spectroscopy: the case of the antioxidant curcumin, *J Am Chem Soc*, 131 (2009) 4490-4498.
- [87] M. Tsukamoto, K. Kuroda, A. Ramamoorthy, K. Yasuhara, Modulation of raft domains in a lipid bilayer by boundary-active curcumin, *Chemical communications (Cambridge, England)*, 50 (2014) 3427-3430.
- [88] H.-J. Koo, S. Shin, J.Y. Choi, K.-H. Lee, B.-T. Kim, Y.S. Choe, Introduction of Methyl Groups at C2 and C6 Positions Enhances the Antiangiogenesis Activity of Curcumin, *Scientific Reports*, 5 (2015) 14205.
- [89] A.K. Agrawal, C.M. Gupta, Tuftsin-bearing liposomes in treatment of macrophage-based infections, *Adv Drug Deliv Rev*, 41 (2000) 135-146.
- [90] W.-F. Chen, S.-L. Deng, B. Zhou, L. Yang, Z.-L. Liu, Curcumin and its analogues as potent inhibitors of low density lipoprotein oxidation: H-atom abstraction from the phenolic groups and possible involvement of the 4-hydroxy-3-methoxyphenyl groups, *Free Radical Biology and Medicine*, 40 (2006) 526-535.
- [91] H. Ohtsu, Z. Xiao, J. Ishida, M. Nagai, H.K. Wang, H. Itokawa, C.Y. Su, C. Shih, T. Chiang, E. Chang, Y. Lee, M.Y. Tsai, C. Chang, K.H. Lee, Antitumor agents. 217. Curcumin analogues as novel androgen receptor antagonists with potential as anti-prostate cancer agents, *J Med Chem*, 45 (2002) 5037-5042.
- [92] L. Lin, Q. Shi, C.Y. Su, C.C. Shih, K.H. Lee, Antitumor agents 247. New 4-ethoxycarbonylethyl curcumin analogs as potential antiandrogenic agents, *Bioorg Med Chem*, 14 (2006) 2527-2534.
- [93] Q. Shi, C.C.Y.S.a.K.H. Lee, Novel Anti-Prostate Cancer Curcumin Analogues That Enhance Androgen Receptor Degradation Activity, *Anti-Cancer Agents in Medicinal Chemistry*, 9 (2009) 904-912.
- [94] M.A. Cheng, F.-J. Chou, K. Wang, R. Yang, J. Ding, Q. Zhang, G. Li, S. Yeh, D. Xu, C. Chang, Androgen receptor (AR) degradation enhancer ASC-J9[®] in an FDA-approved formulated solution suppresses castration resistant prostate cancer cell growth, *Cancer Letters*, 417 (2018) 182-191.
- [95] T.H. Lin, K. Izumi, S.O. Lee, W.J. Lin, S. Yeh, C. Chang, Anti-androgen receptor ASC-J9 versus anti-androgens MDV3100 (Enzalutamide) or Casodex (Bicalutamide) leads to opposite effects on prostate cancer metastasis via differential modulation of macrophage infiltration and STAT3-CCL2 signaling, *Cell death & disease*, 4 (2013) e764.
- [96] P. Verderio, L. Pandolfi, S. Mazzucchelli, M.R. Marinozzi, R. Vanna, F. Gramatica, F. Corsi, M. Colombo, C. Morasso, D. Prosperi, Antiproliferative Effect of ASC-J9 Delivered by PLGA Nanoparticles against Estrogen-Dependent Breast Cancer Cells, *Molecular Pharmaceutics*, 11 (2014) 2864-2875.
- [97] X. Qiu, Y. Du, B. Lou, Y. Zuo, W. Shao, Y. Huo, J. Huang, Y. Yu, B. Zhou, J. Du, H. Fu, X. Bu, Synthesis and identification of new 4-arylidene curcumin analogues as potential anticancer agents targeting nuclear factor-kappaB signaling pathway, *J Med Chem*, 53 (2010) 8260-8273.

- [98] E. Ferrari, S. Lazzari, G. Marverti, F. Pignedoli, F. Spagnolo, M. Saladini, Synthesis, cytotoxic and combined cDDP activity of new stable curcumin derivatives, *Bioorganic & Medicinal Chemistry*, 17 (2009) 3043-3052.
- [99] Y.K. Cao, H.J. Li, Z.F. Song, Y. Li, Q.Y. Huai, Synthesis and biological evaluation of novel curcuminoid derivatives, *Molecules (Basel, Switzerland)*, 19 (2014) 16349-16372.
- [100] G. Xu, Y. Chu, N. Jiang, J. Yang, F. Li, The Three Dimensional Quantitative Structure Activity Relationships (3D-QSAR) and docking studies of curcumin derivatives as androgen receptor antagonists, *International journal of molecular sciences*, 13 (2012) 6138-6155.
- [101] B. Yadav, S. Taurin, R.J. Rosengren, M. Schumacher, M. Diederich, T.J. Somers-Edgar, L. Larsen, Synthesis and cytotoxic potential of heterocyclic cyclohexanone analogues of curcumin, *Bioorganic & Medicinal Chemistry*, 18 (2010) 6701-6707.
- [102] S.K. Sandur, M.K. Pandey, B. Sung, K.S. Ahn, A. Murakami, G. Sethi, P. Limtrakul, V. Badmaev, B.B. Aggarwal, Curcumin, demethoxycurcumin, bisdemethoxycurcumin, tetrahydrocurcumin and turmerones differentially regulate anti-inflammatory and anti-proliferative responses through a ROS-independent mechanism, *Carcinogenesis*, 28 (2007) 1765-1773.
- [103] M.E. Davis, Z.G. Chen, D.M. Shin, Nanoparticle therapeutics: an emerging treatment modality for cancer, *Nature reviews. Drug discovery*, 7 (2008) 771-782.
- [104] M. Sun, X. Su, B. Ding, X. He, X. Liu, A. Yu, H. Lou, G. Zhai, Advances in nanotechnology-based delivery systems for curcumin, *Nanomedicine (London, England)*, 7 (2012) 1085-1100.
- [105] O. Naksuriya, S. Okonogi, R.M. Schiffelers, W.E. Hennink, Curcumin nanoformulations: A review of pharmaceutical properties and preclinical studies and clinical data related to cancer treatment, *Biomaterials*, 35 (2014) 3365-3383.
- [106] F. Danhier, E. Ansorena, J.M. Silva, R. Coco, A. Le Breton, V. Préat, PLGA-based nanoparticles: An overview of biomedical applications, *Journal of Controlled Release*, 161 (2012) 505-522.
- [107] S. Fredenberg, M. Wahlgren, M. Reslow, A. Axelsson, The mechanisms of drug release in poly(lactic-co-glycolic acid)-based drug delivery systems—A review, *International Journal of Pharmaceutics*, 415 (2011) 34-52.
- [108] C. Dende, J. Meena, P. Nagarajan, V.A. Nagaraj, A.K. Panda, G. Padmanaban, Nanocurcumin is superior to native curcumin in preventing degenerative changes in Experimental Cerebral Malaria, *Scientific Reports*, 7 (2017) 10062.
- [109] J. Shaikh, D.D. Ankola, V. Beniwal, D. Singh, M.N.V.R. Kumar, Nanoparticle encapsulation improves oral bioavailability of curcumin by at least 9-fold when compared to curcumin administered with piperine as absorption enhancer, *European Journal of Pharmaceutical Sciences*, 37 (2009) 223-230.
- [110] W. Punfa, S. Yodkeeree, P. Pitchakarn, C. Ampasavate, P. Limtrakul, Enhancement of cellular uptake and cytotoxicity of curcumin-loaded PLGA nanoparticles by conjugation with anti-P-glycoprotein in drug resistance cancer cells, *Acta pharmacologica Sinica*, 33 (2012) 823-831.
- [111] Y. Malam, M. Loizidou, A.M. Seifalian, Liposomes and nanoparticles: nanosized vehicles for drug delivery in cancer, *Trends in Pharmacological Sciences*, 30 (2009) 592-599.
- [112] A. Karczmarczyk, D. Bielska, B. Gzyl-Malcher, M. Kepczynski, R. Lach, M. Nowakowska, Interaction of curcumin with lipid monolayers and liposomal bilayers, *Colloids and surfaces. B, Biointerfaces*, 88 (2011) 231-239.
- [113] X. Li, K. Nan, L. Li, Z. Zhang, H. Chen, In vivo evaluation of curcumin nanoformulation loaded methoxy poly(ethylene glycol)-graft-chitosan composite film for wound healing application, *Carbohydrate Polymers*, 88 (2012) 84-90.
- [114] K. Fujita, Y. Hiramatsu, H. Minematsu, M. Somiya, S.i. Kuroda, M. Seno, S. Hinuma, Release of siRNA from liposomes induced by curcumin, *Journal of Nanotechnology*, 2016 (2016).
- [115] C. Amano, H. Minematsu, K. Fujita, S. Iwashita, M. Adachi, K. Igarashi, S. Hinuma, Nanoparticles Containing Curcumin Useful for Suppressing Macrophages In Vivo in Mice, *PLoS One*, 10 (2015) e0137207.

- [116] W.-H. Lee, C.-Y. Loo, P.M. Young, D. Traini, R.S. Mason, R. Rohanizadeh, Recent advances in curcumin nanoformulation for cancer therapy, *Expert Opinion on Drug Delivery*, 11 (2014) 1183-1201.
- [117] M. Hamidi, A. Azadi, P. Rafiei, Hydrogel nanoparticles in drug delivery, *Advanced Drug Delivery Reviews*, 60 (2008) 1638-1649.
- [118] S. Mangalathillam, N.S. Rejinold, A. Nair, V.K. Lakshmanan, S.V. Nair, R. Jayakumar, Curcumin loaded chitin nanogels for skin cancer treatment via the transdermal route, *Nanoscale*, 4 (2012) 239-250.
- [119] M.A.C. Stuart, W.T.S. Huck, J. Genzer, M. Müller, C. Ober, M. Stamm, G.B. Sukhorukov, I. Szleifer, V.V. Tsukruk, M. Urban, F. Winnik, S. Zauscher, I. Luzinov, S. Minko, Emerging applications of stimuli-responsive polymer materials, *Nature Materials*, 9 (2010) 101.
- [120] R.K. Das, N. Kasoju, U. Bora, Encapsulation of curcumin in alginate-chitosan-pluronic composite nanoparticles for delivery to cancer cells, *Nanomedicine : nanotechnology, biology, and medicine*, 6 (2010) 153-160.
- [121] A. Hatefi, B. Amsden, Biodegradable injectable in situ forming drug delivery systems, *J Control Release*, 80 (2002) 9-28.
- [122] H.J. Chung, T.G. Park, Self-assembled and nanostructured hydrogels for drug delivery and tissue engineering, *Nano Today*, 4 (2009) 429-437.
- [123] A. Altunbas, S.J. Lee, S.A. Rajasekaran, J.P. Schneider, D.J. Pochan, Encapsulation of curcumin in self-assembling peptide hydrogels as injectable drug delivery vehicles, *Biomaterials*, 32 (2011) 5906-5914.
- [124] M. Esmaili, S.M. Ghaffari, Z. Moosavi-Movahedi, M.S. Atri, A. Sharifzadeh, M. Farhadi, R. Yousefi, J.-M. Chobert, T. Haertlé, A.A. Moosavi-Movahedi, Beta casein-micelle as a nano vehicle for solubility enhancement of curcumin; food industry application, *LWT - Food Science and Technology*, 44 (2011) 2166-2172.
- [125] N. Lomis, S. Westfall, L. Farahdel, M. Malhotra, D. Shum-Tim, S. Prakash, Human Serum Albumin Nanoparticles for Use in Cancer Drug Delivery: Process Optimization and In Vitro Characterization, *Nanomaterials (Basel, Switzerland)*, 6 (2016) 116.
- [126] T.H. Kim, H.H. Jiang, Y.S. Youn, C.W. Park, K.K. Tak, S. Lee, H. Kim, S. Jon, X. Chen, K.C. Lee, Preparation and characterization of water-soluble albumin-bound curcumin nanoparticles with improved antitumor activity, *Int J Pharm*, 403 (2011) 285-291.
- [127] I. Dal Pra, G. Freddi, J. Minic, A. Chiarini, U. Armato, De novo engineering of reticular connective tissue in vivo by silk fibroin nonwoven materials, *Biomaterials*, 26 (2005) 1987-1999.
- [128] C. Vepari, D.L. Kaplan, Silk as a Biomaterial, *Prog Polym Sci*, 32 (2007) 991-1007.
- [129] R.L. Thangapazham, A. Puri, S. Tele, R. Blumenthal, R.K. Maheshwari, Evaluation of a nanotechnology-based carrier for delivery of curcumin in prostate cancer cells, *Int J Oncol*, 32 (2008) 1119-1123.
- [130] M. Gou, K. Men, H. Shi, M. Xiang, J. Zhang, J. Song, J. Long, Y. Wan, F. Luo, X. Zhao, Z. Qian, Curcumin-loaded biodegradable polymeric micelles for colon cancer therapy in vitro and in vivo, *Nanoscale*, 3 (2011) 1558-1567.
- [131] S. Ganta, M. Amiji, Coadministration of Paclitaxel and curcumin in nanoemulsion formulations to overcome multidrug resistance in tumor cells, *Molecular pharmaceutics*, 6 (2009) 928-939.
- [132] A. Karewicz, D. Bielska, A. Loboda, B. Gzyl-Malcher, J. Bednar, A. Jozkowicz, J. Dulak, M. Nowakowska, Curcumin-containing liposomes stabilized by thin layers of chitosan derivatives, *Colloids and Surfaces B: Biointerfaces*, 109 (2013) 307-316.
- [133] Y.-L. Lin, Y.-K. Liu, N.-M. Tsai, J.-H. Hsieh, C.-H. Chen, C.-M. Lin, K.-W. Liao, A Lipo-PEG-PEI complex for encapsulating curcumin that enhances its antitumor effects on curcumin-sensitive and curcumin-resistance cells, *Nanomedicine: Nanotechnology, Biology and Medicine*, 8 (2012) 318-327.
- [134] X. Li, S. Chen, B. Zhang, M. Li, K. Diao, Z. Zhang, J. Li, Y. Xu, X. Wang, H. Chen, In situ injectable nano-composite hydrogel composed of curcumin, N,O-carboxymethyl chitosan and oxidized alginate for wound healing application, *Int J Pharm*, 437 (2012) 110-119.

- [135] F. Re, I. Cambianica, C. Zona, S. Sesana, M. Gregori, R. Rigolio, B. La Ferla, F. Nicotra, G. Forloni, A. Cagnotto, M. Salmona, M. Masserini, G. Sancini, Functionalization of liposomes with ApoE-derived peptides at different density affects cellular uptake and drug transport across a blood-brain barrier model, *Nanomedicine: Nanotechnology, Biology and Medicine*, 7 (2011) 551-559.
- [136] A. Zanotto-Filho, K. Coradini, E. Braganhol, R. Schröder, C.M. de Oliveira, A. Simões-Pires, A.M.O. Battastini, A.R. Pohlmann, S.S. Guterres, C.M. Forcelini, R.C.R. Beck, J.C.F. Moreira, Curcumin-loaded lipid-core nanocapsules as a strategy to improve pharmacological efficacy of curcumin in glioma treatment, *European Journal of Pharmaceutics and Biopharmaceutics*, 83 (2013) 156-167.
- [137] D. Wang, M.S. Veena, K. Stevenson, C. Tang, B. Ho, J.D. Suh, V.M. Duarte, K.F. Faull, K. Mehta, E.S. Srivatsan, M.B. Wang, Liposome-encapsulated curcumin suppresses growth of head and neck squamous cell carcinoma in vitro and in xenografts through the inhibition of nuclear factor kappaB by an AKT-independent pathway, *Clin Cancer Res*, 14 (2008) 6228-6236.
- [138] W.B. Liechty, D.R. Kryscio, B.V. Slaughter, N.A. Peppas, *Polymers for drug delivery systems*, *Annu Rev Chem Biomol Eng*, 1 (2010) 149-173.
- [139] V.P. Torchilin, Multifunctional, stimuli-sensitive nanoparticulate systems for drug delivery, *Nature Reviews Drug Discovery*, 13 (2014) 813.
- [140] E.M. Pritchard, T. Valentin, B. Panilaitis, F. Omenetto, D.L. Kaplan, Antibiotic-Releasing Silk Biomaterials for Infection Prevention and Treatment, *Advanced functional materials*, 23 (2013) 854-861.
- [141] Z. Luo, J. Li, J. Qu, W. Sheng, J. Yang, M. Li, Cationized Bombyx mori silk fibroin as a delivery carrier of the VEGF165–Ang-1 coexpression plasmid for dermal tissue regeneration, *Journal of Materials Chemistry B*, 7 (2019) 80-94.
- [142] E. Wenk, H.P. Merkle, L. Meinel, Silk fibroin as a vehicle for drug delivery applications, *Journal of Controlled Release*, 150 (2011) 128-141.
- [143] S.Y. Kim, D. Naskar, S.C. Kundu, D.P. Bishop, P.A. Doble, A.V. Boddy, H.-K. Chan, I.B. Wall, W. Chrzanowski, Formulation of Biologically-Inspired Silk-Based Drug Carriers for Pulmonary Delivery Targeted for Lung Cancer, *Scientific Reports*, 5 (2015) 11878.
- [144] M. Choi, D. Choi, J. Hong, Multilayered Controlled Drug Release Silk Fibroin Nanofilm by Manipulating Secondary Structure, *Biomacromolecules*, 19 (2018) 3096-3103.
- [145] A.B. Li, J.A. Kluge, N.A. Guzewicz, F.G. Omenetto, D.L. Kaplan, Silk-based stabilization of biomacromolecules, *Journal of Controlled Release*, 219 (2015) 416-430.
- [146] W. Song, D.A. Gregory, H. Al-janabi, M. Muthana, Z. Cai, X. Zhao, Magnetic-silk/polyethyleneimine core-shell nanoparticles for targeted gene delivery into human breast cancer cells, *International Journal of Pharmaceutics*, 555 (2019) 322-336.
- [147] F.P. Seib, Reverse-engineered silk hydrogels for cell and drug delivery, *Therapeutic Delivery*, 9 (2018) 469-487.
- [148] H.-J. Jin, D.L. Kaplan, Mechanism of silk processing in insects and spiders, *Nature*, 424 (2003) 1057-1061.
- [149] B. Crivelli, S. Perteghella, E. Bari, M. Sorrenti, G. Tripodo, T. Chlapanidas, M.L. Torre, Silk nanoparticles: from inert supports to bioactive natural carriers for drug delivery, *Soft Matter*, 14 (2018) 546-557.
- [150] J. Rnjak-Kovacina, L.S. Wray, K.A. Burke, T. Torregrosa, J.M. Golinski, W. Huang, D.L. Kaplan, Lyophilized Silk Sponges: A Versatile Biomaterial Platform for Soft Tissue Engineering, *ACS Biomater Sci Eng*, 1 (2015) 260-270.
- [151] G.G. Leisk, T.J. Lo, T. Yucel, Q. Lu, D.L. Kaplan, Electrogelation for protein adhesives, *Adv Mater*, 22 (2010) 711-715.
- [152] Q. Lu, H. Zhu, C. Zhang, F. Zhang, B. Zhang, D.L. Kaplan, Silk self-assembly mechanisms and control from thermodynamics to kinetics, *Biomacromolecules*, 13 (2012) 826-832.
- [153] Y. Dong, P. Dong, D. Huang, L. Mei, Y. Xia, Z. Wang, X. Pan, G. Li, C. Wu, Fabrication and characterization of silk fibroin-coated liposomes for ocular drug delivery, *Eur J Pharm Biopharm*, 91 (2015) 82-90.

- [154] T. Deptuch, H. Dams-Kozłowska, Silk Materials Functionalized via Genetic Engineering for Biomedical Applications, *Materials (Basel, Switzerland)*, 10 (2017) 1417.
- [155] N.A. Guziewicz, A.J. Massetti, B.J. Perez-Ramirez, D.L. Kaplan, Mechanisms of monoclonal antibody stabilization and release from silk biomaterials, *Biomaterials*, 34 (2013) 7766-7775.
- [156] M.C. Manning, D.K. Chou, B.M. Murphy, R.W. Payne, D.S. Katayama, Stability of protein pharmaceuticals: an update, *Pharm Res*, 27 (2010) 544-575.
- [157] A. Hawe, M. Wigggenhorn, M. van de Weert, J.H.O. Garbe, H.-c. Mahler, W. Jiskoot, Forced Degradation of Therapeutic Proteins, *Journal of Pharmaceutical Sciences*, 101 (2012) 895-913.
- [158] T. Yucel, M.L. Lovett, D.L. Kaplan, Silk-based biomaterials for sustained drug delivery, *Journal of controlled release : official journal of the Controlled Release Society*, 190 (2014) 381-397.
- [159] Y. Liu, Z. Zheng, H. Gong, M. Liu, S. Guo, G. Li, X. Wang, D.L. Kaplan, DNA preservation in silk, *Biomaterials Science*, 5 (2017) 1279-1292.
- [160] B. Subia, S.C. Kundu, Drug loading and release on tumor cells using silk fibroin-albumin nanoparticles as carriers, *Nanotechnology*, 24 (2013) 035103.
- [161] A.S. Mehta, B.K. Singh, N. Singh, D. Archana, K. Snigdha, R. Harniman, S.S. Rahatekar, R.P. Tewari, P.K. Dutta, Chitosan silk-based three-dimensional scaffolds containing gentamicin-encapsulated calcium alginate beads for drug administration and blood compatibility, *J Biomater Appl*, 29 (2015) 1314-1325.
- [162] R. Elia, D.R. Newhite, P.D. Pedevillano, G.R. Reiss, M.A. Firpo, E.W. Hsu, D.L. Kaplan, G.D. Prestwich, R.A. Peattie, Silk-hyaluronan-based composite hydrogels: a novel, securable vehicle for drug delivery, *J Biomater Appl*, 27 (2013) 749-762.
- [163] B. Yavuz, J.L. Morgan, C. Herrera, K. Harrington, B. Perez-Ramirez, P.J. LiWang, D.L. Kaplan, Sustained release silk fibroin discs: Antibody and protein delivery for HIV prevention, *Journal of Controlled Release*, 301 (2019) 1-12.
- [164] F.P. Seib, G.T. Jones, J. Rnjak-Kovacina, Y. Lin, D.L. Kaplan, pH-Dependent Anticancer Drug Release from Silk Nanoparticles, *Advanced Healthcare Materials*, 2 (2013) 1606-1611.
- [165] M. Chen, Z. Shao, X. Chen, Paclitaxel-loaded silk fibroin nanospheres, *Journal of Biomedical Materials Research Part A*, 100A (2012) 203-210.
- [166] M.A. Tomeh, R. Hadianamrei, X. Zhao, A review of curcumin and its derivatives as anticancer agents, *International journal of molecular sciences*, 20 (2019) 1033.
- [167] J. Qu, Y. Liu, Y. Yu, J. Li, J. Luo, M. Li, Silk fibroin nanoparticles prepared by electrospray as controlled release carriers of cisplatin, *Materials Science and Engineering: C*, 44 (2014) 166-174.
- [168] D. Yao, S. Dong, Q. Lu, X. Hu, D.L. Kaplan, B. Zhang, H. Zhu, Salt-leached silk scaffolds with tunable mechanical properties, *Biomacromolecules*, 13 (2012) 3723-3729.
- [169] C. Theodora, P. Sara, F. Silvio, B. Alessandra, T. Giuseppe, V. Barbara, C. Barbara, R. Sabrina, D. Silvia, P. Stefania, Platelet lysate and adipose mesenchymal stromal cells on silk fibroin nonwoven mats for wound healing, *Journal of Applied Polymer Science*, 133 (2016).
- [170] B. Kundu, R. Rajkhowa, S.C. Kundu, X. Wang, Silk fibroin biomaterials for tissue regenerations, *Adv Drug Deliv Rev*, 65 (2013) 457-470.
- [171] K. Luo, Y. Yang, Z. Shao, Physically Crosslinked Biocompatible Silk-Fibroin-Based Hydrogels with High Mechanical Performance, *Advanced functional materials*, 26 (2016) 872-880.
- [172] Q. Lu, X. Hu, X. Wang, J.A. Kluge, S. Lu, P. Cebe, D.L. Kaplan, Water-insoluble silk films with silk I structure, *Acta Biomater*, 6 (2010) 1380-1387.
- [173] J. Melke, S. Midha, S. Ghosh, K. Ito, S. Hofmann, Silk fibroin as biomaterial for bone tissue engineering, *Acta Biomater*, 31 (2016) 1-16.
- [174] K. Numata, J. Hamasaki, B. Subramanian, D.L. Kaplan, Gene delivery mediated by recombinant silk proteins containing cationic and cell binding motifs, *Journal of Controlled Release*, 146 (2010) 136-143.
- [175] L. Meinel, V. Karageorgiou, S. Hofmann, R. Fajardo, B. Snyder, C. Li, L. Zichner, R. Langer, G. Vunjak-Novakovic, D.L. Kaplan, Engineering bone-like tissue in vitro using human bone marrow stem cells and silk scaffolds, *J Biomed Mater Res A*, 71 (2004) 25-34.

- [176] H.J. Jin, J. Chen, V. Karageorgiou, G.H. Altman, D.L. Kaplan, Human bone marrow stromal cell responses on electrospun silk fibroin mats, *Biomaterials*, 25 (2004) 1039-1047.
- [177] L. Meinel, S. Hofmann, O. Betz, R. Fajardo, H.P. Merkle, R. Langer, C.H. Evans, G. Vunjak-Novakovic, D.L. Kaplan, Osteogenesis by human mesenchymal stem cells cultured on silk biomaterials: comparison of adenovirus mediated gene transfer and protein delivery of BMP-2, *Biomaterials*, 27 (2006) 4993-5002.
- [178] L. Meinel, S. Hofmann, V. Karageorgiou, C. Kirker-Head, J. McCool, G. Gronowicz, L. Zichner, R. Langer, G. Vunjak-Novakovic, D.L. Kaplan, The inflammatory responses to silk films in vitro and in vivo, *Biomaterials*, 26 (2005) 147-155.
- [179] B. Panilaitis, G.H. Altman, J. Chen, H.J. Jin, V. Karageorgiou, D.L. Kaplan, Macrophage responses to silk, *Biomaterials*, 24 (2003) 3079-3085.
- [180] H. Xie, J. Wang, Y. He, Z. Gu, J. Xu, L. Li, Q. Ye, Biocompatibility and safety evaluation of a silk fibroin-doped calcium polyphosphate scaffold copolymer in vitro and in vivo, *RSC Advances*, 7 (2017) 46036-46044.
- [181] S. Zhao, Y. Chen, B.P. Partlow, A.S. Golding, P. Tseng, J. Coburn, M.B. Applegate, J.E. Moreau, F.G. Omenetto, D.L. Kaplan, Bio-functionalized silk hydrogel microfluidic systems, *Biomaterials*, 93 (2016) 60-70.
- [182] A.D. Bhrany, C.J. Lien, B.L. Beckstead, N.D. Futran, N.H. Muni, C.M. Giachelli, B.D. Ratner, Crosslinking of an oesophagus acellular matrix tissue scaffold, *J Tissue Eng Regen Med*, 2 (2008) 365-372.
- [183] N.E. Kurland, Z. Drira, V.K. Yadavalli, Measurement of nanomechanical properties of biomolecules using atomic force microscopy, *Micron*, 43 (2012) 116-128.
- [184] G.H. Altman, R.L. Horan, H.H. Lu, J. Moreau, I. Martin, J.C. Richmond, D.L. Kaplan, Silk matrix for tissue engineered anterior cruciate ligaments, *Biomaterials*, 23 (2002) 4131-4141.
- [185] B. Kundu, N.E. Kurland, S. Bano, C. Patra, F.B. Engel, V.K. Yadavalli, S.C. Kundu, Silk proteins for biomedical applications: Bioengineering perspectives, *Progress in polymer science*, 39 (2014) 251-267.
- [186] B.M. Min, L. Jeong, K.Y. Lee, W.H. Park, Regenerated silk fibroin nanofibers: water vapor-induced structural changes and their effects on the behavior of normal human cells, *Macromol Biosci*, 6 (2006) 285-292.
- [187] H.J. Jin, J. Park, V. Karageorgiou, U.J. Kim, R. Valluzzi, P. Cebe, D.L. Kaplan, Water-Stable Silk Films with Reduced β -Sheet Content, *Advanced functional materials*, 15 (2005) 1241-1247.
- [188] J. Guan, Y. Wang, B. Mortimer, C. Holland, Z. Shao, D. Porter, F. Vollrath, Glass transitions in native silk fibres studied by dynamic mechanical thermal analysis, *Soft Matter*, 12 (2016) 5926-5936.
- [189] R. Nazarov, H.-J. Jin, D.L. Kaplan, Porous 3-D Scaffolds from Regenerated Silk Fibroin, *Biomacromolecules*, 5 (2004) 718-726.
- [190] R. You, Y. Zhang, Y. Liu, G. Liu, M. Li, The degradation behavior of silk fibroin derived from different ionic liquid solvents, *Natural Science*, 5 (2013) 10.
- [191] M. Li, M. Ogiso, N. Minoura, Enzymatic degradation behavior of porous silk fibroin sheets, *Biomaterials*, 24 (2003) 357-365.
- [192] R.L. Horan, K. Antle, A.L. Collette, Y. Wang, J. Huang, J.E. Moreau, V. Volloch, D.L. Kaplan, G.H. Altman, In vitro degradation of silk fibroin, *Biomaterials*, 26 (2005) 3385-3393.
- [193] S. Winkler, D. Wilson, D.L. Kaplan, Controlling beta-sheet assembly in genetically engineered silk by enzymatic phosphorylation/dephosphorylation, *Biochemistry*, 39 (2000) 12739-12746.
- [194] T.V. Chirila, S. Suzuki, C. Papolla, A comparative investigation of Bombyx mori silk fibroin hydrogels generated by chemical and enzymatic cross-linking, *Biotechnol Appl Biochem*, 64 (2017) 771-781.
- [195] A. Matsumoto, J. Chen, A.L. Collette, U.-J. Kim, G.H. Altman, P. Cebe, D.L. Kaplan, Mechanisms of Silk Fibroin Sol-Gel Transitions, *The Journal of Physical Chemistry B*, 110 (2006) 21630-21638.
- [196] Z. Karahaliloğlu, Curcumin-loaded silk fibroin e-gel scaffolds for wound healing applications, *Materials Technology*, 33 (2018) 276-287.

- [197] A. Sundarakrishnan, E. Herrero Acero, J. Coburn, K. Chwalek, B. Partlow, D.L. Kaplan, Phenol red-silk tyrosine cross-linked hydrogels, *Acta Biomater*, 42 (2016) 102-113.
- [198] M.C. Lee, D.-K. Kim, O.J. Lee, J.-H. Kim, H.W. Ju, J.M. Lee, B.M. Moon, H.J. Park, D.W. Kim, S.H. Kim, C.H. Park, Fabrication of silk fibroin film using centrifugal casting technique for corneal tissue engineering, *Journal of Biomedical Materials Research Part B: Applied Biomaterials*, 104 (2016) 508-514.
- [199] Y. Qi, H. Wang, K. Wei, Y. Yang, R.Y. Zheng, I.S. Kim, K.Q. Zhang, A Review of Structure Construction of Silk Fibroin Biomaterials from Single Structures to Multi-Level Structures, *Int J Mol Sci*, 18 (2017).
- [200] A. Sagnella, A. Pistone, S. Bonetti, A. Donnadio, E. Saracino, M. Nocchetti, C. Dionigi, G. Ruani, M. Muccini, T. Posati, V. Benfenati, R. Zamboni, Effect of different fabrication methods on the chemo-physical properties of silk fibroin films and on their interaction with neural cells, *RSC Advances*, 6 (2016) 9304-9314.
- [201] D. Terada, Y. Yokoyama, S. Hattori, H. Kobayashi, Y. Tamada, The outermost surface properties of silk fibroin films reflect ethanol-treatment conditions used in biomaterial preparation, *Materials Science and Engineering: C*, 58 (2016) 119-126.
- [202] C. Jiang, X. Wang, R. Gunawidjaja, Y.H. Lin, M.K. Gupta, D.L. Kaplan, R.R. Naik, V.V. Tsukruk, Mechanical Properties of Robust Ultrathin Silk Fibroin Films, *Advanced functional materials*, 17 (2007) 2229-2237.
- [203] M.A. de Moraes, M.F. Silva, R.F. Weska, M.M. Beppu, Silk fibroin and sodium alginate blend: Miscibility and physical characteristics, *Materials Science and Engineering: C*, 40 (2014) 85-91.
- [204] X. Wang, T. Yucel, Q. Lu, X. Hu, D.L. Kaplan, Silk nanospheres and microspheres from silk/pva blend films for drug delivery, *Biomaterials*, 31 (2010) 1025-1035.
- [205] Y. Cao, F. Liu, Y. Chen, T. Yu, D. Lou, Y. Guo, P. Li, Z. Wang, H. Ran, Drug release from core-shell PVA/silk fibroin nanoparticles fabricated by one-step electrospaying, *Scientific Reports*, 7 (2017) 11913.
- [206] P. Shi, J.C.H. Goh, Self-assembled silk fibroin particles: Tunable size and appearance, *Powder Technology*, 215-216 (2012) 85-90.
- [207] A.S. Lammel, X. Hu, S.H. Park, D.L. Kaplan, T.R. Scheibel, Controlling silk fibroin particle features for drug delivery, *Biomaterials*, 31 (2010) 4583-4591.
- [208] Y. Tian, X. Jiang, X. Chen, Z. Shao, W. Yang, Doxorubicin-Loaded Magnetic Silk Fibroin Nanoparticles for Targeted Therapy of Multidrug-Resistant Cancer, *Advanced Materials*, 26 (2014) 7393-7398.
- [209] A.N. Mitropoulos, G. Perotto, S. Kim, B. Marelli, D.L. Kaplan, F.G. Omenetto, Synthesis of silk fibroin micro- and submicron spheres using a co-flow capillary device, *Advanced materials (Deerfield Beach, Fla.)*, 26 (2014) 1105-1110.
- [210] T. Wongpinyochit, J.D. Totten, B.F. Johnston, F.P. Seib, Microfluidic-assisted silk nanoparticle tuning, *Nanoscale Advances*, 1 (2019) 873-883.
- [211] H.J. Jin, D.L. Kaplan, Mechanism of silk processing in insects and spiders, *Nature*, 424 (2003) 1057-1061.
- [212] S.J. Myung, H.-S. Kim, Y. Kim, P. Chen, H.-J. Jin, Fluorescent silk fibroin nanoparticles prepared using a reverse microemulsion, *Macromolecular Research*, 16 (2008) 604-608.
- [213] T. Wongpinyochit, P. Uhlmann, A.J. Urquhart, F.P. Seib, PEGylated Silk Nanoparticles for Anticancer Drug Delivery, *Biomacromolecules*, 16 (2015) 3712-3722.
- [214] A. Gholami, H. Tavanai, A.R. Moradi, Production of fibroin nanopowder through electrospaying, *Journal of Nanoparticle Research*, 13 (2011) 2089-2098.
- [215] V. Gupta, A. Aseh, C.N. Ríos, B.B. Aggarwal, A.B. Mathur, Fabrication and characterization of silk fibroin-derived curcumin nanoparticles for cancer therapy, *International journal of nanomedicine*, 4 (2009) 115-122.

- [216] Z. Zhao, M. Xie, Y. Li, A. Chen, G. Li, J. Zhang, H. Hu, X. Wang, S. Li, Formation of curcumin nanoparticles via solution-enhanced dispersion by supercritical CO₂, *International journal of nanomedicine*, 10 (2015) 3171-3181.
- [217] H. Perry, A. Gopinath, D.L. Kaplan, L. Dal Negro, F.G. Omenetto, Nano- and Micropatterning of Optically Transparent, Mechanically Robust, Biocompatible Silk Fibroin Films, *Advanced Materials*, 20 (2008) 3070-3072.
- [218] N. Guzewicz, A. Best, B. Perez-Ramirez, D.L. Kaplan, Lyophilized silk fibroin hydrogels for the sustained local delivery of therapeutic monoclonal antibodies, *Biomaterials*, 32 (2011) 2642-2650.
- [219] K. Numata, M.R. Reagan, R.H. Goldstein, M. Rosenblatt, D.L. Kaplan, Spider Silk-Based Gene Carriers for Tumor Cell-Specific Delivery, *Bioconjugate Chemistry*, 22 (2011) 1605-1610.
- [220] L. Meinel, D.L. Kaplan, Silk constructs for delivery of musculoskeletal therapeutics, *Advanced drug delivery reviews*, 64 (2012) 1111-1122.
- [221] E.M. Pritchard, P.B. Dennis, F. Omenetto, R.R. Naik, D.L. Kaplan, Review physical and chemical aspects of stabilization of compounds in silk, *Biopolymers*, 97 (2012) 479-498.
- [222] X. Zhang, I.V. Berghe, P. Wyeth, Heat and moisture promoted deterioration of raw silk estimated by amino acid analysis, *Journal of Cultural Heritage*, 12 (2011) 408-411.
- [223] X.H. Zong, P. Zhou, Z.Z. Shao, S.M. Chen, X. Chen, B.W. Hu, F. Deng, W.H. Yao, Effect of pH and copper(II) on the conformation transitions of silk fibroin based on EPR, NMR, and Raman spectroscopy, *Biochemistry*, 43 (2004) 11932-11941.
- [224] S.-z. Lu, X.-q. Wang, N. Uppal, D.L. Kaplan, M.-z. Li, Stabilization of horseradish peroxidase in silk materials, *Frontiers of Materials Science in China*, 3 (2009) 367.
- [225] M. Demura, T. Asakura, T. Kuroo, Immobilization of biocatalysts with bombyx mori silk fibroin by several kinds of physical treatment and its application to glucose sensors, *Biosensors*, 4 (1989) 361-372.
- [226] A. Kuzuhara, T. Asakura, R. Tomoda, T. Matsunaga, Use of silk fibroin for enzyme membrane, *Journal of Biotechnology*, 5 (1987) 199-207.
- [227] S.-F. Ng, N.-A. Anuwi, T.-N. Tengku-Ahmad, Topical Lyogel Containing Corticosteroid Decreases IgE Expression and Enhances the Therapeutic Efficacy Against Atopic Eczema, *AAPS PharmSciTech*, 16 (2015) 656-663.
- [228] S. Mao, C. Guo, Y. Shi, L.C. Li, Recent advances in polymeric microspheres for parenteral drug delivery – part 1, *Expert Opinion on Drug Delivery*, 9 (2012) 1161-1176.
- [229] D.J. Hines, D.L. Kaplan, Mechanisms of Controlled Release from Silk Fibroin Films, *Biomacromolecules*, 12 (2011) 804-812.
- [230] X. Wang, E. Wenk, A. Matsumoto, L. Meinel, C. Li, D.L. Kaplan, Silk microspheres for encapsulation and controlled release, *Journal of Controlled Release*, 117 (2007) 360-370.
- [231] J. Zhou, T. Fang, J. Wen, Z. Shao, J. Dong, Silk coating on poly(ϵ -caprolactone) microspheres for the delayed release of vancomycin, *Journal of Microencapsulation*, 28 (2011) 99-107.
- [232] A.S. Gobin, R. Rhea, R.A. Newman, A.B. Mathur, Silk-fibroin-coated liposomes for long-term and targeted drug delivery, *International journal of nanomedicine*, 1 (2006) 81-87.
- [233] Y.-Q. Zhang, Y. Ma, Y.-Y. Xia, W.-D. Shen, J.-P. Mao, X.-M. Zha, K. Shirai, K. Kiguchi, Synthesis of silk fibroin-insulin bioconjugates and their characterization and activities in vivo, *Journal of Biomedical Materials Research Part B: Applied Biomaterials*, 79B (2006) 275-283.
- [234] V. Karageorgiou, L. Meinel, S. Hofmann, A. Malhotra, V. Volloch, D. Kaplan, Bone morphogenetic protein-2 decorated silk fibroin films induce osteogenic differentiation of human bone marrow stromal cells, *J Biomed Mater Res A*, 71 (2004) 528-537.
- [235] P. Wang, C. Qi, Y. Yu, J. Yuan, L. Cui, G. Tang, Q. Wang, X. Fan, Covalent Immobilization of Catalase onto Regenerated Silk Fibroins via Tyrosinase-Catalyzed Cross-Linking, *Appl Biochem Biotechnol*, 177 (2015) 472-485.
- [236] Q. Lu, X. Wang, H. Zhu, D.L. Kaplan, Surface immobilization of antibody on silk fibroin through conformational transition, *Acta biomaterialia*, 7 (2011) 2782-2786.

- [237] Y. Cao, Y. Gu, H. Ma, J. Bai, L. Liu, P. Zhao, H. He, Self-assembled nanoparticle drug delivery systems from galactosylated polysaccharide–doxorubicin conjugate loaded doxorubicin, *International journal of biological macromolecules*, 46 (2010) 245-249.
- [238] A.S. Gobin, C.E. Butler, A.B. Mathur, Repair and regeneration of the abdominal wall musculofascial defect using silk fibroin-chitosan blend, *Tissue Eng*, 12 (2006) 3383-3394.
- [239] B. Subia, S. Talukdar, S.C. Kundu, S. Chandra, Folate conjugated silk fibroin nanocarriers for targeted drug delivery, *Integrative Biology*, 6 (2013) 203-214.
- [240] C. Patra, S. Talukdar, T. Novoyatleva, S.R. Velagala, C. Muhlfeld, B. Kundu, S.C. Kundu, F.B. Engel, Silk protein fibroin from *Antheraea mylitta* for cardiac tissue engineering, *Biomaterials*, 33 (2012) 2673-2680.
- [241] Y. Zhang, H. Hong, D.V. Myklejord, W. Cai, Molecular imaging with SERS-active nanoparticles, *Small*, 7 (2011) 3261-3269.
- [242] C.J. Witton, J.R. Reeves, J.J. Going, T.G. Cooke, J.M.S. Bartlett, Expression of the HER1–4 family of receptor tyrosine kinases in breast cancer, *The Journal of Pathology*, 200 (2003) 290-297.
- [243] A.K. Kozłowska, A. Florczak, M. Smialek, E. Dondajewska, A. Mackiewicz, M. Kortylewski, H. Dams-Kozłowska, Functionalized bioengineered spider silk spheres improve nuclease resistance and activity of oligonucleotide therapeutics providing a strategy for cancer treatment, *Acta Biomaterialia*, 59 (2017) 221-233.
- [244] P.M. Valencia, O.C. Farokhzad, R. Karnik, R. Langer, Microfluidic technologies for accelerating the clinical translation of nanoparticles, *Nat Nanotechnol*, 7 (2012) 623-629.
- [245] J.K. Patra, G. Das, L.F. Fraceto, E.V.R. Campos, M.d.P. Rodriguez-Torres, L.S. Acosta-Torres, L.A. Diaz-Torres, R. Grillo, M.K. Swamy, S. Sharma, S. Habtemariam, H.-S. Shin, Nano based drug delivery systems: recent developments and future prospects, *Journal of Nanobiotechnology*, 16 (2018) 71.
- [246] T.A. Balbino, N.T. Aoki, A.A.M. Gasperini, C.L.P. Oliveira, A.R. Azzoni, L.P. Cavalcanti, L.G. de la Torre, Continuous flow production of cationic liposomes at high lipid concentration in microfluidic devices for gene delivery applications, *Chemical Engineering Journal*, 226 (2013) 423-433.
- [247] S.T. Sanjay, W. Zhou, M. Dou, H. Tavakoli, L. Ma, F. Xu, X. Li, Recent advances of controlled drug delivery using microfluidic platforms, *Advanced Drug Delivery Reviews*, 128 (2018) 3-28.
- [248] Y. Hui, X. Yi, F. Hou, D. Wibowo, F. Zhang, D. Zhao, H. Gao, C.-X. Zhao, Role of Nanoparticle Mechanical Properties in Cancer Drug Delivery, *ACS Nano*, 13 (2019) 7410-7424.
- [249] C. Su, Y. Liu, R. Li, W. Wu, J.P. Fawcett, J. Gu, Absorption, distribution, metabolism and excretion of the biomaterials used in Nanocarrier drug delivery systems, *Advanced Drug Delivery Reviews*, 143 (2019) 97-114.
- [250] A. Wicki, D. Witzigmann, V. Balasubramanian, J. Huwyler, Nanomedicine in cancer therapy: Challenges, opportunities, and clinical applications, *Journal of Controlled Release*, 200 (2015) 138-157.
- [251] S. Köstler, V. Ribitsch, *Synthetic Approaches to Organic Nanoparticles*, in, Weinheim, Germany: Wiley-VCH Verlag GmbH & Co. KGaA, Weinheim, Germany, 2007.
- [252] L. Capretto, D. Carugo, S. Mazzitelli, C. Nastruzzi, X. Zhang, Microfluidic and lab-on-a-chip preparation routes for organic nanoparticles and vesicular systems for nanomedicine applications, *Advanced drug delivery reviews*, 65 (2013) 1496-1532.
- [253] C.S. Nadrian, F.S. Hanadi, DNA nanotechnology, *Nature Reviews Materials*, 3 (2017).
- [254] H. Zhang, Y. Zhu, Y. Shen, Microfluidics for cancer nanomedicine: from fabrication to evaluation, *Small*, 14 (2018) 1800360.
- [255] J. Xu, S. Zhang, A. Machado, S. Lecommandoux, O. Sandre, F. Gu, A. Colin, Controllable microfluidic production of drug-loaded PLGA nanoparticles using partially water-miscible mixed solvent microdroplets as a precursor, *Scientific reports*, 7 (2017) 1-12.
- [256] W. Song, D.A. Gregory, H. Al-Janabi, M. Muthana, Z. Cai, X. Zhao, Magnetic-silk/polyethyleneimine core-shell nanoparticles for targeted gene delivery into human breast cancer cells, *Int J Pharm*, 555 (2019) 322-336.

- [257] W. Song, M. Muthana, J. Mukherjee, R.J. Falconer, C.A. Biggs, X. Zhao, Magnetic-Silk Core–Shell Nanoparticles as Potential Carriers for Targeted Delivery of Curcumin into Human Breast Cancer Cells, *ACS Biomater Sci Eng*, 3 (2017) 1027-1038.
- [258] X. Zhao, F. Pan, Z. Zhang, C. Grant, Y. Ma, S.P. Armes, Y. Tang, A.L. Lewis, T. Waigh, J.R. Lu, Nanostructure of Polyplexes Formed between Cationic Diblock Copolymer and Antisense Oligodeoxynucleotide and Its Influence on Cell Transfection Efficiency, *Biomacromolecules*, 8 (2007) 3493-3502.
- [259] X. Zhao, Z. Zhang, F. Pan, T.A. Waigh, J.R. Lu, Plasmid DNA complexation with phosphorylcholine diblock copolymers and its effect on cell transfection, *Langmuir*, 24 (2008) 6881-6888.
- [260] X. Zhao, F. Pan, C.M. Holt, A.L. Lewis, J.R. Lu, Controlled Delivery of Antisense Oligonucleotides (ASOs): a Brief Review of Current Strategies, *Expert Opin. Drug Deliv.*, 6 (2009) 673-686.
- [261] M.A. Tomeh, R. Hadianamrei, X. Zhao, Silk Fibroin as a Functional Biomaterial for Drug and Gene Delivery, *Pharmaceutics*, 11 (2019) 494.
- [262] N. Nishiyama, K. Kataoka, Current state, achievements, and future prospects of polymeric micelles as nanocarriers for drug and gene delivery, *Pharmacology & Therapeutics*, 112 (2006) 630-648.
- [263] R. Di Santo, L. Digiacomio, S. Palchetti, V. Palmieri, G. Perini, D. Pozzi, M. Papi, G. Caracciolo, Microfluidic manufacturing of surface-functionalized graphene oxide nanoflakes for gene delivery, *Nanoscale*, 11 (2019) 2733-2741.
- [264] J.S. Murday, R.W. Siegel, J. Stein, J.F. Wright, Translational nanomedicine: status assessment and opportunities, *Nanomedicine: Nanotechnology, Biology and Medicine*, 5 (2009) 251-273.
- [265] B.K. Johnson, R.K. Prud'homme, Mechanism for Rapid Self-Assembly of Block Copolymer Nanoparticles, *Physical Review Letters*, 91 (2003) 118302.
- [266] M.E. Gindy, A.Z. Panagiotopoulos, R.K. Prud'homme, Composite block copolymer stabilized nanoparticles: simultaneous encapsulation of organic actives and inorganic nanostructures, *Langmuir*, 24 (2008) 83-90.
- [267] A. Abou-Hassan, R. Bazzi, V. Cabuil, Multistep continuous-flow microsynthesis of magnetic and fluorescent γ -Fe₂O₃@ SiO₂ core/shell nanoparticles, *Angewandte Chemie*, 121 (2009) 7316-7319.
- [268] L. Zhang, Q. Feng, J. Wang, J. Sun, X. Shi, X. Jiang, Microfluidic synthesis of rigid nanovesicles for hydrophilic reagents delivery, *Angewandte Chemie*, 127 (2015) 4024-4028.
- [269] A.J. Demello, Control and detection of chemical reactions in microfluidic systems, *Nature*, 442 (2006) 394-402.
- [270] D. Chen, K.T. Love, Y. Chen, A.A. Eltoukhy, C. Kastrup, G. Sahay, A. Jeon, Y. Dong, K.A. Whitehead, D.G. Anderson, Rapid Discovery of Potent siRNA-Containing Lipid Nanoparticles Enabled by Controlled Microfluidic Formulation, *Journal of the American Chemical Society*, 134 (2012) 6948-6951.
- [271] P.S. Clegg, J.W. Tavaoli, P.J. Wilde, One-step production of multiple emulsions: microfluidic, polymer-stabilized and particle-stabilized approaches, *Soft Matter*, 12 (2016) 998-1008.
- [272] H. Feng, T. Zheng, M. Li, J. Wu, H. Ji, J. Zhang, W. Zhao, J. Guo, Droplet-based microfluidics systems in biomedical applications, *ELECTROPHORESIS*, 40 (2019) 1580-1590.
- [273] N.V. Montoya, R. Peterson, K.J. Ornell, D.R. Albrecht, J.M. Coburn, Silk Particle Production Based on Silk/PVA Phase Separation Using a Microfabricated Co-flow Device, *Molecules*, 25 (2020) 890.
- [274] M. Maeki, N. Kimura, Y. Sato, H. Harashima, M. Tokeshi, Advances in microfluidics for lipid nanoparticles and extracellular vesicles and applications in drug delivery systems, *Adv Drug Deliv Rev*, 128 (2018) 84-100.
- [275] A. Ghazal, M. Gontsarik, J.P. Kutter, J.P. Lafleur, D. Ahmadvand, A. Labrador, S. Salentinig, A. Yaghmur, Microfluidic Platform for the Continuous Production and Characterization of Multilamellar Vesicles: A Synchrotron Small-Angle X-ray Scattering (SAXS) Study, *The Journal of Physical Chemistry Letters*, 8 (2017) 73-79.

- [276] B. Amoyav, O. Benny, Controlled and tunable polymer particles' production using a single microfluidic device, *Applied Nanoscience*, 8 (2018) 905-914.
- [277] J. Wang, W. Li, L. Zhang, L. Ban, P. Chen, W. Du, X. Feng, B.-F. Liu, Chemically Edited Exosomes with Dual Ligand Purified by Microfluidic Device for Active Targeted Drug Delivery to Tumor Cells, *ACS applied materials & interfaces*, 9 (2017) 27441-27452.
- [278] Z. Liu, F. Fontana, A. Python, J.T. Hirvonen, H.A. Santos, Microfluidics for Production of Particles: Mechanism, Methodology, and Applications, *Small*, 16 (2020) n/a-n/a.
- [279] S.M. D'Addio, R.K. Prud'homme, Controlling drug nanoparticle formation by rapid precipitation, *Advanced Drug Delivery Reviews*, 63 (2011) 417-426.
- [280] V.K. LaMer, R.H. Dinegar, Theory, production and mechanism of formation of monodispersed hydrosols, *Journal of the American Chemical Society*, 72 (1950) 4847-4854.
- [281] W.S. Saad, R.K. Prud'homme, Principles of nanoparticle formation by flash nanoprecipitation, *Nano Today*, 11 (2016) 212-227.
- [282] J. Tao, S.F. Chow, Y. Zheng, Application of flash nanoprecipitation to fabricate poorly water-soluble drug nanoparticles, *Acta pharmaceutica sinica B*, 9 (2019) 4-18.
- [283] R. Karnik, F. Gu, P. Basto, C. Cannizzaro, L. Dean, W. Kyei-Manu, R. Langer, O.C. Farokhzad, Microfluidic platform for controlled synthesis of polymeric nanoparticles, *Nano letters*, 8 (2008) 2906-2912.
- [284] X. Zhao, F. Bian, L. Sun, L. Cai, L. Li, Y. Zhao, Microfluidic Generation of Nanomaterials for Biomedical Applications, *Small*, 16 (2020) 1901943.
- [285] B.K. Johnson, R.K. Prud'homme, Chemical processing and micromixing in confined impinging jets, *AIChE Journal*, 49 (2003) 2264-2282.
- [286] C.K. Batchelor, G.K. Batchelor, *An introduction to fluid dynamics*, Cambridge university press, 2000.
- [287] N.-T. Nguyen, S.T. Wereley, S.A.M. Shaegh, *Fundamentals and applications of microfluidics*, Artech house, 2019.
- [288] M.E. Aulton, *Pharmaceutics: The science of dosage form design*, Churchill livingstone, 2002.
- [289] J.T. Edward, Molecular volumes and the Stokes-Einstein equation, *Journal of Chemical Education*, 47 (1970) 261.
- [290] A. Einstein, *Investigations on the Theory of the Brownian Movement*, Courier Corporation, 1956.
- [291] Z. Zhang, P. Zhao, G. Xiao, M. Lin, X. Cao, Focusing-enhanced mixing in microfluidic channels, *Biomicrofluidics*, 2 (2008) 14101.
- [292] Z. Chen, M. Bown, B. O'Sullivan, J. MacInnes, R. Allen, M. Mulder, M. Blom, R. van't Oever, Performance analysis of a folding flow micromixer, *Microfluidics and Nanofluidics*, 6 (2009) 763-774.
- [293] R. Thiermann, W. Mueller, A. Montesinos-Castellanos, D. Metzke, P. Löb, V. Hessel, M. Maskos, Size controlled polymersomes by continuous self-assembly in micromixers, *Polymer*, 53 (2012) 2205-2210.
- [294] N. Kimura, M. Maeki, Y. Sato, Y. Note, A. Ishida, H. Tani, H. Harashima, M. Tokeshi, Development of the iLiNP Device: Fine Tuning the Lipid Nanoparticle Size within 10 nm for Drug Delivery, *ACS Omega*, 3 (2018) 5044-5051.
- [295] A. Jahn, W.N. Vreeland, M. Gaitan, L.E. Locascio, Controlled Vesicle Self-Assembly in Microfluidic Channels with Hydrodynamic Focusing, *Journal of the American Chemical Society*, 126 (2004) 2674-2675.
- [296] A. Jahn, S.M. Stavis, J.S. Hong, W.N. Vreeland, D.L. DeVoe, M. Gaitan, Microfluidic Mixing and the Formation of Nanoscale Lipid Vesicles, *ACS Nano*, 4 (2010) 2077-2087.
- [297] J.-M. Lim, A. Swami, L.M. Gilson, S. Chopra, S. Choi, J. Wu, R. Langer, R. Karnik, O.C. Farokhzad, Ultra-high throughput synthesis of nanoparticles with homogeneous size distribution using a coaxial turbulent jet mixer, *ACS nano*, 8 (2014) 6056-6065.
- [298] Y. He, K. Park, Effects of the Microparticle Shape on Cellular Uptake, *Molecular Pharmaceutics*, 13 (2016) 2164-2171.

- [299] N. Hao, Y. Nie, J.X.J. Zhang, Microfluidic Flow Synthesis of Functional Mesoporous Silica Nanofibers with Tunable Aspect Ratios, *ACS Sustainable Chemistry & Engineering*, 6 (2018) 1522-1526.
- [300] E. Dashtimoghadam, H. Mirzadeh, F.A. Taromi, B. Nyström, Microfluidic self-assembly of polymeric nanoparticles with tunable compactness for controlled drug delivery, *Polymer*, 54 (2013) 4972-4979.
- [301] D. Liu, C.R. Bernuz, J. Fan, W. Li, A. Correia, J. Hirvonen, H.A. Santos, A Nano-in-Nano Vector: Merging the Best of Polymeric Nanoparticles and Drug Nanocrystals, *Advanced Functional Materials*, 27 (2017) 1604508.
- [302] J. Sun, L. Zhang, J. Wang, Q. Feng, D. Liu, Q. Yin, D. Xu, Y. Wei, B. Ding, X. Shi, X. Jiang, Tunable Rigidity of (Polymeric Core)–(Lipid Shell) Nanoparticles for Regulated Cellular Uptake, *Advanced Materials*, 27 (2015) 1402-1407.
- [303] A.I. Shallan, C. Priest, Microfluidic process intensification for synthesis and formulation in the pharmaceutical industry, *Chemical Engineering and Processing - Process Intensification*, 142 (2019) 107559.
- [304] K.F. Jensen, Flow chemistry—Microreaction technology comes of age, *AIChE Journal*, 63 (2017) 858-869.
- [305] C.-H. Chang, B.K. Paul, V.T. Remcho, S. Atre, J.E. Hutchison, Synthesis and post-processing of nanomaterials using microreaction technology, *Journal of Nanoparticle Research*, 10 (2008) 965-980.
- [306] C. Amador, A. Gavriilidis, P. Angeli, Flow distribution in different microreactor scale-out geometries and the effect of manufacturing tolerances and channel blockage, *Chemical Engineering Journal*, 101 (2004) 379-390.
- [307] L. Capretto, S. Mazzitelli, E. Brognara, I. Lampronti, D. Carugo, M. Hill, X. Zhang, R. Gambari, C. Nastruzzi, Mithramycin encapsulated in polymeric micelles by microfluidic technology as novel therapeutic protocol for beta-thalassemia, *International journal of nanomedicine*, 7 (2012) 307-324.
- [308] Y. Ying, G. Chen, Y. Zhao, S. Li, Q. Yuan, A high throughput methodology for continuous preparation of monodispersed nanocrystals in microfluidic reactors, *Chemical Engineering Journal*, 135 (2008) 209-215.
- [309] N.R. Danielle, C.P. Rucsanda, Y. Tuna, W. Xiaoqin, L.L. Michael, L.K. David, Materials fabrication from Bombyx mori silk fibroin, *Nature Protocols*, 6 (2011) 1612.
- [310] Z. Chen, M.R. Bown, B. O’Sullivan, J.M. MacInnes, R.W.K. Allen, M. Mulder, M. Blom, R. van’t Oever, Performance analysis of a folding flow micromixer, *Microfluidics and nanofluidics*, 6 (2009) 763-774.
- [311] M. Jullian, A. Hernandez, A. Maurras, K. Puget, M. Amblard, J. Martinez, G. Subra, N-terminus FITC labeling of peptides on solid support: the truth behind the spacer, *Tetrahedron Letters*, 50 (2009) 260-263.
- [312] X. Hu, D. Kaplan, P. Cebe, Determining beta-sheet crystallinity in fibrous proteins by thermal analysis and infrared spectroscopy, *Macromolecules*, 39 (2006) 6161-6170.
- [313] W. Zhang, B. Han, X. Lai, C. Xiao, S. Xu, X. Meng, Z. Li, J. Meng, T. Wen, X. Yang, J. Liu, H. Xu, Stiffness of cationized gelatin nanoparticles is a key factor determining RNAi efficiency in myeloid leukemia cells, *Chemical Communications*, 56 (2020) 1255-1258.
- [314] M. Zaroni, F. Piccinini, C. Arienti, A. Zamagni, S. Santi, R. Polico, A. Bevilacqua, A. Tesei, 3D tumor spheroid models for in vitro therapeutic screening: a systematic approach to enhance the biological relevance of data obtained, *Scientific Reports*, 6 (2016) 19103.
- [315] E. Fennema, N. Rivron, J. Rouwkema, C. van Blitterswijk, J. de Boer, Spheroid culture as a tool for creating 3D complex tissues, *Trends Biotechnol*, 31 (2013) 108-115.
- [316] U. Schillinger, T. Brill, C. Rudolph, S. Huth, S. Gersting, F. Krötz, J. Hirschberger, C. Bergemann, C. Plank, Advances in magnetofection—magnetically guided nucleic acid delivery, *Journal of Magnetism and Magnetic Materials*, 293 (2005) 501-508.

- [317] Y. Namiki, S. Matsunuma, T. Inoue, S. Koido, A. Tsubota, Y. Kuse, N. Tada, Magnetic Nanostructures for Biomedical Applications: An Iron Nitride Crystal/Cationic Lipid Nanocomposite for Enhanced Magnetically Guided RNA Interference in Cancer Cells, InTech: Rijeka, 2011.
- [318] P.N. Pusey, W. Van Megen, Dynamic light scattering by non-ergodic media, *Physica A: Statistical Mechanics and its Applications*, 157 (1989) 705-741.
- [319] R. Pecora, Dynamic Light Scattering Measurement of Nanometer Particles in Liquids, *Journal of Nanoparticle Research*, 2 (2000) 123-131.
- [320] S. Bhattacharjee, DLS and zeta potential – What they are and what they are not?, *Journal of Controlled Release*, 235 (2016) 337-351.
- [321] M. Kaszuba, J. Corbett, F.M. Watson, A. Jones, High-concentration zeta potential measurements using light-scattering techniques, *Philosophical Transactions of the Royal Society A: Mathematical, Physical and Engineering Sciences*, 368 (2010) 4439-4451.
- [322] N. Meulendijks, R. Van Ee, R. Stevens, M. Mourad, M. Verheijen, N. Kambly, R. Armenta, P. Buskens, Flow Cell Coupled Dynamic Light Scattering for Real-Time Monitoring of Nanoparticle Size during Liquid Phase Bottom-Up Synthesis, *Applied Sciences*, 8 (2018).
- [323] V. Filipe, A. Hawe, W. Jiskoot, Critical Evaluation of Nanoparticle Tracking Analysis (NTA) by NanoSight for the Measurement of Nanoparticles and Protein Aggregates, *Pharmaceutical Research*, 27 (2010) 796-810.
- [324] R.A. Dragovic, C. Gardiner, A.S. Brooks, D.S. Tannetta, D.J.P. Ferguson, P. Hole, B. Carr, C.W.G. Redman, A.L. Harris, P.J. Dobson, Sizing and phenotyping of cellular vesicles using Nanoparticle Tracking Analysis, *Nanomedicine: Nanotechnology, Biology and Medicine*, 7 (2011) 780-788.
- [325] W.T. Gunning, E.P. Calomeni, A Brief Review of Transmission Electron Microscopy and Applications in Pathology, *Journal of Histotechnology*, 23 (2000) 237-246.
- [326] D.B. Williams, C.B. Carter, The transmission electron microscope, in: *Transmission electron microscopy*, Springer, 1996, pp. 3-17.
- [327] N. Jalili, K. Laxminarayana, A review of atomic force microscopy imaging systems: application to molecular metrology and biological sciences, *Mechatronics*, 14 (2004) 907-945.
- [328] M. Kempf, M. Göken, H. Vehoff, Nanohardness measurements for studying local mechanical properties of metals, *Applied Physics A: Materials Science & Processing*, 66 (1998).
- [329] K.D. Jandt, Atomic force microscopy of biomaterials surfaces and interfaces, *Surface Science*, 491 (2001) 303-332.
- [330] E. Meyer, Atomic force microscopy, *Progress in surface science*, 41 (1992) 3-49.
- [331] J.M. Chalmers, *Handbook of vibrational spectroscopy*, 2002.
- [332] G. Ma, H.C. Allen, *Handbook of Spectroscopy*, Volumes 1 and 2 Edited by Günter Gauglitz (University of Tübingen) and Tuan Vo-Dinh (Oak Ridge National Laboratory). Wiley-VCH Verlag GmbH & Co. KGaA: Weinheim. 2003. 1168 pp. \$435.00. ISBN: 3-527-29782-0, in, ACS Publications, 2004.
- [333] L.-E. Amand, C.J. Tullin, The theory behind FTIR analysis, Dep. Of Energy Conversion, Chalmers University of Technology, Sweden, (1999).
- [334] R. Valand, S. Tanna, G. Lawson, L. Bengtström, A review of Fourier Transform Infrared (FTIR) spectroscopy used in food adulteration and authenticity investigations, *Food Additives & Contaminants: Part A*, 37 (2020) 19-38.
- [335] B. Stuart, Analytical techniques in the sciences, *Infrared Spectroscopy: Fundamentals and Applications*, 8 (2004).
- [336] M. Quack, F. Merkt, *Handbook of high-resolution spectroscopy*, Wiley-Blackwell, 2011.
- [337] V. Wagner, A. Dullaart, A.K. Bock, A. Zweck, The emerging nanomedicine landscape, *Nature biotechnology*, 24 (2006) 1211-1217.
- [338] P. Ananthkrishnan, F.L. Balci, J.P. Crowe, Optimizing surgical margins in breast conservation, *Int J Surg Oncol*, 2012 (2012) 585670.
- [339] H. Wang, T. Vo, A. Hajar, S. Li, X. Chen, A.M. Parissenti, D.N. Brindley, Z. Wang, Multiple mechanisms underlying acquired resistance to taxanes in selected docetaxel-resistant MCF-7 breast cancer cells, *BMC Cancer*, 14 (2014) 37.

- [340] J. Chen, L. Lu, Y. Feng, H. Wang, L. Dai, Y. Li, P. Zhang, PKD2 mediates multi-drug resistance in breast cancer cells through modulation of P-glycoprotein expression, *Cancer Lett*, 300 (2011) 48-56.
- [341] K. Dong, Z. Liu, Z. Li, J. Ren, X. Qu, Hydrophobic Anticancer Drug Delivery by a 980 nm Laser-Driven Photothermal Vehicle for Efficient Synergistic Therapy of Cancer Cells In Vivo, *Advanced Materials*, 25 (2013) 4452-4458.
- [342] F. Gentile, C. Chiappini, D. Fine, R.C. Bhavane, M.S. Peluccio, M.M.-C. Cheng, X. Liu, M. Ferrari, P. Decuzzi, The effect of shape on the margination dynamics of non-neutrally buoyant particles in two-dimensional shear flows, *Journal of Biomechanics*, 41 (2008) 2312-2318.
- [343] Y. Geng, P. Dalhaimer, S. Cai, R. Tsai, M. Tewari, T. Minko, D.E. Discher, Shape effects of filaments versus spherical particles in flow and drug delivery, *Nat Nanotechnol*, 2 (2007) 249-255.
- [344] Y. Li, K. Xiao, J. Luo, J. Lee, S. Pan, K.S. Lam, A novel size-tunable nanocarrier system for targeted anticancer drug delivery, *J Control Release*, 144 (2010) 314-323.
- [345] D. Sutton, N. Nasongkla, E. Blanco, J. Gao, Functionalized micellar systems for cancer targeted drug delivery, *Pharm Res*, 24 (2007) 1029-1046.
- [346] J. Liu, H. Lee, C. Allen, Formulation of drugs in block copolymer micelles: drug loading and release, *Curr Pharm Des*, 12 (2006) 4685-4701.
- [347] Y.-J. Lu, E.-Y. Chuang, Y.-H. Cheng, T.S. Anilkumar, H.-A. Chen, J.-P. Chen, Thermosensitive magnetic liposomes for alternating magnetic field-inducible drug delivery in dual targeted brain tumor chemotherapy, *Chemical Engineering Journal*, 373 (2019) 720-733.
- [348] S. Hofmann, C.T. Foo, F. Rossetti, M. Textor, G. Vunjak-Novakovic, D.L. Kaplan, H.P. Merkle, L. Meinel, Silk fibroin as an organic polymer for controlled drug delivery, *J Control Release*, 111 (2006) 219-227.
- [349] Q. Ma, J. Cao, Y. Gao, S. Han, Y. Liang, T. Zhang, X. Wang, Y. Sun, Microfluidic-mediated nano-drug delivery systems: from fundamentals to fabrication for advanced therapeutic applications, *Nanoscale*, 12 (2020) 15512-15527.
- [350] T. Wongpinyochit, B.F. Johnston, F.P. Seib, Degradation Behavior of Silk Nanoparticles—Enzyme Responsiveness, *ACS Biomaterials Science & Engineering*, 4 (2018) 942-951.
- [351] M. Szekalska, A. Puciłowska, E. Szymańska, P. Ciosek, K. Winnicka, Alginate: current use and future perspectives in pharmaceutical and biomedical applications, *International Journal of Polymer Science*, 2016 (2016).
- [352] B.F. Mogharbel, J.C. Francisco, A.C. Irioda, D.S.M. Dziedzic, P.E. Ferreira, D. de Souza, C.M.C.O. de Souza, N.B. Neto, L.C. Guarita-Souza, C.R.C. Franco, C.V. Nakamura, V. Kaplum, L. Mazarino, E. Lemos-Senna, R. Borsali, P.A. Soto, P. Setton-Avruij, E. Abdelwahid, K.A.T. de Carvalho, Fluorescence properties of curcumin-loaded nanoparticles for cell tracking, *International journal of nanomedicine*, 13 (2018) 5823-5836.
- [353] K.S. Elvira, X.C. i Solvas, R.C.R. Wootton, A.J. Demello, The past, present and potential for microfluidic reactor technology in chemical synthesis, *Nature chemistry*, 5 (2013) 905.
- [354] T. Schikarski, H. Trzenschiok, W. Peukert, M. Avila, Inflow boundary conditions determine T-mixer efficiency, *Reaction Chemistry & Engineering*, 4 (2019) 559-568.
- [355] Z. Xu, C. Lu, J. Riordon, D. Sinton, M.G. Moffitt, Microfluidic Manufacturing of Polymeric Nanoparticles: Comparing Flow Control of Multiscale Structure in Single-Phase Staggered Herringbone and Two-Phase Reactors, *Langmuir*, 32 (2016) 12781-12789.
- [356] M.A. Tomeh, X. Zhao, Recent Advances in Microfluidics for the Preparation of Drug and Gene Delivery Systems, *Molecular Pharmaceutics*, (2020).
- [357] T. Baby, Y. Liu, A.P.J. Middelberg, C.-X. Zhao, Fundamental studies on throughput capacities of hydrodynamic flow-focusing microfluidics for producing monodisperse polymer nanoparticles, *Chemical Engineering Science*, 169 (2017) 128-139.
- [358] J.M. MacInnes, Z. Chen, R.W.K. Allen, Investigation of alternating-flow mixing in microchannels, *Chemical Engineering Science*, 60 (2005) 3453-3467.
- [359] J.M. MacInnes, A. Vikhansky, R.W.K. Allen, Numerical characterisation of folding flow microchannel mixers, *Chemical engineering science*, 62 (2007) 2718-2727.

- [360] T. Au - Wongpinyochit, B.F. Au - Johnston, F.P. Au - Seib, Manufacture and Drug Delivery Applications of Silk Nanoparticles, *JoVE*, (2016) e54669.
- [361] V. Rudyak, A. Minakov, Modeling and optimization of Y-type micromixers, *Micromachines*, 5 (2014) 886-912.
- [362] A.E. Kamholz, P. Yager, Theoretical Analysis of Molecular Diffusion in Pressure-Driven Laminar Flow in Microfluidic Channels, *Biophysical Journal*, 80 (2001) 155-160.
- [363] C.-Y. Lee, W.-T. Wang, C.-C. Liu, L.-M. Fu, Passive mixers in microfluidic systems: A review, *Chemical Engineering Journal*, 288 (2016) 146-160.
- [364] E.L. Tóth, E.G. Holczer, K. Iván, P. Fürjes, Optimized Simulation and Validation of Particle Advection in Asymmetric Staggered Herringbone Type Micromixers, *Micromachines*, 6 (2015).
- [365] J.I. Solomun, J.D. Totten, T. Wongpinyochit, A.J. Florence, F.P. Seib, Manual Versus Microfluidic-Assisted Nanoparticle Manufacture: Impact of Silk Fibroin Stock on Nanoparticle Characteristics, *ACS Biomaterials Science & Engineering*, 6 (2020) 2796-2804.
- [366] J.S. Shim, D.H. Kim, H.J. Jung, J.H. Kim, D. Lim, S.K. Lee, K.W. Kim, J.W. Ahn, J.S. Yoo, J.R. Rho, J. Shin, H.J. Kwon, Hydrazinocurcumin, a novel synthetic curcumin derivative, is a potent inhibitor of endothelial cell proliferation, *Bioorg Med Chem*, 10 (2002) 2987-2992.
- [367] R.L. Siegel, K.D. Miller, A. Goding Sauer, S.A. Fedewa, L.F. Butterly, J.C. Anderson, A. Cercek, R.A. Smith, A. Jemal, Colorectal cancer statistics, 2020, *CA: A Cancer Journal for Clinicians*, 70 (2020) 145-164.
- [368] K. Park, S. Lee, E. Kang, K. Kim, K. Choi, I.C. Kwon, New Generation of Multifunctional Nanoparticles for Cancer Imaging and Therapy, *Advanced Functional Materials*, 19 (2009) 1553-1566.
- [369] L. Brannon-Peppas, J.O. Blanchette, Nanoparticle and targeted systems for cancer therapy, *Advanced Drug Delivery Reviews*, 56 (2004) 1649-1659.
- [370] Q. Jin, Y. Deng, X. Chen, J. Ji, Rational Design of Cancer Nanomedicine for Simultaneous Stealth Surface and Enhanced Cellular Uptake, *ACS Nano*, 13 (2019) 954-977.
- [371] H. Maeda, H. Nakamura, J. Fang, The EPR effect for macromolecular drug delivery to solid tumors: Improvement of tumor uptake, lowering of systemic toxicity, and distinct tumor imaging in vivo, *Advanced Drug Delivery Reviews*, 65 (2013) 71-79.
- [372] F.W. Pratiwi, C.W. Kuo, B.-C. Chen, P. Chen, Recent advances in the use of fluorescent nanoparticles for bioimaging, *Nanomedicine*, 14 (2019) 1759-1769.
- [373] V. Torchilin, Tumor delivery of macromolecular drugs based on the EPR effect, *Adv Drug Deliv Rev*, 63 (2011) 131-135.
- [374] L.A. Lane, X. Qian, A.M. Smith, S. Nie, Physical chemistry of nanomedicine: understanding the complex behaviors of nanoparticles in vivo, *Annual review of physical chemistry*, 66 (2015) 521-547.
- [375] S. Mitragotri, J. Lahann, Physical approaches to biomaterial design, *Nature materials*, 8 (2009) 15-23.
- [376] C.Y. Tay, M.I. Setyawati, J. Xie, W.J. Parak, D.T. Leong, Back to Basics: Exploiting the Innate Physico-chemical Characteristics of Nanomaterials for Biomedical Applications, *Advanced Functional Materials*, 24 (2014) 5936-5955.
- [377] J. Wang, W. Mao, L.L. Lock, J. Tang, M. Sui, W. Sun, H. Cui, D. Xu, Y. Shen, The role of micelle size in tumor accumulation, penetration, and treatment, *ACS nano*, 9 (2015) 7195-7206.
- [378] O. Veis, B.C. Tang, K.A. Whitehead, D.G. Anderson, R. Langer, Managing diabetes with nanomedicine: challenges and opportunities, *Nature Reviews Drug Discovery*, 14 (2015) 45-57.
- [379] C. Sheridan, Proof of concept for next-generation nanoparticle drugs in humans, *Nature Biotechnology*, 30 (2012) 471-472.
- [380] R. Duncan, Polymer conjugates as anticancer nanomedicines, *Nature Reviews Cancer*, 6 (2006) 688-701.
- [381] H.H. Tønnesen, J. Karlsen, Alginate in Drug Delivery Systems, *Drug Development and Industrial Pharmacy*, 28 (2002) 621-630.

- [382] J.-M. Rabanel, P. Hildgen, X. Banquy, Assessment of PEG on polymeric particles surface, a key step in drug carrier translation, *Journal of Controlled Release*, 185 (2014) 71-87.
- [383] R. Chen, J.E. Wulff, M.G. Moffitt, Microfluidic Processing Approach to Controlling Drug Delivery Properties of Curcumin-Loaded Block Copolymer Nanoparticles, *Molecular Pharmaceutics*, 15 (2018) 4517-4528.
- [384] X. Wang, T. Yucel, Q. Lu, X. Hu, D.L. Kaplan, Silk nanospheres and microspheres from silk/pva blend films for drug delivery, *Biomaterials*, 31 (2010) 1025-1035.
- [385] E. Wenk, A.J. Wandrey, H.P. Merkle, L. Meinel, Silk fibroin spheres as a platform for controlled drug delivery, *Journal of Controlled Release*, 132 (2008) 26-34.
- [386] F.P. Seib, G.T. Jones, J. Rnjak-Kovacina, Y. Lin, D.L. Kaplan, pH-dependent anticancer drug release from silk nanoparticles, *Adv Healthc Mater*, 2 (2013) 1606-1611.
- [387] S.B. Lim, A. Banerjee, H. Önyüksel, Improvement of drug safety by the use of lipid-based nanocarriers, *Journal of Controlled Release*, 163 (2012) 34-45.
- [388] P.P. Deshpande, S. Biswas, V.P. Torchilin, Current trends in the use of liposomes for tumor targeting, *Nanomedicine*, 8 (2013) 1509-1528.
- [389] C. Lin, X. Zhang, H. Chen, Z. Bian, G. Zhang, M.K. Riaz, D. Tyagi, G. Lin, Y. Zhang, J. Wang, A. Lu, Z. Yang, Dual-ligand modified liposomes provide effective local targeted delivery of lung-cancer drug by antibody and tumor lineage-homing cell-penetrating peptide, *Drug Delivery*, 25 (2018) 256-266.
- [390] R. Bazak, M. Houry, S. El Achy, S. Kamel, T. Refaat, Cancer active targeting by nanoparticles: a comprehensive review of literature, *Journal of Cancer Research and Clinical Oncology*, 141 (2015) 769-784.
- [391] Z.S. Al-Ahmady, O. Chaloin, K. Kostarelos, Monoclonal antibody-targeted, temperature-sensitive liposomes: In vivo tumor chemotherapeutics in combination with mild hyperthermia, *Journal of Controlled Release*, 196 (2014) 332-343.
- [392] G. Mikhaylov, U. Mikac, A.A. Magaeva, V.I. Itin, E.P. Naiden, I. Psakhye, L. Babes, T. Reinheckel, C. Peters, R. Zeiser, M. Bogyo, V. Turk, S.G. Psakhye, B. Turk, O. Vasiljeva, Ferri-liposomes as an MRI-visible drug-delivery system for targeting tumours and their microenvironment, *Nature Nanotechnology*, 6 (2011) 594-602.
- [393] M. Arruebo, R. Fernández-Pacheco, M.R. Ibarra, J. Santamaría, Magnetic nanoparticles for drug delivery, *Nano Today*, 2 (2007) 22-32.
- [394] A.M. Smith, H. Duan, A.M. Mohs, S. Nie, Bioconjugated quantum dots for in vivo molecular and cellular imaging, *Advanced Drug Delivery Reviews*, 60 (2008) 1226-1240.
- [395] E. Kastner, R. Kaur, D. Lowry, B. Moghaddam, A. Wilkinson, Y. Perrie, High-throughput manufacturing of size-tuned liposomes by a new microfluidics method using enhanced statistical tools for characterization, *International Journal of Pharmaceutics*, 477 (2014) 361-368.
- [396] M. Guimarães Sá Correia, M.L. Briuglia, F. Niosi, D.A. Lamprou, Microfluidic manufacturing of phospholipid nanoparticles: Stability, encapsulation efficacy, and drug release, *International Journal of Pharmaceutics*, 516 (2017) 91-99.
- [397] F. Schweizer, Cationic amphiphilic peptides with cancer-selective toxicity, *European Journal of Pharmacology*, 625 (2009) 190-194.
- [398] J.S. Mader, D.W. Hoskin, Cationic antimicrobial peptides as novel cytotoxic agents for cancer treatment, *Expert Opinion on Investigational Drugs*, 15 (2006) 933-946.
- [399] C. Chen, Y. Zhang, Z. Hou, X. Cui, Y. Zhao, H. Xu, Rational Design of Short Peptide-Based Hydrogels with MMP-2 Responsiveness for Controlled Anticancer Peptide Delivery, *Biomacromolecules*, 18 (2017) 3563-3571.
- [400] C.D. Fjell, J.A. Hiss, R.E.W. Hancock, G. Schneider, Designing antimicrobial peptides: form follows function, *Nature reviews Drug discovery*, 11 (2012) 37-51.
- [401] B.M. Peters, M.E. Shirtliff, M.A. Jabra-Rizk, Antimicrobial peptides: primeval molecules or future drugs?, *PLoS Pathog*, 6 (2010) e1001067.
- [402] A.T.Y. Yeung, S.L. Gellatly, R.E.W. Hancock, Multifunctional cationic host defence peptides and their clinical applications, *Cellular and Molecular Life Sciences*, 68 (2011) 2161.

- [403] S. Cirillo, Short cationic peptides for gene delivery into cancer cells, (2017).
- [404] J. Hu, C. Chen, S. Zhang, X. Zhao, H. Xu, X. Zhao, J.R. Lu, Designed Antimicrobial and Antitumor Peptides with High Selectivity, *Biomacromolecules*, 12 (2011) 3839-3843.
- [405] J.E. Cortes, S.L. Goldberg, E.J. Feldman, D.A. Rizzeri, D.E. Hogge, M. Larson, A. Pigneux, C. Recher, G. Schiller, K. Warzocha, H. Kantarjian, A.C. Louie, J.E. Kolitz, Phase II, multicenter, randomized trial of CPX-351 (cytarabine:daunorubicin) liposome injection versus intensive salvage therapy in adults with first relapse AML, *Cancer*, 121 (2015) 234-242.
- [406] S. Joshi, M.T. Hussain, C.B. Roces, G. Anderluzzi, E. Kastner, S. Salmaso, D.J. Kirby, Y. Perrie, Microfluidics based manufacture of liposomes simultaneously entrapping hydrophilic and lipophilic drugs, *International Journal of Pharmaceutics*, 514 (2016) 160-168.
- [407] I.V. Zhigaltsev, N. Belliveau, I. Hafez, A.K.K. Leung, J. Huft, C. Hansen, P.R. Cullis, Bottom-Up Design and Synthesis of Limit Size Lipid Nanoparticle Systems with Aqueous and Triglyceride Cores Using Millisecond Microfluidic Mixing, *Langmuir*, 28 (2012) 3633-3640.
- [408] Y.-Q. Zhang, W.-D. Shen, R.-L. Xiang, L.-J. Zhuge, W.-J. Gao, W.-B. Wang, Formation of silk fibroin nanoparticles in water-miscible organic solvent and their characterization, *Journal of Nanoparticle Research*, 9 (2007) 885-900.
- [409] U. Shimanovich, F.S. Ruggeri, E. De Genst, J. Adamcik, T.P. Barros, D. Porter, T. Müller, R. Mezzenga, C.M. Dobson, F. Vollrath, C. Holland, T.P.J. Knowles, Silk micrococoon for protein stabilisation and molecular encapsulation, *Nature Communications*, 8 (2017) 15902.
- [410] A. Patel, Y. Hu, J.K. Tiwari, K.P. Velikov, Synthesis and characterisation of zein–curcumin colloidal particles, *Soft Matter*, 6 (2010) 6192-6199.
- [411] J. Chen, J. Zheng, D.J. McClements, H. Xiao, Tangeretin-loaded protein nanoparticles fabricated from zein/ β -lactoglobulin: Preparation, characterization, and functional performance, *Food Chemistry*, 158 (2014) 466-472.
- [412] X. Huang, C.S. Brazel, On the importance and mechanisms of burst release in matrix-controlled drug delivery systems, *Journal of Controlled Release*, 73 (2001) 121-136.
- [413] C. Chen, J. Hu, P. Zeng, F. Pan, M. Yaseen, H. Xu, J.R. Lu, Molecular mechanisms of anticancer action and cell selectivity of short α -helical peptides, *Biomaterials*, 35 (2014) 1552-1561.
- [414] R. Zhang, N. Zheng, Z. Song, L. Yin, J. Cheng, The effect of side-chain functionality and hydrophobicity on the gene delivery capabilities of cationic helical polypeptides, *Biomaterials*, 35 (2014) 3443-3454.
- [415] S. Kolusheva, T. Shahal, R. Jelinek, Peptide–Membrane Interactions Studied by a New Phospholipid/Polydiacetylene Colorimetric Vesicle Assay, *Biochemistry*, 39 (2000) 15851-15859.
- [416] B.A. Smith, D.S. Daniels, A.E. Coplin, G.E. Jordan, L.M. McGregor, A. Schepartz, Minimally Cationic Cell-Permeable Miniature Proteins via α -Helical Arginine Display, *Journal of the American Chemical Society*, 130 (2008) 2948-2949.
- [417] G. Mehta, A.Y. Hsiao, M. Ingram, G.D. Luker, S. Takayama, Opportunities and challenges for use of tumor spheroids as models to test drug delivery and efficacy, *Journal of Controlled Release*, 164 (2012) 192-204.
- [418] M. Yu, L. Xu, F. Tian, Q. Su, N. Zheng, Y. Yang, J. Wang, A. Wang, C. Zhu, S. Guo, X. Zhang, Y. Gan, X. Shi, H. Gao, Rapid transport of deformation-tuned nanoparticles across biological hydrogels and cellular barriers, *Nature Communications*, 9 (2018) 2607.
- [419] T.K. Kim, J.H. Eberwine, Mammalian cell transfection: the present and the future, *Analytical and Bioanalytical Chemistry*, 397 (2010) 3173-3178.
- [420] X. Du, J. Wang, Q. Zhou, L. Zhang, S. Wang, Z. Zhang, C. Yao, Advanced physical techniques for gene delivery based on membrane perforation, *Drug Delivery*, 25 (2018) 1516-1525.
- [421] M. Reberšek, D. Miklavčič, Advantages and Disadvantages of Different Concepts of Electroporation Pulse Generation, *Automatika*, 52 (2011) 12-19.

Supplementary data

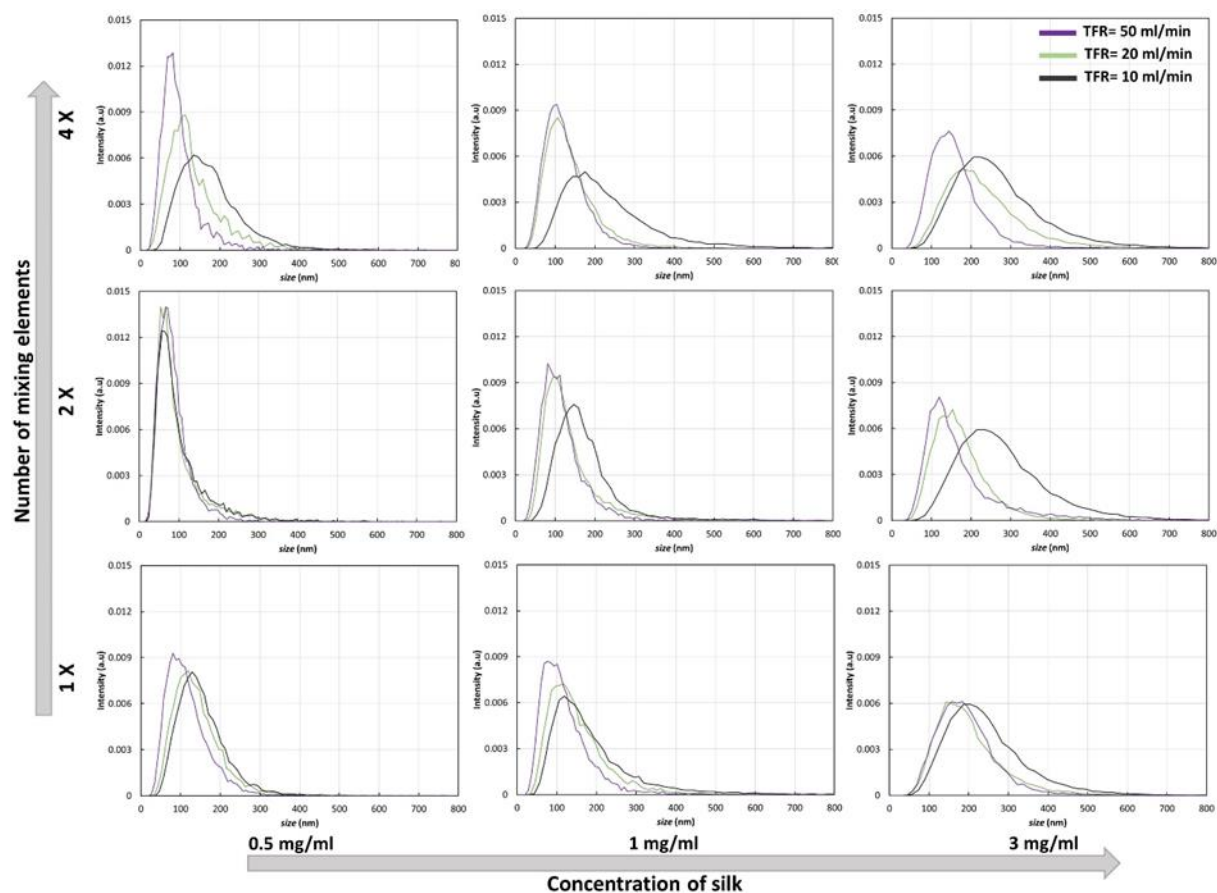


Figure S1. The impact of concentration and mixing elements on the size and size distribution of silk nanoparticles.

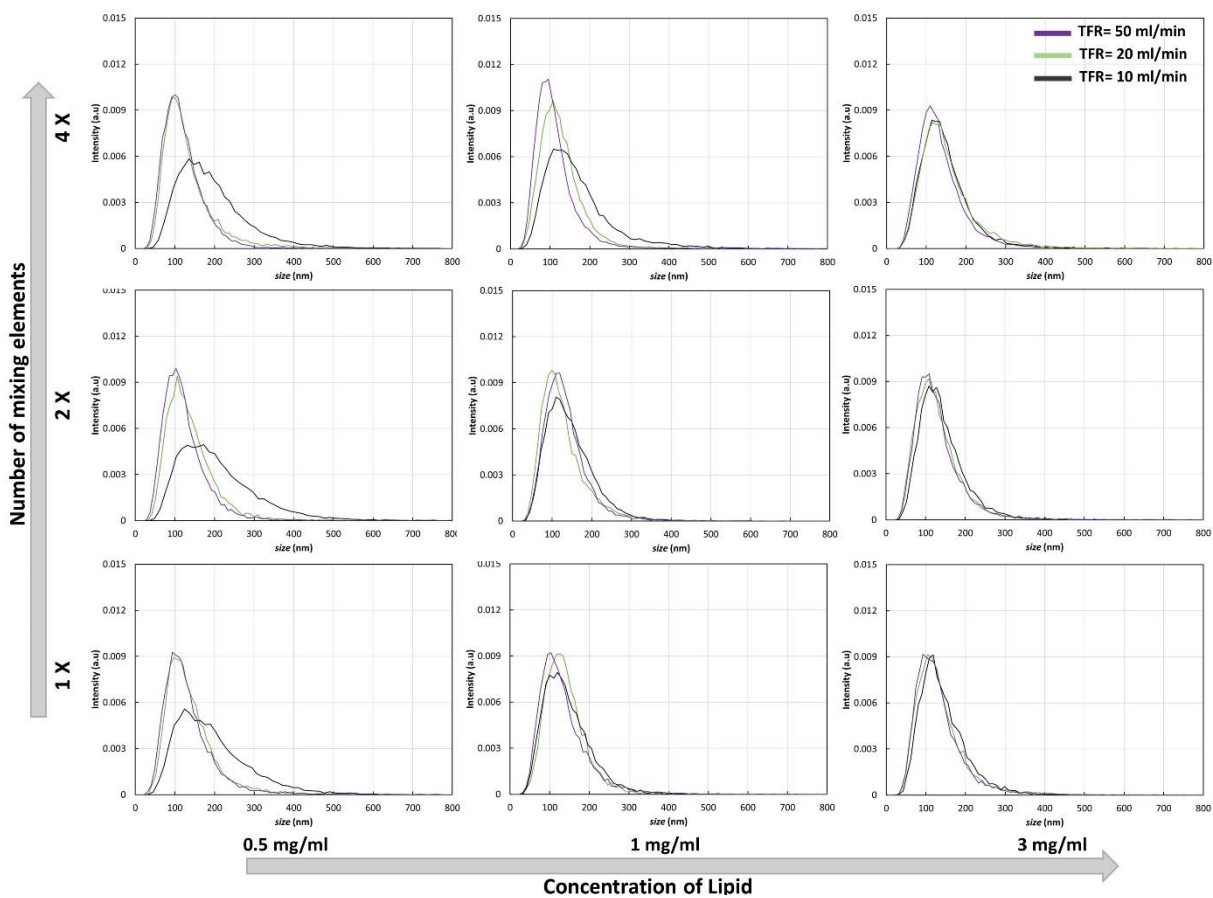


Figure S2. The impact of concentration and mixing elements on the size and size distribution of dipalmitoylphosphatidylcholine (DPPC) lipid nanoparticles.